

2016

# Thermal emission signatures in non-thermal blazars

---

<https://hdl.handle.net/2144/19757>

*Boston University*

BOSTON UNIVERSITY  
GRADUATE SCHOOL OF ARTS AND SCIENCES

Dissertation

**Thermal Emission Signatures in Non-thermal Blazars**

by

**Michael Paul Malmrose**

B.S., Weber State University, Ogden, UT, 2007  
M.A., Boston University, Boston, MA, 2010

Submitted in partial fulfillment of the  
requirements for the degree of  
Doctor of Philosophy

2016

© Copyright by  
Michael Paul Malmrose  
2016

Approved by

First Reader

---

Alan P. Marscher, PhD  
Professor of Astronomy  
Boston University

Second Reader

---

Paul Withers, PhD  
Assistant Professor of Astronomy  
Boston University

*Words are flowing out like endless rain into a paper cup,  
they slither wildly as they slip away across the Universe.  
-The Beatles-*

# Acknowledgments

I wish to begin by thanking the many wonderful teachers I've had up to this point in my life, especially the faculty in the Physics Department at Weber State University. An aspiring Astronomer from a small town in Utah could not have asked for a better group of people to acquire the physics background necessary for tackling a PhD in astrophysics from. I thank my advisor Alan Marscher for taking me on as his graduate student, and for the many pep-talks he has given these past eight years.

When I began working in the blazar group in the summer of 2009, I inherited some old *Spitzer* data that appeared likely to head for a null result, but would be a great starting off point for casting my line into the data analysis stream. Much to my surprise, not only were there fish in the water, they were biting, and I had a live one instantly. What was supposed to be a summer project became my 2011 ApJ paper and the basis for Chapter 3 of this dissertation. I want to thank my committee members: Alan Marscher, Svetlana Jorstad, Elizabeth Blanton, Paul Withers, and Martin Elvis whose insightful comments made this work stronger. I wish to thank Paul Smith for making available the large dataset on which this dissertation relies.

I would to thank my family for their support of my educational goals throughout my entire life. My father Eric helped instill in me my love of Physics, and The Beatles, and nobody would have been prouder than him to see this day. My Stepfather Chad reignited my love for fishing, which had lied dormant for many years, and provided me with a hobby that enriched my undergraduate years. My Mother,

Roberta, has been very supportive throughout my life, and without her, I could not have accomplished writing this dissertation. My brother, London, shares my passion for both professional basketball and professional wrestling and the most memorable moments of my life during graduate school include our mutual shock at the Undertaker's defeat at Wrestlemania XXX, and the sad realization that John Stockton is not going to be walking through that door.

I thank my friends back in Utah, Ron Proctor and Jackson Hogg, whose friendship has been cherished as long as I have known them. My pub trivia team, consisting at various times of Rachel Paterno-Mahler, Carl Boone, Christina Kay, Ren Cashman, Mary Gordon, Sierra Grant, Stephanie Morrison, and Sam Bessey have given me some of the most fun moments I've had in Boston. I thank my good friends Elizabeth Fucetola and Nicholas Lee for our many years long tradition of walking the Freedom Trail every Fourth of July. Without Emmet Golden-Marx, I might never have seen not one, but both surviving Beatles in Concert, and those memories will be with me for a lifetime. Meredith Danowski and Jan Marie Andersen completed my study triumvirate of Teaching Fellows during our first semester which helped each of us through difficult coursework. I'd like to thank my partner Stephanie Morrison, whose support throughout the process of writing this dissertation, including providing copy-editing services, helped me push through the tense situation that is preparing to defend a dissertation.

Finally, I wish to acknowledge financial support, and data access that I have been provided during my time at Boston University. This work is based on observations made with the Spitzer Space Telescope, which is operated by the Jet Propulsion Laboratory (JPL), California Institute of Technology under a contract with NASA. Funding for this project was supplied by JPL through Spitzer grant 1289764, by NASA

through Fermi Guest Investigator grant NNX08AV65G, and by National Science Foundation (NSF) grant AST-0907893. This study included observations with the PRISM camera (PI: Kenneth Janes), and the Mimir instrument (PI: Dan Clemens), both developed at Boston University and Lowell Observatory, with financial support from NSF, Boston University, and Lowell Observatory. This dissertation makes use of data products from the Two Micron All Sky Survey, which is a joint project of the University of Massachusetts and the Infrared Processing and Analysis Center/California Institute of Technology, funded by NASA and the NSF. Funding for the SDSS and SDSS-II has been provided by the Alfred P. Sloan Foundation, the Participating Institutions, NSF, the U.S. Department of Energy, NASA, the Japanese Monbukagakusho, the Max Planck Society, and the Higher Education Funding Council for England. The SDSS Web site is <http://www.sdss.org/>. Funding for this work was partially supplied by the NSF GK12 GLACIER (Global Change Initiative-Education and Research) program, grant DGE-0947950, and by the *Fermi* Guest Investigator program NASA grant NNX11AO40. Data from the Steward Observatory spectropolarimetric monitoring project were used. This program is supported by Fermi Guest Investigator grants NNX08AW56G, NNX09AU10G, NNX12AO93G, and NNX15AU81G.



# Thermal Emission Signatures in Non-thermal Blazars

Michael Paul Malmrose

Boston University, Graduate School of Arts and Sciences, 2016

Major Professor: Alan P. Marscher, Professor of Astronomy.

## ABSTRACT

Blazars, a subclass of active galactic nuclei with powerful relativistic plasma jets, are among the most luminous and violently variable objects in the universe. They emit radiation across the entire electromagnetic spectrum, and often change in brightness over the course of hours or days. Different emission mechanisms are necessary in order to explain the observed flux in different frequency ranges. In the ultraviolet-optical-infrared regime these include components that arise from: 1) polarized synchrotron radiation emanating from a powerful parsec-scale jet flowing from near the central accreting black hole, 2) a multi-temperature accretion disk emitting thermal radiation, and 3) an optically thick dusty torus located several parsecs from the central engine that absorbs and re-emits, at infrared wavelengths, radiation originating in the accretion disk. The goal of this study is to determine the relative importance of these spectral components in the spectra of blazars. I use data from the *Spitzer* Space Telescope in order to search for the presence of the dusty torus surrounding four blazars, as well as to determine its luminosity and temperature. In two of the observed sources, 1222+216 and CTA102, I determine that the torus can be modeled as a 1200 K blackbody emitting at nearly  $10^{46}$  erg s<sup>-1</sup>. Furthermore, I determine the relative variability of the accretion disk of a sample of blazars by using spectropolarimetry observations to separate the optical-UV spectrum into a polarized

component, consisting of radiation described by a power-law  $F_\nu \propto \nu^{-\alpha}$ , and an accretion disk which consists of a thin disk described by the power-law  $F_{disk} \propto \nu^{1/3}$  plus a hot-spot of variable temperature. The spectra of several blazars are explained by a version of this model in which the thin disk component is held constant, while the blackbody varies on timescales of approximately years resulting with a flux of the blackbody component comparable to the power-law disk component. I find that variations in the emission from the hot-spot occurs approximately within 100 days of  $\gamma$ -ray variations.

# Contents

<b>1</b>	<b>Introduction</b>	<b>1</b>
1.1	Active Galactic Nuclei . . . . .	1
1.1.1	Blazars . . . . .	2
1.2	The Emission Mechanisms of Active Galactic Nuclei . . . . .	4
1.2.1	Thermal Emission Processes . . . . .	4
1.2.2	Overview of Synchrotron Radiation . . . . .	9
1.2.3	Inverse-Compton Radiation . . . . .	15
1.3	Dusty Tori . . . . .	18
1.3.1	An Introduction to Astrophysical Dust . . . . .	18
1.3.2	Continuous Medium . . . . .	20
1.3.3	Clumpy Torus . . . . .	21
1.3.4	Apparent Superluminal Motion in Blazars . . . . .	22
<b>2</b>	<b>Observational Data</b>	<b>24</b>
2.1	Observations and Analysis . . . . .	24
2.1.1	<i>Spitzer</i> Space Telescope . . . . .	24
2.1.2	The Sample Chosen for Analysis with the <i>Spitzer</i> Space Telescope	27
2.2	Data Selected from the Steward Observatory Blazar Monitoring Project	29
2.3	Near-Infrared Ground Based Observations . . . . .	30
2.3.1	IR observations obtained at Lowell Observatory . . . . .	31
2.3.2	Observations Obtained with the IRTF . . . . .	33
2.4	Gamma-ray Observations From the <i>Fermi</i> Gamma-ray Telescope . . . . .	34

<b>3</b>	<b>Emission from Hot Dust in the Infrared Spectra of Gamma-ray Bright Blazars</b>	<b>36</b>
3.1	Introduction . . . . .	37
3.2	Data . . . . .	40
3.3	Results . . . . .	42
3.4	Discussion . . . . .	46
3.4.1	Dust Properties of 4C 21.35 and Comparison with Non-blazars	46
3.4.2	Relation between Dust and Gamma-ray Emission . . . . .	51
3.5	Summary . . . . .	54
<b>4</b>	<b>Analysis of the Level of Variability of the Components of Optical- UV Emission</b>	<b>59</b>
4.1	Introduction . . . . .	59
4.2	Determining the Contribution of Synchrotron Radiation and the Big Blue Bump to the Optical-Ultraviolet Spectrum . . . . .	62
4.2.1	Preparing the Spectra for the Two-Component Fit . . . . .	62
4.2.2	Determining the Spectral Index of the Synchrotron Component from the Polarized Flux . . . . .	68
4.2.3	Performing the Two-Component Fit . . . . .	71
4.3	Keeping the Big Blue Bump Component Constant . . . . .	74
4.4	Modifying the Disk Component to Contain an Additional Blackbody Component . . . . .	78
4.5	The Effect of Wavelength Dependent Polarization on the BBB and Synchrotron Radiation Components of the Optical Spectrum . . . . .	86
4.6	Composing Difference Spectra of the Flux and Polarized Flux . . . . .	91
4.7	Application to Other Sources . . . . .	94
4.7.1	BL Lacs . . . . .	94
4.7.2	FSRQs . . . . .	108

4.8	Calculated Properties of the Optical-UV Spectra of Blazars . . . . .	112
<b>5</b>	<b>Comparison of Optical Variability to Variability at Infrared Wave- lengths</b>	<b>132</b>
5.1	Infrared Variability of a Sample of Blazars . . . . .	132
5.1.1	Introduction . . . . .	132
5.1.2	Near Infrared Variability of Other Blazars . . . . .	137
<b>6</b>	<b>Gamma-Ray Variability of a Sample of Blazars Compared to Vari- ability of the Accretion Disk</b>	<b>153</b>
6.1	The Discrete Correlation Function . . . . .	153
6.2	Computing the Discrete Correlation Function (DCF) for a Small Sam- ple of Blazars . . . . .	155
6.2.1	1222+216 . . . . .	155
6.2.2	OJ248 . . . . .	159
6.2.3	3C273 . . . . .	162
6.2.4	CTA102 . . . . .	164
<b>7</b>	<b>Conclusions</b>	<b>166</b>
	<b>References</b>	<b>172</b>
	<b>Curriculum Vitae</b>	<b>179</b>

# List of Tables

2.1	Luminosity Distances and Dates of Observations . . . . .	29
2.2	Observing Campaigns at Lowell Observatory and Infrared Telescope Facility (IRTF) . . . . .	31
3.1	Data for 4C 21.35 . . . . .	53
3.2	Data for PKS 1510-089 . . . . .	55
3.3	Data for CTA102 . . . . .	57
3.4	Data for ON231 . . . . .	58
4.1	Subset of Blazars Monitored by the Steward Observatory Fermi Support Mission . . . . .	61
4.1	Subset of Blazars Monitored by the Steward Observatory Fermi Support Mission . . . . .	63
4.2	Host Galaxy Flux of BL Lacertae . . . . .	107
4.3	Properties of Optical Spectral Components of Select Blazars . . . . .	113
5.1	Near-IR Excess Flux in Selected Blazars . . . . .	138
6.1	Parameters of Superluminal Motion in Two Blazars . . . . .	158

# List of Figures

1.1	FSRQ spectrum vs. BL Lac . . . . .	5
1.2	Multi-temperature disk compared to a blackbody . . . . .	8
1.3	Expected inner radius of torus at various active galactic nucleus (AGN) luminosities . . . . .	10
1.4	Synchrotron emission spectrum of a single particle . . . . .	12
1.5	The Compton effect . . . . .	16
1.6	Apparent Superluminal Motion in a Blazar Jet . . . . .	23
2.1	Irac mosaic . . . . .	25
2.2	MIPS mosaic . . . . .	26
2.3	Mimir images . . . . .	33
2.4	SpeX image . . . . .	34
3.1	Initial <i>Spitzer</i> SED for 1222+216 . . . . .	38
3.2	Initial <i>Spitzer</i> SED for 1219+285 . . . . .	40
3.3	Initial <i>Spitzer</i> SED for CTA102 . . . . .	41
3.4	Initial <i>Spitzer</i> SED for 1510-089 . . . . .	42
3.5	<i>Spitzer</i> SED for 4C 21.35 . . . . .	45
3.6	<i>Spitzer</i> SED for CTA102 . . . . .	46
3.7	<i>Spitzer</i> SED for 1510-089 . . . . .	48
3.8	<i>Spitzer</i> SED for 1219+285 . . . . .	49
3.9	Spectra for all four targets. . . . .	50

4.1	Polarization spectrum . . . . .	64
4.2	FSRQ emission line template for 1222+216 . . . . .	66
4.3	Emission line template removed from a spectrum of 1222+216 . . . . .	67
4.4	1222+216 spectral indices . . . . .	70
4.5	Reduced $\chi^2$ of 1222+216 resulting from a fit with a single power-law . . . . .	71
4.6	1222+216 spectral components . . . . .	72
4.7	Reduced $\chi^2$ to initial fit of 1222+216 . . . . .	73
4.8	1222+216 spectral component decomposition . . . . .	74
4.9	1222+216 spectral component histograms . . . . .	75
4.10	1222+216 fit with a constant BBB . . . . .	76
4.11	Spectrum of 1222+216 fit with a constant BBB . . . . .	77
4.12	Spectral components fit to 1222+216 with the accretion disk model modified to include a hot blackbody . . . . .	80
4.13	The spectral components of 1222+216 after adding a variable temper- ature blackbody component to the accretion disk model . . . . .	82
4.14	Histograms of the spectral components of 1222+216 after adding a hot blackbody component to the accretion disk model . . . . .	83
4.15	Calculated blackbody temperature and size for 1222+216 . . . . .	87
4.16	Simulation of wavelength dependent polarization . . . . .	88
4.17	TEMZ histogram of wavelength dependent polarization . . . . .	89
4.18	Wavelength dependent polarization in 1222+216 . . . . .	90
4.19	Difference spectra for 1222+216 . . . . .	93
4.20	Spectral indices of 3C66A . . . . .	94
4.21	Spectral Components and reduced $\chi^2$ for fitting spectra from 3C66A . . . . .	96
4.22	Wavelength dependence of the linear polarization of 3C66A and dif- ference spectrum . . . . .	97



4.23	Spectral indices of OJ287 . . . . .	98
4.24	Wavelength dependence of the linear polarization of OJ287 . . . . .	100
4.25	Reduced $\chi^2$ for fitting spectra from OJ287 . . . . .	101
4.26	Spectral indices for 1219+285 . . . . .	102
4.27	Reduced $\chi^2$ for fitting spectra from 1219+285 . . . . .	103
4.28	Wavelength dependence of the linear polarization off S31227+25 . . . . .	104
4.29	Spectral components of S31227+25 . . . . .	105
4.30	Spectral indices for 1219+285 . . . . .	106
4.31	Spectral components of BL Lac . . . . .	108
4.32	Spectral components of 0735+178 . . . . .	116
4.33	Wavelength dependence of the linear polarization of 0420-014 . . . . .	117
4.34	Spectral components of 0420-014 . . . . .	118
4.35	Wavelength dependence of the linear polarization of CTA26 . . . . .	119
4.36	Spectral components of 0420-014 . . . . .	120
4.37	Wavelength dependence of the linear polarization of 3C279 . . . . .	121
4.38	Spectral components of 3C279 . . . . .	122
4.39	Wavelength dependence of the linear polarization of 1510-089 . . . . .	123
4.40	Spectral components of 1510-089 . . . . .	124
4.41	Difference spectra for 1510-089 . . . . .	125
4.42	Wavelength dependence of the linear polarization of CTA102 . . . . .	125
4.43	Spectral components of CTA102 . . . . .	126
4.44	Spectral components of 3C454.3 . . . . .	127
4.45	Wavelength dependence of the linear polarization of 3C454.3 . . . . .	128
4.46	Wavelength dependence of the linear polarization of OJ248 . . . . .	128
4.47	Spectral components of CTA102 . . . . .	129
4.48	Wavelength dependence of the linear polarization of 3C273 . . . . .	130

4.49	Spectral components of 3C273 . . . . .	131
5.1	Infrared flux measurements of 1222+216 . . . . .	133
5.2	Infrared flux excess of 1222+216 . . . . .	135
5.3	Infrared excess SED of 1222+216 . . . . .	136
5.4	Infrared flux measurements of 1219+285 . . . . .	139
5.5	Infrared excess SED of 1219+285 . . . . .	140
5.6	Infrared flux measurements of 3C66A . . . . .	141
5.7	Infrared excess SED of 3C66A . . . . .	142
5.8	Infrared flux measurements of BL Lac . . . . .	143
5.9	Infrared excess SED of BL Lac . . . . .	144
5.10	Infrared flux measurements of 3C273 . . . . .	145
5.11	Infrared excess SED of 3C273 . . . . .	146
5.12	Infrared flux measurements of 1510-089 . . . . .	147
5.13	Infrared flux measurements of CTA102 . . . . .	148
5.14	Infrared flux measurements of 3C454.3 . . . . .	149
5.15	Infrared flux measurements of 0420-014 . . . . .	150
5.16	Infrared flux measurements of OJ248 . . . . .	151
6.1	Gamma-ray and accretion disk light curve of 1222+216 . . . . .	156
6.2	UDCF and DCF of 1222+216 between gamma-ray flux and accretion disk flux . . . . .	157
6.3	Zoomed in DCF of 1222+216 between gamma-ray flux and accretion disk flux . . . . .	159
6.4	Gamma-ray and accretion disk light curve of OJ248 . . . . .	160
6.5	DCF of OJ248 between gamma-ray flux and accretion disk flux . . . .	161
6.6	Gamma-ray and accretion disk light curve of 3C273 . . . . .	162
6.7	DCF of 3C273 between gamma-ray flux and accretion disk flux . . . .	163

6.8	Gamma-ray and accretion disk light curve of 3C273 . . . . .	164
6.9	DCF of CTA102 between gamma-ray flux and accretion disk flux . .	165

# List of Abbreviations

2MASS	Two-Micron All Sky Survey . . . . .	26, 43
AGN	active galactic nucleus xiii, 1–4, 7–9, 11, 17, 19–21, 35, 39, 42, 44, 54	
ALMA	Atacama Large Millimeter/submillimeter Array . . . . .	145
AU	astronomical unit . . . . .	82, 103
BBB	big blue bump 3, 57, 59, 60, 63, 66, 68–71, 82, 87, 91, 95, 97, 100, 101, 106, 110, 115, 118, 128, 130	
BLR	broad line region . . . . .	2
CGRO	<i>Compton</i> Gamma-Ray Observatory . . . . .	25
CMB	cosmic microwave background . . . . .	17
DCF	Discrete Correlation Function . . . . .	140, 141
EGRET	Energetic Gamma-Ray Experiment Telescope . . . . .	25
ERC	external-radiation Compton . . . . .	35, 37, 50
FSRQ	flat-spectrum radio quasar . 2, 3, 22, 58, 60, 62, 63, 89, 100, 106, 110, 115, 117, 118, 142, 143	
GBM	Gamma-ray Burst Monitor . . . . .	32
IC	inverse-Compton . . . . .	15, 17, 18, 34, 35, 49, 50, 52
IR	infrared3, 8, 19, 22, 23, 25, 26, 28, 29, 31, 34, 36–38, 40, 42–46, 49, 50, 52–54, 115, 117, 120–125, 128, 130, 132, 134, 138–140, 142–145	
IRAC	Infrared Array Camera . . . . .	22, 23, 25, 36, 43, 51
IRAF	Image Reduction and Analysis Facility . . . . .	28
IRS	Infrared Spectrograph . . . . .	23–25, 36, 42–45, 48, 51

IRTF	Infrared Telescope Facility . . . . .	xii, 28, 29, 31, 120, 121
JWST	James Webb Space Telescope . . . . .	145
Jy	Jansky . . . . .	123
LAT	Large Area Telescope . . . . .	25, 32, 33
LH	Long-High . . . . .	24
LL	Long-Low . . . . .	24, 25
MAGIC	Major Atmospheric Gamma Imaging Cherenkov . . . . .	50
MIPS	Multiband Imaging Photometer . . . . .	22, 24, 25, 36, 39–41, 43, 46
NASA	National Aeronautics and Space Administration . . . . .	22, 23, 120
NLR	narrow line region . . . . .	2
NOAO	National Optical Astronomy Observatories . . . . .	28
pc	parsec . . . . .	2, 19, 41, 42
PRISM	Perkins Reimaging System . . . . .	26
<i>SDSS</i>	Sloan Digital Sky Survey . . . . .	26, 62, 88
SED	spectral energy distribution 2–4, 13, 19, 24, 34–37, 39, 44, 45, 50, 54, 57, 120, 124, 125, 128, 130, 132, 142, 145	
SH	Short-High . . . . .	24
SL	Short-Long . . . . .	24, 25
SMBH	super-massive black hole . . . . .	1
SSC	synchrotron self-Comptonization . . . . .	3, 17
SST	<i>Spitzer</i> Space Telescope . . . . .	22, 25, 26, 37
STScI	Space Telescope Science Institute . . . . .	27
TEMZ	Turbulent Emission Multi-zone . . . . .	85, 86, 96, 119
UDCF	Unbinned Discrete Correlation Function . . . . .	141
UV	ultraviolet . . . . .	54
VERITAS	Very Energetic Radiation Imaging Telescope Array System . . . . .	98

VLBI	very long baseline interferometry . . . . .	2
------	---	---

# Chapter 1

## Introduction

### 1.1 Active Galactic Nuclei

Some of the most luminous astrophysical phenomena across the entire electromagnetic spectrum involve active galactic nuclei (AGN). These are a highly diverse class of objects, distinguished by observational characteristics, unified under a model that explains the diversity in observational properties as arising largely due to the random orientation of the observer relative to the non-spherically symmetric AGN (e.g., Urry & Padovani, 1995; Antonucci, 1993a). Characteristics commonly observed from AGN include: 1) non-thermal continuum emission spanning several orders of magnitude in frequency (see, e.g., Jorstad & Marscher, 2006), 2) very broad ( $\Delta V \gtrsim 1000$  km s<sup>-1</sup>) or relatively narrow ( $\Delta V \gtrsim 500$  km s<sup>-1</sup>) optical-UV emission lines from ionized species (Yee, 1980; Marziani et al., 1996), 3) highly polarized emission with the polarized flux often exceeding  $\sim 10$  % of the total flux (e.g., Marscher, 2010), and 4) rapid, non-periodic variability across the electromagnetic spectrum, often on time scales of a few hours to a few days (e.g., Edelson et al., 1996).

The underlying theoretical model of an AGN consists of a super-massive black hole (SMBH), with  $M \sim 10^6 - 10^{10} M_{\odot}$ , surrounded by a disk of accreting material (e.g., Shields, 1978; Malkan & Sargent, 1982). Gravitational potential energy of this accretion disk is converted into radiation and kinetic energy of bi-polar outflowing jets, which can extend for many kiloparsecs and even megaparsecs from the central black

hole (van Breugel et al., 1984, for example). Clouds of ionized gas, known as the broad line region (BLR) and narrow line region (NLR), surround the central engine at distances of approximately 0.1-1.0 parsecs (pcs), and 100-1000 pc, respectively, and are responsible for the emission lines seen in most AGN. A dusty torus located approximately 1-10 pc from the black hole shields the central engine from observers with lines of sight intersecting the equatorial plane (see, e.g., Pier & Krolik, 1992, 1993). In the relatively small number of cases in which the viewer's line of sight is nearly parallel to the orientation of a powerful outflowing jet, the AGN is classified as a blazar.

### 1.1.1 Blazars

Blazars are observationally distinguished from other AGN by their relatively strong radio emission,  $F_\nu$ , in which  $\frac{F_\nu(5GHz)}{F_\nu(Bolometric)} \geq 10$ , highly polarized, variable emission, very high apparent luminosity (often exceeding  $10^{46}$  erg s<sup>-1</sup>), and  $\gamma$ -ray emission that often dominates the spectral energy distribution (SED) (von Montigny et al., 1995; Abdo et al., 2010). In fact, of all identified sources detected by the *Fermi*  $\gamma$ -ray telescope, the majority are blazars (Nolan et al., 2012). Relativistic beaming from motion of the plasma in the jets in blazars is common and leads to observational properties such as apparent super-luminal motion in very long baseline interferometry (VLBI) images (e.g., Marscher, 1987) and apparent luminosities that overwhelm the starlight of the host galaxy. Another side effect of relativistic beaming is that usually only a single jet is observed in blazars, as the radiation emanating from the jet flowing away from the observer is beamed out of the line of sight. Blazars are subdivided into two distinct groups: 1) BL Lac type objects, and 2) flat-spectrum radio quasars (FSRQs).



## BL Lac Type Blazars

BL Lac type objects, sources sharing characteristics with the eponymous AGN BL Lacertae, are distinct in numerous ways, the most striking of which is the lack of prominent emission lines in their optical-UV spectra. A smooth featureless spectrum extends from radio to optical frequencies, where often a single power-law  $F_\nu \propto \nu^{-\alpha}$  is adequate to characterize the SED. Thermal radiation from the accretion disk in this frequency regime does not provide an appreciable contribution to the SED.

In some BL Lacs the x-ray spectrum is described by a power-law with the same spectral index,  $\alpha$ , as the radio-optical emission. This is evidence that synchrotron radiation dominates the low frequency emission from BL Lacs, while the high-energy emission results from synchrotron self-Comptonization (SSC) of the same population of photons. In other BL Lacs, the x-ray spectrum is steep, consistent with its representation of the higher frequency tail of the synchrotron emission. BL Lacs tend to have lower overall apparent luminosities than FSRQs; however the  $\gamma$ -ray SED usually peaks at higher energies (see, e.g., D’Elia & Cavaliere, 2001).

## Flat Spectrum Radio Quasars

Unlike BL Lacs, FSRQs tend to exhibit both broad and narrow emission lines in their optical-uv spectra. Also the SED is often augmented by thermal emission from the accretion disk that is visible in the optical-UV portion of the spectrum (e.g., Shang et al., 2005; Raiteri et al., 2007), the so-called big blue bump (BBB). In the mid-infrared (IR), the  $10.0 \mu\text{m}$  silicate emission line has been observed in the FSRQs 3C 273 (Hao et al., 2005) and 4C 21.35 (Malmrose et al., 2011), showing that a dusty torus is present in some, if not all, FSRQs. Synchrotron emission is prominent in FSRQs, as evidenced by significant linear polarization of the emission. However, thermal emission mechanisms may dominate the SED at optical-IR frequen-

cies, while Comptonization of photons emitted by thermal processes may dominate the  $\gamma$ -ray portion of the SED. Figure 1.1 displays some of the main observational differences in the optical spectra of two  $\gamma$ -ray bright blazars.

## 1.2 The Emission Mechanisms of Active Galactic Nuclei

### 1.2.1 Thermal Emission Processes

The ultimate driving mechanism for an AGN's luminosity is the conversion of gravitational potential energy of matter in the accretion disk into electromagnetic radiation and into kinetic energy of the outflowing jets. The gravitational potential energy of an infinitesimal piece of matter,  $dm$ , at radius,  $r$ , with respect to the center of a larger mass,  $M$ , is given by

$$dU = \frac{-GMdm}{r}. \quad (1.1)$$

Denoting the kinetic energy of the system as  $KE$ , the virial theorem states

$$2KE + U = 0. \quad (1.2)$$

Therefore, the total energy (neglecting the thermal energy of the system) of the matter in orbit is given by

$$E = \frac{GMm}{2r}. \quad (1.3)$$

As matter moves from the outermost edge of the accretion disk to the innermost edge, orbital kinetic energy must either be removed from the system, or converted into thermal energy. Under the assumption that most of the thermal energy is eventually converted into radiation, the virial theorem gives the luminosity,  $L$ , of an accreting object as

$$L \propto \frac{GM}{2r} \dot{m}, \quad (1.4)$$

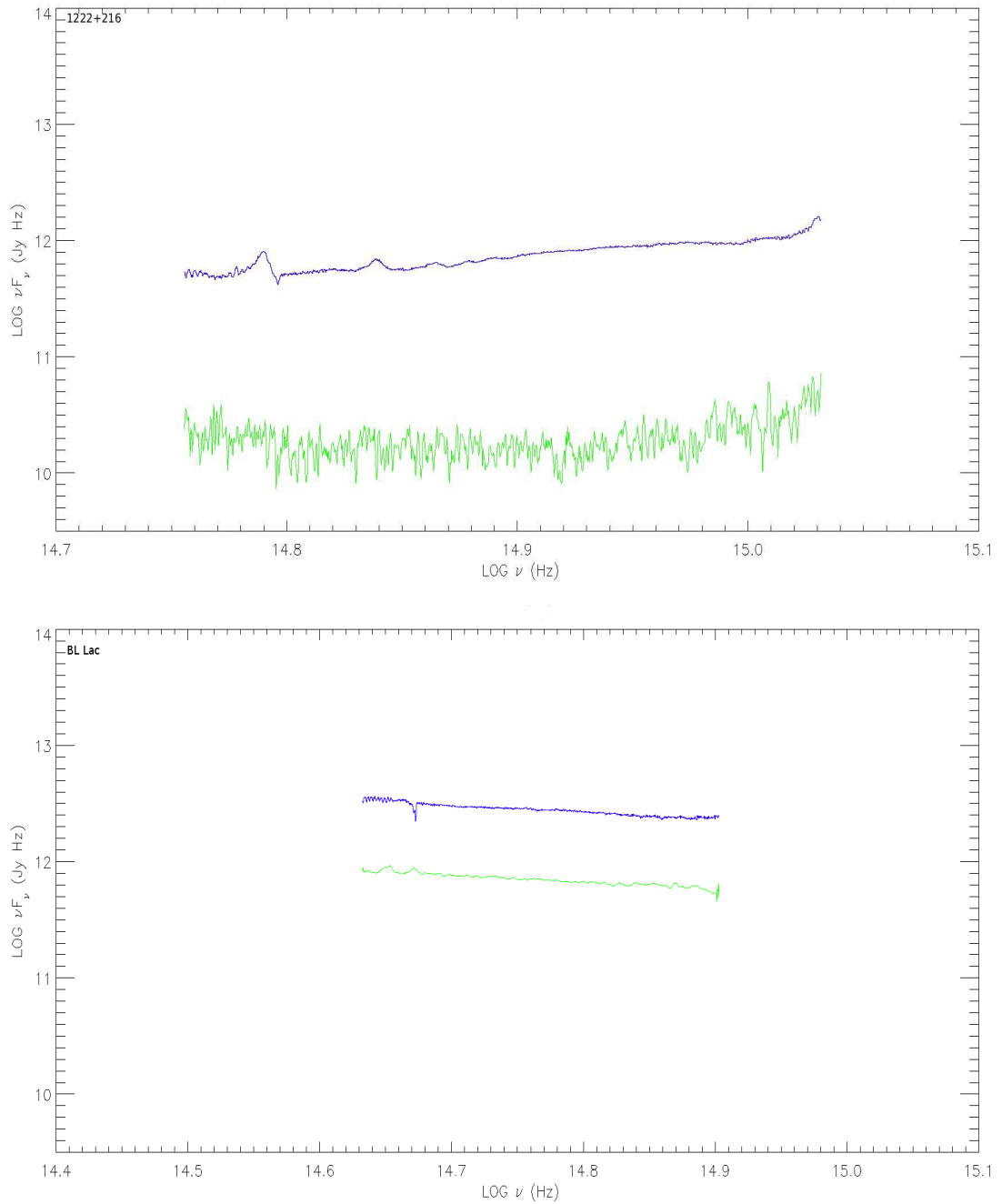


Fig. 1.1 Top panel: Optical SED of the FSRQ 4C 21.35 (1222+216) showing prominent emission lines in blue along with the polarized flux SED shown in green. The spectral index of the flux SED does not mirror that of the polarized flux, suggesting a secondary, non-polarized component to the spectrum. Bottom panel: Same as above but for BL Lacertae. The spectral index is the same for the total and polarized spectra, suggesting that synchrotron emission is dominant.

where  $\dot{m}$  is the accretion rate of matter. If the emission is blackbody radiation, the luminosity also satisfies

$$L \propto r^2 T^4, \quad (1.5)$$

where  $T$  is the temperature of the accretion disk at radius  $r$ . Combining equations 1.4 and 1.5 shows that the the temperature of the accretion disk scales with radius as

$$T \propto r^{-3/4}. \quad (1.6)$$

Therefore, in order to obtain the spectrum of the accretion disk, it is necessary to integrate the Planck function along the radius of the disk. The flux density,  $F_\nu$ , of a radiating disk with a radially dependent temperature profile is given by

$$F_\nu = \int_X^\infty \frac{2h\nu^3}{c^2} \frac{1}{e^{\frac{h\nu}{k_B T(r)}} - 1} 2\pi r dr, \quad (1.7)$$

where  $h$  is Planck's constant,  $c$  is the speed of light,  $k_B$  is Boltzmann's constant, and  $X$  is the minimum radius of the accretion disk. The lower limit of integration is the inner radius of the disk. Defining a gravitaional radius,  $r_g$ , as one half of the Schwarzschild radius of a black hole

$$r_g \equiv \frac{GM_{BH}}{c^2}, \quad (1.8)$$

in which  $M_{BH}$  is the mass of the black hole, and performing the substitutions  $\epsilon = h\nu$ , and  $u = \frac{\epsilon}{k_b T_0 \frac{r}{r_g}^{-3/4}}$ , the relation

$$F_\epsilon \propto \epsilon^{1/3} \int_{u_{max}}^\infty \frac{u^{5/3}}{e^u - 1} du \quad (1.9)$$

results (Krolik, 1999). The parameter  $u_{max}$  is determined by first identifying the temperature corresponding to a blackbody peaking at frequency  $\nu$ , i.e., obtaining

the temperature of a blackbody from the Wien-peak,  $h\nu_{max} = 2.82 k_B T$ . Using the temperature gradient of the disk, the distance from the central engine corresponding to that temperature in gravitational radii can be determined. The corresponding parameter  $u_{max}$  can then be determined. From equation 1.9 and following the arguments set forth in Krolik (1999) it can be inferred that for  $u_{max} \ll 1$  the value of the integral becomes of order unity, while when  $u_{max} \gg 1$  the exponential in the denominator dominates the value of the integral. Therefore an approximation of the spectrum of the disk can be given by

$$F_\nu \propto \nu^{1/3} e^{\frac{-h\nu}{k_B T_{max}}}, \quad (1.10)$$

where  $T_{max}$  is the maximum temperature of the accretion disk. This result implies that the accretion disk will have a spectrum that is proportional to  $\nu^{1/3}$  over a large frequency range and then will have an exponential cutoff beyond  $h\nu \approx k_B T_{max}$ , as opposed to a single temperature blackbody, which has a spectrum proportional to  $\nu^2$  and an exponential cutoff above  $h\nu \approx k_B T$ . A more rigorous derivation of this result is provided in Krolik (1999) and Shakura & Sunyaev (1976). See Figure 1.2 for a graphical representation of an accretion disk spectrum generated from equation 1.9 using a fiducial temperature  $T_0 = 10^5 \text{K}$  at the inner radius of the disk.

In addition to the accretion disk at a size scale of  $10^{-4}$  pc (Morgan et al., 2010), another likely source of thermal emission is the dusty torus located roughly 1-10 pc from the central engine of the AGN. The prominent  $10 \mu\text{m}$  emission feature associated with silicates has long been observed in non-blazar AGN (see, e.g., Spoon et al., 2007; Sturm et al., 2005; Pier & Krolik, 1993), leading to the conclusion that the heavy extinction of x-ray emission in type II AGN occurs in an optically thick dusty torus surrounding the central engine, composed largely of silicate grains. The energy

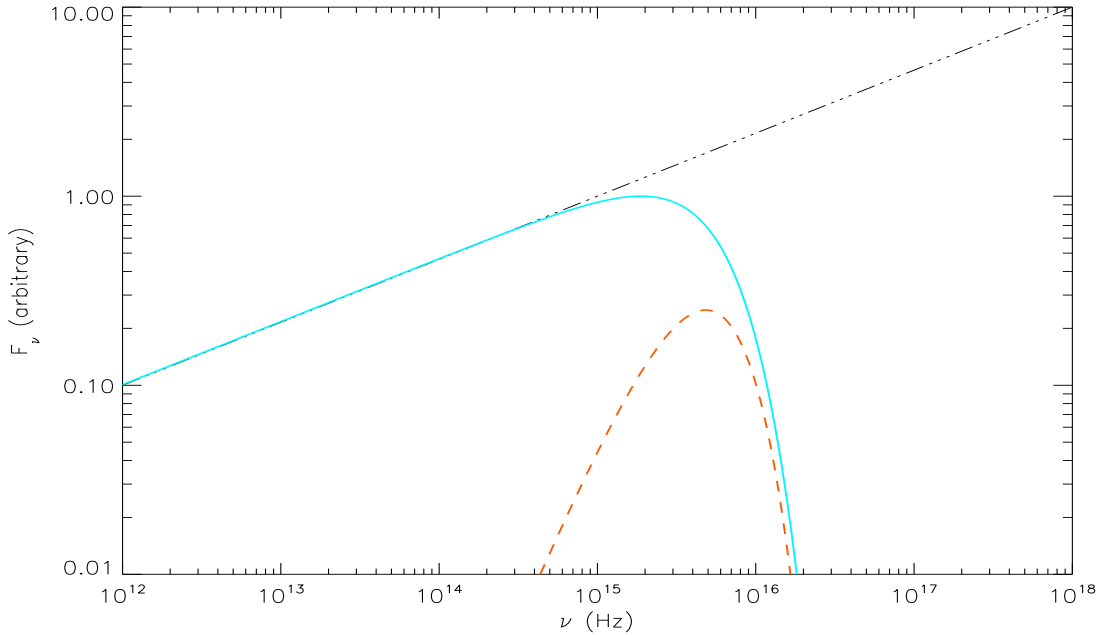


Fig. 1.2 Emission spectrum from a disk with maximum temperature of  $T_0 = 10^5$  K and a temperature gradient of  $T \propto r^{-3/4}$  is shown by the solid turquoise line. The emission model for the disk was generated using equation 1.9. For comparison, the emission from a  $T = 10^5$  K blackbody is shown by the red dashed line. The spectra have been scaled to arbitrary units. Unlike the blackbody, the disk with a temperature gradient is well fit by a power-law with a spectral index of  $1/3$ , which is shown by the black dot-dash line over frequency ranges spanning many orders of magnitude.

of any photon absorbed in the torus will ultimately go into heating the surrounding environment. A simple energy balance requires the temperature of the torus at radius  $r$  to be given by

$$T_{Torus} = \left( \frac{L_{AGN}}{4\pi r^2(1-A)\sigma} \right)^{1/4}, \quad (1.11)$$

where  $L_{AGN}$  is the luminosity of the central engine,  $A$  is the albedo of the dust grains, meaning the fraction of the incoming radiation that is reflected, and  $\sigma$  is the Steffan-Boltzmann constant. At temperatures above  $T_{sub} \sim 1300$  K, the chemical bonds holding silicate grains together are broken and the solid grains sublimate.

A blackbody with effective temperature  $T = 1300$  K has its peak emission at a rest frequency of  $\nu = 7.6 \times 10^{13}$  Hz or at a wavelength of  $\lambda = 2.15 \mu\text{m}$ , which is approximately the effective wavelength of the near-IR  $K_s$  band. For blazars at low redshift,  $z$ , this means that direct emission from the dusty torus should be detectable using NIR filters, while the emission from sublimating dust will be seen in higher redshift blazars. Figure 1.3 displays the expected inner radius for the dusty torus using  $T_{sub} = 1300$  K and an albedo of  $A = 0.5$  at different AGN luminosities. Also plotted is the expected temperature at different distances from the central engine for AGN of different luminosities. This paints a very simplistic picture of the nature of the dusty torus; a more detailed treatment will be given in section 1.3.

### 1.2.2 Overview of Synchrotron Radiation

One of the main non-thermal emission mechanisms of an AGN is synchrotron radiation. This arises from matter that, rather than accreting onto the black hole, is launched into one of two bi-polar, collimated jets of hot plasma. If the plasma is relativistic, synchrotron radiation results. The Lorentz force,  $\mathbf{F}$ , experienced by a single, relativistic, charged particle is given by

$$\mathbf{F} = \frac{d}{dt}(\gamma m \mathbf{v}) = q \left( \mathbf{E} + \frac{\mathbf{v}}{c} \times \mathbf{B} \right) \quad (1.12)$$

where  $\gamma$  is the Lorentz factor of the particle,  $q$  is the charge of the particle,  $\mathbf{E}$  is the electric field,  $\mathbf{v}$  is the velocity of the particle and  $\mathbf{B}$  is the magnetic field vector.

In the absence of an appreciable electric field, the total energy of the particle (neglecting losses to radiation) will remain constant, and the particle will gyrate around the magnetic field lines in a helical pattern at a gyration frequency of

$$\omega_B = \frac{qB}{\gamma mc}, \quad (1.13)$$

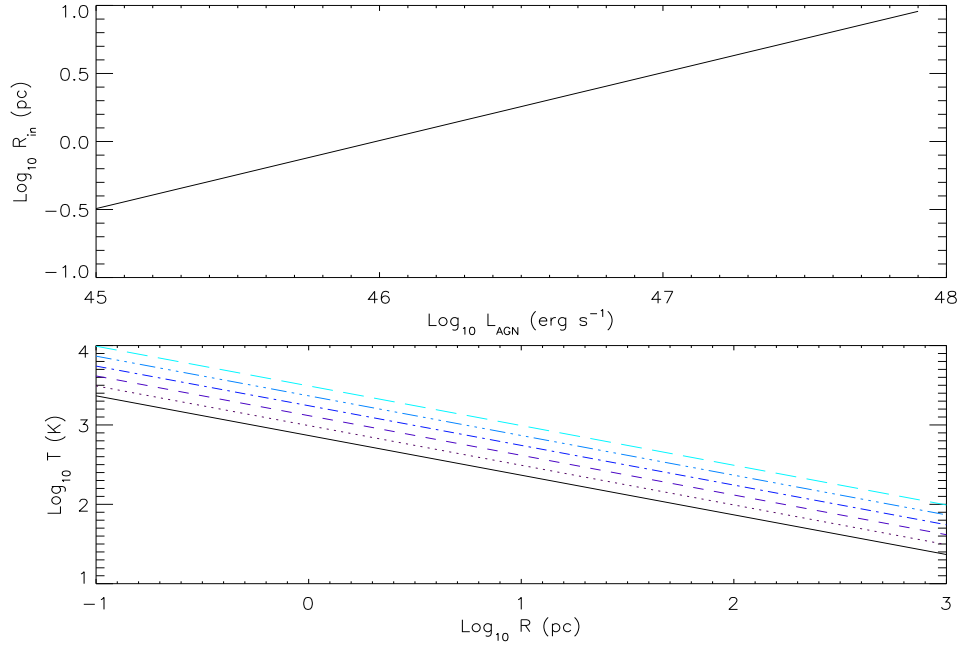


Fig. 1.3 *Top*: Distance from central engine at which a simple energy balance for an albedo of  $A = 0.5$  produces a temperature of  $T = 1300$  K. *Bottom*: The expected temperature as a function of distance from the central engine for a sample of AGN luminosities. *Solid black line*:  $L = 10^{45}$  erg s $^{-1}$ , *dotted black*:  $L = 3.2 \times 10^{45}$  erg s $^{-1}$ , *purple short-dash*:  $L = 10^{46}$  erg s $^{-1}$ , *blue dash-dot*:  $L = 3.2 \times 10^{46}$  erg s $^{-1}$  *light-blue triple dot-dash*:  $L = 10^{47}$  erg s $^{-1}$ , *turquoise long-dash*:  $L = 3.2 \times 10^{47}$  erg s $^{-1}$ . All models show that beyond 10 pc from the central engine, the effective temperature is  $\sim 300 - 1000$  K, indicating that absorbed photons will be re-radiated at near-mid IR wavelengths.

which is the same frequency at which a non-relativistic particle would gyrate multiplied by a factor of  $\frac{1}{\gamma}$ . In cases where the velocity of the particle is non-relativistic ( $\gamma \approx 1$ ), the particle emits cyclotron radiation in the form of emission lines at the gyration frequency and its harmonics. In the case of a relativistic particle, relativistic beaming causes the emission to become highly non-isotropic and therefore doppler shifted by different factors at each point of the spiral gyration. This smoothes the emission lines into what is essentially a continuous spectrum of synchrotron radiation.



It can be shown that (see, e.g., Rybicki & Lightman, 1986; Jackson, 1991; Blumenthal & Gould, 1970, for detailed derivations) the resultant synchrotron radiation spectrum,  $\frac{dI}{d\omega}$ , can be expressed in terms of a modified Bessel function,  $K_{5/3}$ , by

$$\frac{dI}{d\omega} \propto \frac{\omega\gamma^3}{\omega_B} \times \int_{\frac{\omega\gamma^3}{\omega_B}}^{\infty} K_{5/3}(x) dx, \quad (1.14)$$

in which the dimensionless parameter  $x$  represents the ratio of the emission frequency to the gyration frequency of the particle.

Figure 1.4 shows a plot of Equation 1.14 and shows that, even though the radiation is not monochromatic, the emission from a single particle is narrowly peaked at a frequency of approximately one-third of the gyration frequency multiplied by a factor of  $\gamma^3$ , and quickly declines. Because of this, the emission from a single particle can be approximated as monochromatic when estimating emission over a frequency range spanning several orders of magnitude. When viewing astrophysical objects, an observer sees radiation not just from a single particle, but from a distribution of particles, therefore the spectrum from single particles must be integrated over the particle distribution in order to obtain the observed spectrum.

Following the arguments set forth in Rybicki & Lightman (1986), power-law particle distributions in kinetic energy  $N_E \propto E^{-s} dE$ , where  $s$  is known as the spectral index, are common in the cosmos. Since  $E = (\gamma - 1)mc^2$ , the distribution can be rewritten as  $N_\gamma \propto \gamma^{-s} d\gamma$  for  $\gamma \gg 1$ . In the case of synchrotron radiation, the emitted spectrum is then represented by

$$P(\omega) \propto \int_{\gamma_1}^{\gamma_2} \frac{\omega\gamma^3}{\omega_B} \gamma^{-s} K_{5/3}(\gamma) d\gamma, \quad (1.15)$$

in which  $\gamma_1$  and  $\gamma_2$  correspond to the Lorentz factor of the lowest and highest energy electrons in the distribution respectively. Making the substitution  $x = \frac{\omega\gamma^3}{\omega_B}$  and

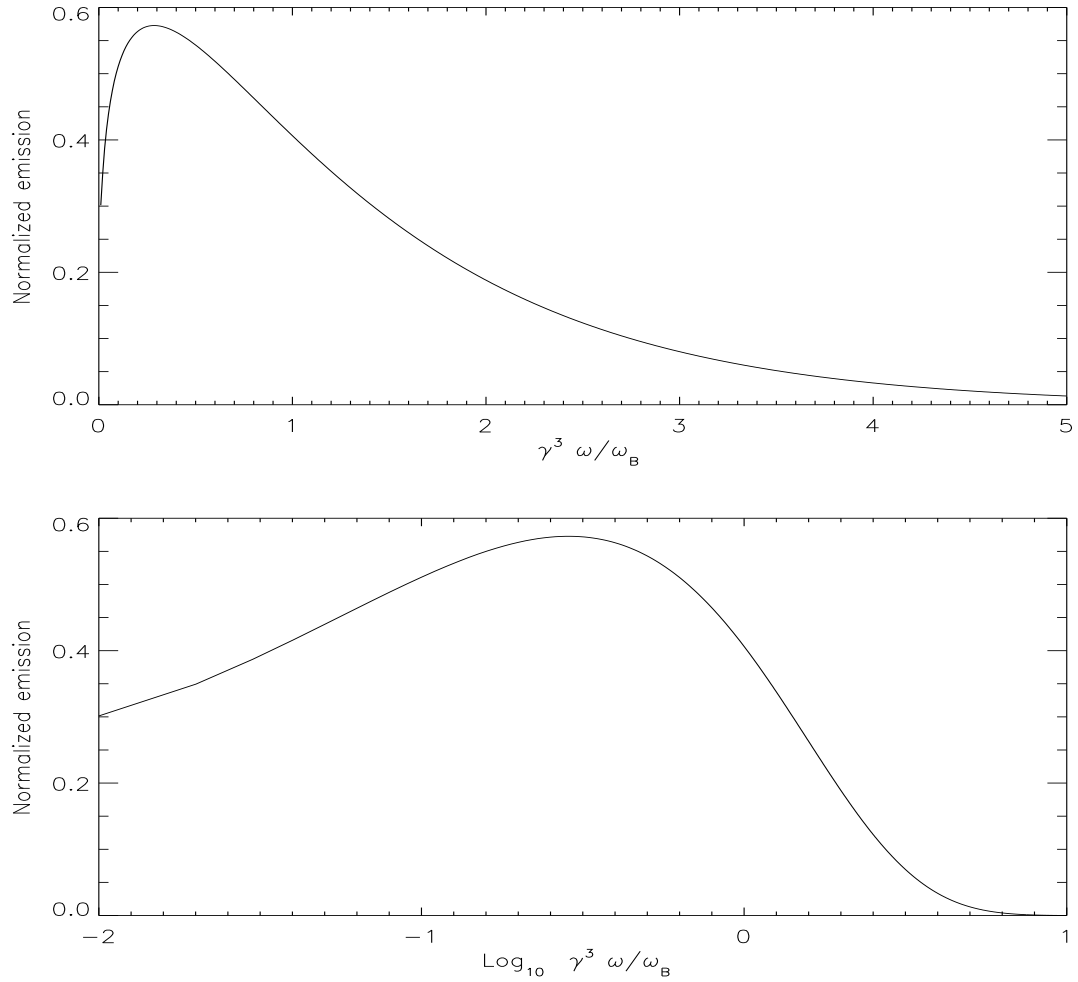


Fig. 1.4 *Top*: Plot of 1.14 normalized showing that the peak emission is narrow. *Bottom*: Same as above, but with a logarithmic scale for  $\omega$ . Adapted from Jackson (1991).

$dx = 2\gamma d\gamma$ , the spectrum becomes

$$P(\omega) \propto \omega^{\frac{1-s}{2}}. \quad (1.16)$$

Therefore, a power-law particle distribution with spectral index  $s$  yields a power-law synchrotron radiation spectrum  $F_\nu \propto \nu^{-\alpha}$  with spectral index  $\alpha = \frac{s-1}{2}$ . This is consistent with the power-law spectra of the radio-IR-optical emission in many AGN arising mainly because of synchrotron emission.

### The Polarization of Synchrotron Emission

One interesting aspect of synchrotron radiation is its highly polarized nature. This arises from the non-isotropic nature of the synchrotron process. In terms of the Bessel functions,  $F(x) \equiv X \int_x^\infty K_{5/3}(X) dX$  and  $G(x) \equiv x K_{2/3}(x)$ , the components of the radiation emitted normal ( $P_\perp$ ) and parallel ( $P_\parallel$ ) to the magnetic field for a single particle are given by  $P_\perp = CF(x) + G(x)$  and  $P_\parallel = C(F(x) - G(x))$ , respectively, where  $C$  is a constant (Rybicki & Lightman, 1986). For a power-law particle distribution, this leads to a degree of polarization  $\Pi = \frac{s+1}{s+7/3}$  for frequencies at which the emission is optically thin.

In this derivation, Rybicki & Lightman (1986) assumed a uniform magnetic field with a constant direction. In nature, such a magnetic field is rarely achieved and the actual magnetic field has a tangled spaghetti-like structure. The true magnetic field, however, may be approximated by a number,  $n$ , of cells, in each of which the assumption of uniform  $B$  holds approximately. In this case the maximum polarization is attenuated by a factor of  $n^{-1/2}$  (e.g., Marscher, 2013, 2014a).

The polarized nature of synchrotron emission becomes useful in the study of the SEDs of blazars. For SEDs in which there are multiple emission components, it is

possible to uncover the spectral index of the synchrotron component, if the fraction of polarized flux is known. From there one can model the the synchrotron emission and, if the spectral indices of the polarized flux and total flux differ, determine the relative strength of other sources of emission in the SED. This technique is an integral part of this dissertation and will be explored further in Chapter 4.

### A Brief Introduction to Stokes Parameters

The need to be able to infer the polarization of an electromagnetic wave solely from limited intensity measurements led to the advent of the Stokes parameters,  $I$ ,  $Q$ ,  $U$ , and  $V$ . The Stokes parameters  $Q$ ,  $U$ , and  $V$ , can be thought of as the directions in a 3-D cartesian coordinate system. A vector beginning at the origin will have a length equal to  $\sqrt{Q^2 + U^2 + V^2}$ . This corresponds to the intensity of polarized electromagnetic radiation described by a set of Stokes parameters; in the case of purely linear polarization,  $V = 0$ . Such a vector can also be described in spherical coordinates by the vector length  $I$  as well as coordinate angles  $\theta$ , and  $\beta$ , where  $\theta$  is the orientation angle of the polarization vector in the plane of the sky, and  $\beta$  is the elevation angle. Thus the Stokes parameters can be written as

$$\begin{aligned} Q &= I \Pi \cos 2\theta \cos 2\beta \\ U &= I \Pi \sin 2\theta \cos 2\beta \\ V &= I \Pi \sin 2\beta. \end{aligned} \tag{1.17}$$

Initially, this formulation seems cumbersome and unintuitive, however its usefulness becomes apparent while carrying out polarization observations. By rotating a polarized filter (or a half-wave plate combined with a polarized filter) through position

angles of  $0^\circ$ ,  $45^\circ$ ,  $90^\circ$  and  $135^\circ$ , the Stokes parameters in the case of linear polarization can be simply determined by

$$Q = \frac{F_\nu(0^\circ) - F_\nu(90^\circ)}{F_\nu(0^\circ) + F_\nu(90^\circ)}$$

$$U = \frac{F_\nu(45^\circ) - F_\nu(135^\circ)}{F_\nu(45^\circ) + F_\nu(135^\circ)}.$$

(1.18)

The direction of polarization in the plane of the sky is obtained by solving the transcendental equation  $\frac{U}{Q} = \tan 2\theta$ , while the total intensity of polarized radiation  $I_{\text{II}} = \sqrt{Q^2 + U^2}$ . This allows for the total polarization of the radiation to be characterized with the minimum number of observations.

### 1.2.3 Inverse-Compton Radiation

#### The Compton Effect

The Compton effect occurs when a photon of wavelength  $\lambda_0$  interacts with a free electron. A free electron has a collisional cross-section equal to the Thomson cross-section,  $\sigma_T = \frac{8\pi}{3} \left(\frac{e^2}{m_e c^2}\right)^2$ , to scattering by an incoming photon. When a collision with a stationary electron does occur, a fraction of the energy and momentum of the photon is transferred to the electron. Using the principles of conservation of energy, and of momentum, the final energy of the photon and recoiling electron can be described as function of the recoil angle.

A new photon will recoil at an angle  $\theta$  to the original direction of motion and the wavelength,  $\lambda_1$ , will lengthen such that  $\lambda_1 - \lambda_0 = \frac{h}{m_e c}(1 - \cos \theta)$ , as shown in Figure 1.5. In the general case where the electron has some initial momentum, it is

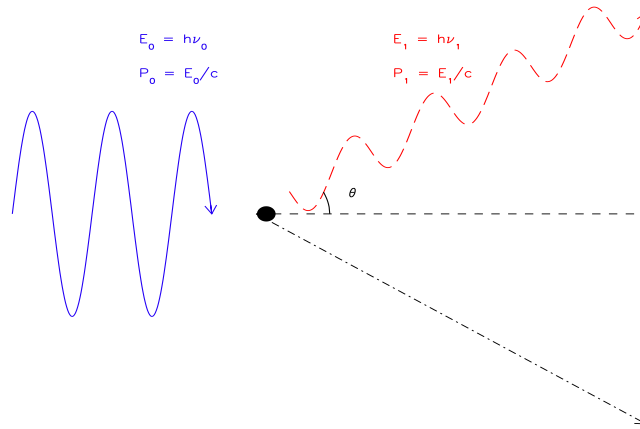


Fig. 1.5 The scattering of a photon in the electron's rest frame. Energy and momentum is transferred from the photon to the electron resulting in a longer wavelength photon. The reverse process where energy and momentum is transferred from the electron into the photon results in the result of this same process viewed from a reference frame in which the electron is at rest. Adapted from Rybicki & Lightman (1986).

possible that the net exchange of energy goes from the electron to the photon. This is called inverse-Compton (IC) scattering. This effect can be analyzed in three steps.

First, a change of reference frames from one in which the electron is in motion, to one in which the electron is at rest, must take place. Second, the scattering may then be treated as Compton scattering. From the relativistic Doppler shift (see, e.g., Rybicki & Lightman, 1986; Blumenthal & Gould, 1970), the frequency and momentum of an incident photon become boosted by a factor of  $\sim \gamma$ , when making a change of reference frame from one where the electron is moving to one

where the electron is initially stationary. In this reference frame, the photon will scatter off of the electron and both will recoil, with the electron having momentum,  $p \sim \gamma m_e c \cos \theta'$ , in the direction that the photon was traveling. Defining  $\mu' \equiv \cos \theta'$  then in the original reference frame, the change of the electron's momentum is of order

$$\Delta p \sim p_0 \mu = p_0 \frac{\mu' + \beta}{1 + \beta \mu'}. \quad (1.19)$$

The scattering angle in the electron rest frame is small, so  $\mu' \approx 1$ , while substitution of the definition  $\beta = (1 - \frac{1}{\gamma^2})^{1/2}$  and performing a binomial expansion yields the result  $\Delta p \sim -\gamma^2 p_0$  in the direction along which the electron was originally traveling.

To conserve momentum, the scattered photon must also have momentum of magnitude  $\gamma^2 p_0$  and hence an energy of  $\gamma^2 E_0$ . Therefore IC scattering typically boosts the frequency of the scattered photons by a factor of  $\sim \gamma^2$  of the scattering electron.

## Inverse-Compton Radiation in AGN

IC scattering is a very important emission mechanism in AGN because an abundance of very high energy photons can be generated from a distribution of high energy electrons scattering photons from various sources. For example, a photon emitted by cool dust ( $T \sim 20$  K, for example) has a rest frequency of  $\nu_{rest} \sim 10^{12}$  s<sup>-1</sup>. IC scattering this photon off of an electron with  $\gamma \sim 10^3$  can yield an x-ray photon at  $\nu \sim 10^{18}$  Hz. In order to obtain the full spectrum of IC radiation, the output from a single scattering must be integrated across the electron and photon distributions. As was the case with synchrotron radiation, the distribution of the scattering electrons is often a power-law,  $N_E \propto \gamma^{-s}$ , which results in a power-law spectrum of

photons

$$P(\omega) \propto \int_{\gamma_1}^{\gamma_2} \int_{\omega_1}^{\omega_2} \gamma^{2-s} U_{ph}(\omega) d\omega d\gamma, \quad (1.20)$$

where  $U_{ph}(\omega)$  is the density of the seed photons at angular frequency  $\omega = 2\pi\nu$ .

The IC scattering of radiation is a very efficient process in AGN. This is in part due to a multitude of possible sources of seed photons that include the broad, and narrow emission line clouds (Joshi et al., 2014), the hot, dusty torus surrounding the central engine (Arbeiter et al., 2001), synchrotron photons produced in the jet in a process called synchrotron self-comptonization, SSC (Sikora et al., 1994; Ghisellini et al., 1998, and references therein), and the cosmic microwave background (CMB) (Harris & Krawczynski, 2002). Another important aspect of IC scattering is that the approximation of the scattering cross-section of the electrons is equal to the Thomson cross-section is accurate only up until the seed photon energy becomes comparable to the rest mass energy of an electron,  $\gamma h\nu \approx m_e c^2$ , or about 0.5 MeV. For IC scattering of photons above this threshold energy, the cross-section enters the Klein-Nishina regime (Klein & Nishina, 1929), where the decreasing with energy and initial frequency cross-section to IC scattering must be taken into account in simulations designed to accurately reproduce the full IC spectrum.

## 1.3 Dusty Tori

### 1.3.1 An Introduction to Astrophysical Dust

Dust, in the parlance of astrophysics, refers to solid-state sub-micron sized particles that pervade the universe (Whittet, 1992). The particles are composed largely of graphite as well as complex minerals known as silicates that are constructed from base



units of  $\text{SiO}_4$ , which act as “Lego” bricks, chained together with charged ions of  $\text{Mg}^{2+}$  and  $\text{Fe}^{2+}$  (Whittet, 1992). The dust itself, like most baryonic, complex matter in the universe, is star stuff. Dust grains are likely assembled in the upper atmospheres and outflows of red giant stars which have long since evolved off of the main sequence (Salpeter, 1977), and inside supernova remnants (see e.g., Liffman & Clayton, 1989; Gomez et al., 2012; Matsuura et al., 2015; Lau et al., 2015, and references therein), where the temperature of the expanding gas has become low enough such that complex chemistry can occur.

In star forming galaxies such as the Milky Way, dust is thought to help increase the efficiency of star formation as the relatively high specific heat of dust grains provides a mechanism for the cooling of a collapsing gaseous cloud (Calzetti et al., 2000). This can be seen in dusty galaxies at high redshifts corresponding to lookback times of  $\sim 800$  Myr after the Big Bang (Casey et al., 2014). In the Milky Way, the optically thick nature of dust grains betrays their presence in the high absolute extinction,  $A_\lambda$ , of optical and higher frequency radiation measured in the Galactic Plane (Schlafly & Finkbeiner, 2011; Schlegel et al., 1998). In the Solar System, the highly reflective nature of the dusty grains is evidenced by the faint reflections of solar radiation by the interplanetary medium, the so-called “zodiacal light” (e.g., Rowan-Robinson & May, 2013; May, 2008; Leinert et al., 1981; Leinert, 1975).

In addition to probing the emission from the accretion disk of blazars, a major point of focus for this dissertation is the exploration of the dusty torus thought to exist 1-10 pc from the central engine of most AGN. Direct observation of this obscuring dust is common for “edge on”, also known as type II AGN, and is evidenced by the strong infrared excess, caused by the re-radiation of light absorbed by the dust grains, seen in the SEDs of these sources. In blazars, observations of the torus are

complicated by the dominance of the synchrotron component in the IR portion of the electromagnetic spectrum. Before proceeding, it is helpful to discuss two very different pictures concerning the composition of the dusty torus; one in which the dust is assembled in a continuous radially dependent distribution, and one in which the dust aggregates into very dense, optically thick clumps in which the sizes of the clumps are small compared to the distances between them.

### 1.3.2 Continuous Medium

Perhaps the simplest way to model the torus is to have the density of the grains,  $n_{gr}$ , be dependent only on the radial distance to the central engine as a power law such that  $n_{gr}(r) \propto r^{-\beta}$ . In such a case, balancing the energy absorbed by grains from UV radiation with radiation emitted by the dust grains is relatively simple and yields the temperature profile shown in Figure 1.3. In reality, the emissivity of the dust grains,  $Q$ , is a function of frequency. One way to model the frequency dependence of the dust emissivity is a power law  $Q_\nu = Q_0 \nu^{-\beta}$  as in Barvainis (1987), which arises by assuming that the IR emission is optically thin. Replacing the albedo in the energy balance with the optical depth,  $\tau$ , the energy balance becomes

$$\frac{L_{AGN} e^{-\tau}}{4\pi R^2} \propto Q_0 \int \nu^\delta B_\nu(T) d\nu. \quad (1.21)$$

This integral can only be solved in terms of the  $\Gamma$  and Riemann zeta,  $\zeta$ , functions such that  $\frac{L_{AGN} e^{-\tau}}{r^2} \propto T^{4+\delta} \Gamma(4+\delta) \zeta(4+\delta)$ , where  $\tau = \int \pi a^2 n_{gr} dr$  and  $a$  is the cross-sectional radius of the dust grain. Using reasonable values for the cross-section, radial dependence of the dust distribution, and frequency dependence of the emissivity,  $a = 1 \mu\text{m}$ ,  $\delta = 1 - 2$ , respectively, yields an inner radius of the torus of  $\sim 1 \text{ pc}$  for a sublimation temperature of 1500 K and an AGN luminosity of  $L_{AGN} \approx 10^{46} \text{ erg s}^{-1}$  (Barvainis, 1987). In this model, dust grains cannot survive

inside the sublimation radius and thus a dust-free “donut hole” is carved out of AGN inwards of that radius.

### 1.3.3 Clumpy Torus

An alternative to a continuous distribution of dust calls for the dust to be distributed in a number of very dense, optically thick clouds that are far apart compared to their size. In such a model, each individual cloud is typically treated as a continuous medium for the purposes of determining the emission from the cloud. In order to reproduce the IR SED of the torus, clouds are distributed in the torus at various filling factors that are usually radius and viewing angle dependent (see, e.g., Hönic & Kishimoto, 2010; Nenkova et al., 2008a,b; Barvainis, 1992).

The clumpy models predict similar SEDs to the continuous medium models with a couple of notable exceptions. Because the individual clumps are optically thick, each clump will have a temperature profile dependent not just on the distance from the center of the AGN, but also on the column density of the intervening dust. This allows for dust clumps to exhibit a range of temperatures and exist slightly inwards of the putative sublimation radius, provided that (1) the radius of the clump is sufficiently large that the side of the cloud not facing the central engine is cool enough that it does not exceed the sublimation temperature, and (2) dust grains that do sublimate can reform before the constituent particles are swept away from the region by radiation pressure. Clumpy torus models predict the same overall  $R^{-2}$  dependence for the inner radius of the torus, but because of the shielding of the dust that is not near the surface of the clump, the inner radius of the torus can be inwards of  $\sim 0.4$  pc for an AGN luminosity of  $L_{AGN} \approx 10^{45}$  erg s $^{-1}$  (Nenkova et al., 2008b).

The clumpy models are also successful in reproducing the  $10.0 \mu\text{m}$  silicate feature caused by excitation of vibrational modes of the individual silicate units of dust molecules. Depending on the viewing geometry, the continuous models predict the feature to be in deep absorption when viewed “edge-on”, or in emission if viewed face-on, while more elaborate patterns emerge when using a clumpy model (Nenkova et al., 2008b). Reverberation mapping studies, in which the distance between the optical and IR emitting regions is estimated from the time delay between luminosity changes in those wavelength regimes respectively, yield results in which the inner radius of the torus is more consistent with clumpy models. However, the observed time lags are factors of  $\sim 3 - 4$  lower than expected even for clumpy models (Minezaki et al., 2004; Suganuma et al., 2006).

### 1.3.4 Apparent Superluminal Motion in Blazars

Apparent superluminal motion has been detected in the movement of many substructures in the radio jets of many blazars. This is an optical illusion due to a combination of special relativistic effects and the fact that astronomical observations only provide a two-dimensional look at the three-dimensional structure being observed. The observed apparent velocity of emitting material,  $v_{app}$ , is described by,

$$v_{app} = \frac{\beta c \sin \theta}{1 - \beta \cos \theta}, \quad (1.22)$$

where  $\theta$  is the angle between the line of sight and the direction of the object’s motion,  $\beta$  the ratio of the object’s true velocity to the speed of light, and  $c$  is the speed of light. Because of this, it is possible to observe two events occur many parsecs away from each other, yet only be separated by a short amount of time. Figure 1.6, adapted from Rybicki & Lightman (1986), depicts the geometry of an a knot traveling down a blazar jet at apparent superluminal velocities.

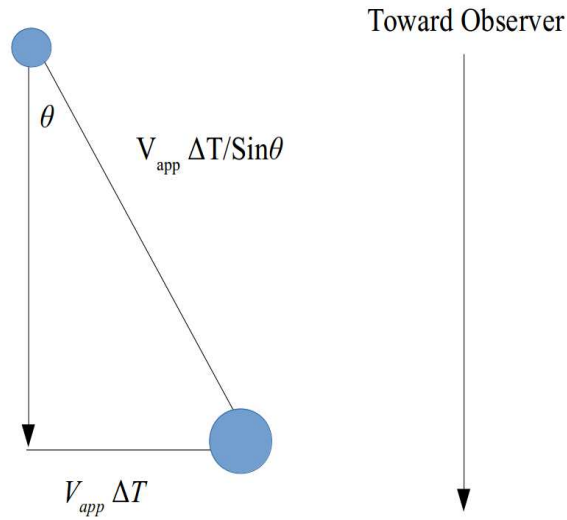


Fig. 1.6 Apparent superluminal motion in the jet of a blazar. The blob is traveling at an angle  $\theta$  to the observer at nearly the speed of light. Photons that are emitted when the blob is closer to the observer travel a shorter distance and therefore have a shorter travel time  $\Delta T$ . As a result, an observer will calculate an apparent velocity,  $V_{app}$ , for the blob that is larger than its true velocity.

## Chapter 2

# Observational Data

### 2.1 Observations and Analysis

This chapter provides an introduction to the data set used throughout this project. Data were acquired from different space-based and ground-based observatories, covering different wavelength regimes, thus probing different emission mechanisms. This chapter contains some material previously published in Malmrose et al. (2011).

#### 2.1.1 *Spitzer* Space Telescope

The study described in Chapter 3 relies on near-infrared (IR) and mid-IR observations of three flat-spectrum radio quasars (FSRQs) and one BL Lac object obtained with the *Spitzer* Space Telescope (SST). This telescope, the last of the National Aeronautics and Space Administration (NASA) “Great Observatories Program”, launched into an Earth trailing solar orbit in August, 2003 (Werner et al., 2004), with a 0.85 m primary mirror and three instruments on board. The spacecraft utilized both active and passive cooling techniques in order for its instruments to operate at 5 K for observations that required this and up to 15 K for other observations. Switching between instruments was performed via a movable pick-up mirror.

The on-board instruments included two photometers, the Infrared Array Camera (IRAC), described in Fazio et al. (2004), for the near-IR, and the Multiband Imaging Photometer (MIPS) for the mid-IR and far-IR (Rieke et al., 2004). In addition to

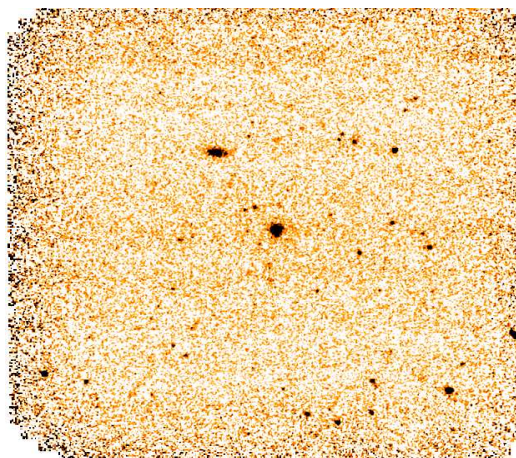


Fig. 2.1 IRAC mosaic of 1222+216 taken through channel 1. Aperture photometry was performed to obtain the flux density of the source at the center.

the two photometers, a mid-IR spectrograph, the Infrared Spectrograph (IRS), provided medium-resolution spectroscopy over the wavelength range  $\lambda = 5.0\text{-}36.0 \mu\text{m}$  (Houck et al., 2004).

### The Infrared Array Camera (IRAC)

IRAC<sup>1</sup> consists of a 4 channel imager, with a  $256 \times 256$  pixel  $27' \times 27'$  field of view for each array for each channel. Channels 1 and 2 consisting of InSb arrays spanning a wavelength range of  $\lambda_1 = 3.19 - 3.94 \mu\text{m}$ , and  $\lambda_2 = 4.00 - 5.02 \mu\text{m}$  respectively, can still as of mid-2016 provide science quality images without the use of the liquid helium cooling cryogen. Channels 3 and 4, composed from Si:As arrays  $\lambda_3 = 4.98 - 6.41 \mu\text{m}$ , and  $\lambda_4 = 6.45 - 9.34 \mu\text{m}$ , became inoperable when the spacecraft ran out of coolant in May 2009 and could no longer be kept at a low operating temperature (Fazio et al., 2004). An example of a mosaiced IRAC image in Channel 1 for the source 1222+216 is shown in Fig. 2.1.

---

<sup>1</sup>PI: G. G. Fazio, Smithsonian Astrophysical Observatory. The Instrument was assembled at NASA Goddard Space Flight Center.

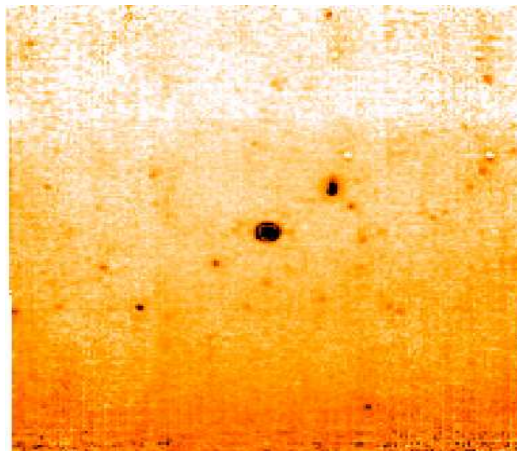


Fig. 2.2 MIPS mosaic of 1222+216 taken through channel 1. Aperture photometry was performed to obtain the flux density of the source at the center.

### **The Multiband Imaging Photometer (MIPS)**

MIPS<sup>2</sup> was capable of imaging at wavebands centered on  $\lambda = 24, 70,$  and  $160 \mu\text{m}$ . The  $24 \mu\text{m}$  field was made from a Si:As array, while the  $70$  and  $160 \mu\text{m}$  imaging arrays were composed of a Ge:Ga detector. Array sizes for the three bandpasses were  $128 \times 128$ ,  $32 \times 32$ , and  $2 \times 20$  pixels, respectively. In addition to imaging, the MIPS was capable of providing low-resolution spectral energy distributions (SEDs) in a special observing mode. A complete description of the technical details of the MIPS can be found in Rieke et al. (2004), while a sample MIPS mosaic is shown in Figure 2.2.

### **The Infrared Spectrograph (IRS)**

The IRS<sup>3</sup> consisted of four separate modules, such that when data from each was combined, it provided a spectrum spanning from  $\lambda = 5.2 - 38 \mu\text{m}$  (Houck et al., 2004). Each module, Long-Low (LL), Long-High (LH), Short-Long (SL), and Short-High (SH) was named according to its wavelength coverage and the resolution avail-

---

<sup>2</sup>P.I.: George H. Rieke

<sup>3</sup>P.I.: James R. Houck



able in that module. Each module captured spectra on a  $128 \times 128$  pixel array. The short-wavelength modules used Si:As arrays, while the long-wavelength modules employed Si:Sb arrays. For this project, data were acquired using the LL and SL modules.

### 2.1.2 The Sample Chosen for Analysis with the *Spitzer* Space Telescope

The small sample selected for our study consists of four blazars detected at  $\gamma$ -ray energies by both the *Compton* Gamma-Ray Observatory (CGRO) Energetic Gamma-Ray Experiment Telescope (EGRET) and *Fermi* Large Area Telescope (LAT) instruments (Hartman et al., 1999; Abdo & et al., 2010). These four blazars were also found to contain an apparent IR excess over a pure power-law in their continuum spectra compiled by Impey & Neugebauer (1988): 4C 21.35 (alternately known as 1222+216,  $z = 0.435$ ), CTA102 ( $z = 1.037$ ), PKS 1510-089 ( $z = 0.361$ ), and ON 231 (1219 + 285,  $z = 0.102$ ). IR observations were obtained of these blazars with the IRAC, IRS, and MIPS instruments aboard SST between March 20, 2007 and February 16, 2008. This involved a complete set of observations with each instrument for each target at two different epochs separated by several months. Table 2.1 presents the observation times and the luminosity distance  $D_l$  for each blazar.

Each source was observed with both the SL and LL modules of IRS in order to acquire a spectrum over the range  $\lambda = 5.0\text{-}36.0 \mu\text{m}$ . A mosaicked spectrum of the target was created with observations from each of two slits of the spectrometer. The spectra from the two slits were then averaged together and smoothed over 10 adjacent wavelength bins. The IRAC observations employed either a 5-position Gaussian or 12-position Reuleaux triangle dither pattern, with 2 s frames. Both the MIPS and IRAC photometric measurements were accomplished with the Basic Calibrated Data (BCD) images and Post-BCD products provided by the *Spitzer* data reduction

pipeline, the latter of which combined all individual BCD frames to form a single mosaicked image at each IRAC (3.6, 4.5, 5.8, and 8.0  $\mu\text{m}$ ) and MIPS (24, 70, and 160  $\mu\text{m}$ ) band. I then applied a correction to account for the finite-sized aperture and a color adjustment to the measured flux according to the SST guidelines contained in the MIPS <sup>4</sup> and IRAC<sup>5</sup> handbooks. The spectral overlap between the IRS and other two SST instruments allowed the scaling of the fluxes to compensate for temporal variability or systematic errors in calibration.

In order to cover a wider spectral range, *R*-band images of each blazar were obtained by S. Jorstad during the epochs of the SST observations with the Perkins Reimaging System (PRISM)<sup>6</sup> on the Perkins 1.8 m telescope of Lowell Observatory in Flagstaff, Arizona. For 4C 21.35, I also include flux densities at five optical bands from the Sloan Digital Sky Survey (*SDSS*) described in Schneider et al. (2010), obtained only two days after epoch 2, and at three IR bands from the Two-Micron All Sky Survey (2MASS)<sup>7</sup> described in Skrutskie et al. (2006). The 2MASS magnitudes were converted into flux densities using the zero magnitude flux densities published by Cohen et al. (2003).

For comparison, I add later data from the Ultraviolet/Optical Telescope (UVOT) of the *Swift* satellite (Roming et al., 2005), obtained on 16 June 2010 during a major outburst in flux. These data were calibrated following the method of Poole et al. (2008). The optical and UV data were corrected for extinction according to Schlegel et al. (1998), interpolated or extrapolated at some bands.

---

<sup>4</sup><http://ssc.spitzer.caltech.edu/mips/mipsinstrumenthandbook/51/>

<sup>5</sup><http://ssc.spitzer.caltech.edu/irac/iracinstrumenthandbook/101/>

<sup>6</sup>P.I.: Kenneth Janes

<sup>7</sup><http://www.ipac.caltech.edu/2mass/releases/allsky/>

Table 2.1. Luminosity Distances and Dates of Observations

Source	$D_l$ (Gpc)	Epoch	IRS Dates (y-m-d)	MIPS Dates (y-m-d)	IRAC Dates (y-m-d)
4C 21.35	2.39	1	2007-06-11	2007-07-13	2007-06-28
		2	2008-01-12	2008-02-16	2008-02-01
CTA102	6.94	1	2007-06-27	2007-07-13	2007-07-02
		2	2007-12-06	2008-01-08	2007-12-22
PKS 1510-089	1.91	1	2007-03-20	2007-03-01	2007-03-31
		2	2007-08-06	2007-09-15	2007-08-07
ON231	0.465	1	2007-06-15	2007-06-05	2007-07-04
		2	2008-01-10	2008-01-08	2008-01-30

## 2.2 Data Selected from the Steward Observatory Blazar Monitoring Project

The study described in Chapter 4 relies on data obtained from the Steward Observatory blazar monitoring project<sup>8</sup>. This project utilizes two different telescopes in order to obtain spectropolarimetry for a number of blazars in a wavelength range spanning  $\lambda = 4000 - 7500 \text{ \AA}$  (Smith et al., 2009). The telescopes are the 1.54 m Kuiper Telescope located on Mt. Bigelow, AZ and the 2.3 m Bok Telescope situated on Kitt Peak, AZ. In addition to the smaller aperture providing lower sensitivity, the Mt. Bigelow telescope is mounted in such a way that sources with a declination north of  $\delta = 61^\circ$  are inaccessible due to the mount of the telescope, which was designed only to observe solar system objects.

Spectropolarimetry is performed using the SPOL spectropolarimeter developed at Steward Observatory and Space Telescope Science Institute (STScI) and detailed in

---

<sup>8</sup>P. I.: Paul Smith

Schmidt et al. (1992). SPOL contains a dual-beam medium-resolution spectrometer ( $\frac{\Delta\lambda}{\lambda} = 300 - 1000$ ), while polarization can be measured by inserting a half-wave plate in the beam path just behind the slit. The instrument has seven  $50''$  slits with widths in the range of  $1'' - 13''$ . This provides a resolution of  $15\text{-}25 \text{ \AA}$  for spectroscopy. The data are reduced in Image Reduction and Analysis Facility (IRAF) software suite of National Optical Astronomy Observatories (NOAO) and made publicly available on the P.I.'s website<sup>9</sup>. Flux calibration of a spectrum is calculated by performing synthetic photometry on a difference spectrum between the source and a comparison star in the photometric V-band, and then scaling to the measured V-band flux of the comparison star.

The Steward Observatory data provide access to time-domain flux-calibrated spectra as well as Stokes q and Stokes u spectra, which are defined as the Stokes Q and Stokes U parameters divided by 100. Sources are monitored nightly during roughly 1-2 week-long observing campaigns that occur monthly. Since the commencement of the project in 2008, approximately 1,000 nights of observations have been completed with the two facilities providing a rich dataset for the analysis presented in this dissertation.

## 2.3 Near-Infrared Ground Based Observations

In addition to space-based IR observations, I was able to acquire ground-based near-IR observations of several sources using separate facilities. These data, discussed in chapter 5, include using the Mimir instrument<sup>10</sup> (Clemens et al., 2007) mounted on Lowell Observatory's 1.8 m Perkins telescope located on Anderson Mesa near Flagstaff, Arizona, and remote observations using the SpeX instrument of the NASA

---

<sup>9</sup><http://james.as.arizona.edu/~psmith/Fermi/>

<sup>10</sup>P.I.: Dan Clemens

Table 2.2. Observing Campaigns at Lowell Observatory and IRTF

Campaign Calendar Month	Observing Dates	SpeX (Y/N)	Mimir (Y/N)
March 2011	2011-03-15:2011-03-24	N	Y
September 2011	2011-09-29:2011-10-04	N	Y
February 2012	2012-02-02:2012-02-10	N	Y
April 2012	2012-04-27:2012-05-05	N	Y
September 2012	2012-09-04:2012-09-07	Y	N
October 2012	2012-10-19:2012-10-20	N	Y (No data due to weather)
December 2012	2012-12-01:2012-12-09	N	Y
January 2013	2013-01-30:2013-02-08	N	Y
May 2013	2013-05-22	Y	N
June 2013	2013-06-28	Y	N
September 2013	2013-09-13:2013-09-16	N	Y
November 2013	2013-11-01	Y	N
January 2014	2014-01-06:2014-01-12	N	Y

Infrared Telescope Facility (IRTF) located on Mauna Kea, HI. Table 2.2 contains a listing of the observing campaigns I performed and instruments that I used to acquire data for this dissertation.

### 2.3.1 IR observations obtained at Lowell Observatory

Between March 2011 and January 2014 I performed near-IR imaging on a sample of gamma-ray bright sources using the Mimir instrument. Mimir is a multi-use  $1024 \times 1024$  pixel,  $10' \times 10'$  field of view instrument capable of providing photometry in the  $J$ ,  $H$ ,  $K_s$ ,  $L$ , and  $M$ , near-IR bandpasses. It is also capable of performing spectroscopy and polarimetry in the  $H$ , and  $K_s$  bands. I performed  $J$ ,  $H$ , and  $K_s$  band photometry on my sample, as well as polarimetry on a smaller subset of the sample. Because of the  $10'$  field of view, differential photometry between the source

and a comparison star was performed in order to determine the brightness of the source.

Photometry was typically performed by obtaining many short (integration times usually  $\leq 5$  s) exposure images. A typical observation involved taking several images in each position of a six point hexagonal dither pattern. The final image on which photometry was performed was generated by combining each individual image through median filtering. Flat fielding was accomplished through the use of dome flats, taken once per observing campaign, and each image was corrected for non-linearity of the instrumental response. Dark images, of identical exposure time to the source images, were obtained at the end of each observing night. Data reduction was performed through the use of the PPOL software suite written in IDL by Dan Clemens<sup>11</sup>. Figure 2.3 shows two Mimir images, one being an image just after the usual corrections for debiasing, flat-fielding, and dark-current removal have been applied, and another after several dozen such images have been coadded.

Polarimetry measurements, especially in the IR, are more complicated than photometry. To measure polarization, Mimir employs a rotating half-wave plate and a wire grid in front of the detector. The half-wave plate is rotated throughout 16 distinct orientations and then repeated throughout a dither pattern. After combining the images sharing identical half-wave plate positions, the modulation of the source brightness is used to determine the Stokes parameters and the degree of linear polarization. Polarization in the IR is very sensitive to the sky conditions, and more often than not, my attempts to measure the linear polarization in the  $H$ , and  $K_s$  bands failed to produce usable polarization measurements; however the images are still useful for providing photometric measurements.

---

<sup>11</sup><http://people.bu.edu/clemens/mimir/>

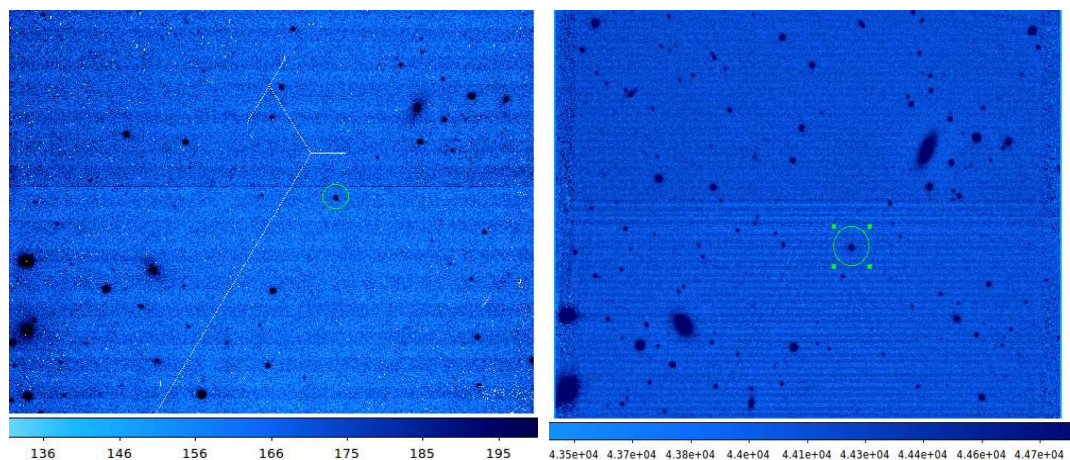


Fig. 2.3 *Left*: Bias, dark, flat, and linearity corrected individual image of 3C66A taken with Mimir in the J Band. To the left of the source, a crack in the detector array can be seen. The effects of this crack can be mostly removed by dithering the telescope while observing and combining the images through median-filtering of individual images at each dither position. *Right*: Deep coadd of the same source in the H-band. This image was generated by combining images taken while measuring the linear polarization of the source.

### 2.3.2 Observations Obtained with the IRTF

Boston University has access to two engineering nights per semester on the 3.0 m IRTF. On six separate nights between April, 2012 and December 2014, I observed several sources with the SpeX instrument (Rayner et al., 2003), operating in imaging mode. SpeX is a medium-resolution spectrometer optimized to operate between 0.7-5.3  $\mu\text{m}$ . To use SpeX as an imager, I employed the  $512 \times 512$ ,  $1' \times 1'$  array inside the instrument that is typically used for guiding the telescope. Because of the large primary mirror relative to the Perkins Telescope, the number of exposures could be kept low relative to Mimir.

A rectangular dither pattern was typically performed while observing in order to obtain photometry in the  $J$ ,  $H$ , and  $K$  photometric bands. Because of the small field of view of the instrument, comparison stars could not usually be captured in the same

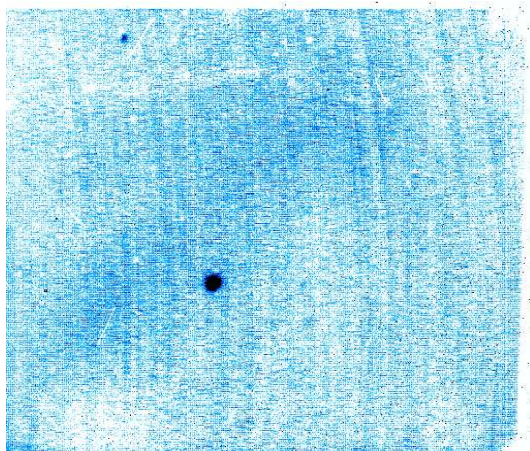


Fig. 2.4 SpeX Image of 3C66A obtained through a K-band filter. The exposure time is 10 s.

image, and therefore photometric standards were observed in separate pointings of the telescope. Flat-fielding was accomplished via sky-flats at dawn following each night of observing. A set of dark images was obtained for each exposure time used in order to remove the effects of dark current from the science images.

Aperture photometry was performed on both the source and several comparison stars observed throughout the night, correcting for extinction using the airmass at the time of observation, as well as the standard near-IR extinction values for Mauna Kea (Tokunaga et al., 2002). The flux adopted is the average after calibrating the flux scale with comparison star data. Figure 2.4 shows an example of a single SpeX frame obtained for 3C66A with through the K-band.

## 2.4 Gamma-ray Observations From the *Fermi* Gamma-ray Telescope

The *Fermi* Gamma-ray Telescope, launched in June 2008, is a low Earth orbiting satellite with two main instruments: 1) a Gamma-ray Burst Monitor (GBM), which is sensitive to the lower-energy range of the  $\gamma$ -ray spectrum, from a few keV



to 1 MeV (Meegan et al., 2009), and 2) the LAT, the main workhorse instrument of the satellite sensitive to  $\gamma$ -ray at energies spanning 100 MeV to 300 GeV. The LAT consists of a pair conversion instrument with a calorimeter to measure the energy of incoming  $\gamma$ -rays, and a precision converter-tracker to measure the trajectory of incoming  $\gamma$ -rays (Atwood et al., 2009). While in normal operation, the Large Area Telescope LAT alternates pointing between  $\pm 35^\circ$  from zenith on subsequent orbit, which coupled with the instruments large field of view, allows for complete sky coverage every three hours.

Because the LAT is in continuous operation, enormous amounts of data are generated, and an automated pipeline for the processing the  $\gamma$ -rays incident from a subset of sources is provided in the form of lightcurves with time resolutions of both 7 and 30 days<sup>12</sup>. This is done for the purposes of identifying both sources of  $\gamma$ -ray bursts and blazars undergoing flaring activity, of which immediate multi-wavelength follow-up observations would be desired. In this dissertation, I make use of the provided 7 day resolution light curves, in order to compare the variability of the  $\gamma$ -ray flux of some blazars with the variability of a component of their optical spectrum which I attribute to a variable component of the accretion disk surrounding the central black hole of the blazar.

---

<sup>12</sup><http://fermi.gsfc.nasa.gov/ssc/data/access/lat/msl.c/>

## Chapter 3

# Emission from Hot Dust in the Infrared Spectra of Gamma-ray Bright Blazars

This chapter contains some material previously published in Malmrose et al. (2011). A possible source of  $\gamma$ -ray photons observed from the jets of blazars is inverse Compton scattering by relativistic electrons of infrared seed photons from a hot, dusty torus in the nucleus. I use observations from the Spitzer Space Telescope to search for signatures of such dust in the infrared spectra of four  $\gamma$ -ray bright blazars, the quasars 4C 21.35, CTA102, and PKS 1510089, and the BL Lacertae object ON231. The spectral energy distribution (SED) of 4C 21.35 (1222+216) contains a prominent infrared excess indicative of dust emission. After subtracting a non-thermal component with a power-law spectrum, I fit a dust model to the residual SED. The model consists of a blackbody with temperature  $\sim 1200$  K, plus a much weaker optically thin component at  $\sim 660$  K. The total luminosity of the thermal dust emission is  $7.9 \pm 0.2 \times 10^{45} \text{erg s}^{-1}$ . If the dust lies in an equatorial torus, the density of infrared (IR) photons from the torus is sufficient to explain the  $\gamma$ -ray flux from 4C 21.35 as long as the scattering occurs within a few parsecs of the central engine. I also report a tentative detection of dust in the quasar CTA102, in which the luminosity of the IR excess is  $7 \pm 2 \times 10^{45} \text{erg s}^{-1}$ . However, in CTA102 the far-IR spectra are too noisy to detect the  $10\mu\text{m}$  silicate feature. Upper limits to the luminosity from thermal emission from dust in PKS 1510-089, and ON231 (1219+285), are  $2.3 \times 10^{45}$ , and  $6.6 \times 10^{43} \text{erg s}^{-1}$  respectively. These upper limits do not rule out

the possibility of inverse-Compton (IC) up-scattering of IR photons to  $\gamma$ -ray energies in these two sources. The estimated covering factor of the hot dust in 4C 21.35, 22%, is similar to that of non-blazar quasars; however, 4C 21.35 is deficient in cooler dust.

### 3.1 Introduction

The SED of a blazar over most of the electromagnetic spectrum is dominated by nonthermal emission from a relativistic jet (see, e.g., Marscher, 2010). The continuum at radio through infrared, optical, or even X-ray wavelengths is mainly or completely from synchrotron radiation. The  $\gamma$ -ray flux, which can dominate the SED much of the time (e.g., von Montigny et al., 1995; Abdo et al., 2010), is probably generated by IC scattering of lower energy seed photons by relativistic electrons in the jet (Sikora et al., 2009).

The source of the seed photons for the IC scattering is controversial. Both Begelman & Sikora (1987) and Dermer & Schlickeiser (1993) have suggested that photons emitted by the accretion disk, possibly reprocessed in the broad emission-line clouds or a dusty torus, are scattered to higher energies—the external-radiation Compton (ERC) scenario. Multi-frequency monitoring campaigns, on the other hand, indicate that flares in  $\gamma$ -ray flux often occur after outbursts in the 20-40 GHz range have begun and apparently superluminal knots have appeared in very-long-baseline interferometric images (Jorstad et al., 2001; Lähteenmäki & Valtaoja, 2003; Marscher et al., 2010). This implies that the  $\gamma$ -ray emission has an origin parsecs from the central engine of the active galactic nucleus (AGN). In this case, photons originating from the accretion disk or broad-line region would strike the jet plasma nearly from behind, so that the efficiency of IC scattering would be too low to explain the high  $\gamma$ -ray fluxes observed (Sikora et al., 2009).

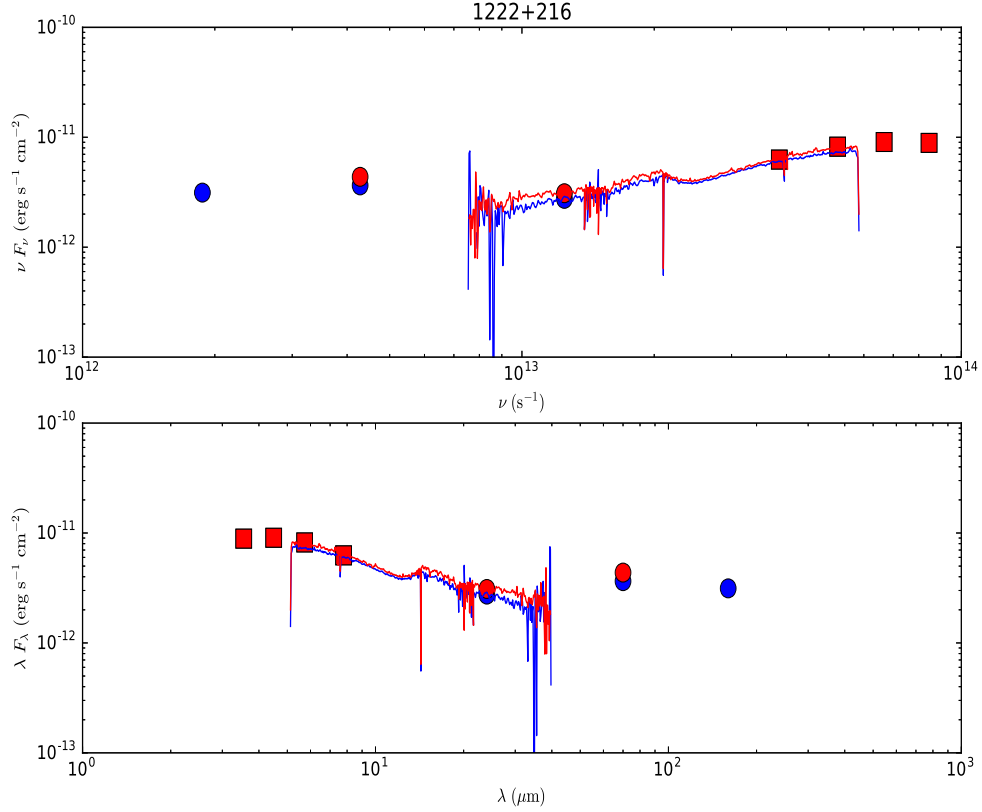


Fig. 3.1 Observed *Spitzer* SED of 4C 21.35/1222+216 in (a) frequency space and (b) wavelength space. Data obtained with Multiband Imaging Photometer (MIPS) are indicated with circles while Infrared Array Camera (IRAC) observations are shown with squares. The spectrum obtained with the two Infrared Spectrograph (IRS) modules is also shown. Blue symbols indicate observations obtained during the first epoch of observations, while red symbols indicate the second epoch. The source is slightly variable redwards of 10.0  $\mu\text{m}$ , with the flux increasing during 7-8 months between epochs indicating that the source of that emission is likely due to synchrotron radiation. This figure represents the data before the redshift of the source has been accounted for. The conclusion that synchrotron emission originating in the jet dominates the near-IR portion of the spectrum is also supported by optical and millimeter-wave linear polarization measurements (Jorstad et al., 2007), which can be described by a power-law  $F_\lambda \propto \lambda^{-\beta}$  (i.e.,  $F_\nu \propto \nu^{-\alpha}$ , where  $\alpha = 2 - \beta$  is the spectral index).

A variation of the ERC mechanism invokes as the main source of seed photons a molecular torus containing hot dust positioned roughly between  $\sim 1$  and 10 pc from the central engine (Błażejowski et al., 2000). Such a torus would be similar to that inferred from the SEDs of quasars (Hao et al., 2005; Ogle et al., 2006; Cleary et al., 2007) and directly imaged in the Seyfert 2 galaxy NGC 1068 (Jaffe et al., 2004; Raban et al., 2009). Thermal radiation, from warm-to-hot ( $T \approx 1100$  K) dust, has long been thought to be primarily responsible for the IR SEDs of radio-quiet quasars (Barvainis, 1990, 1992). However, detection of a similar dust component inferred in the IR SEDs of blazars has proven difficult owing to the dominance of a nonthermal component. The presence of a hot dust component has been inferred in the quasar 3C273 (Wills, 1989; Soldi et al., 2008), which is a luminous  $\gamma$ -ray source, based on its SED and variability as a function of wavelength. The case of 3C 273 is, however, difficult to disentangle with certainty because its IR emission includes a variable synchrotron component whose SED peaks near the same wavelength as that of the derived dust feature.

In this chapter, I report *Spitzer* Space Telescope (SST) (Werner et al., 2004) observations of four  $\gamma$ -ray bright blazars resulting in the detection of thermal emission from hot dust in the IR spectrum of the quasar 4C 21.35 (PG1222+216) and CTA102, and upper limits to the dust luminosity in the other two objects. In Section 3.2 I give an account of the data acquisition, reduction, and analysis, while in Section 3.3 I model the SED with a power-law plus a hot dust torus. Section 3.4 discusses the broader implications of these results, and Section 3.5 provides a summary. I adopt a cosmology consisting of a flat universe with  $\Omega_\Lambda = 0.73$ ,  $\Omega_m = 0.27$ , and  $H_0 = 71$  km s $^{-1}$  Mpc $^{-1}$ .

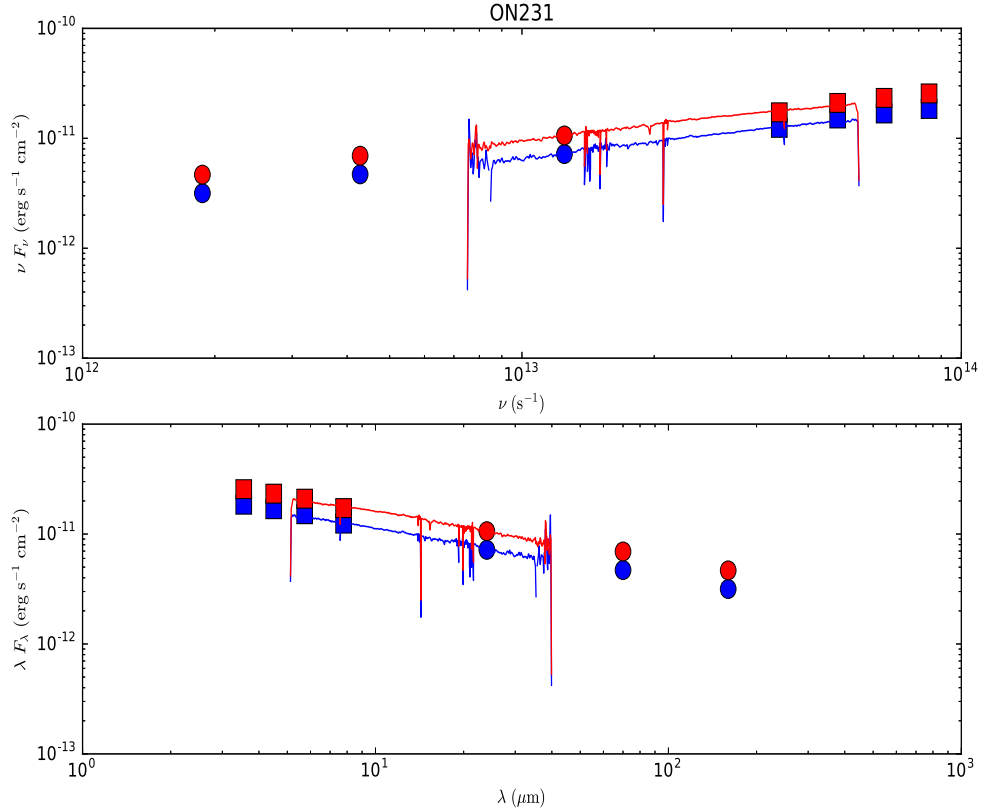


Fig. 3.2 Same as in Figure 3.1 for 1219+285/ON231.

### 3.2 Data

The data set utilized in this chapter is described in detail in Chapter 2. Preliminary inspection of the observed far-IR spectrum (i.e., 15-160  $\mu\text{m}$ ), as shown in Figures 3.1–3.4, indicates that synchrotron emission originating in the jet dominates this portion of the SED. This is because of the significant variability displayed redwards of 10  $\mu\text{m}$  in all four blazars included in the study. This is further supported by the optical and millimeter-wave linear polarization (Jorstad et al. 2007), and can be described by a power-law  $F_\lambda \propto \lambda^{-\beta}$  (i.e.,  $F_\nu \propto \nu^{-\alpha}$ , where  $\alpha = 2 - \beta$  is the spectral index). To determine the nonthermal portion of the SED, we plot  $F_\lambda$  vs.  $\lambda$  for each source,

with  $\lambda$  converted to the AGN rest frame. We then use the MIPS fluxes to fit a power-law to the SED by applying the least-squares criterion to the logarithmic plot of  $F_\lambda$  vs.  $\lambda$ . Panels (a) and (b) of Figure 3.5 display the measured continuum spectra for 4C 21.35, along with the power-law that fits the observed 15-160  $\mu\text{m}$  data. Panels (c) and (d) plot the observed SED, while panels (e) and (f) present the SED after subtraction of the power-law.

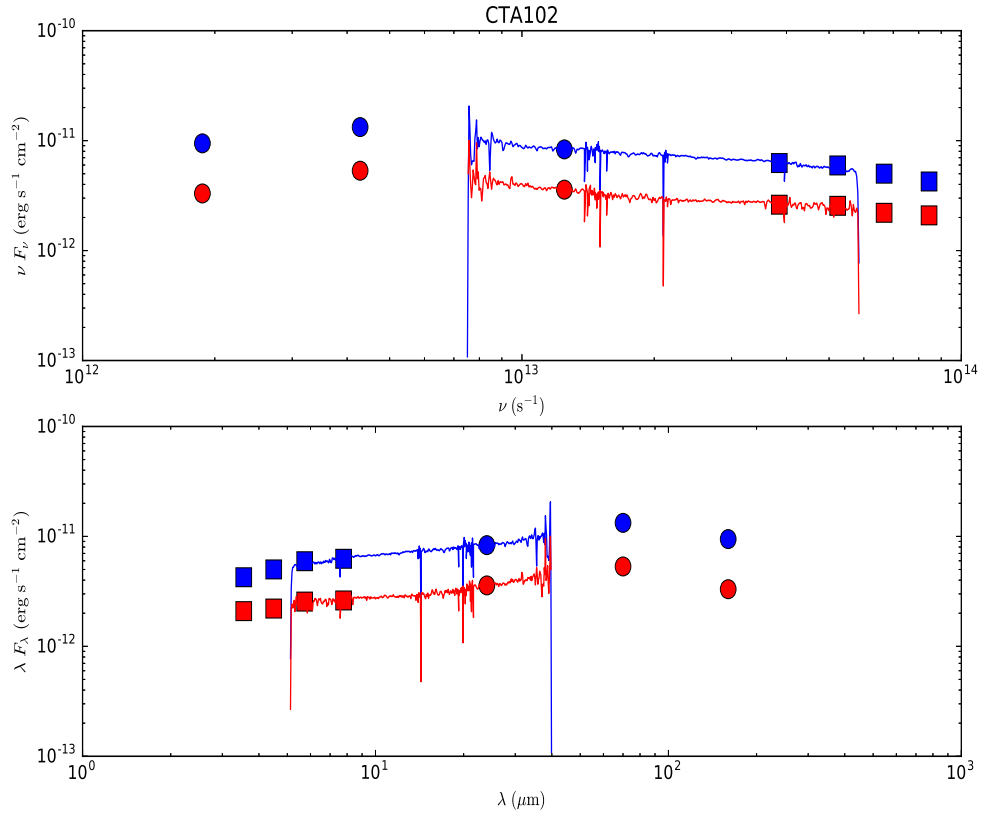


Fig. 3.3 Same as in Figure 3.1 for CTA102.

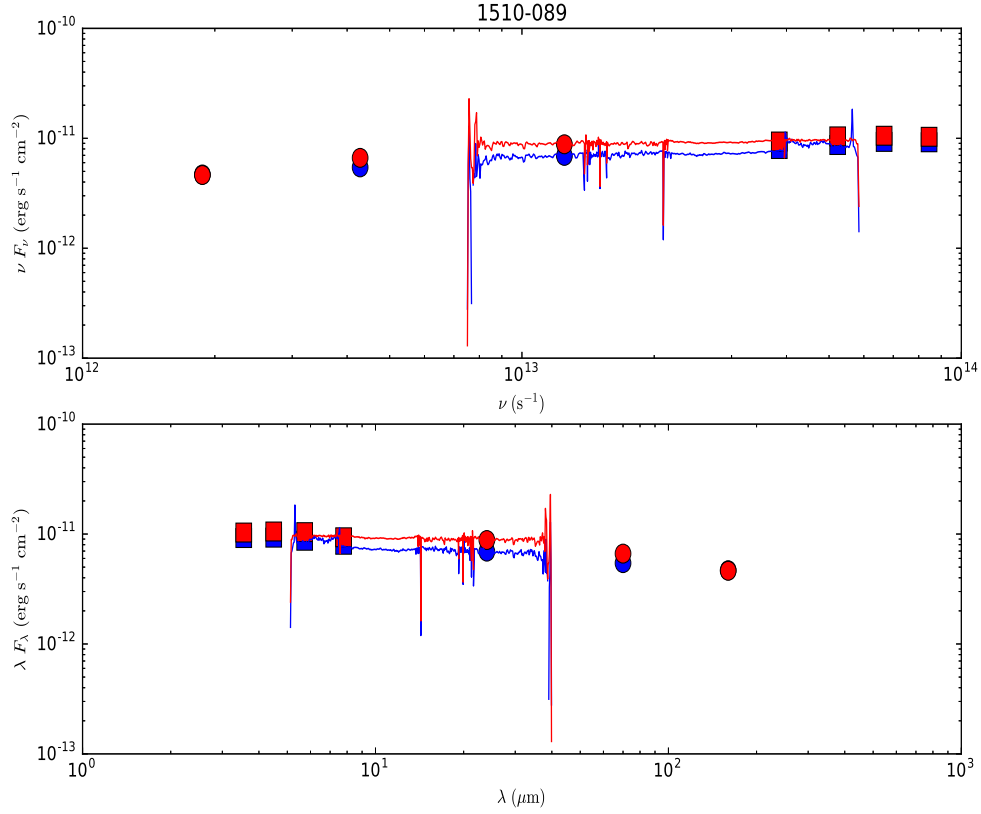


Fig. 3.4 Same as in Figure 3.1 for 1510-089.

### 3.3 Results

The signature of dust components in the SED is an infrared excess with a graybody or blackbody shape after removal of the nonthermal components (Gear et al., 1985). In the case of optically thin silicate dust, prominent features occur in the spectra at  $\lambda \approx 10 \mu\text{m}$  and  $\lambda \approx 18 \mu\text{m}$ . These are thought to be caused by stretching the Si-O bond and bending of the O-Si-O bond, respectively (Knacke & Thomson, 1973). In the case of 4C 21.35, the flat IR spectrum strongly suggests the presence of a thermal emitter even before subtraction of the power-law nonthermal component. The power-law, with spectral index  $\alpha = 0.84$ , was derived using the MIPS observations



during epoch 1. The same power-law was used for epoch 2, when the MIPS 160  $\mu\text{m}$  observation failed. The variability of flux redwards of 10  $\mu\text{m}$ , across epochs, was slight, which justifies this approach.

I first fit the residual SED (Fig. 3.5e,f) with a model consisting of a clumpy, dusty molecular torus (the CLUMPY model of Nenkova et al., 2008a,b), plus a uniform blackbody component with  $T \approx 1200$  K. However, this model did not agree with the data as well as a simpler structure consisting of a blackbody of temperature 1200 K and a more weakly emitting, optically thin dust component of temperature 660 K. The spectrum of this model, shown in panels (c) and (d) of Figure 3.5, results in a reduced  $\chi^2$  of  $\sim 13$ . The well-known silicate feature at 10  $\mu\text{m}$ , present in the observed spectrum, appears in emission.

The integrated luminosity of the dust emission is  $7.9 \pm 0.2 \times 10^{45}$  erg  $\text{s}^{-1}$ . From the luminosity and temperature, I calculate that the surface area of the 1200 K blackbody emitter is equivalent to that of a sphere of radius 2 pc or a torus extending from  $\sim 1$  to 1.5 parsec (pc) from the central engine. It is possible, however, that the dust is contained in multiple clouds, as is the case for the emission-line gas (see Nenkova et al., 2008b). The blackbody temperature of 1200 K in the model for 4C 21.35 is within the range that causes sublimation of dust (Salpeter, 1977), and hence may represent the periphery of dense clouds where sublimation occurs.

Equation (1) of Nenkova et al. (2008b) gives the sublimation radius  $R_d$  for the dust torus at sublimation temperature  $T_{sub}$  as,

$$R_d = 0.4 \left( \frac{L}{10^{45} \text{erg s}^{-1}} \right)^{1/2} \times \left( \frac{1500\text{K}}{T_{sub}} \right)^{2.6} \text{ pc.} \quad (3.1)$$

From this equation I calculate a sublimation radius of  $\sim 4$  pc for a  $T_{sub}$  of 1200 K. However, as Nenkova et al. (2008b) point out, the reverberation measurements of Minezaki et al. (2004) and Suganuma et al. (2006) yield an inner radius of the dust-emitting regions of AGN that is 2-3 times smaller than the theoretical value, perhaps because only the largest dust grains persist in the inner torus. A torus of hot dust 1-2 pc from the central engine is thus consistent with these studies.

The power-laws that best fit the observed 15-160  $\mu\text{m}$  data for the other two blazars do not result in much infrared excess. I therefore derive only an upper limit to the dust contribution to the SED. This requires subtraction of the steepest power-law that can fit the longer wavelength and R-band data while leaving an IR excess in the residual spectrum.

Numerical integration of the residual spectrum over wavelength yields an upper limit to the dust luminosity. Figures 3.6-3.8 display the observed spectra, power-law fits, and residual spectra. A closer look at the residual spectra from  $\lambda = 5 - 40$   $\mu\text{m}$  is shown in Figure 3.9. It is apparent that the IR excess emission over a pure power-law in the quasar 4C 21.35 is an order of magnitude greater than in the other three blazars in our sample. In the case of CTA102, extrapolation to the shorter wavelengths of the power-law that fits the spectrum at longer IRS wavelengths yields an excess consistent with dust emission at roughly the same temperature as found for 4C 21.35,  $\sim 1200$  K. The luminosity of this excess is  $7 \pm 2 \times 10^{45}$  erg s<sup>-1</sup>. The signal is too weak however, to determine whether the 10  $\mu\text{m}$  feature is present. I therefore consider the detection of dust emission in CTA102 to be tentative.

The results for the other two objects are strictly 2- $\sigma$  upper limits: (1) PKS 1510-089:  $\alpha = 0.9$ ,  $L_{dust} < 2.3 \times 10^{45}$  erg s<sup>-1</sup> (epoch 1); (2) ON231/1219+285:  $\alpha = 1.4$ ,  $L_{dust} < 6.6 \times 10^{43}$  erg s<sup>-1</sup> (epoch 1).

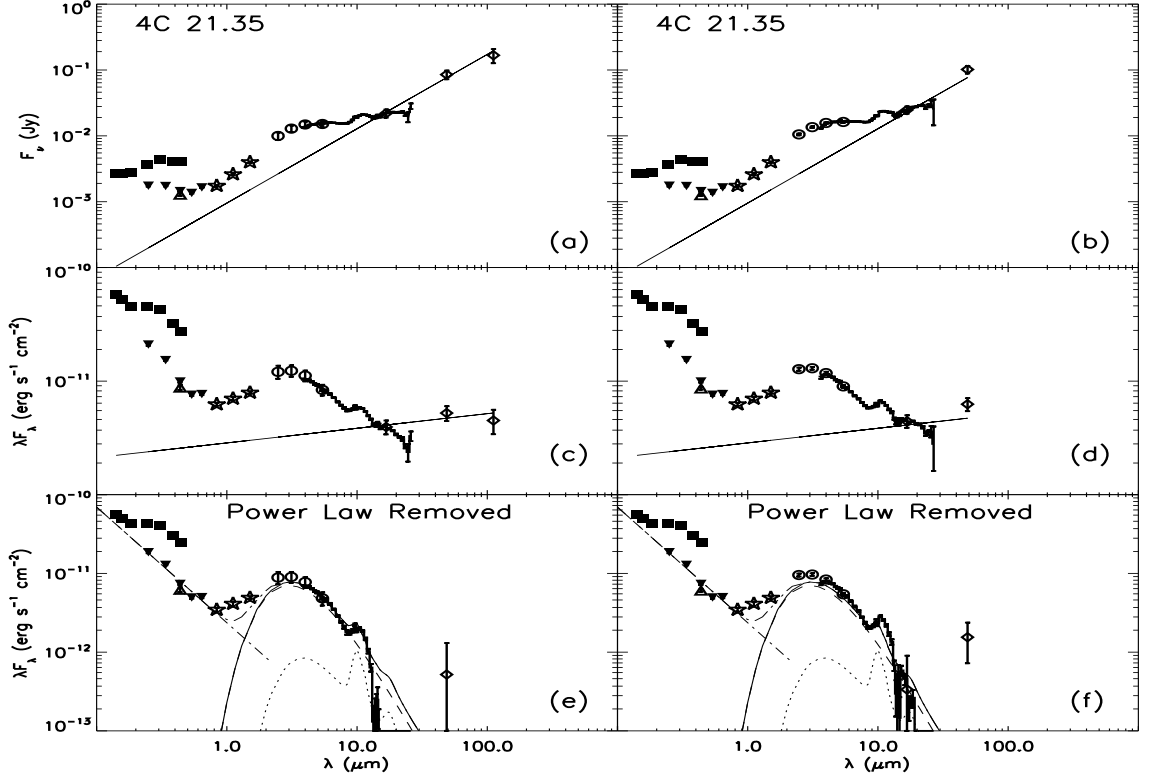


Fig. 3.5 (a) and (b): IR to UV spectra of 4C 21.35 ( $z = 0.435$ ) at epochs 1 and 2, respectively. *Horizontal axis*: wavelength in quasar rest frame. *Solid line*: power-law (spectral index  $\alpha = 0.84$ ) that best fits measurements at observed wavelengths of 20-160  $\mu\text{m}$ . *Circles, small squares, and diamonds*: IRAC, IRS, and MIPS data, respectively; *upward pointing triangle*: ground-based R-band observation; *stars*: fluxes from Two-Micron All Sky Survey (2MASS) survey; *downward pointing triangles*: SDSS measurements; *large squares*: *Swift* observations during an outburst in June 2010, showing that the optical-UV thermal emission is time-variable. (c) and (d): Observed SED. *Line*: as in panels (a) and (b). (e) and (f): Residual SED after subtraction of power-law. *Dashed curve*: SED of a  $\sim 1200$  K blackbody; *dotted curve*: SED of optically thin dust at a temperature of 660 K; *solid curve*: combination of the two dust components; *dash-dot line*: power-law fit to optical; *dash-double-dot curve*: sum of all components at near-IR wavelengths.

### 3.4 Discussion

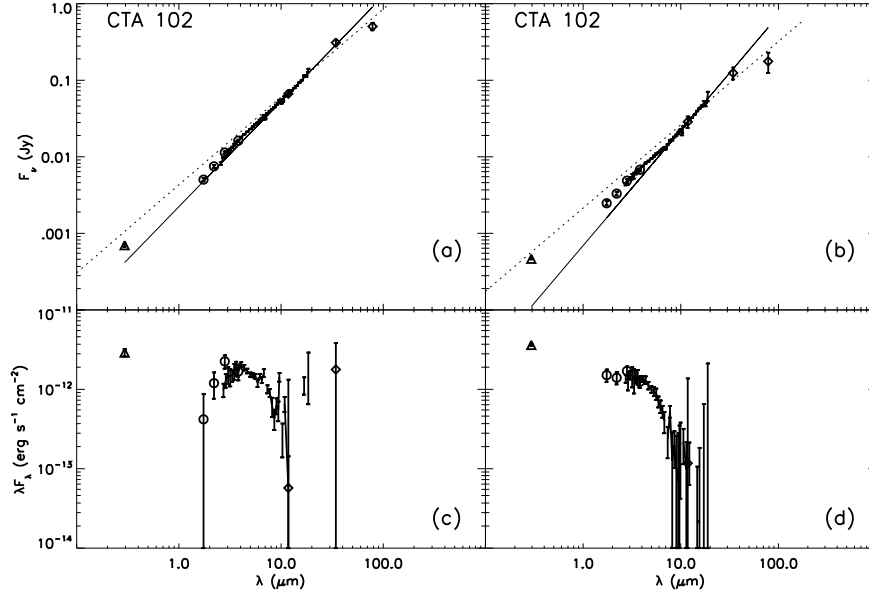


Fig. 3.6 (a) and (b) SED of CTA102 ( $z = 1.037$ ) at epochs 1 and 2, respectively. *Dotted line*: power-law (spectral index  $\alpha = 0.75, 0.79$  for a, b, respectively) that best fits the SED, with spectral index  $\alpha = 0.75$  in (a) and  $\alpha = 0.79$  in (b). *Solid line*: power-law derived from the observations at longer wavelengths of the IRS spectrum, with  $\alpha = 0.50$ . The residuals after subtraction of the second power-law are displayed in panels (c) and (d), the second of which is used to estimate an upper bound on the dust luminosity.

#### 3.4.1 Dust Properties of 4C 21.35 and Comparison with Non-blazars

The quasar 4C 21.35 contains a bent, one-sided extended radio jet that ends in a hot-spot, with a diffuse, complex lobe on the counterjet side (Jorstad & Marscher, 2006). Its radio emission is therefore rather peculiar, although this is partly caused by projection effects owing to a small angle between the jet axis and the line of sight. The deficiency of cool dust in the quasar 4C 21.35 certainly is an anomaly relative to non-blazar AGN. Previously published IR SEDs of radio-loud quasars and radio galaxies

with dust emission features (Ogle et al., 2006; Cleary et al., 2007; Schweitzer et al., 2008; Mor et al., 2009), none of which is classified as a blazar, differ strongly from that of 4C 21.35. Siebenmorgen et al. (2005) observed the  $10\mu\text{m}$  silicate feature in emission with IRS in the quasars 3C 249 and 3C 351, and fit photometric data with three components, with the IR emission dominated by  $\sim 60$  K dust. Landt et al. (2010) employed all three of *Spitzer's* science instruments to investigate the dust geometry on a sample of 12 AGN at various orientations. Of that sample, only the Seyfert 1 galaxy 3C 263, at an orientation angle of  $\theta = 34^\circ$ , was found to be deficient in cooler dust. Hao et al. (2005) observed the  $10\mu\text{m}$  and  $18\mu\text{m}$  silicate features in 5 quasars, however they were unable to derive reliable temperatures for the dust. From the literature it appears that cold dust dominates the IR SEDs of radio-loud quasars when dust has been detected. It is therefore striking that emission from cool to warm dust is suppressed in 4C 21.35.

The bolometric luminosity of the central engine of 4C 21.35 is  $3.5 \times 10^{46}$  erg s $^{-1}$  if I use the same bolometric conversion as Mor et al. (2009). The dust IR to bolometric luminosity ratio is then 0.23. This conforms with the covering factors of hot dust, 0.20-0.33, derived by Hao et al. (2005). However, the blazar's 2-25  $\mu\text{m}$  rest-frame spectrum is considerably flatter,  $\alpha = 0.29$ , compared with a mean of 1.2 for the quasars in the Ogle et al. (2006) study. The drop in flux toward longer wavelengths in the residual spectrum of 4C 21.35 (Fig. 3.5) contrasts strongly with the nearly constant or rising flux of the non-blazars up to  $\sim 20\mu\text{m}$ . This is true (although not as extreme) even if I do not subtract a power-law nonthermal spectrum (Fig. 3.5c,d), in the unlikely limit that the entire IR SED is from the thermal dust component at the two observing epochs.

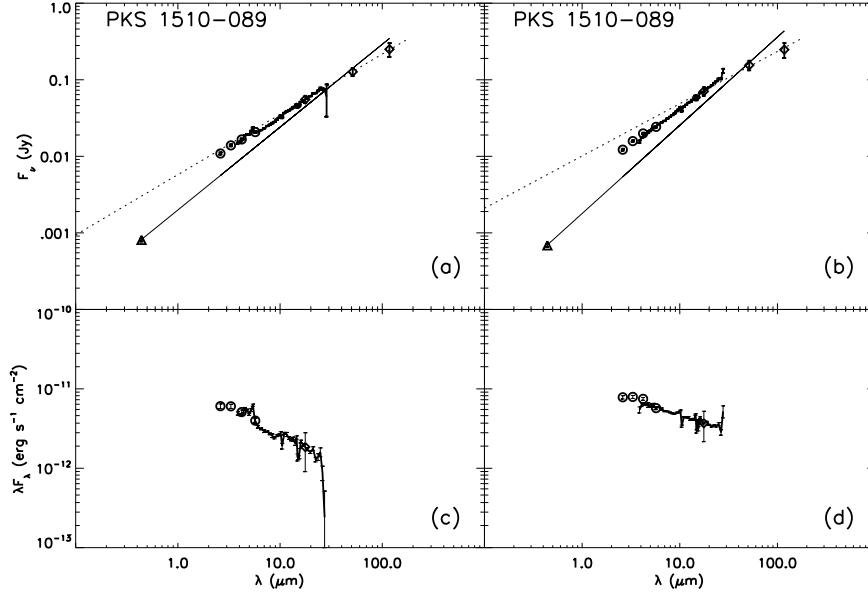


Fig. 3.7 As in Fig. 2, for PKS 1510-089. *Dotted line*: power-law derived solely from the MIPS data, with  $\alpha = 1.22$ ,  $\alpha = 1.29$  for (a), (b), respectively. *Solid line*: power-law with steepest slope consistent with MIPS and *R*-band data, with  $\alpha = 0.91$ ,  $0.82$  for (a), (b), respectively. The resultant spectrum in panel (c) is used to derive an upper limit to the luminosity from dust emission.

Hence, there is an excess of hot dust at  $T \sim 1200$  K, and probably a deficit of warm dust at temperatures between  $\sim 300$  and  $800$  K, in 4C 21.35 compared with the non-blazars. I note that this contrasts strongly with the finding of Landt et al. (2010) and of Siebenmorgen et al. (2005) that the warm ( $T \sim 300$ - $800$  K) and cold ( $T \sim 150$ - $250$  K) dust component is stronger than the hot dust component for sources viewed closer to the jet axis. The hot dust in 4C 21.35 has quite similar properties to those inferred in the  $\gamma$ -ray bright blazar 3C 273 by Soldi et al. (2008), who fit the dust component of the IR emission with a graybody of temperature  $\sim 1200$  K with a visible surface area of  $1$ - $2$   $\text{pc}^2$ , although uncertain extrapolation of the nonthermal IR component precludes a strong conclusion regarding the relative abundance of dust at lower temperatures.

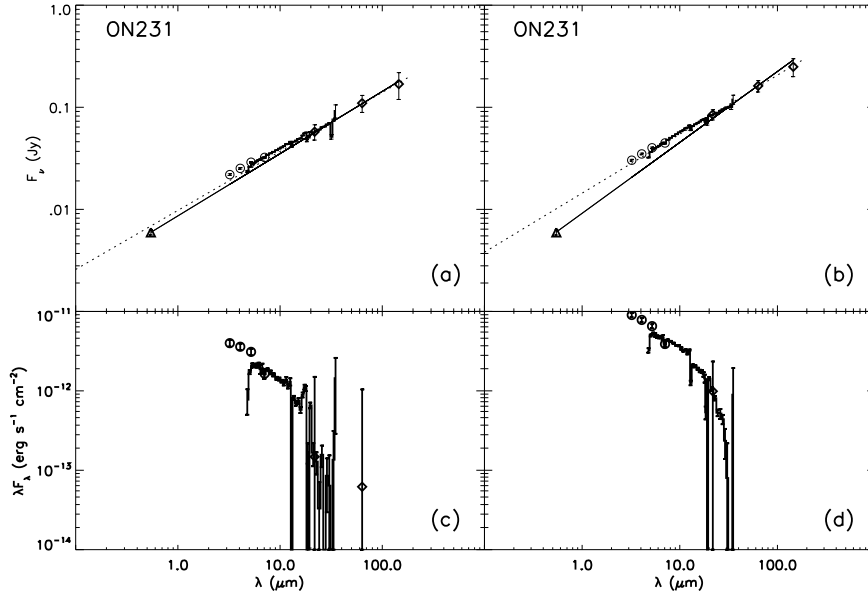


Fig. 3.8 As in Fig. 3, for 1219+285. *Dotted line* corresponds to spectral index  $\alpha = 1.41$  at both epochs; *solid line* corresponds to  $\alpha = 1.39, 1.30$  for (a),(b), respectively. The residual spectrum in panel (c) provides an upper limit to the luminosity from dust emission.

These results suggest that a  $\gamma$ -ray bright blazar is a rare phenomenon, not simply a common radio galaxy with a jet that happens to point almost directly toward our line of sight. We can understand this if emission at MeV and GeV energies dominates the SED of a quasar only if the jet has a high Lorentz factor (for observational evidence of this, see Jorstad et al., 2001; Kellermann et al., 2004; Savolainen et al., 2010), and if such highly relativistic quasars are rare (see Lister & Marscher, 1997).

The low warm/cool-to-hot dust ratio in 4C 21.35 compared with non-blazars implies that the presence of a highly relativistic jet either heats or destroys the cooler dust. The jet emission is highly beamed, at least on parsec scales, presumably along the poles of the accretion disk and molecular torus. Measurement of apparent superluminal motion in the jet of 4C 21.35 gives a bulk Lorentz factor  $\Gamma \approx 20$

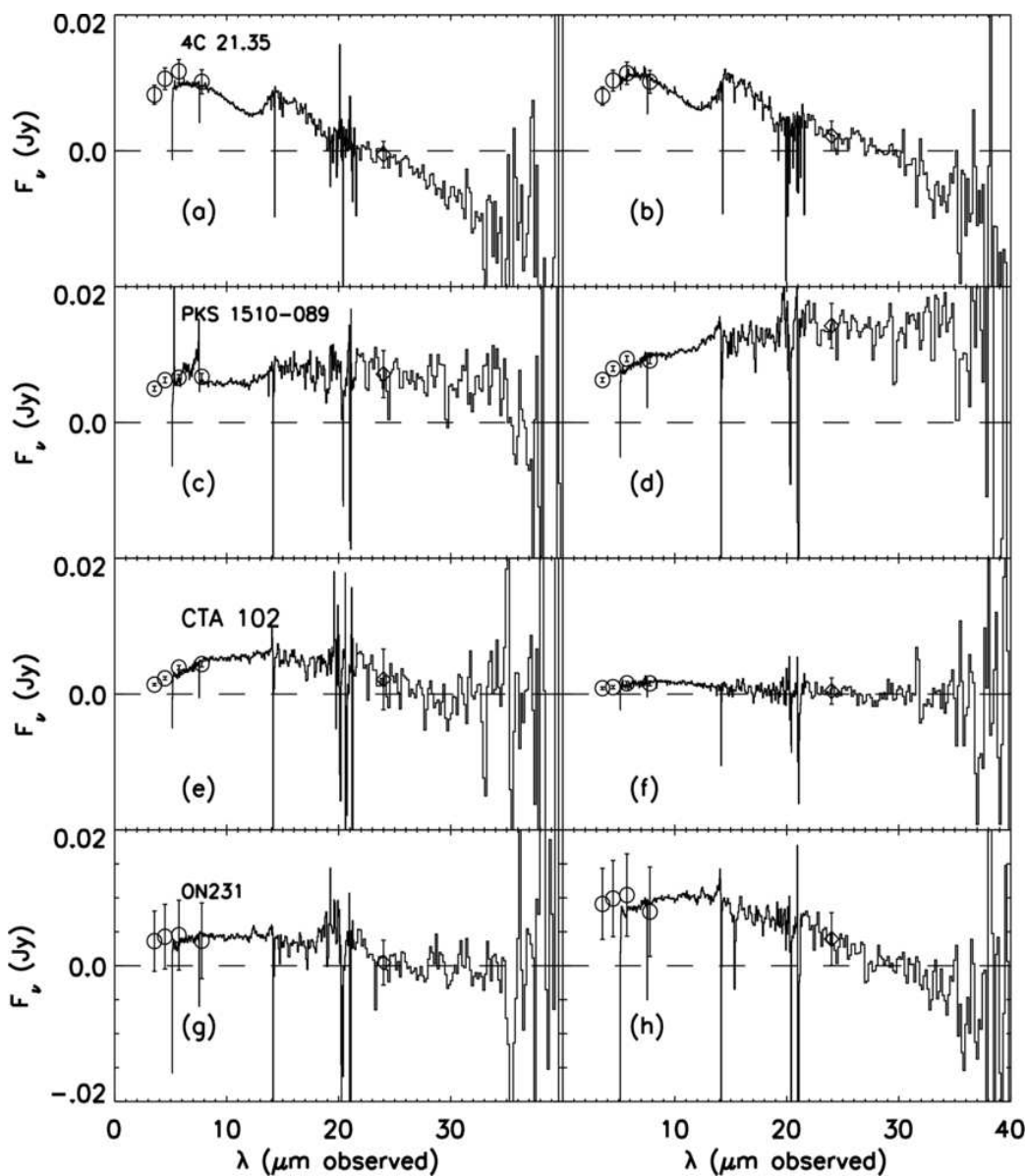


Fig. 3.9 A close-up view of the observed spectra of all four blazars at epoch 1 (a),(c),(e), and (g) and epoch 2 (b), (d), (f), (h), respectively, at  $\lambda = 0 - 40 \mu\text{m}$ . Symbols as in Fig. 4. (a)-(b) 4C 21.35, (c)-(d) PKS 1510-089, (e)-(f) CTA 102, (g)-(h) ON231. *Horizontal axis*: observed wavelengths. *Vertical axis*: flux density in Janskys after the power-law has been removed. Note that the infrared excess in 4C 21.35 is an order of magnitude greater than in the other three blazars. The feature near  $14 \mu\text{m}$  in all eight spectra is an artifact of the IRS where the instrument observes the shorter wavelengths in the SL module and the longer wavelengths in the LL module.



(Jorstad et al., 2001) on parsec scales, with the jet axis pointing within  $\sim 3^\circ$  of our line of sight. However, the optical-ultraviolet SED of 4C 21.35 (Fig. 3.5) indicates that the big blue bump (BBB) dominates over nonthermal emission from the jet, so that the jet supplies a minority of the photons that could affect the physical state of the dust. Nevertheless, it is possible for photons emitted by the jet to illuminate and heat the outer parts of a dust torus that are shielded from the central engine by the inner torus, as in the geometry adopted by Kawaguchi & Mori (2010). Given the beaming of the parsec-scale jet emission, this process would be most effective if the bulk Lorentz factor of the section of the jet  $< 1$  pc from the central engine were less than that measured farther downstream (see Marscher et al., 2008). Alternatively, a slower sheath of the jet could produce less well-beamed ultraviolet radiation that shines down on and heats the outer torus (see, e. g., MacDonald et al., 2015).

### 3.4.2 Relation between Dust and Gamma-ray Emission

The quasar 4C 21.35 is one of only 16 blazars from which the *Fermi* LAT<sup>7</sup> detected  $\gamma$ -ray emission at photon energies of 0.1–300 GeV above  $1 \times 10^{-6}$  photons  $\text{cm}^{-2} \text{s}^{-1}$  (with an integration time of 1 week) between 2008 August and 2010 October. The radiation from hot dust provides a high density of seed photons for IC scattering by relativistic electrons in the jet. Formula (5) of Sokolov & Marscher (2005) gives the ratio of energy density of IR photons from hot dust to that of the magnetic field in Gaussian units,  $B$ , in the rest frame of the jet plasma, as

$$u_{\text{phot}}/u_B \approx 20 \left( \frac{T}{1200 \text{ K}} \right)^4 \left( \frac{\Gamma}{20} \right)^2 B^{-2}, \quad (3.2)$$

independent of the distance  $r_{\text{in}}$  from the central engine, as long as the distance along the jet of the scattering site  $r$  satisfies,  $r \leq r_{\text{in}}$ . Theoretically, this is roughly the same

---

<sup>7</sup>Light curves are displayed at <http://fermi.gsfc.nasa.gov/ssc/data/access/lat/msl1c/>

as the ratio of ERC to synchrotron luminosity. Here,  $T$  is the blackbody temperature of the dust and  $B$  is the magnetic field in the jet in Gauss. Since the magnetic field strength of a blazar on parsec scales is typically 0.1-1 G, ERC scattering of IR emission from dust dominates over that of synchrotron emission from the jet (Sikora et al., 2009). While it is possible that local sources of seed photons, such as synchrotron emission from a slower sheath of the jet, might compete with the dust radiation (Marscher et al., 2010), the high ratio of  $\gamma$ -ray to IR synchrotron luminosity observed when 4C 21.35 is in a high flux state (e.g., during the first half of 2010; Donato, 2010) can be explained by IC scattering of IR photons from the hot dust. Recent analysis by Tanaka et al. (2011) of a GeV outburst observed by *Fermi* LAT, coincident with a flare at  $\sim$  TeV energies observed by the Major Atmospheric Gamma Imaging Cherenkov (MAGIC) telescope (Mariotti, 2010), supports the conclusion that  $\gamma$ -rays originate at a scale comparable to  $\sim 1$  pc from the central engine. The lower range of this scale is consistent with hot dust being the source of seed photons for  $\gamma$ -rays.

Because I obtain rather high upper limits to the dust-to-bolometric luminosity ratio of the other two quasars in our program,  $\leq 0.5$  for CTA102 and  $\leq 0.25$  for PKS 1510–089 (with bolometric luminosities estimated from the SEDs displayed in the NASA/IPAC Extragalactic Database), and have no constraint on the ratio in the BL Lac object ON231, I cannot exclude the possibility that all  $\gamma$ -ray bright blazars contain nuclear dust with covering factors exceeding 25%. It is therefore possible that a high flux of IR emission from dust might be required to produce  $\gamma$ -ray fluxes greater than  $1 \times 10^{-6}$  photons  $\text{cm}^{-2} \text{s}^{-1}$  that are sometimes observed in quasars (e.g., Abdo & et al., 2010) It is therefore possible that a high flux of IR emission from dust might be required to produce  $\gamma$ -ray fluxes greater than  $1 \times 10^{-6}$  photons  $\text{cm}^{-2} \text{s}^{-1}$ . Unfortunately, detection of emission from dust is difficult owing to the dominance

Table 3.1. Data for 4C 21.35

Epoch 1			Epoch 2		
$\lambda_{rest}$ ( $\mu\text{m}$ )	$F_\nu$ (mJy)	$\sigma F_\nu$ (mJy)	$\lambda_{rest}$ ( $\mu\text{m}$ )	$F_\nu$ (mJy)	$\sigma F_\nu$ (mJy)
<i>IRS</i>					
3.57	2.42	0.87	3.59	12.75	1.88
3.59	11.21	1.80	3.61	14.18	0.84
3.61	11.82	0.87	3.63	14.45	0.53
<i>IRAC</i>					
2.47	8.36	1.10	2.47	8.61	0.28
3.13	10.82	1.25	3.13	11.11	0.32
3.99	12.50	1.36	3.99	12.85	0.35
5.42	12.71	1.38	5.42	13.31	0.35
<i>MIPS</i>					
16.72	21.03	1.87	16.72	21.59	1.90
48.78	81.32	8.59	48.78	88.76	8.52
111.50	159.80	35.99	-	-	-

Note. — Only the first three lines of the unsmoothed IRS data are presented. The entire contents of this table are provided as a machine readable table in the ApJ version of this chapter.

of the nonthermal IR component in most blazars. Of note, on the other hand, that Leipski et al. (2009), in a study of 15 Fanaroff-Riley Class I (FRI) galaxies, classified as an obscured AGN with compact radio emission (Fanaroff & Riley, 1974), with detected optical activity in the nucleus, a significant IR excess is detected in eight sources (53% of the sample). In four of the eight sources in which an IR excess is detected, the excess is attributed to star formation and stellar emission in the host galaxy. The IR excess in the other four of these sources are attributed to warm dust (hundreds of Kelvins) emission powered by a hidden AGN. This implies that the

number of BL Lac objects with hot dust ( $T > 1000$  K) emission is quite low (27%), since they are thought to reside in FR I galaxies (Urry & Padovani, 1995).

### 3.5 Summary

I have searched for signs of thermal emission from hot dust in the IR spectra of four  $\gamma$ -ray bright blazars. I find clear evidence for dust emission in the quasar 4C 21.35, whose IR spectrum is nearly flat at rest wavelengths between 2 and 25  $\mu\text{m}$ . The luminosity of the thermal emission,  $\sim 8 \times 10^{45}$  erg  $\text{s}^{-1}$ , is sufficient for the radiation to supply the bulk of the seed photons for IC scattering to  $\gamma$ -ray energies during the outburst in the first half of 2010. I also find an infrared excess in the spectrum of CTA 102 with a luminosity of  $\sim 7 \times 10^{45}$  erg  $\text{s}^{-1}$  that is consistent with dust emission. The case for dust emission is weak for the other two blazars, for which I can only determine an upper limit after subtraction of the non-thermal component. These upper limits, however, do not exclude IC scattering of photons emitted by hot dust as the main source of  $\gamma$ -ray seed photons.

The IR spectrum of 4C 21.35 is considerably flatter than that of other non-blazar quasars, with most of the luminosity arising from the hottest dust. The deficit of dust with temperatures in the 150-800 K range may be related to the presence of the highly relativistic jet, which could produce ultraviolet synchrotron photons that heat dust in the outer torus, where only warm or cold dust resides in non-blazar active galactic nuclei.

Thermal emission from dust is difficult to find in blazars owing to the strong nonthermal continuum. Except in exceptional cases such as 4C 21.35, in which the power-law spectrum from synchrotron radiation is less prominent at near- and mid-IR wavelengths, accurate determination and subtraction of the nonthermal component

Table 3.2. Data for PKS 1510-089

Epoch 1			Epoch 2		
$\lambda_{rest}$ ( $\mu\text{m}$ )	$F_\nu$ (mJy)	$\sigma F_\nu$ (mJy)	$\lambda_{rest}$ ( $\mu\text{m}$ )	$F_\nu$ (mJy)	$\sigma F_\nu$ (mJy)
<i>IRS</i>					
3.76	0.002.43	1.17	3.76	4.12	1.22
3.78	0.011.57	2.14	3.78	15.32	3.98
3.81	0.012.16	1.00	3.81	15.42	4.20
<i>IRAC</i>					
2.61	8.51	0.28	2.61	12.11	0.33
3.30	10.86	0.31	3.30	15.67	0.38
4.21	12.98	0.35	4.21	19.72	0.43
5.72	16.20	0.39	5.72	24.05	0.48
<i>MIPS</i>					
17.63	42.10	2.64	17.63	71.73	3.30
51.43	96.51	10.28	51.43	157.43	12.04
117.56	190.03	46.07	117.56	251.21	46.07

Note. — Only the first three lines of the unsmoothed IRS data are presented. The entire contents of this table are provided as a machine readable table in the ApJ version of this chapter.

is essential in the search for dust emission. This requires simultaneous flux measurements at many wavelengths between the optical and millimeter spectral regions. In addition, the nonthermal emission is generally variable and linearly polarized, so determination of the SED at different times and measurement of polarization at different IR to millimeter wavelengths can aid in its subtraction (see Soldi et al., 2008). Future multi-wavelength monitoring campaigns would allow a better definition of the properties of the dust torus and how these depend on the nonthermal luminosity and relativistic beaming of the jet.

Clavel et al. (1989), Minezaki et al. (2004), and Suganuma et al. (2006), have observed changes in the IR flux of Seyfert galaxies, with an approximately one year time delay relative to UV variations in the BBB emission. Barvainis (1992) interprets this as the consequence of hot silicate or graphite dust ( $T \sim 1100 - 1900$  K) with a nearly blackbody spectrum whose total luminosity vs. time is well correlated with variations in the UV luminosity. A dust reverberation model was developed in which higher ultraviolet (UV) flux from the central engine increases the radius of the hot-dust region and therefore increases the flux of IR photons emitted from that region. The AGN unification scheme suggests that (Antonucci, 1993b; Urry & Padovani, 1995) similar reverberations in the IR SED of dust containing blazars should be observable in the quasar 4C 21.35, due to the rapid increase in UV flux in 2010. The time delay between the peak of the UV flare and the IR flux from the dust reverberation would then provide valuable information on the location and geometry of the dusty region. Furthermore, any outbursts observed in the UV emission from the BBB in other blazars could increase the IR emission to facilitate detection of the dust component.

Table 3.3. Data for CTA102

Epoch 1			Epoch 2		
$\lambda_{rest}$ ( $\mu\text{m}$ )	$F_\nu$ (mJy)	$\sigma F_\nu$ (mJy)	$\lambda_{rest}$ ( $\mu\text{m}$ )	$F_\nu$ (mJy)	$\sigma F_\nu$ (mJy)
<i>IRS</i>					
2.51	1.33	1.29	2.51	0.46	1.62
2.53	5.83	2.35	2.53	3.79	4.63
2.54	8.18	1.12	2.54	4.20	1.03
<i>IRAC</i>					
1.74	0.33	0.17	1.74	2.30	0.14
2.21	0.38	0.21	2.21	3.07	0.17
2.81	0.43	0.27	2.81	4.53	0.21
3.82	0.48	0.32	3.82	6.29	0.25
<i>MIPS</i>					
11.78	37.00	2.48	11.78	36.59	2.46
34.36	172.16	12.12	34.36	158.73	11.89
78.55	280.00	43.19	78.55	225.30	44.63

Note. — Only the first three lines of the unsmoothed IRS data are presented. The entire contents of this table are provided as a machine readable table in the ApJ version of this chapter.

Table 3.4. Data for ON231

Epoch 1			Epoch 2		
$\lambda_{rest}$ ( $\mu\text{m}$ )	$F_\nu$ (mJy)	$\sigma F_\nu$ (mJy)	$\lambda_{rest}$ ( $\mu\text{m}$ )	$F_\nu$ (mJy)	$\sigma F_\nu$ (mJy)
<i>IRS</i>					
4.65	6.37	1.21	4.65	7.13	1.11
4.67	24.44	2.21	4.67	29.56	2.12
4.70	24.99	1.02	4.70	31.65	1.05
<i>IRAC</i>					
3.22	21.06	0.44	3.22	25.38	0.48
4.08	24.42	0.47	4.08	29.23	0.52
5.20	27.90	0.51	5.20	33.56	0.55
7.06	31.90	0.55	7.06	37.44	0.60
<i>MIPS</i>					
21.78	50.45	2.89	21.78	78.50	3.60
63.52	105.18	9.82	63.52	149.75	11.28
145.19	212.34	41.75	145.19	230.34	41.75

Note. — Only the first three lines of the unsmoothed IRS data are presented. The entire contents of this table are provided as a machine readable table in the ApJ version of this chapter.



## Chapter 4

# Analysis of the Level of Variability of the Components of Optical-UV Emission

### 4.1 Introduction

In a  $\gamma$ -ray bright blazar, two main components may arise in the optical-ultraviolet spectrum. First, a highly polarized component due to the synchrotron emission emanating from the jet of the blazar, and second, the blackbody emission from the super-massive black hole's multi-temperature accretion disk, known colloquially as the big blue bump (BBB). While the synchrotron component of the spectral energy distribution (SED) has long been known to be variable, the time domain stability of the BBB has been less well explored in blazars.

Paltani et al. (1998), using UV data from the IUE satellite, reported variability of the BBB of 3C273 on a timescale of  $\sim 2$  years. This study, however, lacked measurements of the polarization state of the blazar, and therefore an accurate characterization of any synchrotron component in the spectrum. After the advent of the *Fermi* Gamma-Ray Telescope, time domain monitoring of  $\gamma$ -ray bright blazars became possible, with a scan of the entire sky acquired every three hours. The result of this steady stream of data is the spawning of multi-waveband monitoring projects in support of the *Fermi* mission.

The Steward Observatory spectropolarimetric monitoring project (Smith et al., 2009) provides ground-based support for the *Fermi* mission by monitoring the spectra and polarization characteristics of a sample of  $\gamma$ -ray bright blazars. Beginning in October 2008, and continuing to the present, objects have been observed during many campaigns with the SPOL Imaging/Spectropolarimeter at both the 2.3 m Bok Telescope, located on Kitt Peak, and the 1.54 m Kuiper Telescope, located on Mt. Bigelow. Reduced data products are available online<sup>1</sup> and include 1) flux-calibrated spectra and 2) Stokes-q and Stokes-u spectra, defined as  $\frac{Q}{I}$  and  $\frac{U}{I}$  respectively, for a sample of  $\gamma$ -ray bright blazars spanning a wavelength range of  $\lambda = 4000 - 7500 \text{ \AA}$  in the observer's reference frame. The availability of the Stokes parameters allows for the recovery of the degree of linear polarization,  $\Pi = \sqrt{q^2 + u^2}$ , and the total polarized flux across the bandpass,  $F_{\Pi} = \Pi \times F_{\nu}$ .

Table 4.1 provides a list of blazars analyzed in this chapter, spectral type, celestial coordinates, and redshifts. Figure 1.1 shows a typical flux-calibrated spectrum and the corresponding polarized flux spectrum obtained by the Steward Observatory team for the flat-spectrum radio quasar (FSRQ) 1222+216, while Figure 4.1 displays a typical spectrum for the Stokes parameters, degree of linear polarization, and direction of polarization vector on the plane of the sky, throughout the bandpass. In the case of 1222+216, the decreasing polarized fraction of the total flux with frequency indicates the presence of a strong, non-polarized component to the spectrum that increases in flux toward higher frequencies. The source of this non-polarized emission is likely the accretion disk of the blazar. However, this chapter will also explore the possibility of a wavelength-dependent component of the synchrotron emission causing the decrease in polarization seen at shorter wavelengths.

---

<sup>1</sup><http://james.as.arizona.edu/~psmith/Fermi/>

Table 4.1. Subset of Blazars Monitored by the Steward Observatory Fermi Support Mission

Source Name	Spectral Type	R.A. (hh:mm:ss)	Dec (dd:mm:ss)	N Spectra <sup>a</sup>	Dates Observed <sup>b</sup>	$z$
3C66A	BL Lac	02:22:39.6	+43:02:08	170	2009-09-14–2013-03-13	0.444
CTA26	FSRQ	03:39:31.0	-01:46:36	24	2011-09-29–2014-10-29	0.852
0420-014	FSRQ	04:23:15.8	-01:20:33	53	2009-10-09–2012-01-27	0.916
0735+178	BL Lac	07:38:07.4	+17:42:19	34	2009-10-21–2010-04-11	0.424
OJ248	FSRQ	08:30:52.1	+24:10:59	128	2009-09-16–2014-05-27	0.939
OJ287	BL Lac	08:54:48.9	+20:06:31	168	2009-09-15–2013-04-12	0.306
1219+285	BL Lac	12:21:31.7	+28:13:59	220	2008-10-28–2014-07-22	0.102
1222+216	FSRQ	12:24:54.4	+21:22:46	275	2009-04-27–2015-07-22	0.435
3C273	FSRQ	12:29:06.7	+02:03:09	181	2008-11-21–2014-07-25	0.158
1227+25	BL Lac	12:30:14.1	+25:18:07	21	2015-05-18–2015-07-22	0.135
3C279	FSRQ	12:56:11.1	-05:47:22	199	2008-11-24–2013-06-06	0.536
1510-089	FSRQ	15:12:50.5	-09:05:59	217	2008-12-29–2014-07-29	0.361
BL Lac	BL Lac	22:02:43.3	+42:16:40	320	2008-10-31–2014-07-26	0.069

## 4.2 Determining the Contribution of Synchrotron Radiation and the Big Blue Bump to the Optical-Ultraviolet Spectrum

In order to determine the contribution of synchrotron radiation and the BBB to the Steward Observatory spectra, a couple of premises must be adopted: the emission composing the BBB 1) is emitted by a standard accretion disk whose emission spectrum can be described by  $F_\nu(\text{Disk}) \propto \nu^{1/3}$ , and 2) is unpolarized. Any observed polarization in the observed spectrum must then be the result of the synchrotron emission. In the sections that follow, I will explain the method for this analysis using 1222+216 as an example, and then present the results of performing similar fits for other sources.

### 4.2.1 Preparing the Spectra for the Two-Component Fit

Because I am interested in variability of the BBB over the course of months or years, and since each observing campaign can contain dozens of spectra for each individual source, I average all of the total and polarized flux spectra for a source obtained during the same observing run. I do this by calculating the geometric mean flux in each channel. The reason for choosing the geometric mean, rather than the arithmetic mean for combining spectra, is so that the composite spectrum is not unduly weighted by any high fluxes that occur during the epochs being combined.

In the case of FSRQs, the contribution to the optical spectrum from the broad and narrow emission line regions must be determined before proceeding with the analysis of the synchrotron and BBB components. Due to the range of redshifts of our sample, the frequency range covered in each source, and therefore which emission

Table 4.1 (cont'd)

Source Name	Spectral Type	R.A. (hh:mm:ss)	Dec (dd:mm:ss)	N Spectra <sup>a</sup>	Dates Observed <sup>b</sup>	$z$
CTA102	FSRQ	22:32:36.4	+11:43:51	93	2009-10-20–2014-06-26	1.037
3C454.3	FSRQ	22:53:57.7	+16:08:54	174	2008-10-04–2014-05-27	0.859

<sup>a</sup>The number of spectra present before combining spectra taken during the same observing campaign

<sup>b</sup>The range of dates for which Spectra from the Steward Observatory are available

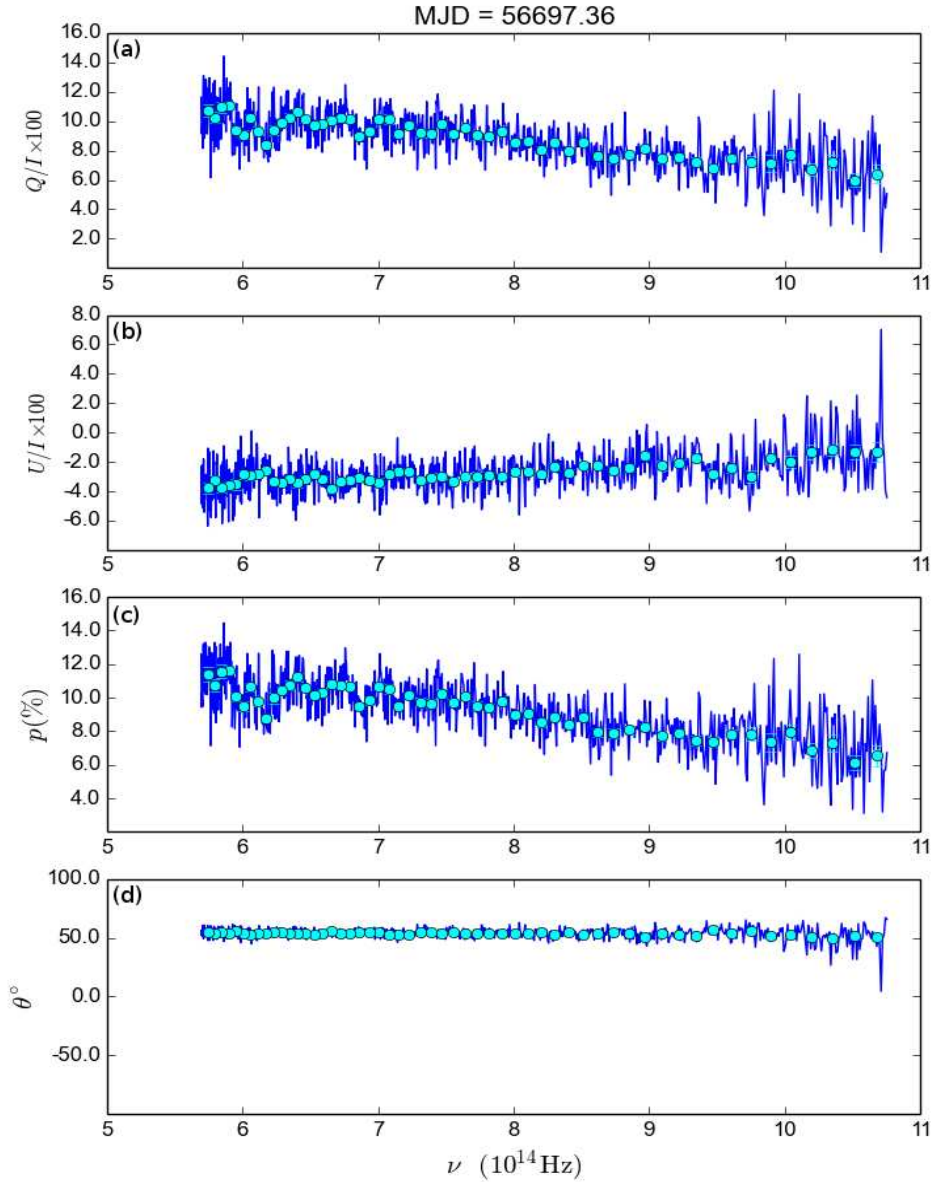


Fig. 4.1 Linear polarization percentage as a function of observed frequency for 4C 21.35. (a): Stokes Q as a percentage of I. (b): Stokes U as a percentage of I. (c): Total percentage of linear polarization throughout the observed bandpass. (d): Direction of linear polarization vector, measured counter-clockwise from north-south. At this epoch, the linear polarization drops from 12% at  $6.0 \times 10^{14}$  Hz to 6% at  $10 \times 10^{14}$  Hz. This indicates that, at higher frequencies, there is an increasing contribution to the spectrum by a non-polarized source of radiation. The spectra are displayed in dark blue, while the spectra binned across 15 channels is displayed in the filled in circles.

lines are present, is unique to that source. The more prominent emission lines include the Balmer series, starting with  $H\beta$  centered at 4861 Å and shorter wavelength transitions. For some objects at high redshift, a  $MgII$  line can be seen at 2800 Å. For many sources with strong emission lines in the optical to UV range of the spectrum, a significant portion of the bandpass contains emission from a series of blended emission lines arising mainly from  $FeII$  (Kovačević et al., 2010). Due to the nature of this iron complex, the emission for each source can be difficult to model accurately, therefore I instead subtract off suspected emission lines before proceeding with the two-component fit of the spectrum.

For the purpose of removing the emission line “contamination” of the spectrum, I construct a template of line contribution to the spectrum with the following procedure. If a spectrum of the source is available from the Sloan Digital Sky Survey (*SDSS*), I fit a power-law to the *SDSS* spectrum in the continuum windows bounded by rest wavelengths  $\lambda_{rest} = 4200\text{-}4230$  Å,  $5600\text{-}5648$  Å, and  $6198\text{-}6218$  Å, as has been done in Shang et al. (2005). These windows are chosen to exclude portions of the spectrum contaminated by emission lines. In the case of BL Lacs, no emission line template was constructed, as these sources do not display prominent emission lines. An example of a derived emission line template is displayed in Figure 4.2, while an example of a spectrum with the derived template subtracted from the observed flux is displayed in Figure 4.3.

The flux in excess of the power-law is taken as a template for non-variable emission from the broad and narrow emission line regions. For FSRQs for which an *SDSS* spectrum is not available, the template was constructed from a geometric-mean combined spectrum assembled from all of the flux-calibrated spectra in the dataset. The spectra were corrected for Galactic extinction using the prescription of Schlafly & Finkbeiner

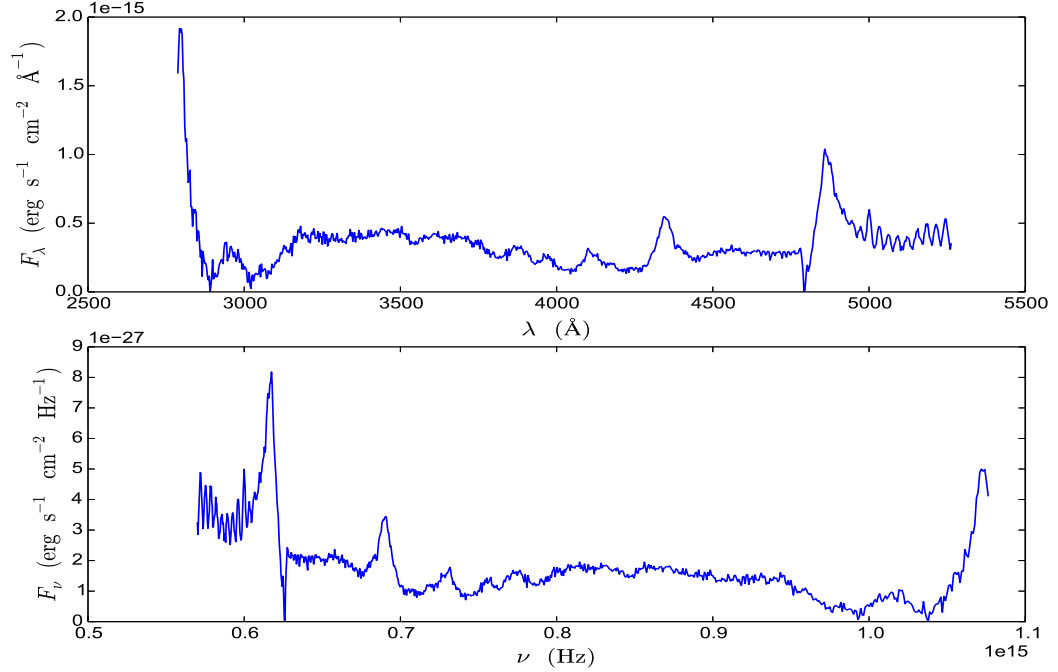


Fig. 4.2 Top panel: Redshift corrected emission line template for 1222+216 in wavelength space. Bottom: Same but converted into frequency space. In this plot, the  $H\beta$ ,  $H\gamma$ , and  $H\delta$  emission lines are visible, in addition to a broad  $FeII$  complex. Part of the  $MgII$  line at  $2800 \text{ \AA}$  is also visible.

(2011) and assuming that The ratio of the extinction coefficient,  $A_v$ , to the color excess,  $E(B - V)$ , is given by,  $A_v/E(B - V) = 3.1$ . The extinction corrected spectra, and emission line template when applicable, were converted into the quasar's rest frame by using

$$\lambda_{rest} = \frac{\lambda_{observed}}{1 + z}, \quad (4.1)$$

where  $z$  is the blazar's redshift. The emission line template was then subtracted from the observed total flux spectrum, and the resulting spectrum was converted from wavelength to frequency space using the conversion

$$F_\nu = \frac{\lambda^2}{c} F_\lambda. \quad (4.2)$$



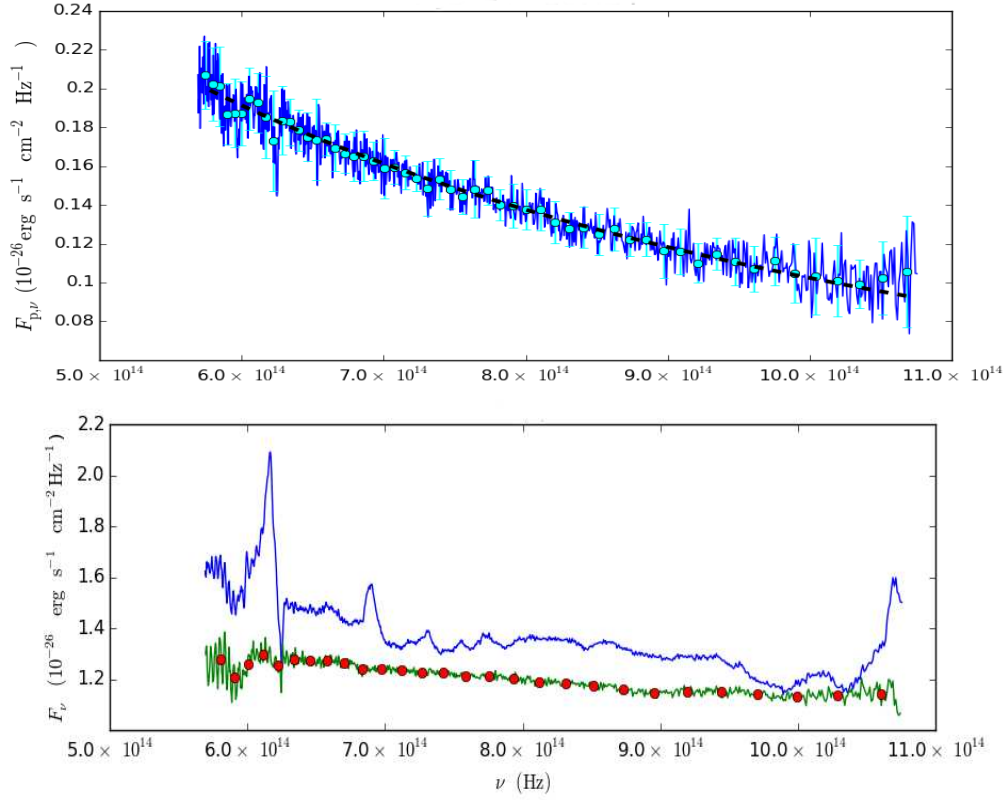


Fig. 4.3 Top panel: Redshift corrected polarized-flux spectrum for 1222+216 in blue. The turquoise circles represent the spectrum after applying a 15 channel boxcar smooth. The dashed black line represents the best-fit power law to the polarized flux. Bottom panel: The total spectrum without an emission line template removed is shown in blue. The resultant spectrum after subtracting the template shown in Figure 4.2 is displayed in green. The red circles represent a boxcar smooth of the spectrum.

This conversion factor was derived using the definition

$$F_\nu = \frac{dF}{d\nu}, \quad (4.3)$$

the chain rule,

$$\frac{dF}{d\nu} = \left| \frac{-dF}{d\lambda} \frac{d\lambda}{d\nu} \right|, \quad (4.4)$$

and the relation  $\lambda\nu = c$ .

In the case of FSRQs with a prominent BBB, it is often the case that the degree of linear polarization is relatively low, hovering around a few percent. In this situation, it is possible that the measured polarization has become statistically biased, as it is necessary to always have a measured degree of polarization  $\Pi \geq 0$ . In this case, the measured polarization must be corrected for this statistical bias following the formula set forth in Wardle & Kronberg (1974):

$$\Pi_{corrected} = \Pi_{measured} \times \sqrt{1 - \left( \frac{err_{\Pi}}{\Pi_{corrected}} \right)^2}, \quad (4.5)$$

where  $err_{\Pi}$  is the measurement uncertainty of the polarization.

Alternatively, the polarization can be calculated in cases where the direction of the polarization vector does not change throughout the observed bandpass. This is accomplished by first rotating the Stokes parameters such that all of the polarization information is contained in a new parameter  $q'$ . The new parameter, calculated as in Smith et al. (2003),

$$q' = q \cos(2\theta) + u \sin(2\theta), \quad (4.6)$$

removes the statistical bias as  $q'$  is not a strictly positive quantity. The polarization,  $\Pi_{measured}$ , is then simply  $|q'|$ .

#### 4.2.2 Determining the Spectral Index of the Synchrotron Component from the Polarized Flux

I obtained the spectral index of the synchrotron radiation,  $\alpha$ , by performing a least-squares fit to the polarized flux spectrum of a function of the form  $F_{\nu}(\Pi) = A\nu^{-\alpha}$ . The fit was obtained for a polarized flux spectrum in a frequency range bounded by the windows  $\nu = 6.4 \times 10^{14} - 6.85 \times 10^{14}$  Hz, and  $7.8 \times 10^{14} - 9.4 \times 10^{14}$  Hz. These windows were chosen to avoid contamination of the spectrum due to any error in the

estimation of the contribution of the most prominent emission lines to the spectrum. In some cases, it was necessary to alter the windows used for fitting the spectral index of the polarized flux due to the polarized flux spectrum becoming too noisy to obtain a good fit. These cases will be discussed in Section 4.7.

To perform the fit, the polarized flux spectrum was calculated from the total flux spectrum and the Stokes parameters spectra. The spectrum was then re-binned using a 15 channel wide window, and, using the 1-sigma uncertainties in each channel, synthetic spectra were generated. I chose a window in the middle of the bandpass with  $4.7 \times 10^{14} \leq \frac{\nu}{1+z} \leq 6.5 \times 10^{14}$  Hz in order to avoid any systematic errors in flux at the endpoint of the spectrum. I then performed a least-squares fit of a power-law to each synthetic spectrum via the Levenberg-Marquardt method. For each observed spectrum, 250 synthetic spectra were generated. The median spectral index, along with its standard deviation, was taken as the spectral index and uncertainty of the synchrotron radiation component in the later fit of the total flux spectrum.

Figure 4.4 shows the best-fit spectral indices for the quasar 1222+216 extracted from the Steward Observatory data, as well as the best fit single power-law for the full spectrum and a histogram displaying the distributions of both sets of spectral indices. In order to help compare the results of multi-component models, the reduced  $\chi^2$  values that result from fitting a power-law to the full flux spectra are shown in Fig 4.5. A cursory inspection indicates that in the case of 1222+216, the spectral indices of the polarized flux and those of the total flux spectrum have different distributions, and therefore are drawn from different statistical populations. Performing a K-S test on the two spectral index distributions yields a  $D$  value of 0.92, allowing for the rejection of the hypothesis that the parent distributions are the same at a  $> 99\%$  confidence level.

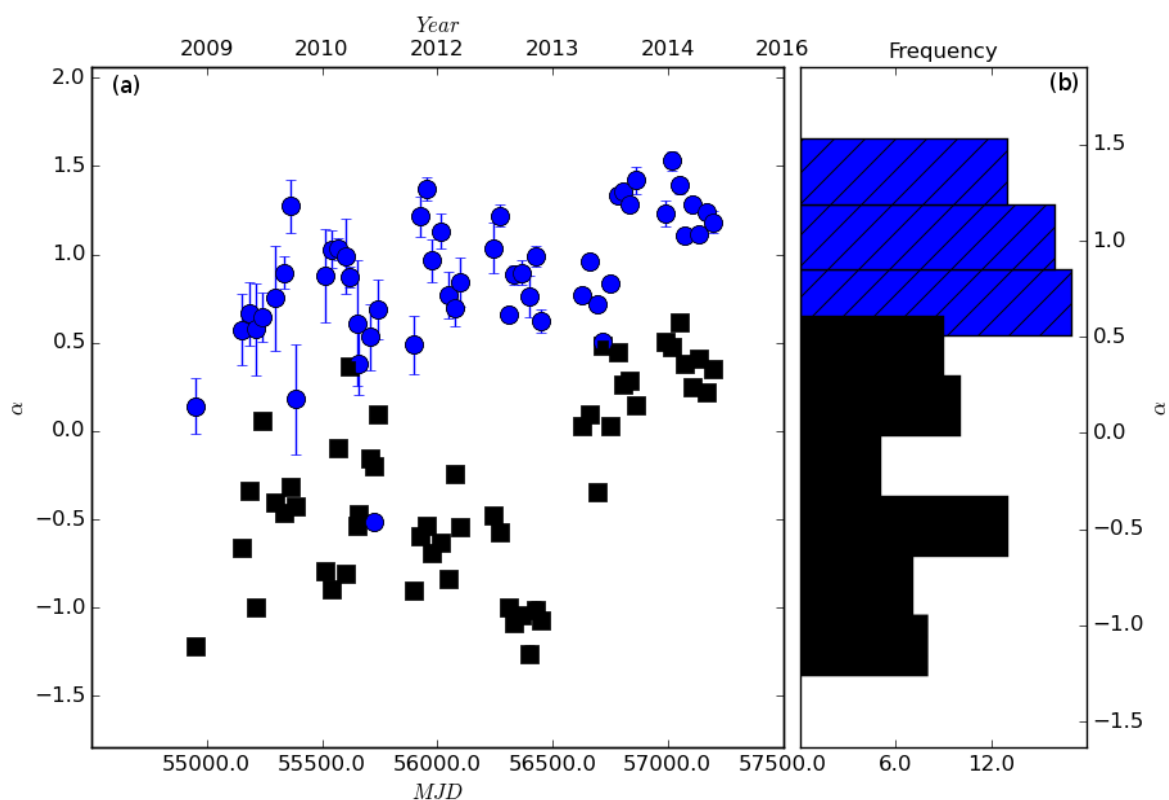


Fig. 4.4 (a): The spectral index,  $\alpha$ , obtained for 1222+216 from the polarized flux spectra is shown in the blue circles, while the best-fit power-law for the full spectrum is shown with black squares. While the night-to-night variation of both sets of spectral indices is high, the trend is toward higher positive values of the spectral index over the course of several years. The difference between the spectral indices of the flux and polarized flux is significant for nearly every observation, indicating at least two sources of emission. (b): Histogram of both sets of spectral indices from (a) with  $\alpha_{polarized}$  shown in hatched blue, and  $\alpha_{spectrum}$  in black. The negative peak for  $\alpha_{spectrum}$  indicates that the total flux density spectrum generally increases with frequency, while  $\alpha_{polarized}$  peak at  $\sim 0.6$  indicates that the polarized flux generally decreases with frequency.

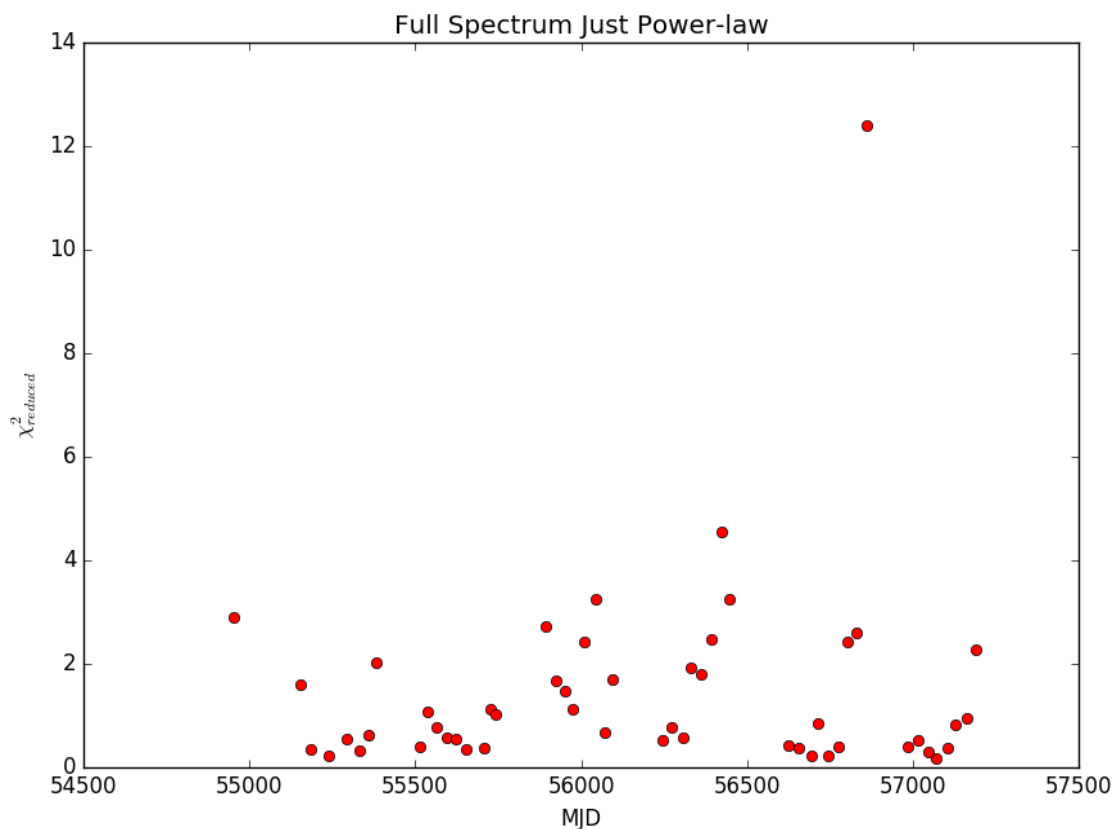


Fig. 4.5 The reduced  $\chi^2$  values for fitting a power-law to the full flux spectrum for 1222+216. For many of the spectra throughout the dataset, this single power-law provides a good fit to the spectrum. However, because the polarized flux has a different spectral index, the presence of multiple emission components is not ruled out.

### 4.2.3 Performing the Two-Component Fit

As with polarized-flux spectra, I generate synthetic spectra using the input spectrum and its one-sigma uncertainties in order to determine the relative contribution of the synchrotron and BBB components via a Monte-Carlo method. I perform a least-squares fit to the line-subtracted spectrum of a function of the form

$$F_\nu = F_{syn} + F_{BBB} = A\nu^{-\alpha} + B\nu^{1/3}. \quad (4.7)$$

The results of the fit for a typical spectrum of 1222+216 are shown in Figure 4.6, while the reduced  $\chi^2$  values for the spectral fits are displayed in Figure 4.7. Once the fit is complete, I integrate the fit spectral components across the bandpass to determine the total synchrotron flux, big blue bump flux, and total observed flux for each of the available spectra. The results of the dissection are displayed in Figure 4.8.

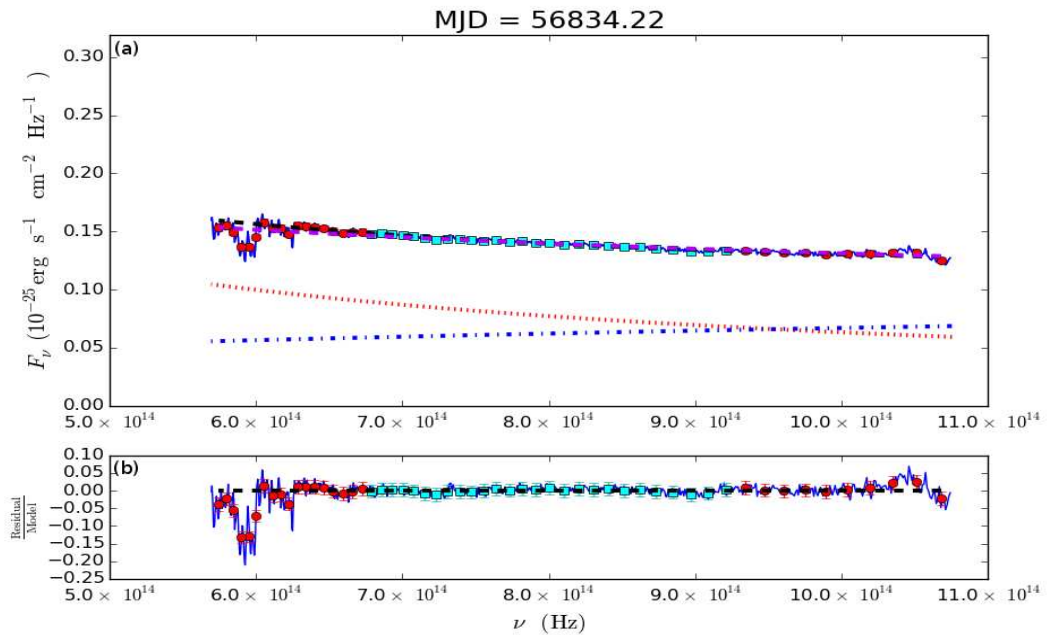


Fig. 4.6 (a): Flux calibrated spectrum for 1222+216 on Julian Date 2456834.2 with the emission line template removed. The fit big blue bump component is shown with the blue dotted line. The red dotted line shows the fit synchrotron component. The dashed black line shows the sum of the two fit spectral components. The result of fitting a power-law to the spectrum is shown in purple for comparison to the two component fit. The frequency windows used in the fit are marked by the blue squares. (b): The residual plot showing the difference between the model and observed spectrum as a fraction of the model flux at each frequency.

The distribution of fit BBB and synchrotron components can be seen in Figure 4.9. From Figure 4.8 and Figure 4.9, it is apparent that the BBB varies by about a factor of 2–3 from its mean value over the course of several years. However, the

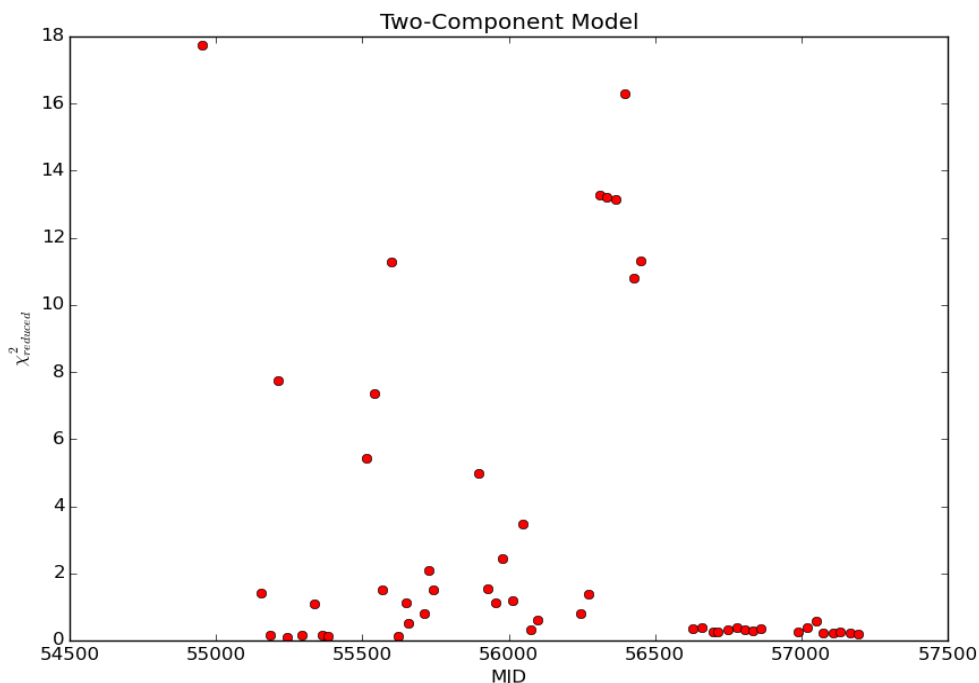


Fig. 4.7 Reduced  $\chi^2$  values for the two-component model that best fits the Steward Observatory spectra of 1222+216. While the two-component model does a good job of fitting many of the spectra in the data set, it fails to fit a significant portion of the observed spectra, and does not do as well as a single power-law fit.

plot betrays some anomalies. Apparent night-to-night variability of the BBB reveals itself in the data, especially during epochs when the blazar is flaring. While the synchrotron and even high-energy emission from blazars is known to be rapidly variable, often changing energy output by factors of 2 or more on very short time-scales, such rapid variability of the BBB would imply that the fundamental structure of the accretion disk is changing on time-scales on the order of days to a week. Such rapid variability of the BBB, and even its apparent disappearance during some epochs, is not very realistic. It is also apparent from Figure 4.7 that the two-component model does not produce a good fit for many of the available spectra.

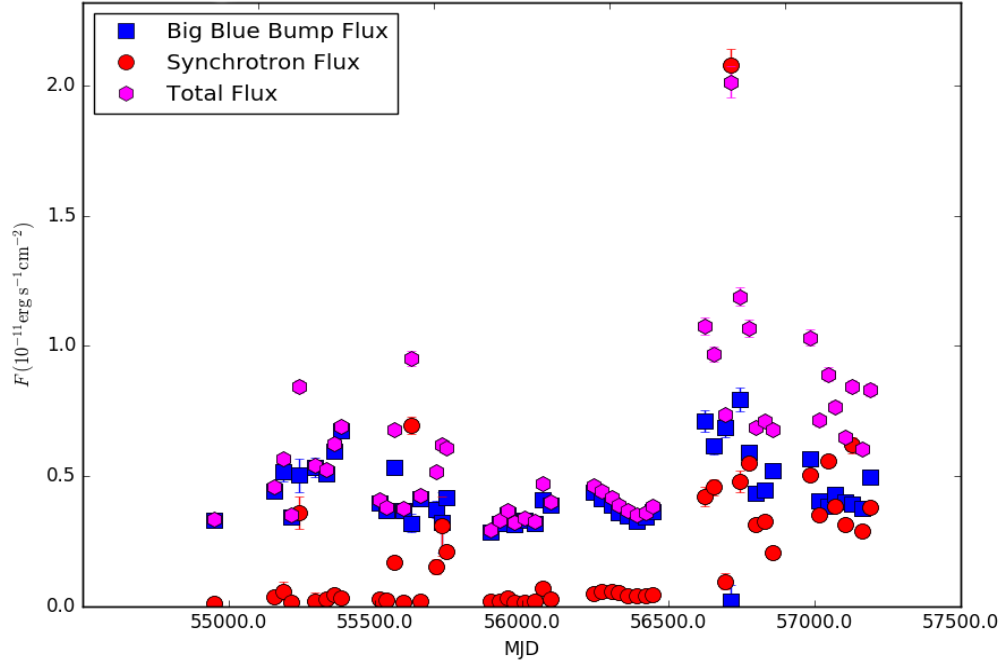


Fig. 4.8 The total flux in the optical spectrum of 1222+216 (pink triangle) along with the least-squares optimized flux for the big blue bump (blue squares), as well as the synchrotron component (red circles). Over the approximately 5 years during which data have been obtained, the BBB varies by a factor of  $\sim 2$  from its median value

In order to combat this inconsistency, I explore several different scenarios: 1) one in which the BBB component is fixed to the mean value of the BBB determined from the two-component fit; 2) the addition of a third component arising from a high temperature blackbody, which would be interpreted as a hot-spot on the accretion disk; and 3) the possibility of wavelength dependent polarization, a scenario that can arise in the synchrotron-emission of blazars under reasonable physical conditions.

### 4.3 Keeping the Big Blue Bump Component Constant

Before concluding that the accretion disk of 1222+216 is variable on the time-scales involved in this project, I attempt to perform the fit while reducing the number of



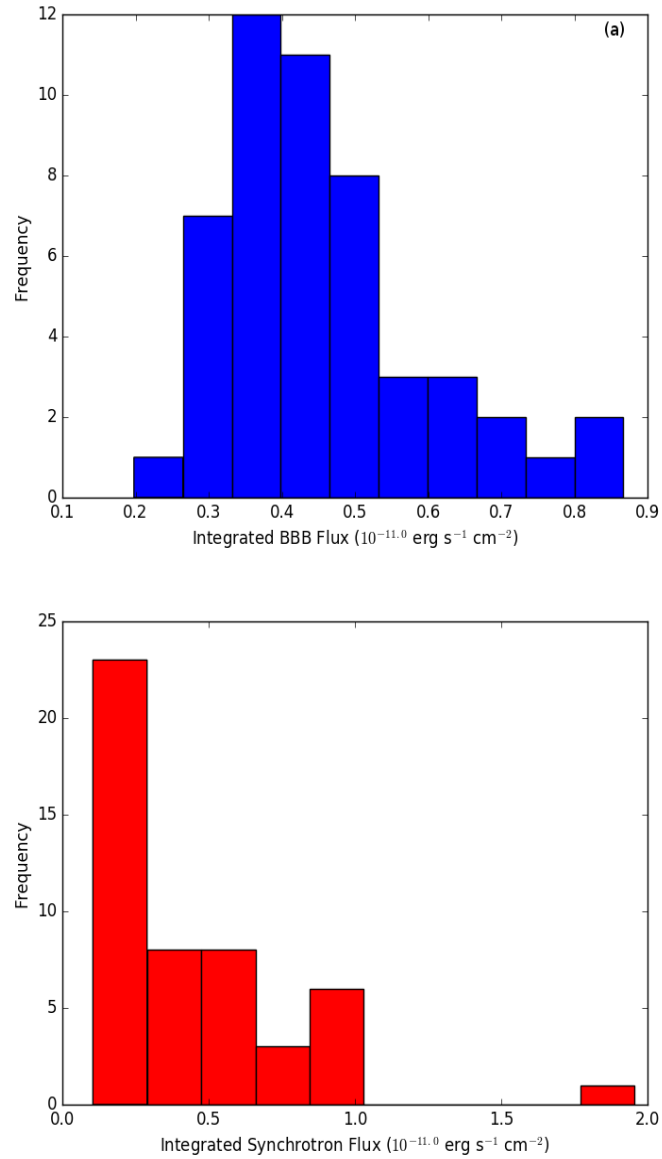


Fig. 4.9 *top*: Histogram depicting the fit integrated-flux values for the BBB using a two-component model for the spectra of 1222+216. *bottom*: A similar histogram depicting the synchrotron component.

free parameters in the model. To do so, I choose the normalization for the BBB parameter by inspecting figures 4.8 and 4.9. Because the total flux of the source is so variable ( $\gtrsim$  a factor of 4 throughout the epochs considered), the median value of the best fit BBB normalization cannot be chosen for this purpose, as this value leads to a BBB flux higher than the total flux of the object at many epochs. Instead, I force the BBB flux to remain constant at roughly half the minimum total flux observed in the dataset. Subsequently, I altered this normalization to produce BBB flux values between none at all, to the minimum total flux at a single epoch, without altering the results.

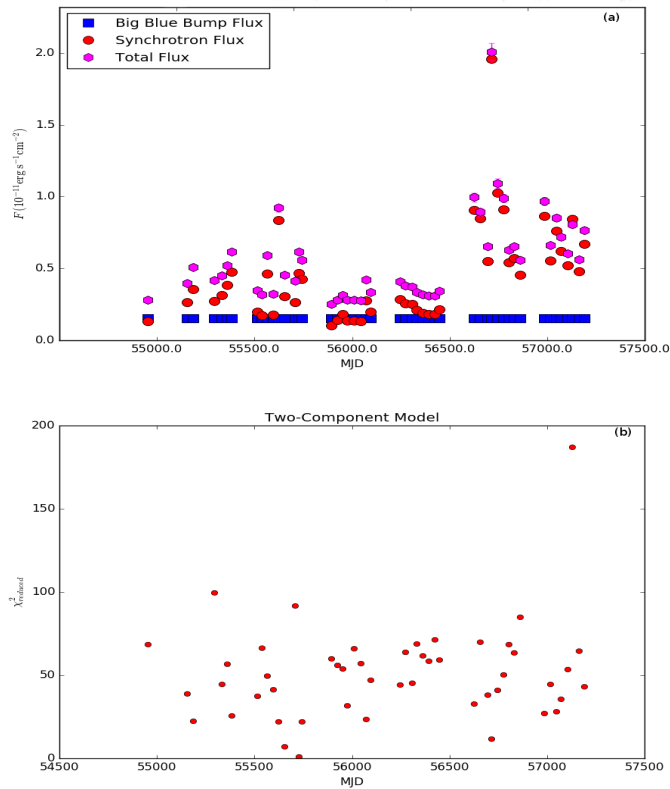


Fig. 4.10 (a): Spectral components resulting from forcing the accretion disk to have constant flux. (b): Reduced  $\chi^2$  values for the best-fit constant BBB model to the Steward Observatory spectra. While this model does a good job of fitting some of the spectra in the data set, it fails to fit most of the observed spectra, and does not do as well as a single power-law model.

While holding the total BBB flux constant, I keep the spectral index of the synchrotron component the same as the spectral index of the polarized flux. The resulting fit and reduced  $\chi^2$  values for a model where the sole variable component arises from synchrotron radiation are shown in Fig 4.10. This analysis does not provide an adequate fit to the spectra, with the reduced  $\chi^2$  averaging  $\sim 50$ . The primary reason that the fits obtained in this exercise do not reproduce the observed spectrum is because the shape of the polarized flux spectrum and the total flux spectrum are significantly different for the vast majority of the spectra in the dataset, as shown in Fig. 4.10 and in Fig. 4.11, where a sample of the best fit spectrum generated using this method is displayed. Because the quality of the fits provided in this exercise are poor, I can effectively rule out a model of the spectra where the accretion disk of 1222+216 has a constant luminosity, in the absence of wavelength dependent polarization of the synchrotron component.

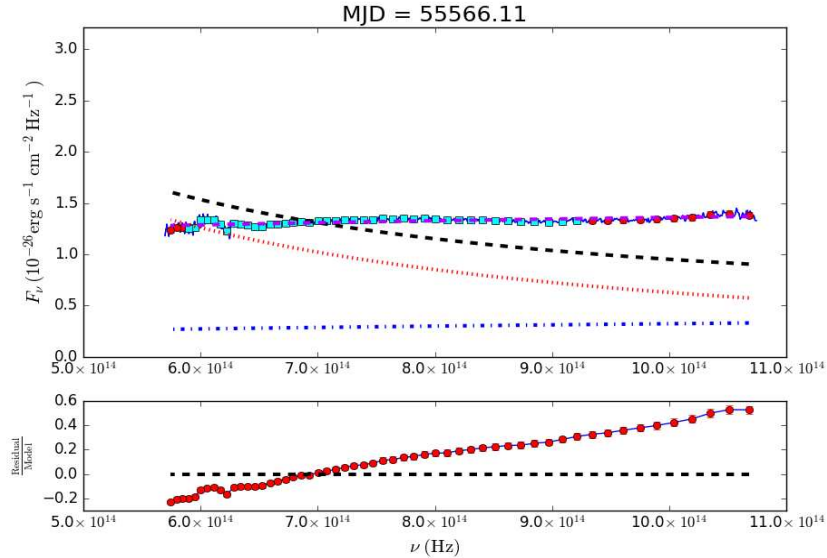


Fig. 4.11 The best fit model obtained by holding the flux of the accretion disk fixed and allowing the the synchrotron component to vary for the data obtained on MJD=245566. Such a model cannot provide a good fit to the data for the majority of spectra in the dataset. Colors and linestyles are the same as in Figure 4.6

## 4.4 Modifying the Disk Component to Contain an Additional Blackbody Component

One major drawback of the two-component model is that it requires the accretion disk to maintain its spectral shape as its luminosity varies. This, in turn, requires that the widely separated parts of the disk vary nearly simultaneously. A more realistic model of how the luminosity of an accreting black hole varies has been proposed by Dexter & Agol (2011), as well as by Ruan et al. (2014) and Kelly et al. (2011). The accretion disk modeled in Dexter & Agol (2011) differs from the standard thin-disk model in the following way. Variability is introduced into the accretion disk by the addition of “hot-spots” to the disk, where the temperature of any region of the disk is effectively allowed to vary from that predicted by the thin disk model according to a damped random-walk algorithm. The hot-spot is allowed to evolve in a way such that local temperature variations regress toward the mean on a characteristic timescale of  $\sim 200$  days. This was expanded upon in Ruan et al. (2014), where it is shown that the variable part of the accretion disk spectrum has a characteristic spectral shape of a high-temperature blackbody with  $T > 10^4$  K. In this section, I explore a simpler accretion disk model that consists of a standard thin disk with a single additional blackbody component. I explore scenarios in which the temperature of the blackbody component is allowed to vary, along with one in which it is held constant.

### Modeling the Accretion Disk as a Thin Disk Along with a Constant Temperature Hot-Spot

In the scenario in which the temperature is held constant, I choose a high temperature such that the observed spectrum is in the Rayleigh-Jeans limit. This is informed by the results of Ruan et al. (2014), in which the variability spectra ob-

tained can be fit by a  $T \sim 10^6$  K blackbody. The resulting fits and goodness-of-fit statistics are shown in Figure 4.12. In order to fit the observed spectrum, the thin disk component must be allowed to vary. Night-to-night variability of both the thin disk component and the blackbody component would need to be dramatic as well, often on the order of a factor of 2 during the course of a few days. Furthermore, the variability of the two disk components would need to be well coordinated. As the flux from the high-temperature blackbody component rises, a corresponding decrease in the thin disk flux is apparent, especially during the 2013 observation. As the thin disk luminosity subsides, a similar increase in the flux from the blackbody is needed. Furthermore, the blackbody component vanishes for observations after 2013, even though variability in the accretion disk is more prominent. Such a cosmic conspiracy between the two components is hard to envision, and thus such a model is hard to justify.

### **Modeling the Accretion Disk as a Constant Thin Disk Along with a Variable Temperature Hot-Spot**

In the scenario where the temperature is allowed to vary, I hold the thin disk component constant so that the only varying component of the disk is due to the changes in the hot-spot. The Wien peak of a blackbody occurs at a frequency such that  $h\nu = 2.82k_B T$ . Because each source of our sample is found at different redshifts, the spectral coverage of the Steward observatory spectra are different for each source. In the case of 1222+216 ( $z = 0.435$ ), the rest-frame spectral coverage spans from  $\nu \approx 6.0 \times 10^{14}$  Hz to  $1.1 \times 10^{15}$  Hz. A blackbody peaking in this spectral range will have temperatures between  $T = 10^4$  K and  $1.8 \times 10^4$  K. I use this to inform my choice of temperature constraints for the blackbody component of the model.

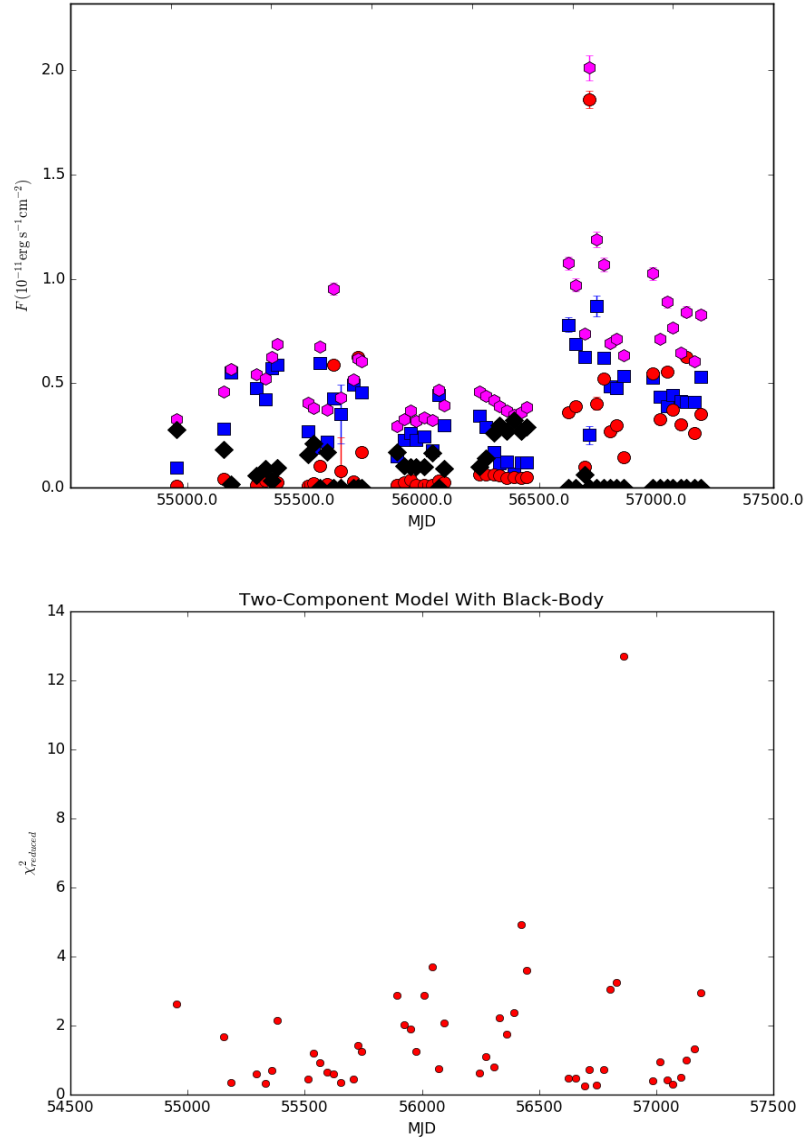


Fig. 4.12 *Top*: Fit of the spectrum of 1222+216 with the accretion disk model modified to include a hot ( $T \approx 10^5$  K) blackbody. *Bottom*: The reduced  $\chi^2$  values of the fit to each spectrum. While modeling the spectra under these constraints does result in fitting the shape of the spectrum, the sums of the flux levels of the two accretion disk components at times appear equal, but with the magnitude of each component switched. Later on, the blackbody component apparently vanishes, while the power-law disk component varies dramatically.

I choose a minimum temperature of 5000 K for this component. A cooler blackbody will peak at frequencies not covered in the available spectral window, declining exponentially, and thus not contribute much beyond the other two components of the observed spectrum. I choose a maximum temperature of 70000 K in order to put the observable portion of the blackbody in the Rayleigh-Jeans regime, and thus parabolic in shape. This does not preclude the existence of a  $T > 70000$  K hot-spot on the accretion disk, however, only the Raleigh-Jeans tail of such a component could be measured in the optical regime, and thus determining the temperature would not be possible.

The results of this fit on 1222+216 are displayed in Figure 4.13. Examining this figure in closer detail shows that the blackbody feature is often the dominant component of the accretion disk. The hot-spot, for the most part, varies smoothly in concert with the total flux of 1222+216, with the exception of some flaring activity in 2011 and 2014, during which epochs occasional spikes in the synchrotron flux apparently overwhelm the flux from the accretion disk component. This model for the variability of the accretion disk is most consistent with other works. It is also of note that the dynamic range of the synchrotron component is higher than that of the accretion disk for 1222+216, as shown in Figure 4.14, which displays histograms of both the total accretion disk flux as well as the synchrotron flux.

### **Determining the Size and Variability Timescale of the Hot-spot**

If the accretion disk varies by the addition of a region on the disk that is hot relative to the surrounding medium, the physical size of the hot-spot, as well as the timescale that it could physically vary upon, is of interest. Determining the size is relatively straightforward. The integrated function across all frequencies and solid angle yields the expected flux from a blackbody. The same quantity can be obtained

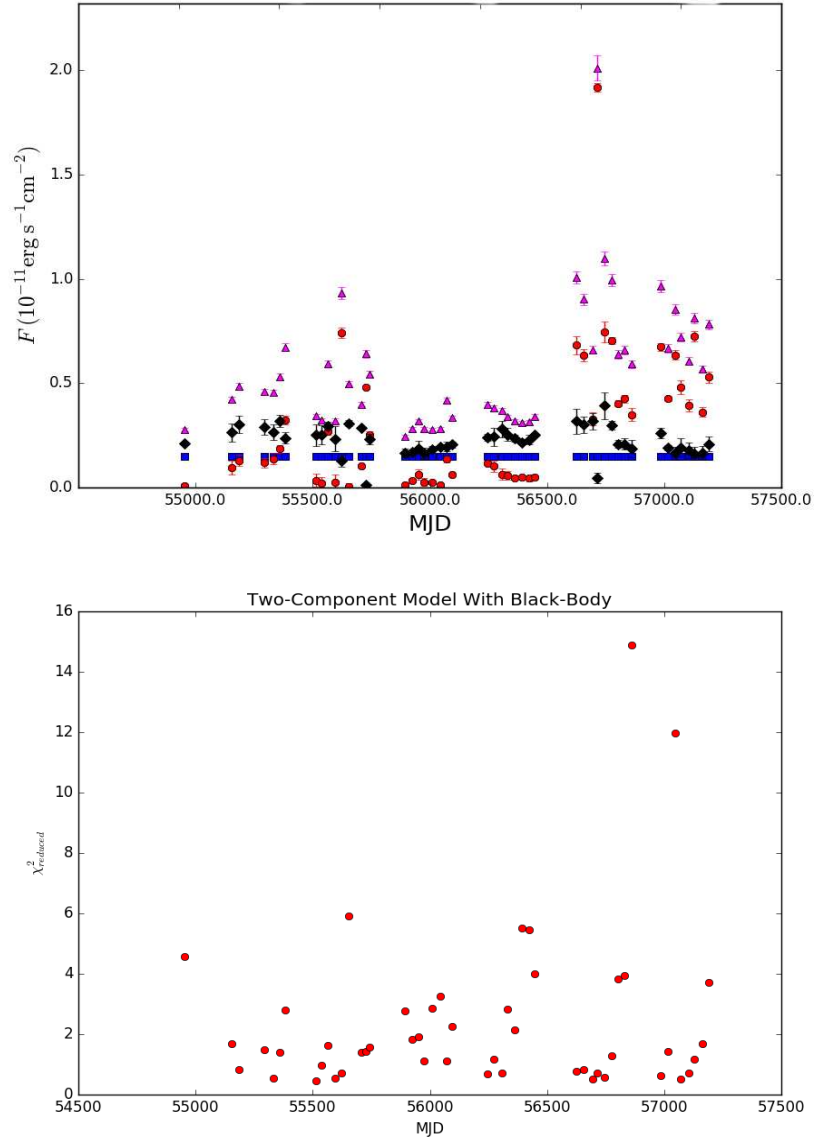


Fig. 4.13 *Top*: The fit components to the spectra of 1222+216 derived from keeping the thin-disk component constant while allowing for variability in the disk in the form of a variable temperature hot-spot. The total flux is shown in the pink triangles, while the synchrotron component is displayed in the red circles. The disk component consists of a constant power-law component displayed in blue squares, and a variable temperature blackbody displayed in black diamonds. *Bottom*: The reduced  $\chi^2$  component of the fit.



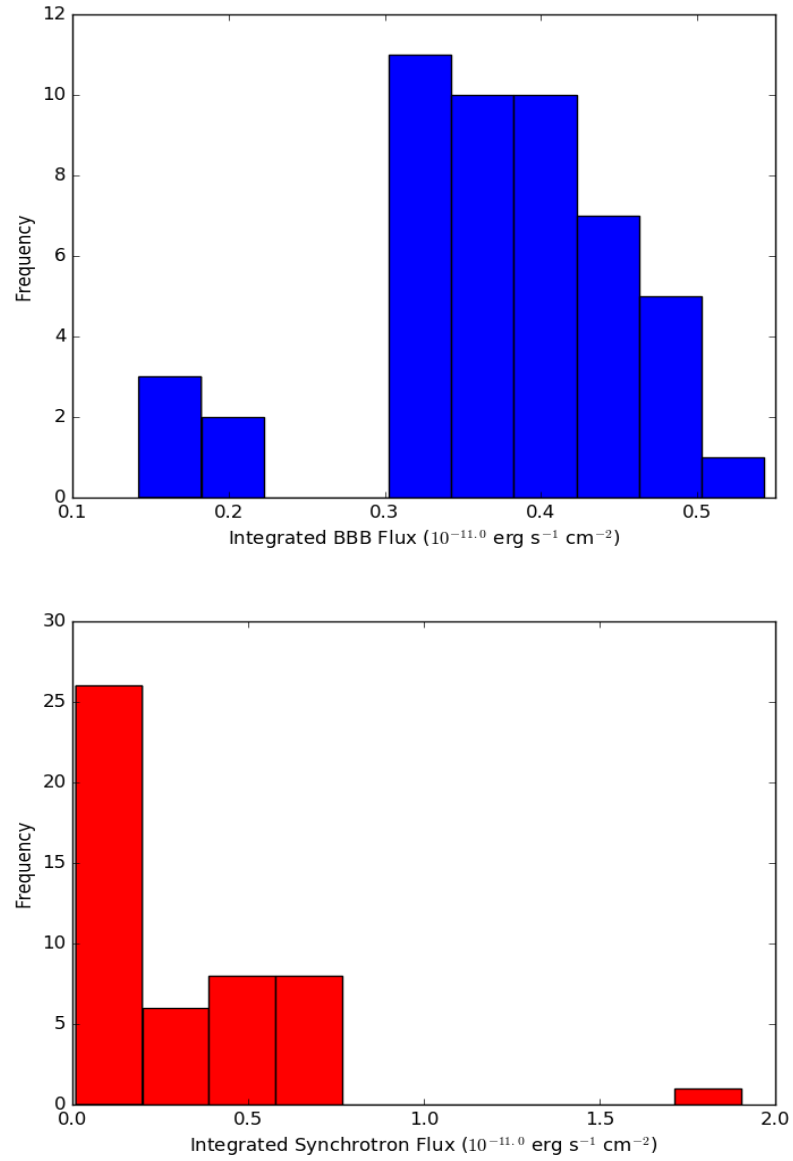


Fig. 4.14 *Top*: Histogram of the total accretion disk flux of 1222+216. *Bottom*: Histogram of the synchrotron component.

by dividing the luminosity of the blackbody by  $4\pi d_L^2$ , where  $d_L$  is the luminosity distance of the source. I obtain the radius of the hot-spot,  $r_{bb}$ , by assuming a thin, cylindrical shape for the hot-spot and solving

$$\int B_\nu(T) d\nu = \frac{r_{bb}^2 \sigma T^4}{2d_L^2} \quad (4.8)$$

for  $r_{bb}$ . This results in

$$r_{bb} = \frac{d_L}{T^2} \times \sqrt{\frac{2 \int B_\nu(T) d\nu}{\sigma}}, \quad (4.9)$$

for the radius of the blackbody.

With the radius of the blackbody in hand, an estimate of the minimum time-scale on which it can vary can be found. In an extreme case where the heating source for the hot-spot suddenly ceases, the hot-spot will continue to radiate as it cools down to the temperature of the surrounding medium. The luminosity of the blackbody is just the rate at which it radiates energy away, therefore, via the chain rule,

$$L = \frac{dE}{dT} \frac{dT}{dt}. \quad (4.10)$$

The total thermal energy of a gas is given by

$$E = \frac{3}{2} N k_b T, \quad (4.11)$$

where  $N$  is the total number of particles in the gas. Substituting in the luminosity of a blackbody results in the relation,

$$4\pi r_{bb}^2 \sigma T^4 = \frac{3}{2} N k_b \frac{dT}{dt}, \quad (4.12)$$

or

$$dt = \frac{3k_b N}{8\pi\sigma r_{bb}^2} \frac{dT}{T^4}. \quad (4.13)$$

This can be integrated to obtain the cooling time,

$$t_{cool} = \frac{k_b N}{8\pi\sigma r_{bb}^2} \left( \frac{1}{T_{final}^3} - \frac{1}{T_{begin}^3} \right), \quad (4.14)$$

or if rewritten in terms of the density,  $n_{bb}$ , of the blackbody component,

$$t_{cool} = \frac{k_b n_{bb} r_{bb}}{6\sigma} \left( \frac{1}{T_{final}^3} - \frac{1}{T_{begin}^3} \right), \quad (4.15)$$

or,

$$t_{cool} = \frac{k_b n_{bb} r_{bb}}{6\sigma T_{final}^3}, \quad (4.16)$$

if  $T_{begin}^3 \gg T_{final}^3$ . If the density and the size of the blackbody component were known, the cool down time of a hot-spot could now be determined.

The radius of the hot-spot follows directly from the observed luminosity

$$r_{bb} = \frac{1}{T^2} \sqrt{\frac{L_{bb}}{2\pi\sigma}}. \quad (4.17)$$

The calculated size, and total luminosity, of the hot-spot, in the case of 1222+116 where only the blackbody component of the accretion disk is allowed to vary, is displayed in Figure 4.15. From the figure, it is apparent that the hot-spot is roughly 100-200 astronomical unit (AU) in radius, and varies quasi-periodically with a time-scale  $\sim$  years. This is similar to the results of the simulations performed in Dexter & Agol (2011) in which the hot-spots cool down on the order of 200 days and observed in 3C273 by Paltani et al. (1998), in which the BBB was seen to vary on a roughly half-year time-scale.

The question of the density of the accretion disk is harder to answer. Because the hotspot is radiating as a blackbody, it is optically thick. At such high temperatures, the hydrogen that makes up the disk is almost certainly completely ionized, and

therefore the optical depth,  $\tau$ , is at least  $\tau = n\sigma_T r_{bb} \sim 1$ . Substituting in 100 AU for the radius of the blackbody and  $\sigma_T = \frac{8\pi}{3} \left(\frac{e^2}{m_e c^2}\right)^2$  results in a density of  $n \approx 10^9 \text{ cm}^{-3}$ . This results in a short cooling time,  $t_{cool} \sim 10^{-2} \text{ s}$  for  $T_{final} = 10^4 \text{ K}$ . It should be noted that this calculation provides a lower limit to the cooling time, as the density calculated is only a minimum required to make  $\tau \sim 1$ . It should also be noted that the cooling time calculated is in the event that the heating mechanism for the blackbody suddenly ceases, an unlikely scenario in an object on the order of 100 AU in radius. This also fails to take into account the light travel time, however, the light travel time of 100 AU is only 13 hours, still too small to be a significant factor for variability on the observed time scales.

#### 4.5 The Effect of Wavelength Dependent Polarization on the BBB and Synchrotron Radiation Components of the Optical Spectrum

So far in this chapter, I have proceeded with the assumption that the shape of the synchrotron radiation spectrum is identical to the shape of the polarized flux spectrum. This may not necessarily always be the case. If there is turbulence in the jet from which the synchrotron radiation arises, a dependence of the linear polarization on emission wavelength may develop. One such model, the Turbulent Emission Multi-zone (TEMZ), proposed by Marscher (2014b) approximates synchrotron emission from the jet of a blazar as the superposition of emission from many turbulent cells contained in the jet. The magnetic field vector in each cell is initially randomly oriented as a result of the turbulence, although it becomes partially ordered as the result of the plasma passing through a standing shock wave which compresses the plasma. Consequently, the polarization vectors from adjacent cells, which have different magnetic field orientations, will partially cancel each other. The observable

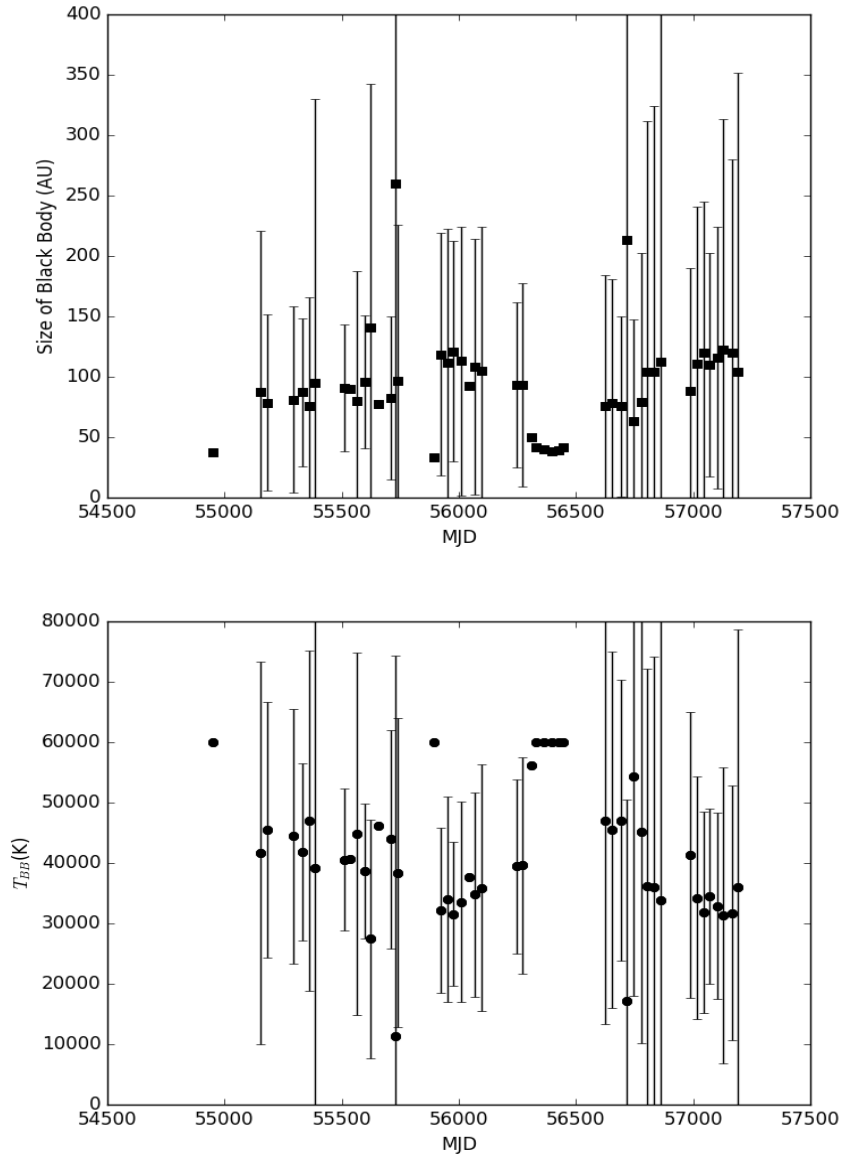


Fig. 4.15 *Top*: the calculated radius, in astronomical units, of the blackbody component to the accretion disk of 1222+216. *Bottom*: The temperature determined for the blackbody.

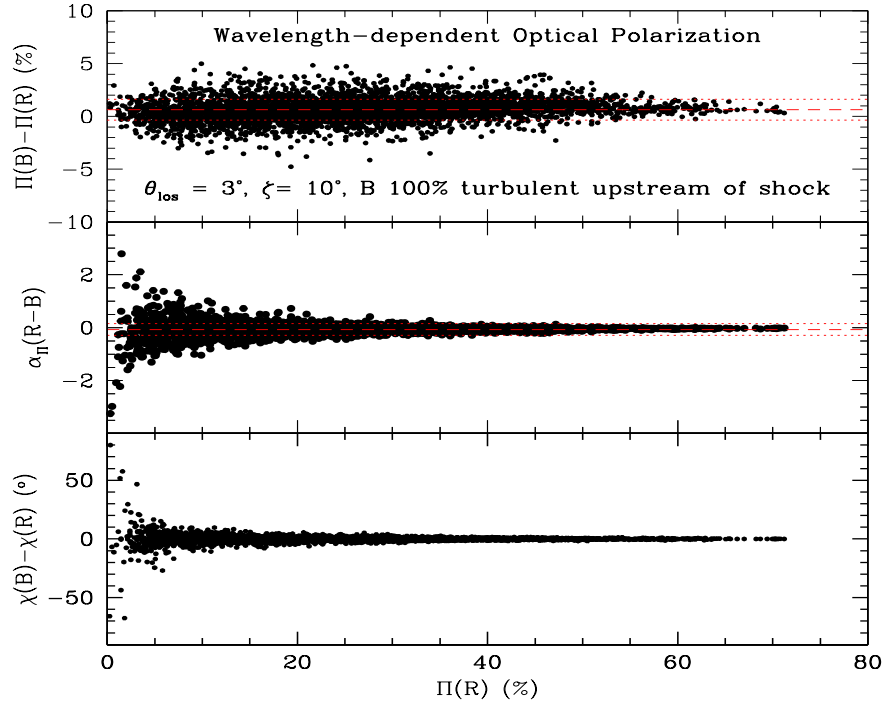


Fig. 4.16 Simulation depicting wavelength dependent polarization in a blazar jet under extreme conditions. The simulation was run with 100% turbulence in the plasma once it has passed through a conical standing shock. *Top*: Depicts the difference in polarization at two optical bands: B, and R, vs the R band polarization. These bands were chosen as they are partially encompassed by the Steward Observatory spectra. *Middle*: The difference in the spectral index of the polarization between the two bands. *Bottom*: Difference in the direction of the polarization vector on the sky. The red lines on the top two panels bound the one- $\sigma$  standard deviation of the simulation values. (Figure courtesy of A. Marscher)

result is that the mean polarization of radiation emitted from a number of cells,  $N_{cells}$ , will be attenuated by a factor of  $0.5N_{cells}^{-1/2}$  (Jones, 1988).

This, alone, would not introduce wavelength dependence into the polarization spectrum. However, if radiation at different frequencies is emitted from a different number of these turbulent cells, the polarization level at each wavelength would be subsequently altered. If the number of cells emitting high energy radiation is smaller than

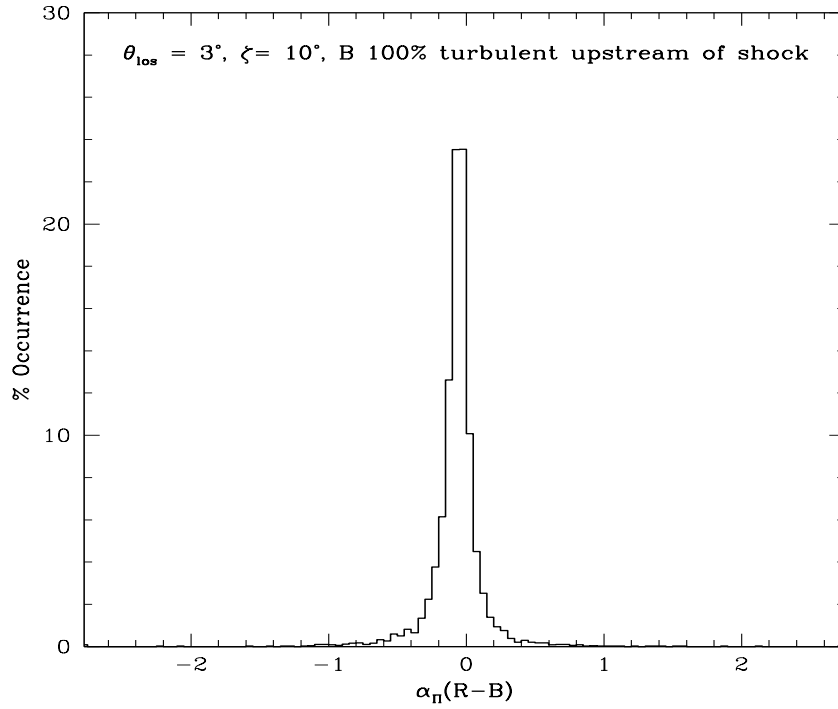


Fig. 4.17 Histogram of the middle panel of Figure 4.16. In this case a positive spectral index  $\alpha_{\Pi}(R - B)$  indicates that the polarization decreases from the  $R$  to  $B$  bands. From the histogram it is evident that this occurs in roughly 30 % of the time steps included in the simulation. The rest of the time, there is a slight increase in the polarization from  $R$  to  $B$ . (Figure courtesy of A. Marscher)

that of low energy radiation, the observed effect would be an increase in the total linear polarization from lower frequencies to higher. Alternately, if the number of cells emitting at lower frequencies extends to a region of the jet with a more ordered magnetic field, the total linear polarization would decrease as frequency increases. High energy synchrotron radiation, however, is produced by high energy electrons. As the jet flows past a shock front at which the electrons are energized, for example, the highest energy electrons will radiate away their energy more quickly than the lower-energy electrons that are not as radiatively efficient. Thus, the number of cells from which higher frequency radiation is observed will often, but not always, be fewer than that from high frequency radiation; see Figure 4.16. This would result in an

observed increasing trend in the linear-polarization with frequency in the Steward Observatory spectra. A direct consequence of this increasing polarization with frequency is the flattening of the spectral index of the polarized flux when compared to the spectral index of the total flux (Figure 4.17).

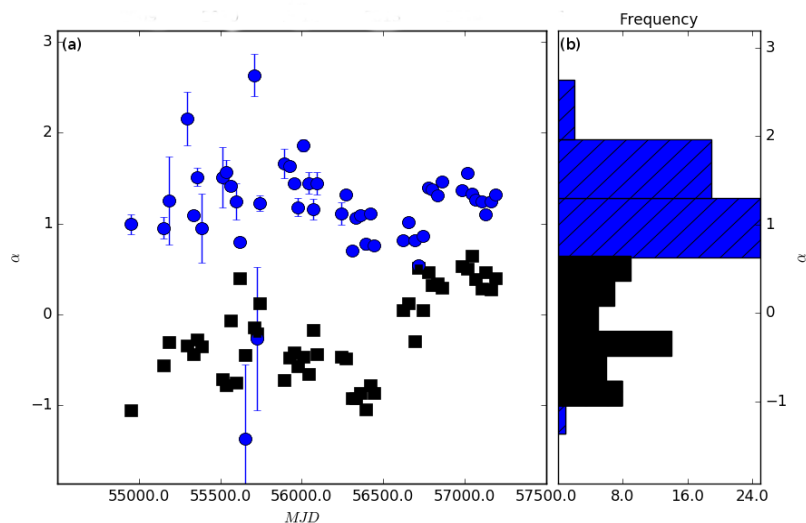


Fig. 4.18 (a): The spectral indices of the 1222+216 spectra after the removal of a constant big blue bump component are displayed in black squares. Even after subtracting the BBB component, the spectral indices correspond to flux increasing toward higher frequency, while the spectral indices of the polarized flux, displayed in blue circles, show that the polarized flux is decreasing toward high frequency. The wavelength dependence of polarization required in order to be able to explain the total spectrum as variable synchrotron radiation with a constant accretion disk is rather extreme and seems unlikely to be sustained over the 8 year timescale during which it has been observed. (b): Histogram depicting the distributions of both sets of spectral indices.

In the case of 1222+216, Figure 4.4 shows that the spectral index of the total flux is almost always greater than that of the polarized flux. This would indicate that if the difference in the spectral indices were caused by wavelength dependent polarization, it would be due to a scenario in which the number of cells containing



high energy electrons exceeded that of their lower energy counterparts. Such a situation is not prohibited by the TEMZ simulations; however, such strong and sustained wavelength dependent polarization, where the polarization at the  $B$ -band is several percent higher than at  $R$ -band, is quite rare. Because of this, I can conclude that wavelength dependent polarization alone is not responsible for the difference in shape between the polarized flux spectrum and total flux spectrum of 1222+216. Some degree of wavelength dependent polarization may, however, still be present in the spectra. In order to rule out such a scenario, I assume that the spectrum of 1222+216 contains a constant BBB component with a frequency dependence  $F_{BBB} \propto \nu^{1/3}$  determined as in section 4.3. I then subtract this component from the total spectrum, and subsequently determine the spectral index of the residual spectrum. The resulting spectral indices of the residual, as well as those of the polarized flux, are displayed in Figure 4.18. As was the case before the subtraction of a BBB component, the spectral index of the spectrum shows the flux increasing toward higher-frequencies at epochs before 2013. After 2013, the total flux begins to decrease as frequency increases; however, the decline is still more apparent in the spectra of the polarized flux. I conclude that wavelength dependent polarization is not a significant factor in determining the relative contribution of synchrotron radiation to the optical spectra of 1222+216.

## 4.6 Composing Difference Spectra of the Flux and Polarized Flux

Another way to explore the variability of different spectral components involves constructing difference spectra from the Steward Observatory data for both the total flux and polarized flux spectra. When a variable source is observed at two epochs,

the difference spectrum is simply defined as  $F_{diff} = F_{HE} - F_{LE}$ , where  $F_{HE}$  is the spectrum during the epoch when the total flux is higher and  $F_{LE}$  is the spectrum during the low-flux epoch. In Ruan et al. (2014), difference spectra were constructed between  $\lambda = 1500\text{--}8000 \text{ \AA}$  using a sample of 604 variable quasars from spectra contained in the *SDSS*. A composite flux spectrum was constructed by normalizing each individual spectrum, and then taking the geometric mean of the flux at each channel.

A similar procedure was performed on the difference spectra in order to obtain a composite difference spectrum. A power-law was fit to both the composite flux spectrum and the composite difference spectrum. The ratio of the difference spectrum to the total spectrum reveals the spectral shape of the variable component, and in the case of a composite spectrum of quasars, the variable component is well fit by the inhomogeneous accretion disk models of Dexter & Agol (2011).

In this section I apply a similar method to the total spectra and polarized flux spectra of 1222+216. Rather than combining spectra from several sources, I construct a composite spectrum from the 275 Steward Observatory spectra for the source. I construct the composite difference spectrum from the  $\frac{N(N-1)}{2}$  pairs of observations in the dataset. The composite spectrum, difference spectrum, and polarized difference spectrum are all well fit with power-laws with spectral indices of  $\alpha = -1.2, 0.88,$  and  $1.0,$  respectively, with typical uncertainties less than 0.02 for  $\alpha$  in 1222+216 and other sources. The difference spectra are shown in Figure 4.19. If the variability of 1222+216 were caused solely by the synchrotron component, the difference spectrum and polarized flux spectrum should be almost identical. The fact that they are different lends further evidence that the accretion disk is an important factor in the variability of this blazar. The difference spectrum is also flatter than the polarized

flux difference spectrum, suggesting a broad positively sloped component in the non-polarized spectrum. It is also of note that because the difference spectrum does not contain significant emission lines, the total flux of the broad and narrow emission line regions is relatively stable on the time-scales involved in this study.

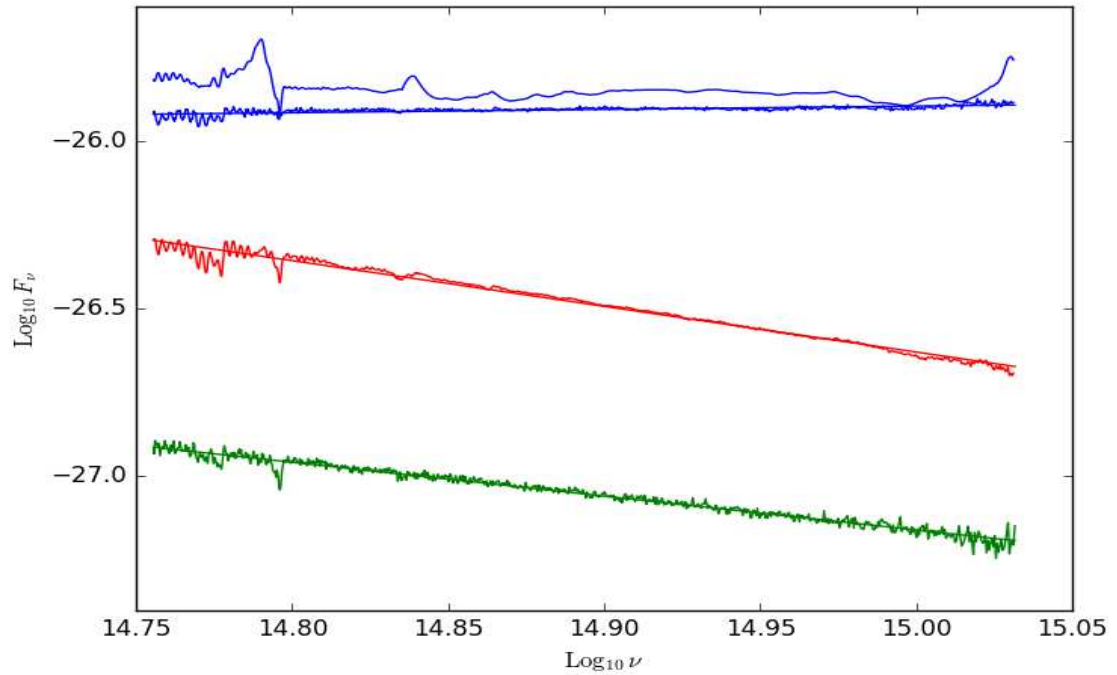


Fig. 4.19 A composite spectrum of 1222+216 constructed from the Steward Observatory spectra both with and without a template for the emission lines subtracted is shown in blue. The best fit power law for the composite spectrum with the emission line component subtracted is also displayed. The composite difference spectrum, derived by combining each pair of observations in the dataset along with its best fit power-law, is shown in red. In green the composite difference spectrum for the polarized flux, as well as a best fit power-law, is shown. The polarized flux difference spectrum and the total flux difference spectrum are fit with power laws with different spectral indices, indicating that a non-synchrotron component is variable.

## 4.7 Application to Other Sources

In this section I present the results of applying the methods of the previous sections to the other sources contained in my sample. The sample contains a mixture of FSRQs and BL Lacs.

### 4.7.1 BL Lacs

#### 3C66A

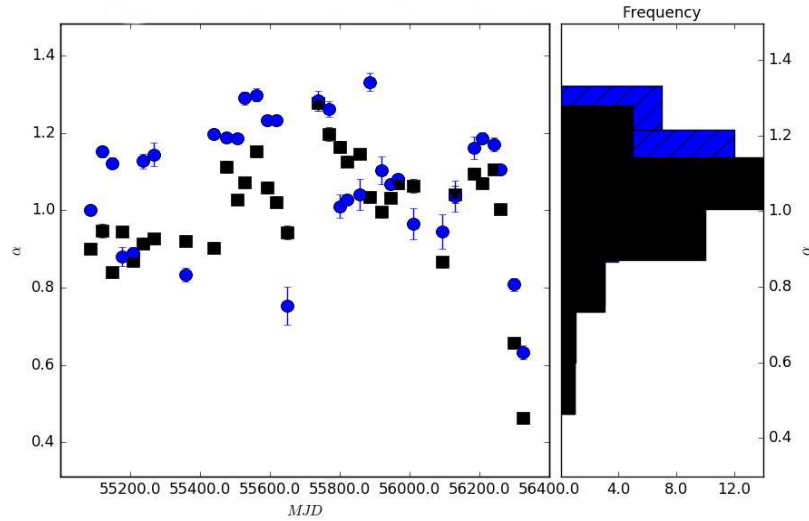


Fig. 4.20 *Left*: The spectral indices of both the polarized spectrum and total spectrum of 3C66A with the symbols and coloring the same as in 1222+216. *Right*: histogram of the values in the left panel.

3C66A, as with other BL Lacs, does not contain significant optical emission line flux. The spectral index of the optical spectrum is consistently positive, meaning that the flux decreases with frequency, as expected for a source dominated by synchrotron emission. The polarized spectral index, as in 1222+216, shows significant periods in which the polarized flux of 3C66A decreases more rapidly with frequency than the

total flux (Figure 4.20). Fitting the spectra of 3C66A with a power-law determined by the polarized spectrum, however, yields fits that are similar in quality to fitting a power-law independent of the polarization (Figure 4.21). The polarization of 3C66A exhibits weak dependence on wavelength, varying between  $\Delta\Pi = -1.5 - 0.8\%$  across the observed bandpass. Of note is that the wavelength dependence is mostly negative with frequency, meaning that the spectrum gets less polarized at higher frequency (Figure 4.22). In order to generate the histogram in Figure 4.22, I fit the polarization,  $\Pi$ , linearly across the observed bandpass. The slope and intercept of the best fit line determines the polarization value at the endpoints while the difference is a good gauge for the variability of  $\Pi$ . The resulting histogram for 3C66A is opposite of the situation depicted in Figure 4.17; however, the negative dependence of polarization with frequency is not strong enough to conclude that a strong BBB is present in the spectra of 3C66A. Inspecting the difference spectrum of 3C66A shows that the total flux composite spectrum has a spectral index of 0.85, while the spectral indices of the difference spectrum and the polarized difference spectrum are both 0.8. This suggests that the variability of 3C66A is well explained by a variable synchrotron component.

### **OJ287**

The optical spectra of OJ287 exhibit interesting behavior between 2010 and 2013. From the plot of the spectral indices of the polarized flux and the full flux (Figure 4.23) it is apparent that the spectral indices are drawn from separate parent distributions. The two distributions, however, are not as widely offset as is seen in 1222+216, with the difference between the peak of the two distributions being 0.1. Also of note is that the slope of the full spectrum (shown in the black squares) is almost always steeper than that of the polarized flux. Inspecting the polarization spectra reveals that the linear polarization is weakly dependent on frequency, often

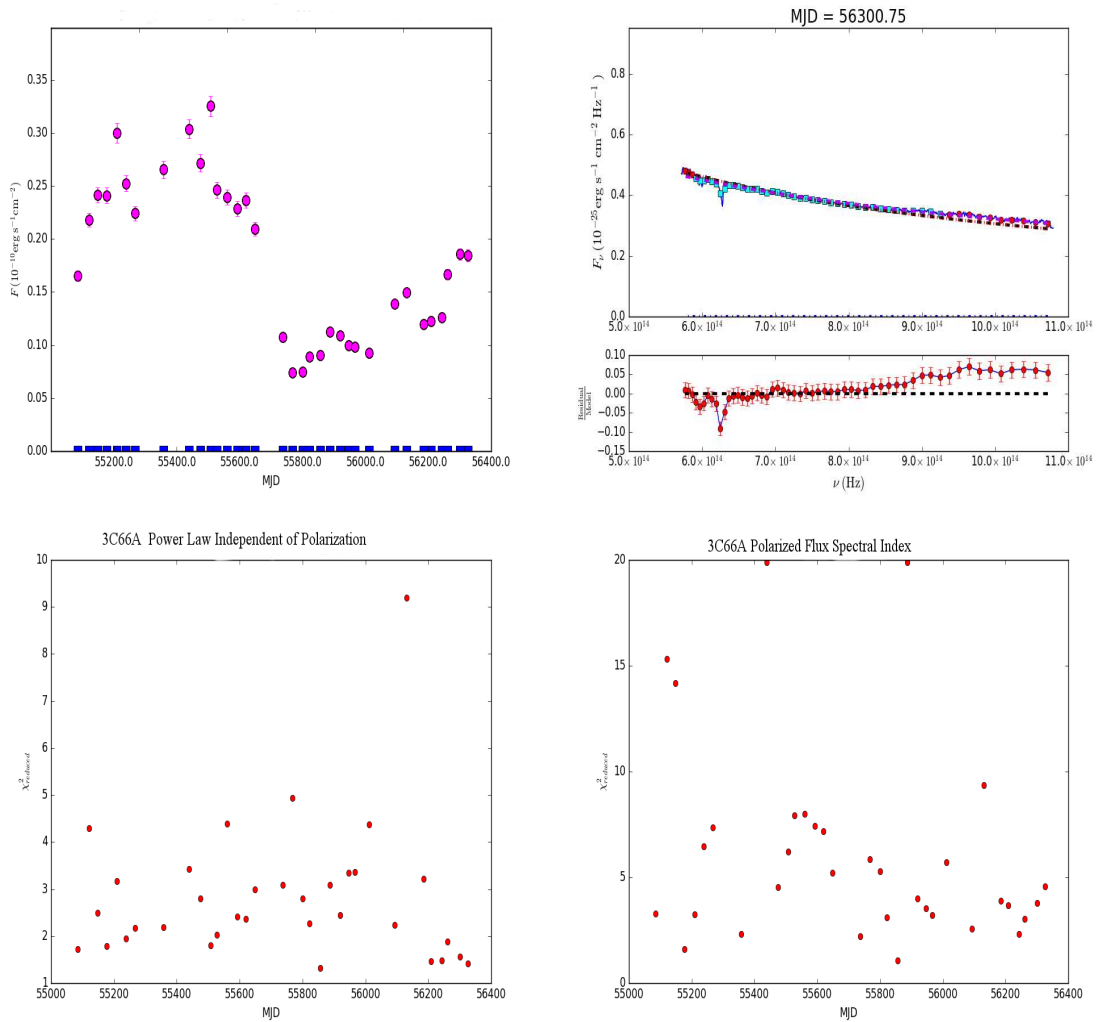


Fig. 4.21 *Left:* The measured flux from 3C66A (Top) and the reduced  $\chi^2$  for fitting spectra of 3C66A in which the spectral index is independent of the polarized flux (Bottom). *Right:* A typical spectrum of 3C66A along with the fit of the synchrotron component is displayed (Top). Reduced  $\chi^2$  resulting from fitting the same spectra using a spectral index identical to that of the polarized flux (bottom). Using the polarized flux spectral index does result in slightly worse fits; however, introducing a variable accretion disk component does not result in a higher quality of fit.

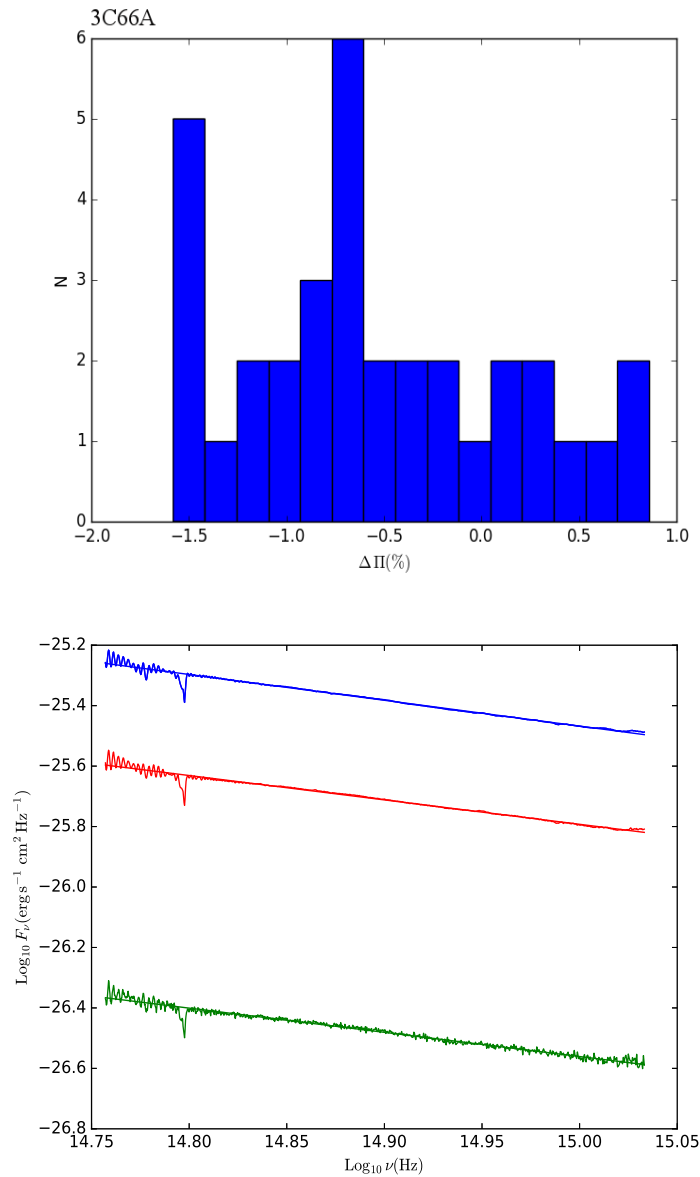


Fig. 4.22 *Top*: histogram depicting the change in linear polarization across the band-pass. 3C66A, at most epochs, displays decreasing linear polarization with increasing frequency. *Bottom*: Difference spectrum of 3C66A. The total flux difference spectrum of 3C66A has the same spectral index as the difference in polarized flux spectrum, suggesting synchrotron radiatio as the driver of the variability.

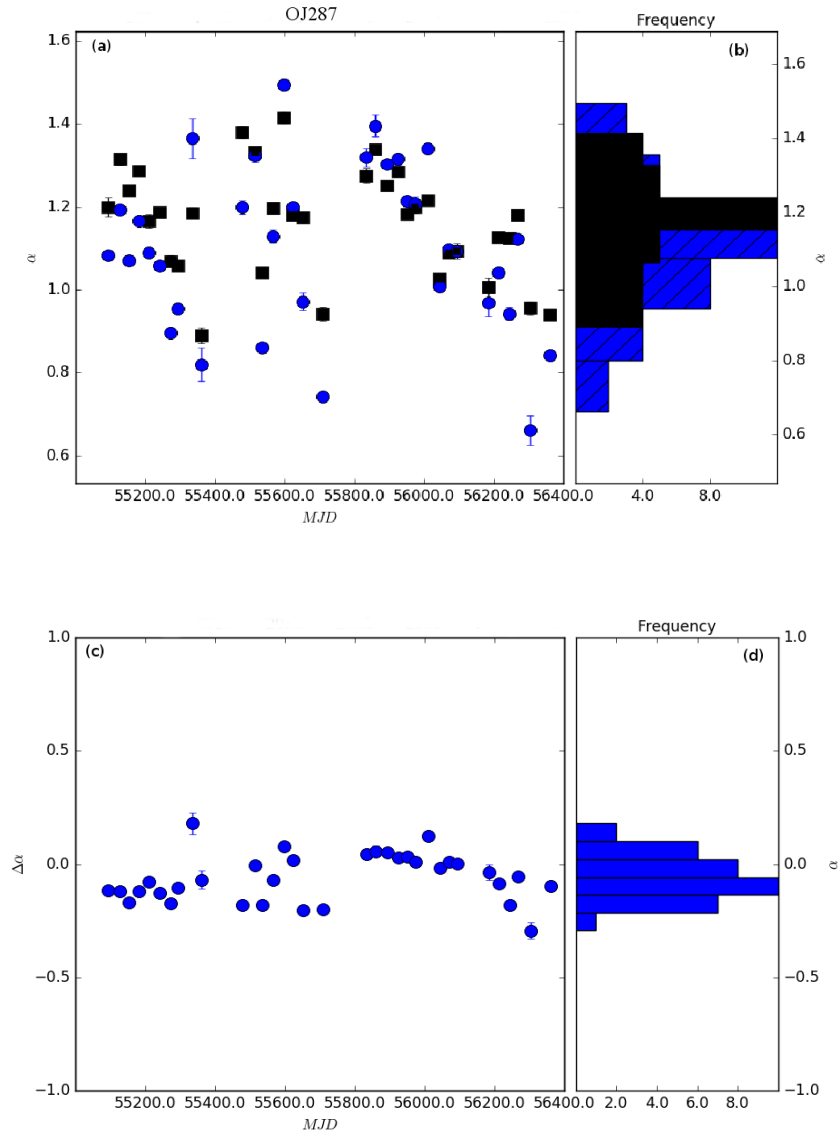


Fig. 4.23 (a): The spectral indices of both the polarized spectrum and total spectrum of OJ287. The symbols and colors are the same as for similar figures. (b): Histograms depicting the distributions of the values in (a). (c): The difference between the two values plotted in (a) depicting the difference in spectral shape between the polarized flux and total flux. (d): Histogram of the values in (c) showing that the difference distribution peaks at 0.1 indicating that the polarized flux is slightly steeper than the unpolarized flux. This is inverted from the situation in 1222+216 which suggests that the linear polarization in OJ287 is slightly wavelength dependent.



increasing by  $\sim 1 - 2\%$  as frequency increases from  $\nu = 5 \times 10^{14} - 1 \times 10^{15}$  Hz. A histogram displaying the wavelength dependence of the linear polarization is shown in in Figure 4.24. If the spectra from OJ287 contained a significant contribution from a BBB, the linear polarization would not show such a strong positive dependence on frequency. It is likely that in the case of OJ287, the observed difference in the shapes of the polarized and total flux spectra is consistent with the effect expected from the turbulence plus shock model.

For OJ287, I fit the full spectrum with a model consisting only of a synchrotron component with the spectral index derived from the observed spectral index of the polarized flux. With visual inspection, the resulting spectra appear to provide a good fit to the data, however the average reduced  $\chi^2$  values for such a fit are significantly worse than the values for the spectral index of the full spectrum determined independently of the polarized flux (Figure 4.25). The composite spectrum and difference spectra (Figure 4.25) of OJ287 show an identical spectral index,  $\alpha = 1.14$ , while the polarized flux spectrum is flatter  $\alpha_{pol} = 0.98$ . Attempting to add a BBB, either through the addition of a blackbody or a thin disk, does not improve the fit. The value of the linear polarization is strongly dependent on frequency (Figure 4.24), often with  $\Delta\Pi > 1\%$  across the observed bandpass, however a net decrease in the linear polarization at higher frequency is observed in about 1/3 of the spectra. OJ287 represents a case in which TEMZ style wavelength dependent polarization may be present.

### **1219+285**

1219+285 behaves mostly as expected for a BL Lac object. No significant emission lines are present in the spectrum, and the source displays no evidence for BBB emission being present. The spectral indices of the polarized flux are con-

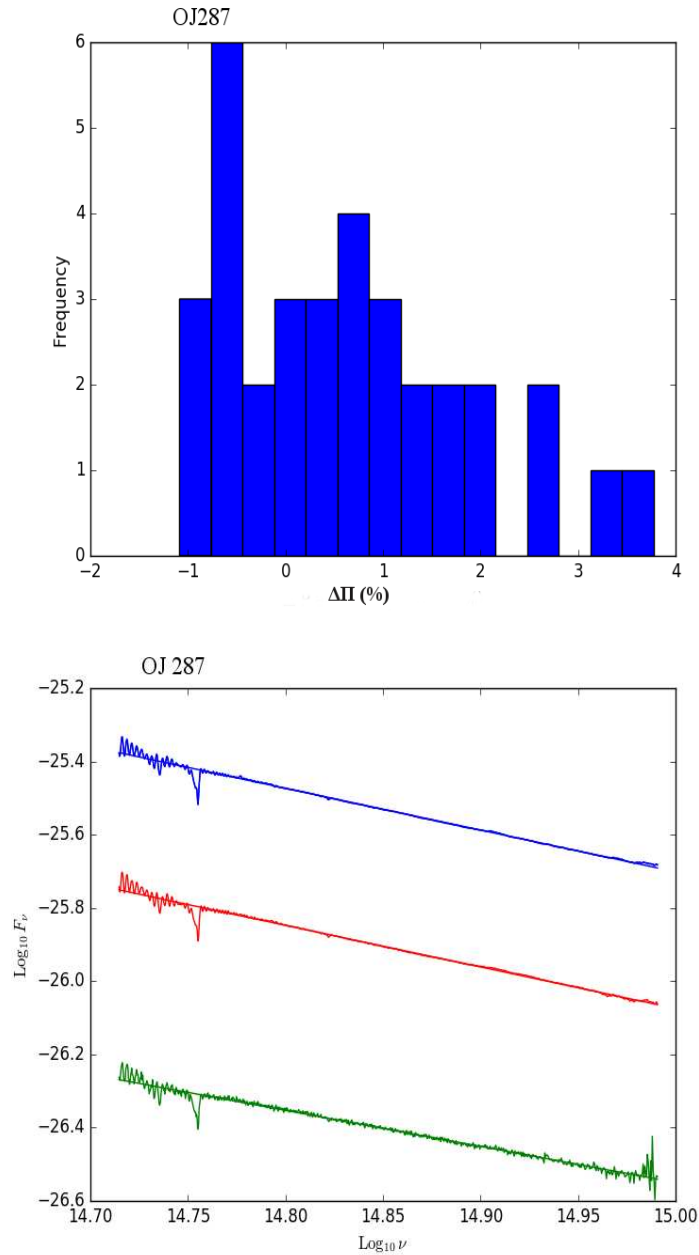


Fig. 4.24 *Top*: Histogram depicting the wavelength dependence of the linear polarization of OJ287. OJ287 displays a strong increase in linear polarization at higher frequencies in most of the observed spectra. An unpolarized thermal component is likely not a contributor to the observed spectrum. *Bottom*: The composite spectrum (blue) along with the difference spectrum (red) and polarized difference spectrum (green) for OJ287. The spectral index for the composite spectrum and difference spectrum is  $\alpha = 1.14$ , while the polarized difference spectrum is flatter at  $\alpha = 0.98$ .

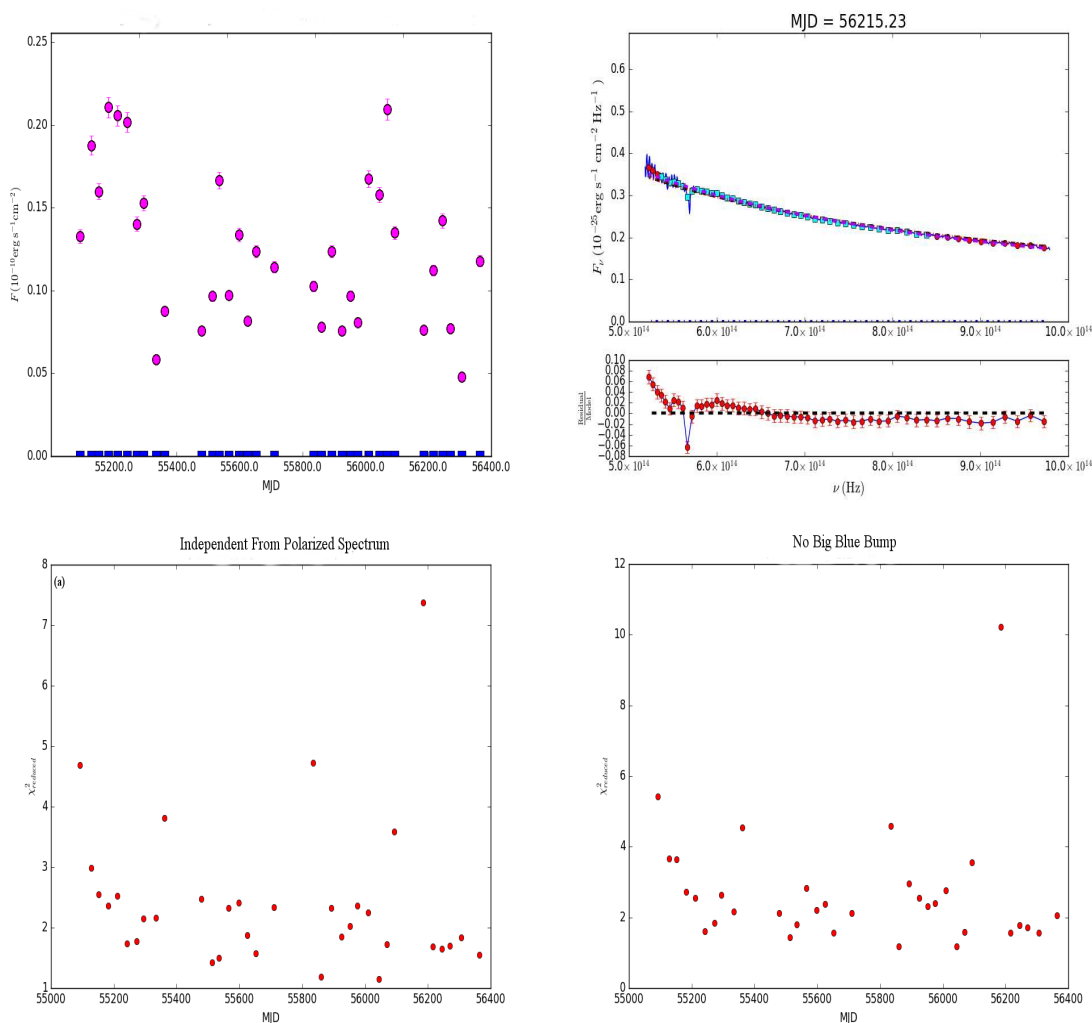


Fig. 4.25 As in Figure 4.21 for OJ287.

sistently flatter than that of fitting the spectrum independent of the polarization (Figure 4.26). This is a similar observation to what is seen in OJ287. Like OJ287, the linear polarization of 1219+285 varies positively with increasing frequency (Figure 4.26), such that the discrepancy between the spectral index measured on the polarized flux spectrum and that of the full flux spectrum likely is accounted for by the wavelength dependence of the linear polarization rather than the presence of a

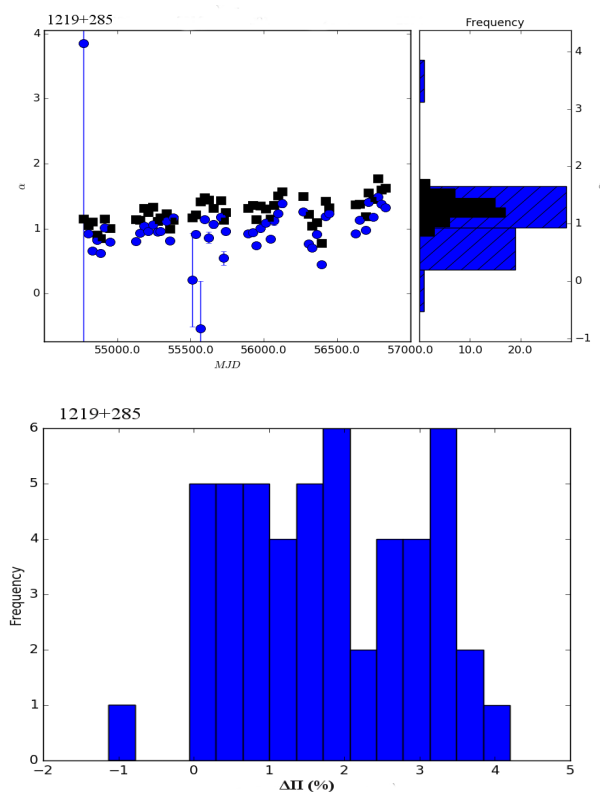


Fig. 4.26 *Top*: The spectral indices of the polarized flux and total flux of the 1219+285 spectra and histograms of the values displayed in the left panel. Symbols and colors are as in similar plots of other sources. *Bottom*: Histogram depicting the wavelength dependence of the linear polarization of 1219+285. Like in OJ287, the blazar displays a strong increase in linear polarization at higher frequency in most of the observed spectra. An unpolarized thermal component is likely not a contributor to the observed spectrum.

thermal non-polarized component in the spectrum. The total spectrum is well fit by a single power-law component (Figure 4.25).

### S3 1227+25

S3 1227+25 is a *Fermi* detected BL Lac which began undergoing significant flaring activity in January 2015 and subsequently in May 2015. The May 2015 flare was observed by the Very Energetic Radiation Imaging Telescope Array Sys-

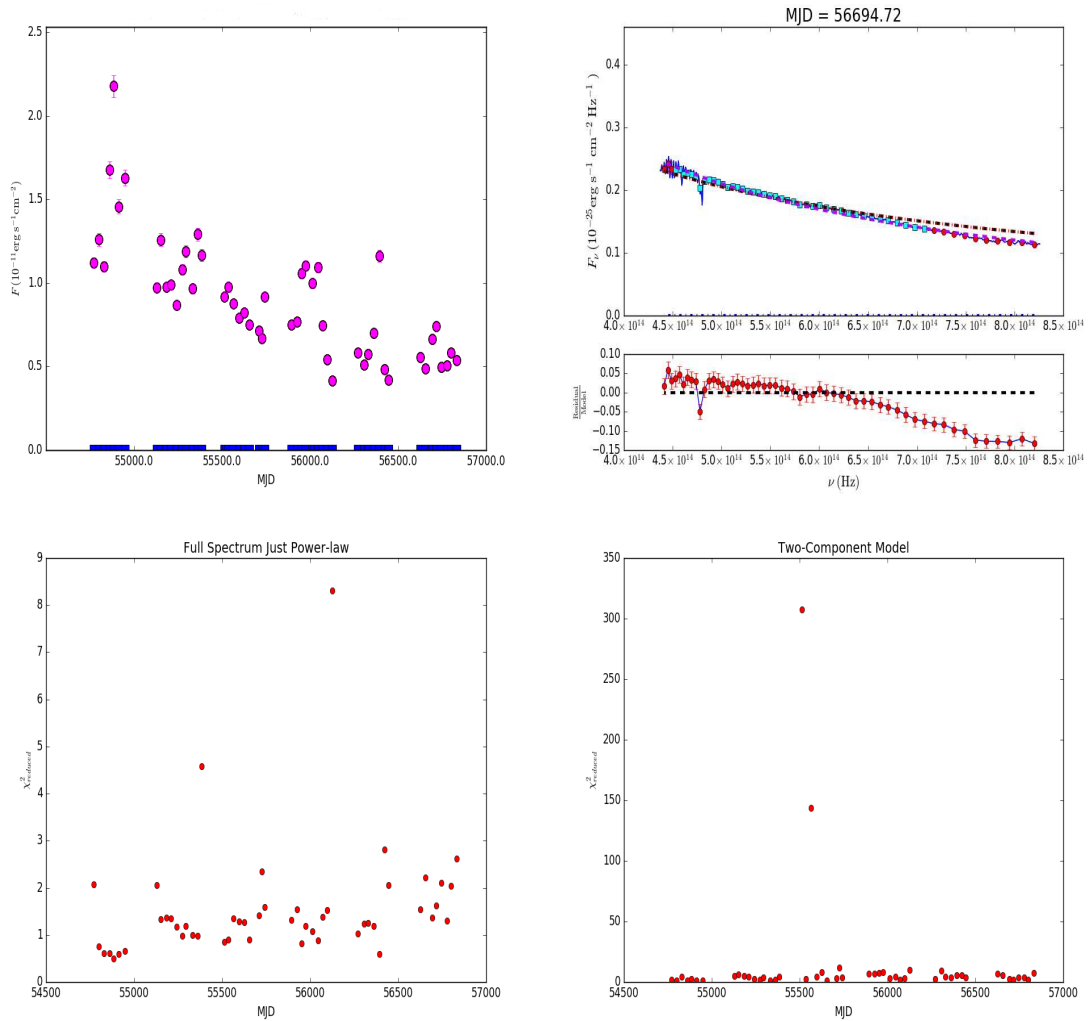


Fig. 4.27 As in Figure 4.21 for 1219+285.

tem (VERITAS) team, collecting a total of 420  $\gamma$ -rays with energies  $\geq 200$  GeV (Fortson & VERITAS Collaboration, 2016). After this flaring activity, Steward Observatory observations of the source were made over the course of two months from 2015-05-18 to 2015-07-21. During this two month period, the linear polarization is  $\sim 20\%$  and it varies on order of  $\Delta\Pi \sim \pm 1.5\%$  over the bandpass (Figure 4.28). As in 1222+216, the spectral index of the total spectrum is flatter than that of the polarized flux for much of this two month window, however, the differences in the

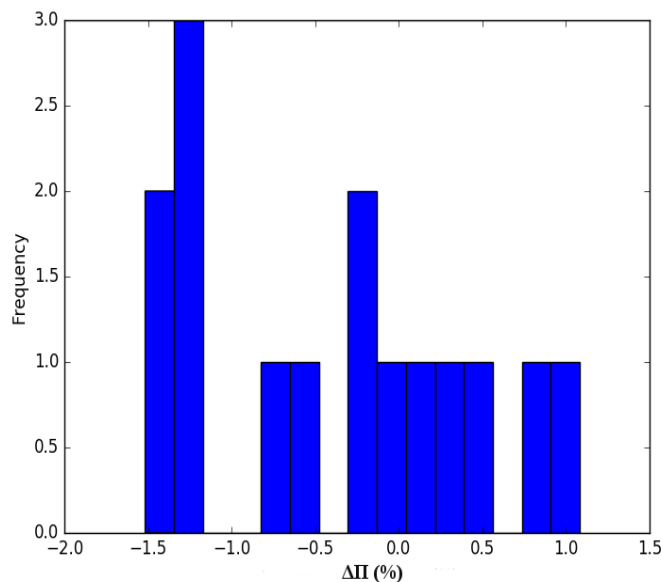


Fig. 4.28 Histogram depicting the wavelength dependence of the linear polarization of S3 1227+25.

spectral indices are not as extreme as in 1222+216. No evidence of a non-polarized thermal flux in the spectrum of S3 1227+25 was found, and fitting the spectra with a power-law with the spectral index decided by the polarized flux spectrum (Figure 4.29) results in reduced  $\chi^2$  values similar to those of fitting the spectrum with a power-law independent of the spectral index of the polarized flux.

### BL Lac

Among the BL Lacs, BL Lac presents an interesting case. BL Lac, by virtue of its relatively small redshift, is bright enough that emission from the host galaxy of the blazar is detectable and significantly reddens the optical spectrum. In order to proceed with fitting of the optical spectrum, I subtract the contribution of the host galaxy spectrum. As in Williamson et al. (2014), I use the *R*-band host galaxy flux value reported in Nilsson et al. (2007) along with the effective colors of a giant elliptical galaxy, as determined in Mannucci et al. (2001), to estimate the host galaxy flux

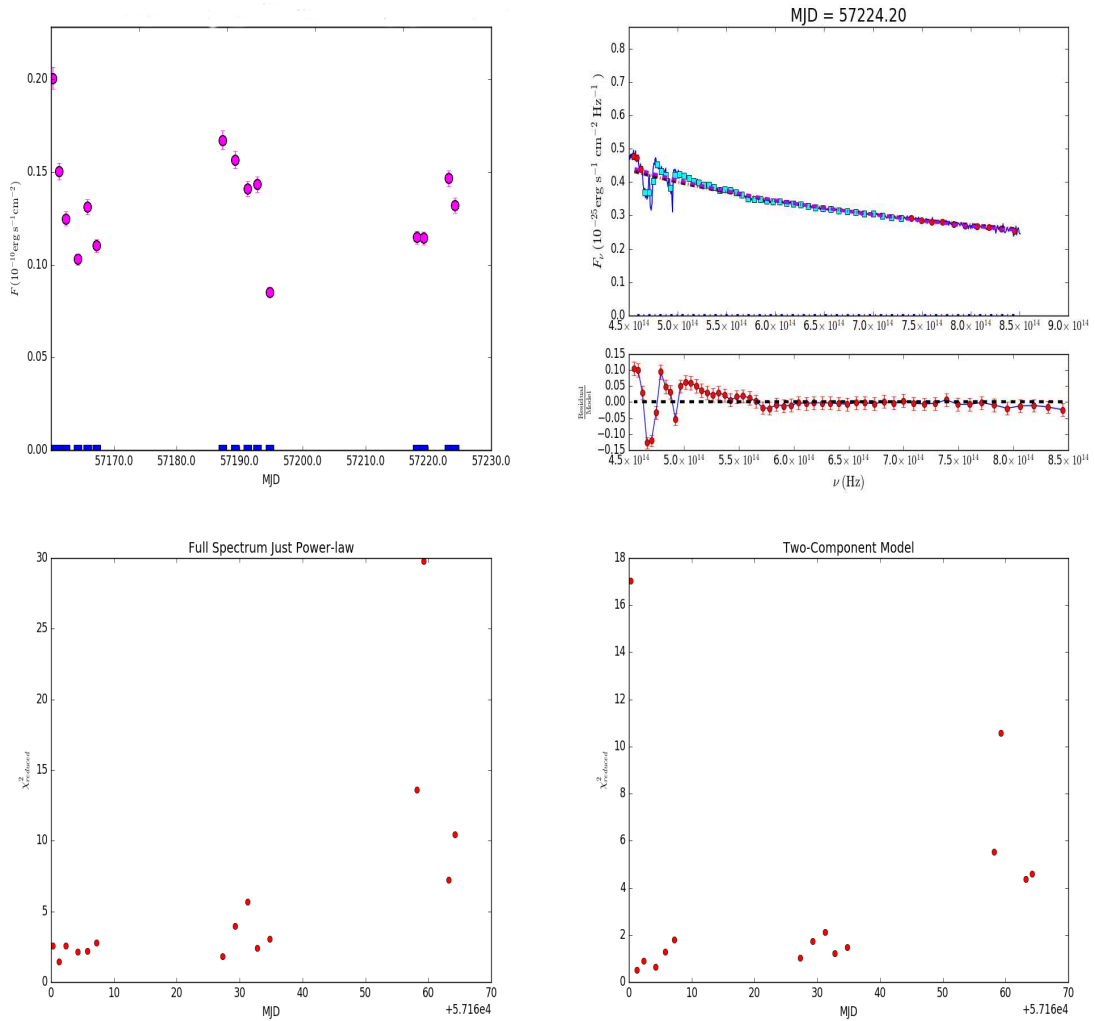


Fig. 4.29 As in Figure 4.21 for 1227+25.

of BL Lac from  $K$ -band to  $U$ -band. Because the values reported in Williamson et al. (2014) are flux values from broad band filters, I interpolate the reported flux values in each filter, using cubic splines and the effective wavelength of each filter as reported in Bessell (2005). The values used for the host galaxy flux of BL Lac is shown in Table 4.2.

As in 3C66A, the polarized flux spectra have steeper spectral indices than the total flux spectra (Figure 4.30). In FSRQs this is taken to be evidence for a BBB

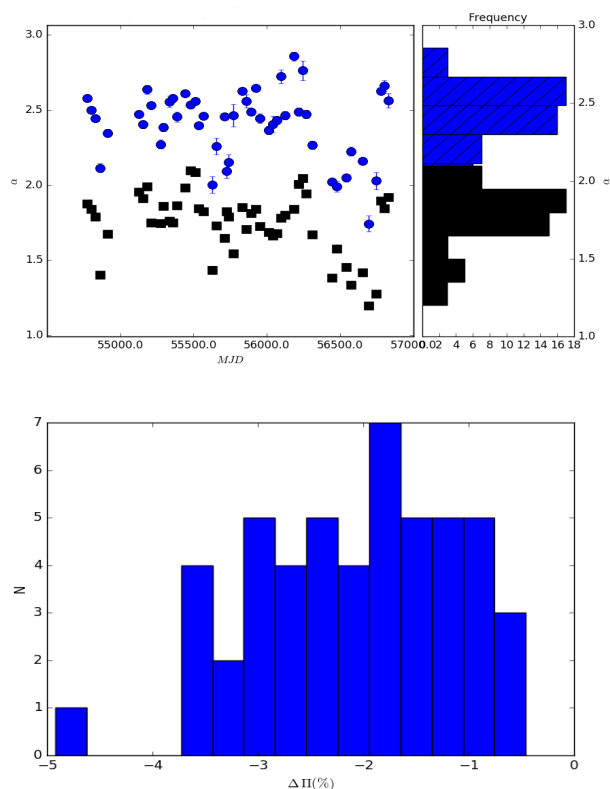


Fig. 4.30 *Top*: The spectral indices of the polarized flux and total flux of the BL Lac spectra and histograms of the values displayed in the left panel. Symbols and colors are as in similar plots of other sources. *Bottom*: Histogram depicting the wavelength dependence of the linear polarization of BL Lac. Like in 3C66A, the blazar displays a strong decrease in linear polarization at higher frequency in most of the observed spectra.

component. For nearly all of the spectra of BL Lac, the polarization decreases with increasing frequency, often by more than 2% across the bandpass. Because of this, I model BL Lac as consisting of a synchrotron component and a BBB corresponding to a constant,  $F_\nu \propto \nu^{1/3}$  thin disk. This model, however, does not result in a high quality fit (Figure 4.31). From the polarization spectra, it is clear that the optical spectra of BL Lac contain a non-polarized component; however, characterizing that component with a BBB model is difficult.



Table 4.2. Host Galaxy Flux of BL Lacertae

Filter Name	De-reddened Host Galaxy Flux <sup>a</sup> (mJy)
<i>U</i>	$0.23 \pm 0.01$
<i>B</i>	$0.84 \pm 0.03$
<i>V</i>	$1.79 \pm 0.07$
<i>R</i>	$2.60 \pm 0.10$
<i>I</i>	$3.85 \pm 0.15$
<i>J</i>	$7.4 \pm 0.3$
<i>H</i>	$9.1 \pm 0.4$
<i>K</i>	$6.8 \pm 0.3$

<sup>a</sup>From Williamson et al. (2014)

### 0735+178

0735+178 was only observed over the course of a few months. The few total spectra are well fit by a power-law, however, the spectral index differs from that of the best fit power-law to the polarized flux. The polarization for all of the combined spectra rises by more than 0.5% throughout the bandpass (Figure 4.32). It should be noted, however, that the polarization spectra are quite noisy, and the total polarization of 0735+178 was often measured to be  $< 2\%$ . Because of the quality of the data available for this source, firm conclusions cannot be drawn about the nature of the optical spectral components; however, it is very unlikely that a strong BBB is present.

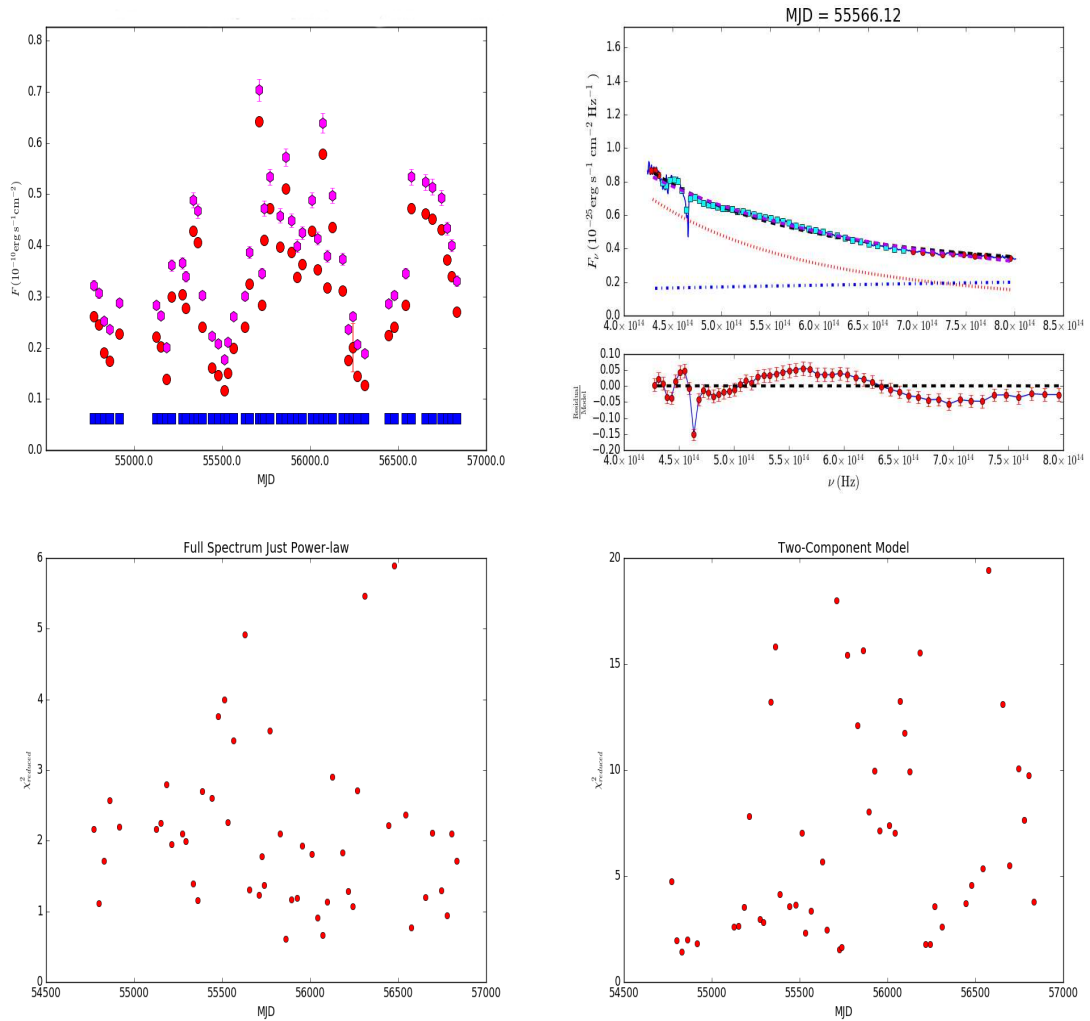


Fig. 4.31 As in Figure 4.21 for BL Lac.

## 4.7.2 FSRQs

### 0420-014

Except for a  $MgII$  line at  $\lambda = 2800\text{\AA}$ , 0420-014 does not exhibit much flux from emission lines in the spectral region observed. The spectra show a strong decline of the value of the linear polarization at higher frequencies, with  $\Delta\Pi$  often  $> 2\%$  (Figure 4.33). As with 1222+216, the total flux spectrum is almost always flatter than that of the polarized flux, with  $\Delta\alpha$  often  $> 0.5$ . The spectra are best fit

with a synchrotron component, which is the dominant source of flux most of the time, along with a weakly varying accretion disk (Figure 4.34). The temperature of the blackbody component varies between  $1\text{--}2 \times 10^3$  K during the 900 day period during which the source was observed. The calculated size of the hot-spot is between 400 – 500 AU. The synchrotron component is the dominant driver of the variability of the optical spectral components, but the flux from the hot spot also appears to vary in late 2009, which coincides with a  $\gamma$ -ray flare, The apparent variability is only on the  $2\sigma$  scale, however, and is thus consistent with being constant.

### **CTA26**

CTA26 contains a strong MgII line at  $\lambda = 2800\text{\AA}$ , which I subtract prior to performing the fits. This source is not well sampled in the Steward Observatory data, having only been observed between 2011-09-29 through 2011-12-28 and then again three years later between 2014-10-21 and 2014-10-29. The polarization dependence on frequency is negative with  $\Delta\Pi$  being several percent across the observed band-pass, indicating a BBB spectral component (Figure 4.35). Both sets of observations were performed during a time at which CTA26 was undergoing flaring activity in the optical . Adding a variable hot-spot to the accretion disk model does not significantly improve the fit of the spectrum over a model in which the BBB flux is held constant with a thin disk spectrum (Figure 4.36).

### **3C279**

3C279 is unique among the sample of FSRQs in this work in that the best deconstruction of the optical components is one in which the spectrum is fit with a synchrotron-only model. The spectral indices of the polarized flux are often flatter than the corresponding spectral indices of the total flux (Figure 4.37), which while common in the BL Lacs studied in this work, is uncommon for FSRQs. The po-

larization of 3C279 often increases toward higher frequency with a median value of  $\sim 1.5\%$  (Figure 4.38).

### **1510-089**

As in many of the FSRQs studied in this work, the spectral indices of the total spectrum are flatter than the polarized flux (Figure 4.39), indicating the presence of a BBB. The optical spectral components of 1510-089 are best fit by an accretion disk component in which the hot-spot emits flux roughly equal to that of the thin disk component (Figure 4.40). The temperature is  $\sim 20000$  K and shows a slight increase in later epochs, however, this is only at the  $1-\sigma$  level and cannot be confirmed. The polarized flux difference spectrum decreases with frequency with a spectral index of 0.9, while the difference spectrum of the total flux increases with frequency with a spectral index of -2.0, and contains significant emission line flux. The variability in the optical spectrum of 1510-089 appears to be driven more by a combination of synchrotron variability, and slight changes in the emission line flux, more than by variability in the accretion disk flux (Figure 4.41). A similar result was obtained by Isler et al. (2015), who reported emission line variability in 1510-089.

### **CTA102**

Like other FSRQs in the sample, the linear polarization shows a slight decrease toward higher frequencies more often than not, however, polarization of CTA102 does exhibit a few cases in which the polarization slightly increases at higher frequencies (Figure 4.42). The optical spectra suggest a BBB component and the optical spectra of CTA102 contain both a thin disk and a hot-spot component. In the case of CTA102, the temperature of the hot spot is  $\sim 15,000$  K. The synchrotron component of CTA102 is the main driver of variability, and the flux level of the hot-spot does not seem to vary significantly over the time scales involved in this study.

### 3C454.3

The spectral decomposition of 3C454.3 works best when there is a constant thin disk component for the thermal flux, and a variable synchrotron component (Figure 4.44). While the disk component is constant, the synchrotron flux at times also becomes very weak, and the thermal flux as a fraction of the total flux becomes very high. This is evident in the strong negative dependence on frequency in several of the spectra, where the linear polarization often decreases by several percent (Figure 4.45). The quality of the fits to 3C454.3 are poor at times; this occurs because as the synchrotron flux decreases, the total polarization becomes very low and the shape of the synchrotron spectrum becomes hard to discern.

### OJ248

The optical spectra of OJ248 contain a significant amount of flux from emission lines, which is difficult to remove. The polarized flux spectra contain a significant amount of noise toward higher frequencies so it was necessary to limit the range of frequencies used for determining the spectral indices. As with 1222+216, the spectral indices of the total flux indicate a spectrum that is much less steep than the one indicated by the polarized flux, but because the polarization measurements are quite noisy, an accurate characterization of the synchrotron flux component is difficult to make. Because the polarization measurements are noisy, the incidence of an increase of the linear polarization toward higher frequencies is common (Figure 4.46). The deconstruction of the spectral components reveals that the spectra contain a thin disk component, along with a variable blackbody component (Figure 4.47). The best fit big blue bump model consists of a constant thin-disk component, along with a variable blackbody, with a temperature at roughly  $1 - 2 \times 10^4$  K. The flux of the

blackbody increases quickly around March 2012, prior to a  $\gamma$ -ray outburst later in the year.

### **3C273**

3C273 is the blazar in the sample most like 1222+216 in the sense that the flux from the optical spectrum increases toward higher frequencies (Figure 4.48). The polarized flux is mostly flat, rarely increasing or decreasing by more than 0.1% throughout the bandpass. As in 1222+216, the  $10\ \mu\text{m}$  emission feature has been observed in the mid-infrared (IR) (Hao et al., 2005), making it one of the few blazars in which thermal emission from the dusty torus is not overwhelmed by the synchrotron flux at near-IR wavelengths. The components of the optical spectrum include a thin-disk, which is the dominant source of emission in the optical spectrum of 3C273 (Figure 4.49). There is also a less luminous blackbody component which varies in flux by  $2\sigma$  during the time span covered by the Steward Observatory observations. The polarization at times is very low, and that makes it difficult to determine the spectral index of the synchrotron component, and thus get an accurate deconstruction of the spectra. While the BBB of 3C273 has been observed to vary in the past (Paltani et al., 1998), in this work the analysis fails to show that the BBB of 3C273 varies above a level of  $2\text{-}\sigma$ .

## **4.8 Calculated Properties of the Optical-UV Spectra of Blazars**

This section summarizes the results obtained by analyzing the optical spectra and polarized spectra of the sample of blazars. In Table 4.3 I present a summary of dates observed, number of spectra present before they were combined, the frequency range used to derive the polarized spectral index, variability of the BBB, and the measured

Table 4.3. Properties of Optical Spectral Components of Select Blazars

Source Name	Spectral Type	$\nu \alpha_{\Pi}$ <sup>a</sup> ( $\times 10^{14}$ Hz)	$\langle L_{Disk} \rangle$ <sup>b</sup> ( $\times 10^{45}$ erg s <sup>-1</sup> )	$L_{Max, Disk}$ <sup>c</sup> ( $\times 10^{45}$ erg s <sup>-1</sup> )	$\Delta F_{BBB}$	$\left\langle \frac{\sigma_F}{F_{BBB}} \right\rangle$ <sup>c</sup>	$\langle \Delta \Pi \rangle$ <sup>d</sup> (%)
3C66A	BL Lac	6.0–10.5	-	-	-	-	-0.8
CTA26	FSRQ	7.5–13.9	-	-	-	-	-0.5
0420-014	FSRQ	8.0–14.0	0.037 ± 0.009	0.058 ± 0.009	0.67	0.25	-0.6
0735+178	BL Lac	5.5–10.0	-	-	-	-	+0.7
OJ248	FSRQ	8.0–12.0	2.8 ± 0.3	4.5 ± 0.3	0.3	0.1	+0.3
OJ287	BL Lac	5.0–10.0	-	-	-	-	0.5
1219+285	BL Lac	4.5–8.0	-	-	-	-	+2
1222+216	FSRQ	5.8–10.8	2.7 ± 0.2	3.7 ± 0.2	0.23	0.07	-3
3C273	FSRQ	4.1–7.5	4.5 ± 0.8	5.7 ± 0.8	0.5	0.2	0
1227+25	BL Lac	4.5–8.5	< 0.3	-	-	-	-0.1
3C279	FSRQ	6.0–11.4	-	-	-	-	+1.5
1510-089	FSRQ	5.5–9.0	0.58 ± 0.08	0.83 ± 0.08	0.38	0.15	-0.5
BL Lac	BL Lac	4.0–8.0	< 0.07	-	-	-	-2
CTA102	FSRQ	8.0–12.5	5.2 ± 0.4	6.6 ± 0.4	0.2	0.1	+0.2
3C454.3	FSRQ	7.0–13.5	< 3	-	-	-	0

<sup>a</sup>Frequency window used to obtain the spectral index of the polarized flux.

<sup>b</sup>Average Integrated accretion disk flux from  $\lambda = \frac{4000-7500\text{\AA}}{1+z}$ .

<sup>c</sup>Maximum Integrated accretion disk flux from  $\lambda = \frac{4000-7500\text{\AA}}{1+z}$ .

<sup>d</sup>Average of the ratio of the uncertainty of the hot-spot flux to the hot-spot flux.

<sup>e</sup>Average change in the linear polarization with frequency.

change in polarization % across the bandpass for both BL Lacs and FSRQs. I define a dimensionless variability parameter for the BBB as

$$\Delta F_{BBB} = \frac{\sigma_{BB}}{\langle F_{BB} \rangle}, \quad (4.18)$$

where  $\sigma_{BB}$  is the standard deviation of the variable component of the disk flux, and  $\langle F_{BB} \rangle$  is the average value of the flux of the variable disk component.

### Summary of FSRQs

Out of my sample, I find some FSRQs in which the accretion disk appears to be variable, in the form of an evolving hot spot, over the course of the several years in which they were observed. This includes one of the blazars for which an excess in the IR was attributed to hot dust in Malmrose et al. (2011), 1222+216.

There is a variable blackbody component that results from modeling OJ248 as well. OJ248 presents an interesting case, as the best fit shows a sudden, and sustained, increase in the blackbody flux early in 2012 prior to a major  $\gamma$ -ray outburst in the source. The flux of the blackbody component remains in a high-state at the conclusion of the outburst, even after the optical flux has returned to its average level.

FSRQs in which the calculated variability of the accretion disk is not observed over  $3\text{-}\sigma$  include 3C454.3, CTA102, 1510-089, 0420-014, and 3C273. In the case of 3C273, visual inspection of the total fit accretion disk flux indicates variability, but because of the difficulty in characterizing the polarization, the uncertainty in the accretion disk flux is too high for a  $3\text{-}\sigma$  detection. CTA26 is best fit with a



constant BBB model, and there are not sufficient observations in the data-set to accurately measure variability, as this source was only observed over the course of two months, with a gap of several years. Like CTA26, 3C454.3 is best fit with a constant accretion disk component, with the optical variability arising solely from the synchrotron component. 3C279 is best fit without a BBB component, with the only excess to synchrotron radiation in the optical arising from broad emission lines.

### **Summary of BL Lacs**

The optical total flux spectra of the BL Lacs contained in this sample, for the most part, can be fit by a power-law. In many cases, however, the spectral index of the best fit power-law differs from that of the best fit power law to the polarized flux. This is an effect of the total polarization of the BL Lac increasing toward higher frequencies. Of the six BL Lacs considered in this study, 1219+285, OJ287, and 0735+178 show a trend toward increasingly higher optical polarization at higher frequencies. 3C66A and 1227+25 show this trend some of the time, however, also display the opposite effect of lower optical polarization toward higher frequencies in many of the spectra. BL Lac itself consistently shows a trend toward lower polarization at higher frequencies, with the change in polarization  $\Delta\Pi$  often  $> 2\%$  in magnitude. While the TEMZ model sometimes produces wavelength dependent polarization like that seen in BL Lac, it occurs infrequently, hence it's more likely that a non-polarized component of emission is present in the optical spectra of BL Lac.

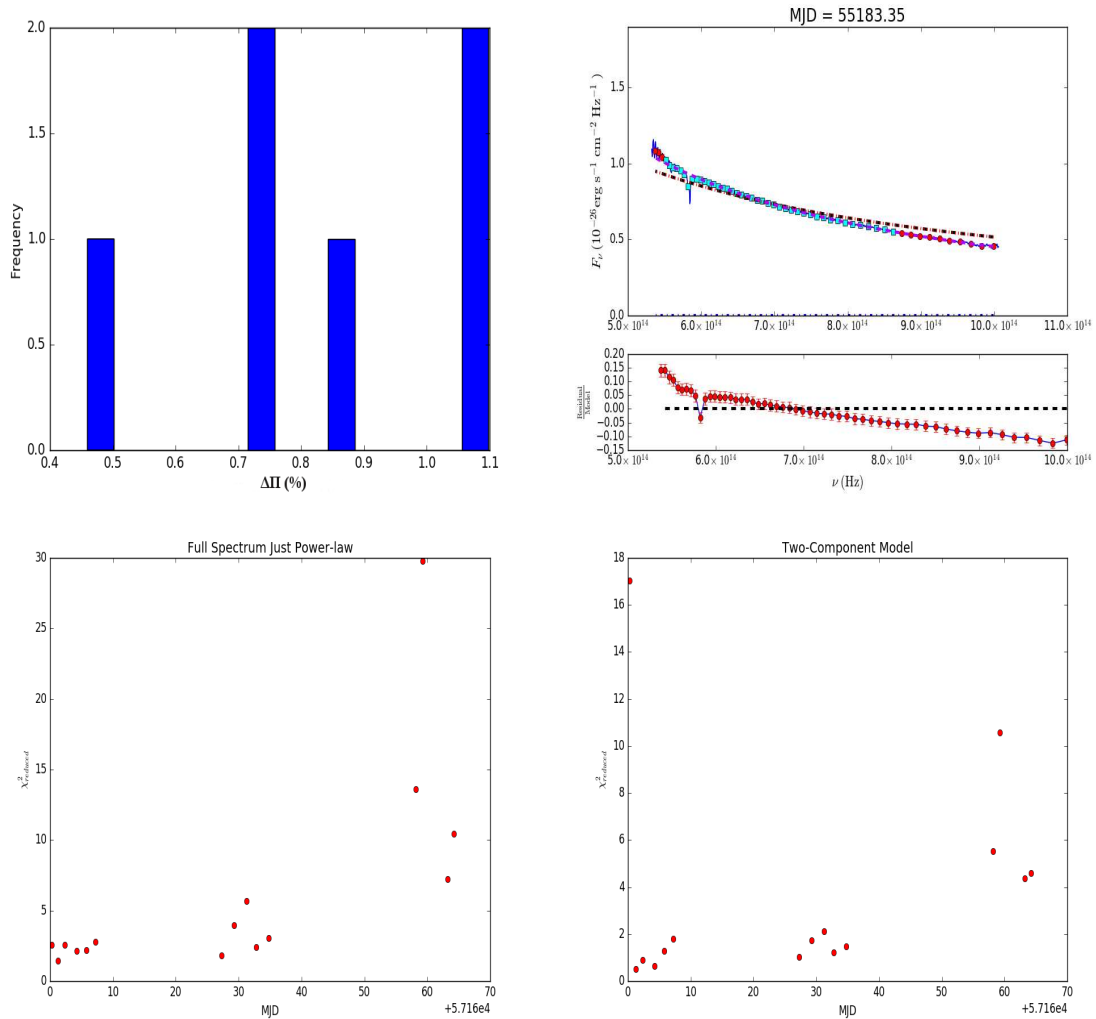


Fig. 4.32 *Top-Left*: Histogram of the wavelength dependent polarization of 0735+178. *Top-Right*: Typical fit to the spectrum. *Bottom-Left*: Reduced  $\chi^2$  from fitting a power-law independent of polarization. *Bottom-Right*: Reduced  $\chi^2$  from fitting a power-law with the same spectral index as the polarized-flux.

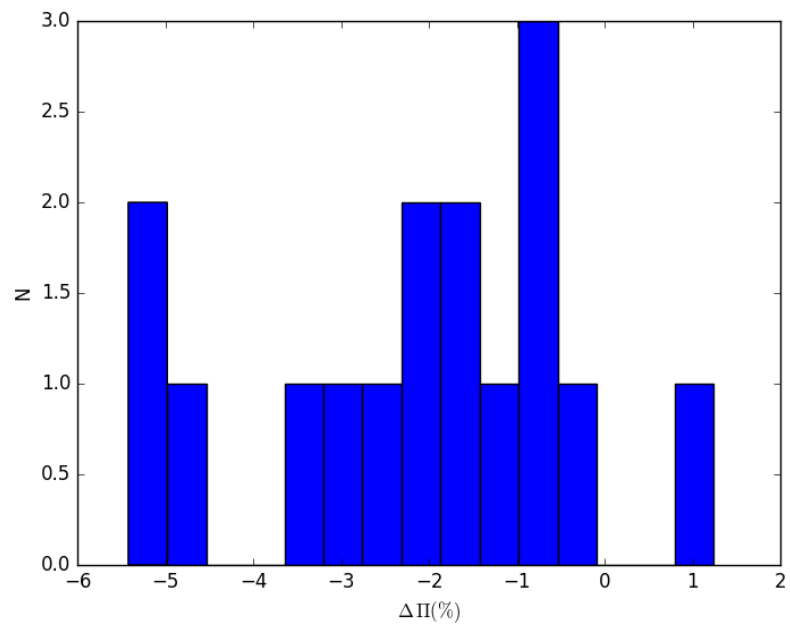


Fig. 4.33 As in Figure 4.28 for 0420-014.

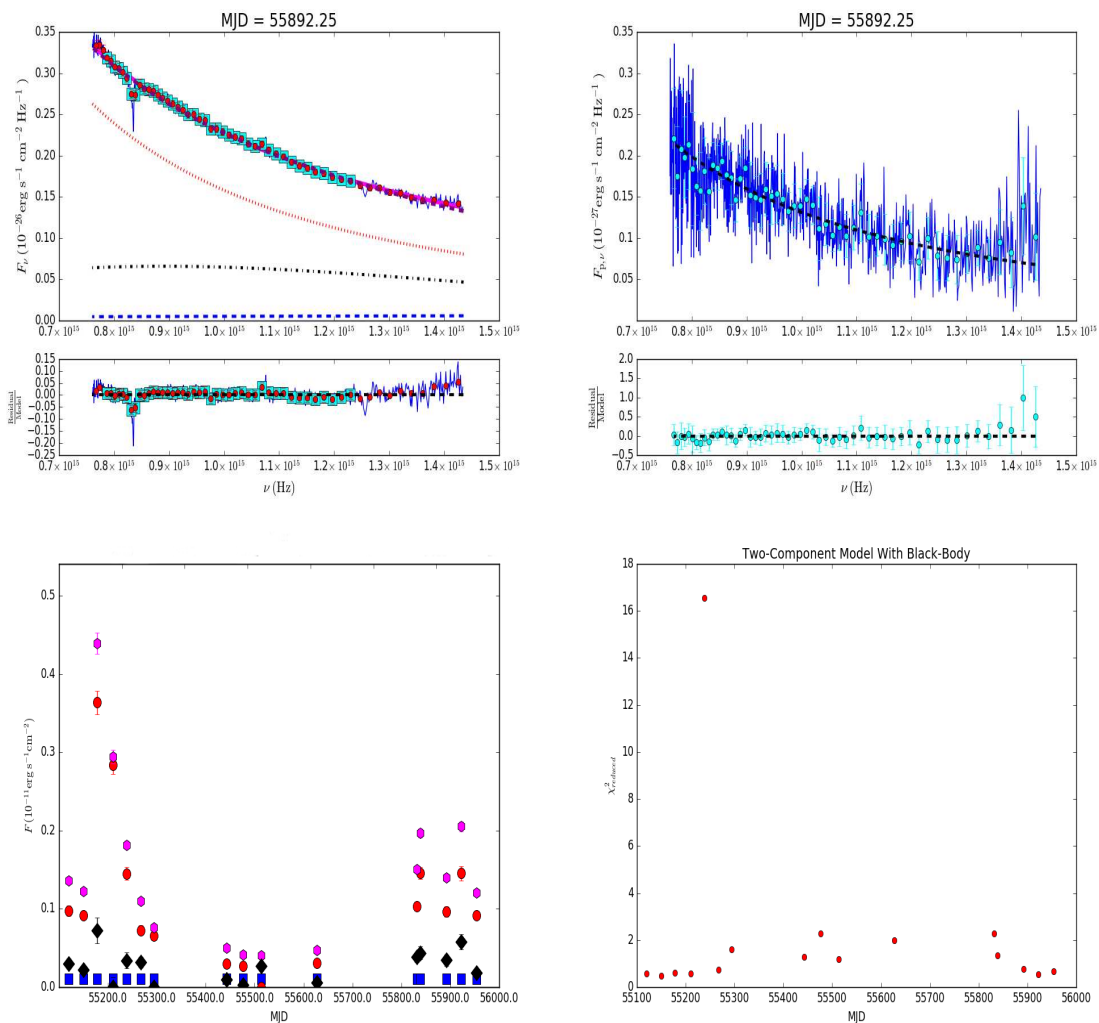


Fig. 4.34 *Top-Left*: Models fit to the spectrum of 0420-014. The synchrotron component is represented by the dotted- red line. The blackbody is represented by the black dot-dash line, while the constant thin-disk component is represented by the dashed blue line. The residual to the model is shown in the bottom panel. *Top-Right*: Fit to the polarized flux. *Bottom-Left*: The best fit spectral components for 0420-014. *Bottom-Right*: Reduced  $\chi^2$  of this model.

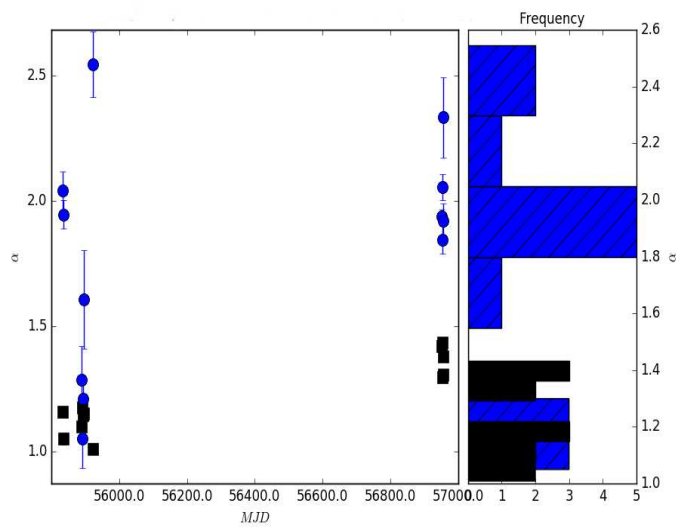
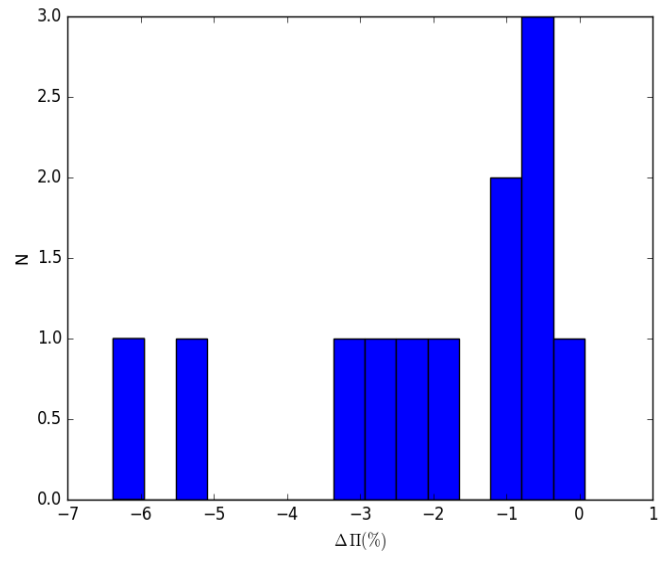


Fig. 4.35 As in Figure 4.28 for CTA26.

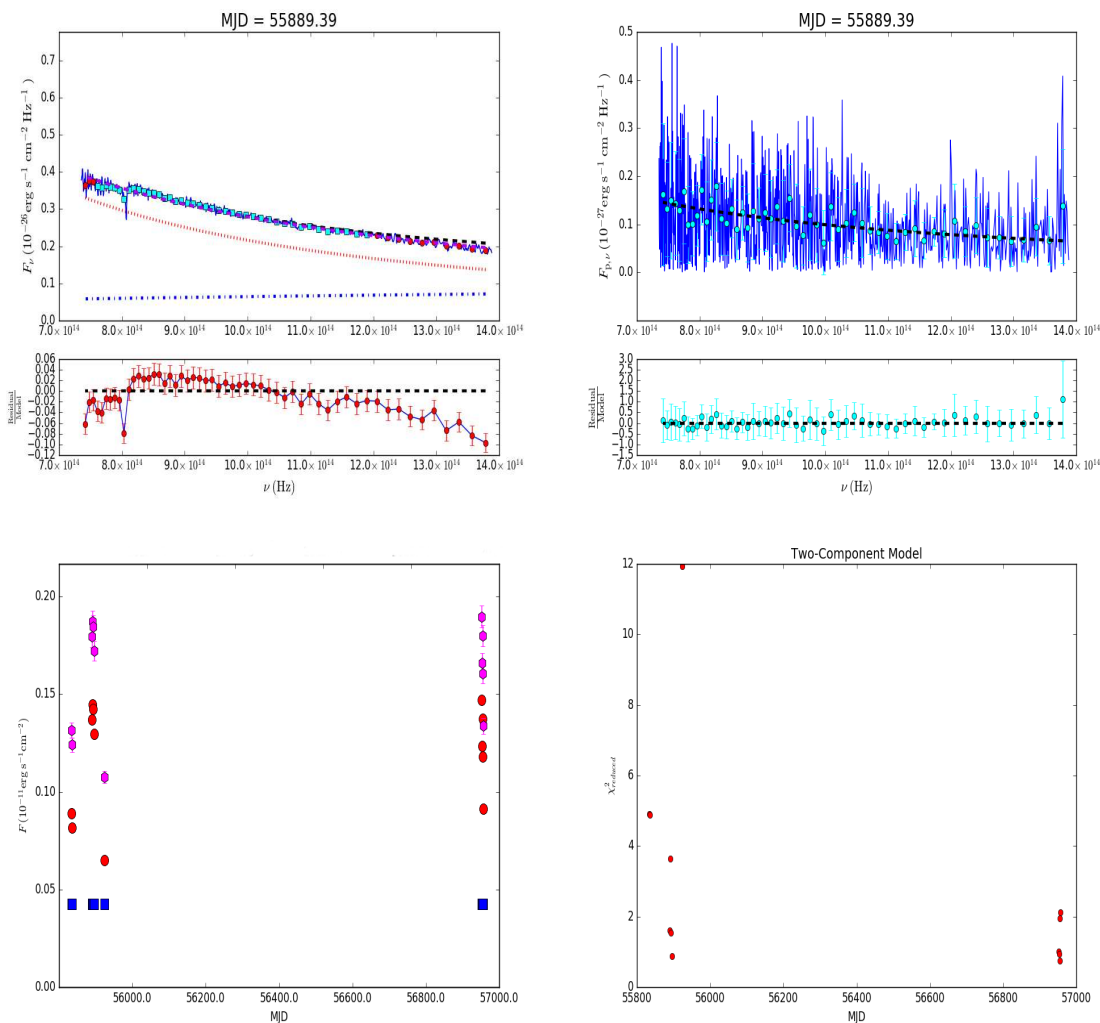


Fig. 4.36 *Top-Left*: Models fit to the Spectrum of 0420-014. The synchrotron component is represented by the dotted- red line. The blackbody is represented by the black dot-dash line, while the constant thin-disk component is represented by the dashed blue line. The residual to the model is shown in the bottom panel. *Top-Right*: Fit to the polarized flux. *Bottom-Left*: The best fit spectral components for 0420-014. *Bottom-Right*: Reduced  $\chi^2$  of this model.

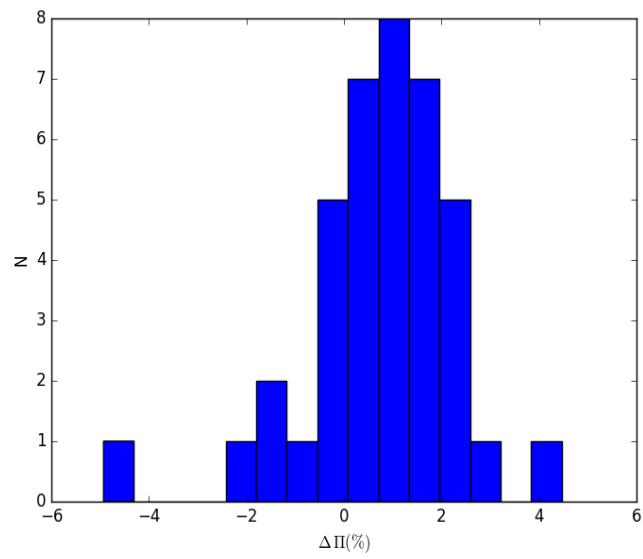


Fig. 4.37 As in Figure 4.28 for 3C279.

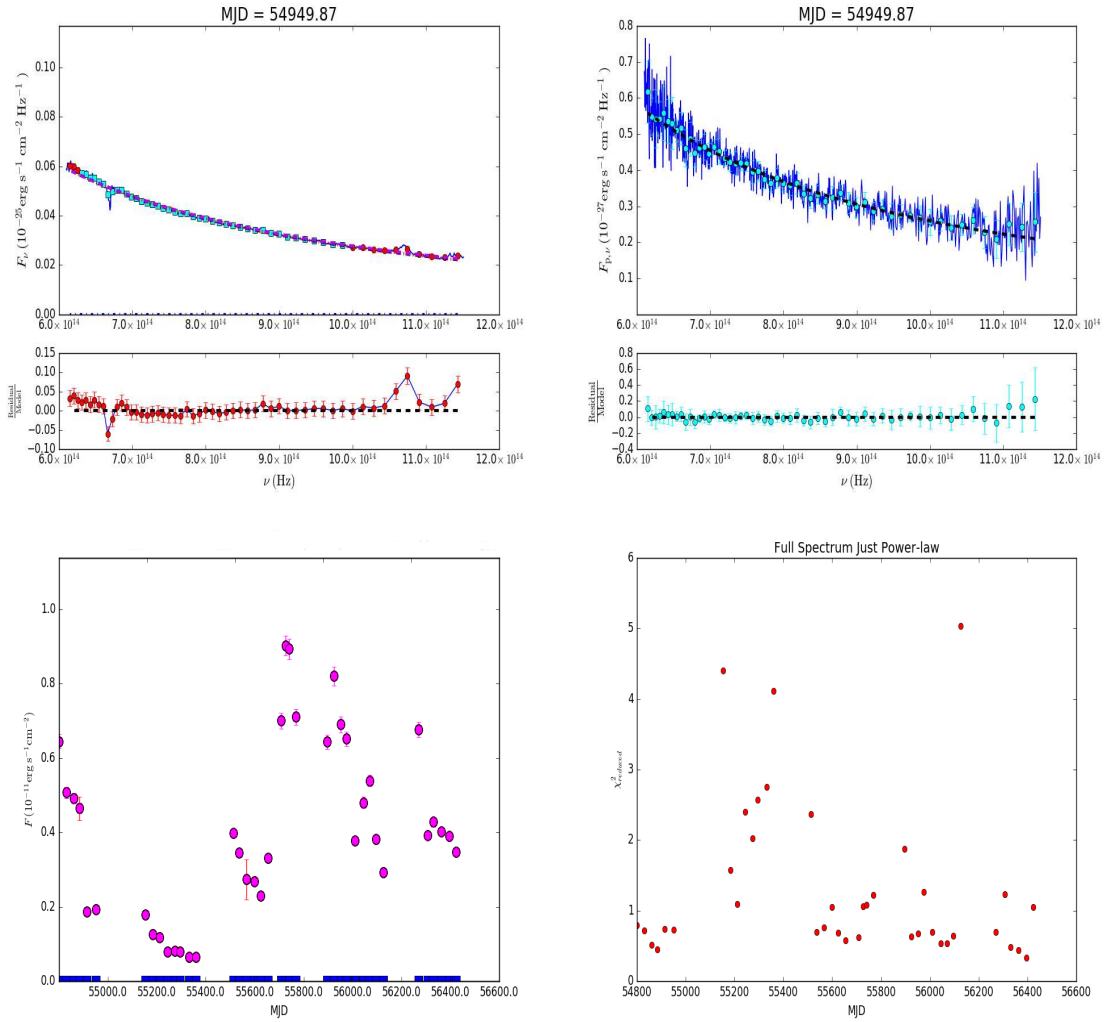


Fig. 4.38 Models fit to the spectra of 3C279 as in Figure 4.34.



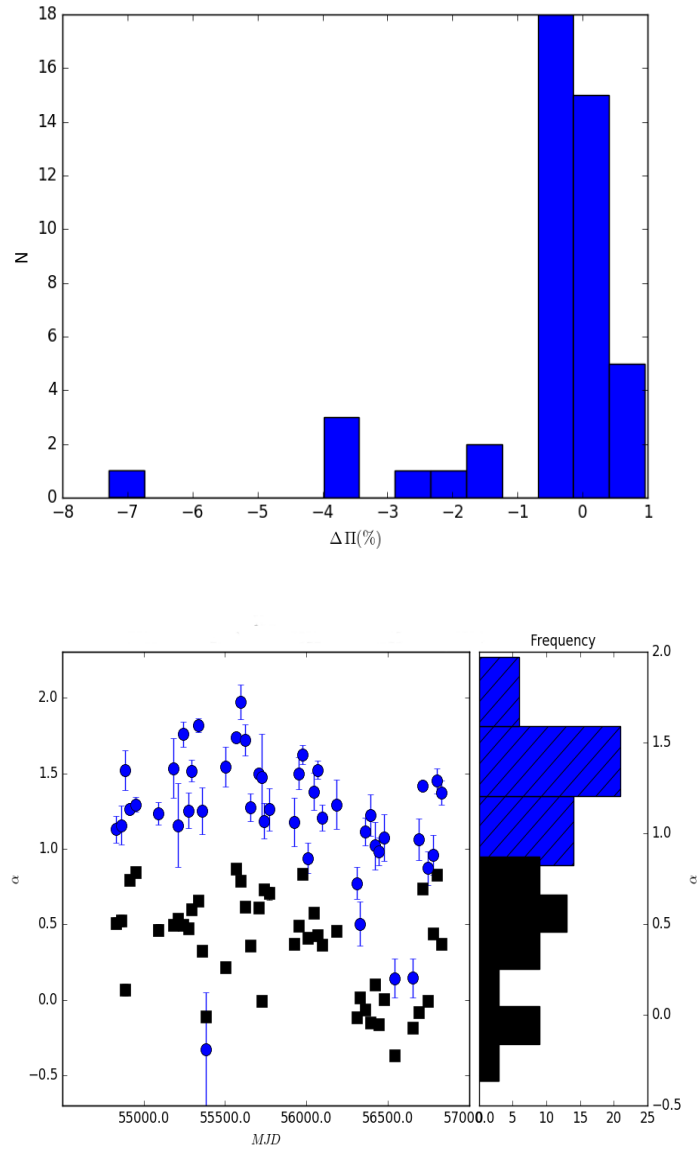


Fig. 4.39 As in Figure 4.28 for 1510-089.

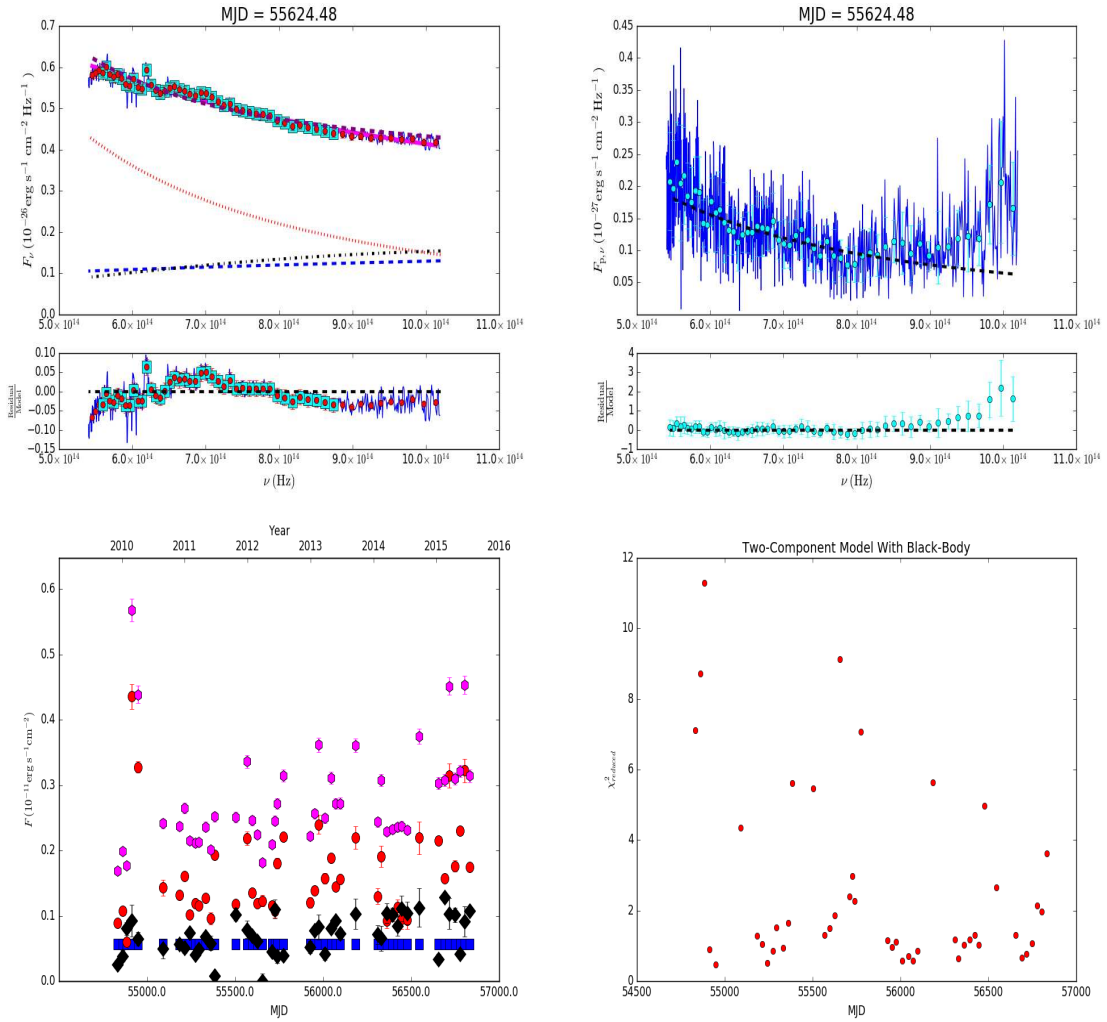


Fig. 4.40 Models fit to the spectrum of 1510-089 as in Figure 4.34.

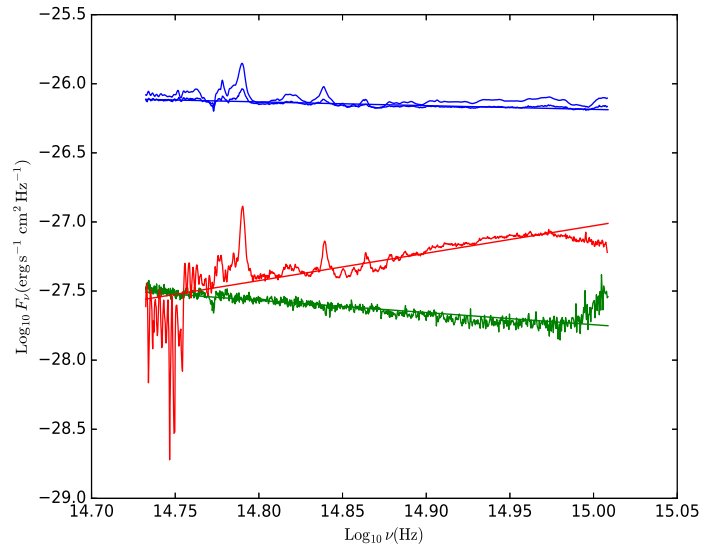


Fig. 4.41 As in Figure 4.19 for 1510-089. Unlike in 1222+216, the emission lines display some variability that is likely the cause of the variability of the non-polarized component of the optical flux in 1510-089 rather than variability in the accretion disk.

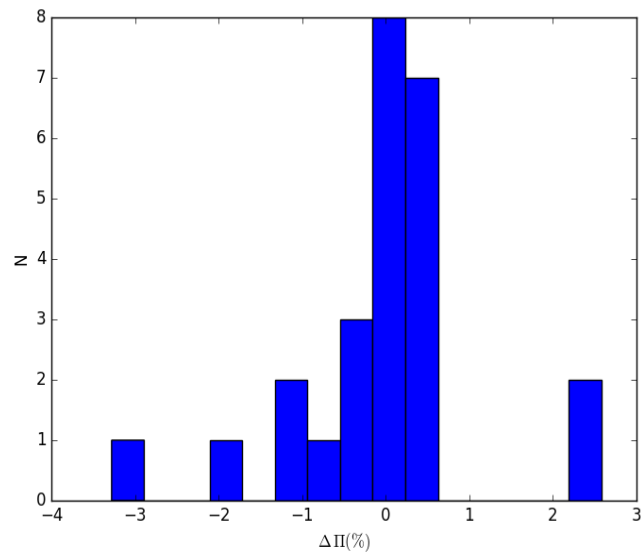


Fig. 4.42 As in Figure 4.37 for CTA102.

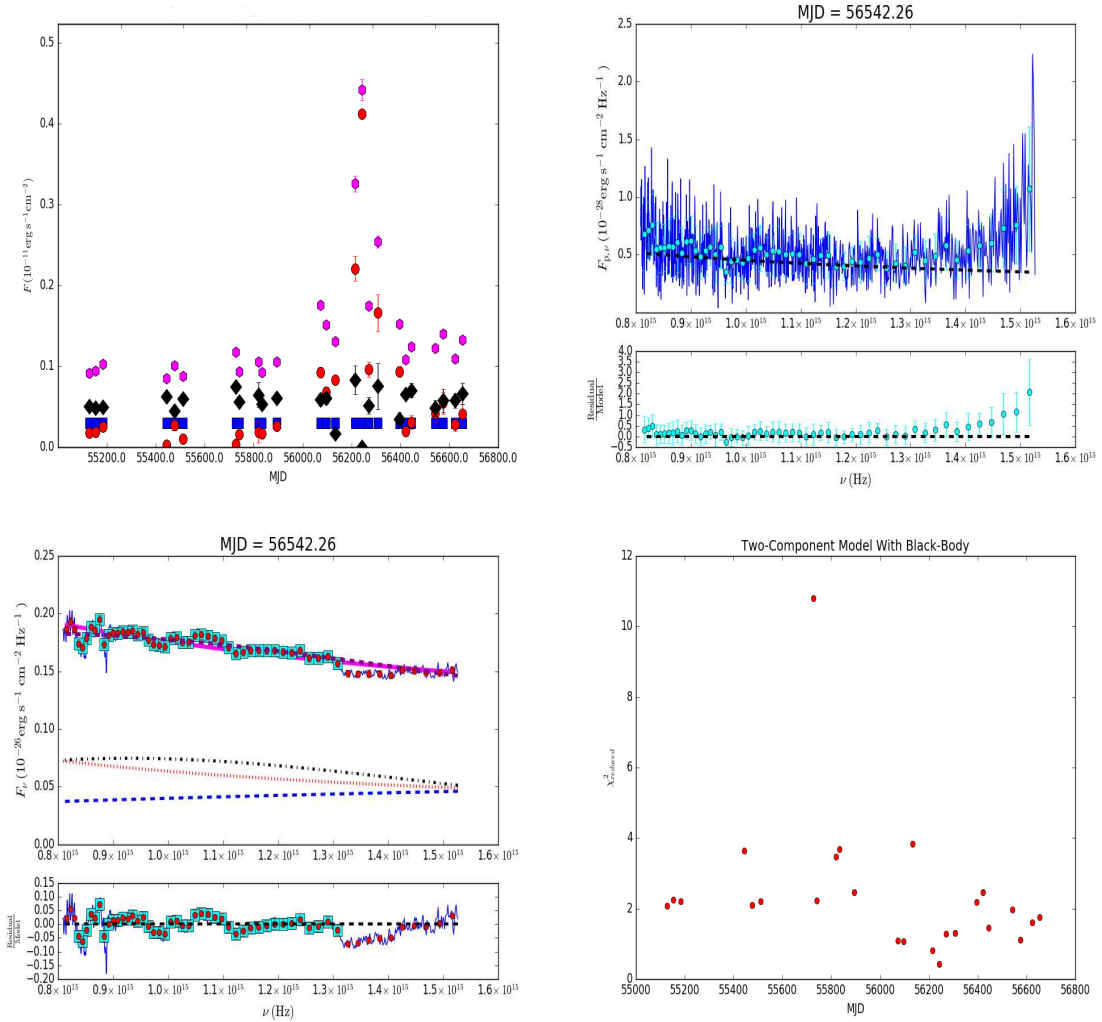


Fig. 4.43 As in Figure 4.34 for CTA102.

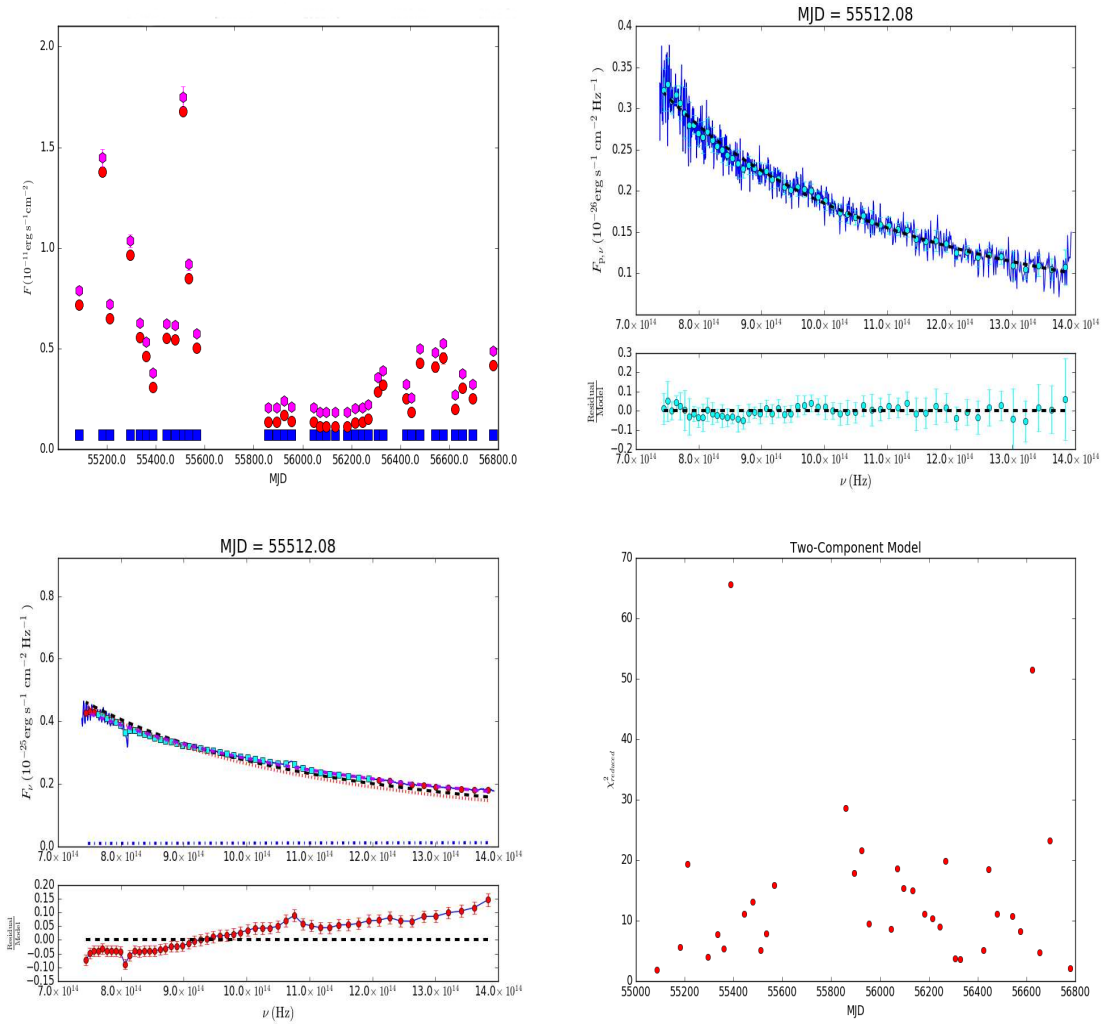


Fig. 4.44 As in Figure 4.34 for 3C454.3.

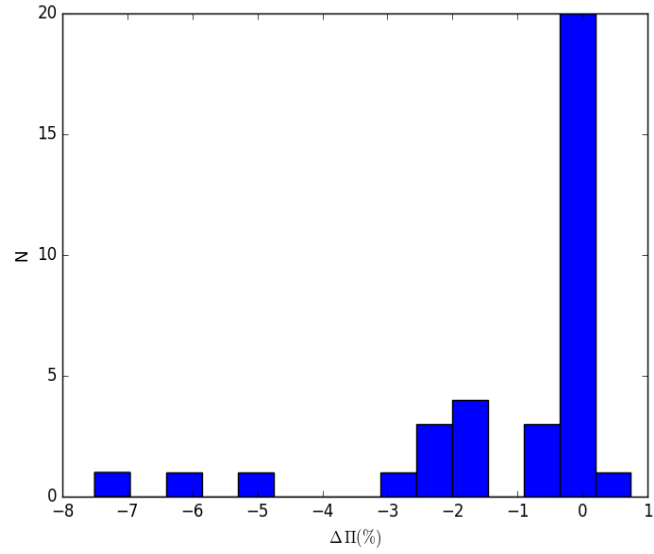


Fig. 4.45 As in Figure 4.28 for 3C454.3.

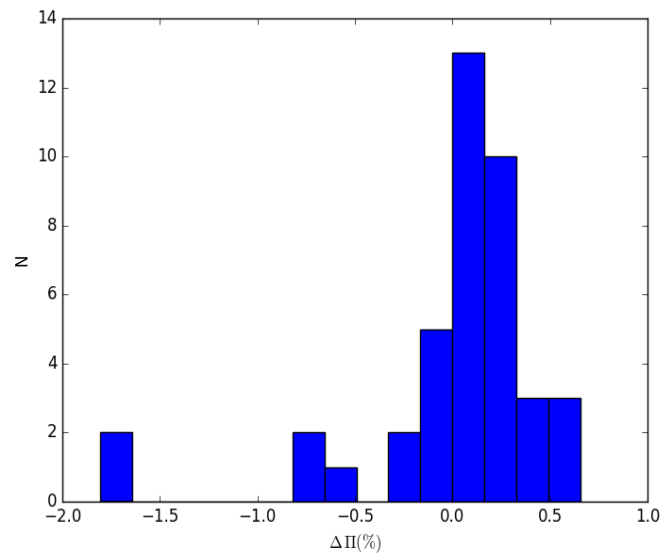


Fig. 4.46 As in Figure 4.28 for OJ248.

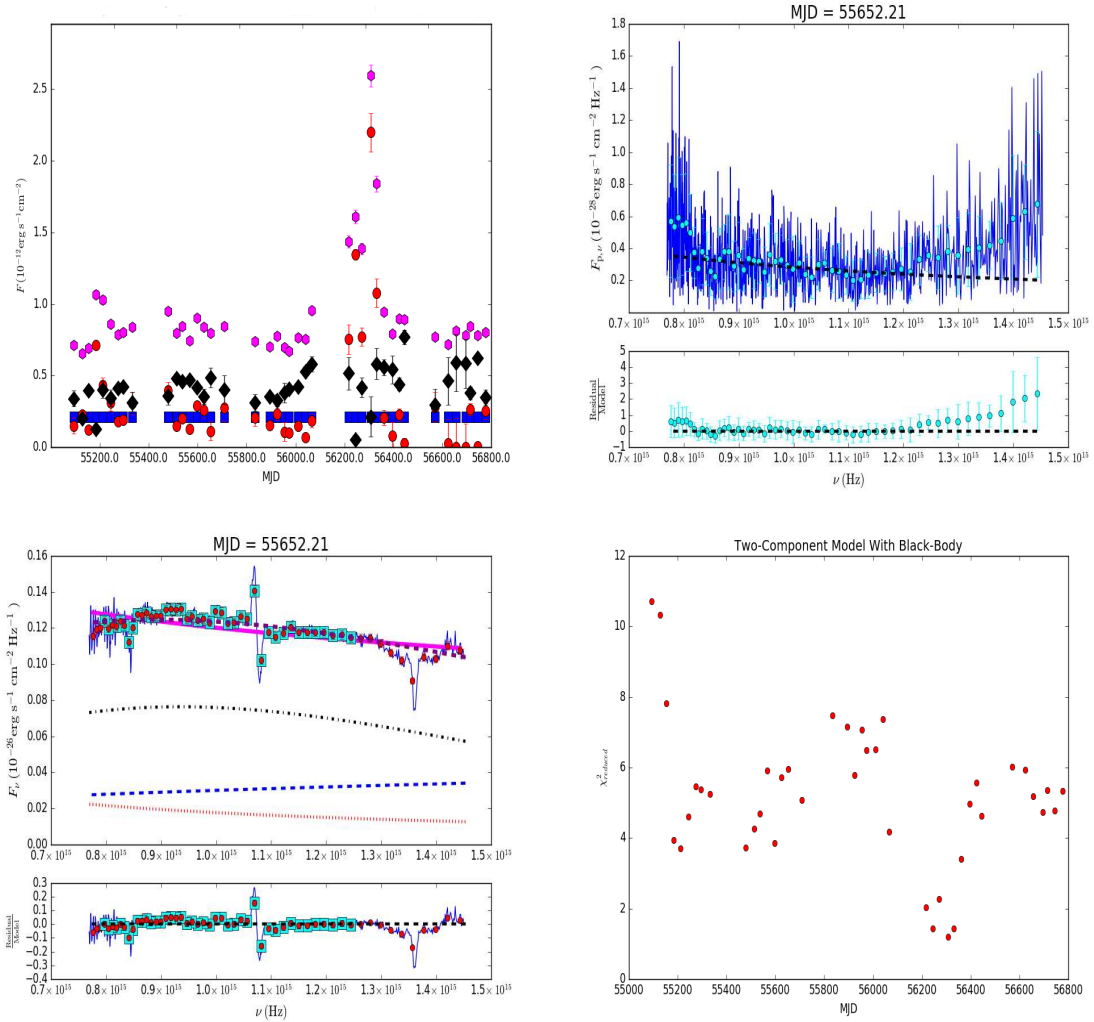


Fig. 4.47 As in Figure 4.34 for OJ248.

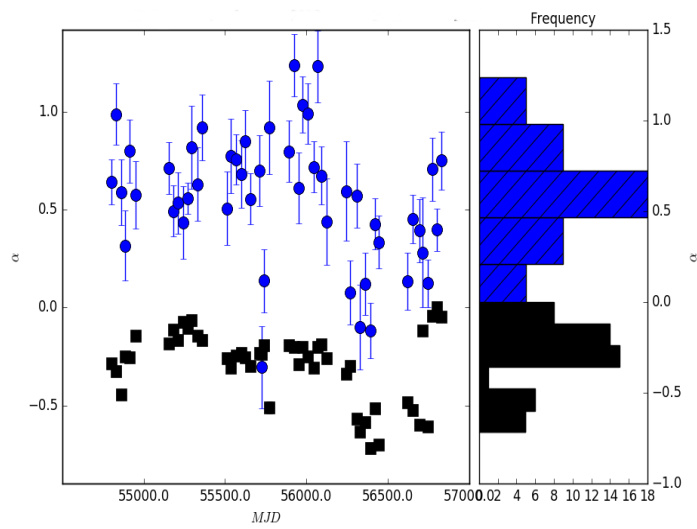
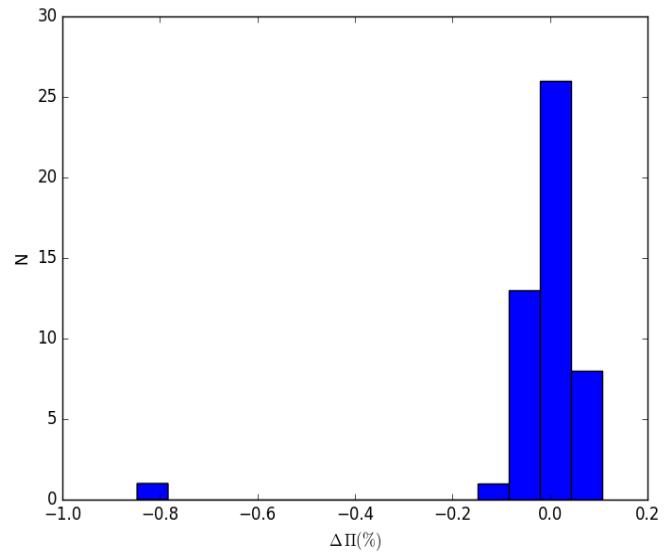


Fig. 4.48 As in Figure 4.28 for 3C273.



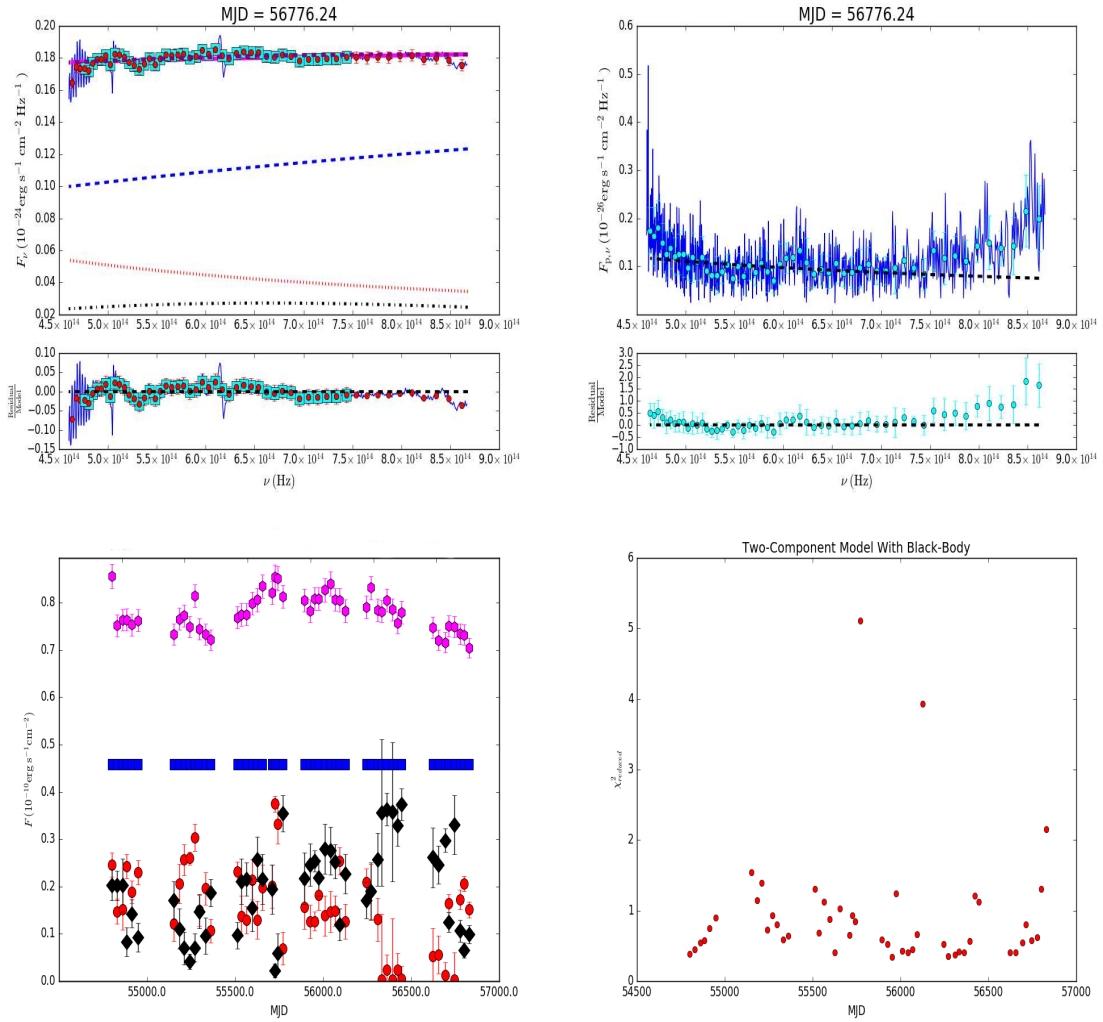


Fig. 4.49 As in Figure 4.34 for 3C273.

## Chapter 5

# Comparison of Optical Variability to Variability at Infrared Wavelengths

### 5.1 Infrared Variability of a Sample of Blazars

#### 5.1.1 Introduction

Commencing in March, 2011, I undertook a several-year campaign to 1) search for evidence of a dusty torus in the infrared (IR) emission of a larger sample of  $\gamma$ -ray bright blazars than was reported on in the Malmrose et al. (2011) sample, and 2) determine, if possible, the amount of variability in the dust luminosity over the course of several years. To accomplish these goals, I utilized the Perkins Telescope of Lowell Observatory, located on Anderson Mesa, near Flagstaff, AZ, and the National Aeronautics and Space Administration (NASA) Infrared Telescope Facility (IRTF), located on Mauna Kea, HI. Between 2011–2014, I performed photometric observations in the  $J$ ,  $H$ , and  $K_s$  bands using the Mimir instrument at the Flagstaff facility, and the guider of the SpeX (Rayner et al., 2003) instrument at the Hawaii facility.

In order to determine the synchrotron contribution to the spectral energy distribution (SED) at IR wavelengths, I also performed  $H$ , and  $K_s$  polarization observations with Mimir (Clemens et al., 2007). Because the dust torus emits thermally, its emission ought to be non-polarized. The spectral index of the synchrotron emission in the

IR,  $\alpha_{IR}$ , can potentially be obtained with accurate polarization measurements in the  $H$ , and  $K_s$  bands. Comparing  $\alpha_{ir}$  to the shape of the total IR flux, in a manner similar to the analysis performed on the optical spectra in the previous chapter, would help determine any IR-excess to the synchrotron radiation that might be present. However, due to the faintness of the sources in the sample, and non-ideal sky conditions during the observations, I was only able to reliably acquire photometric observations.

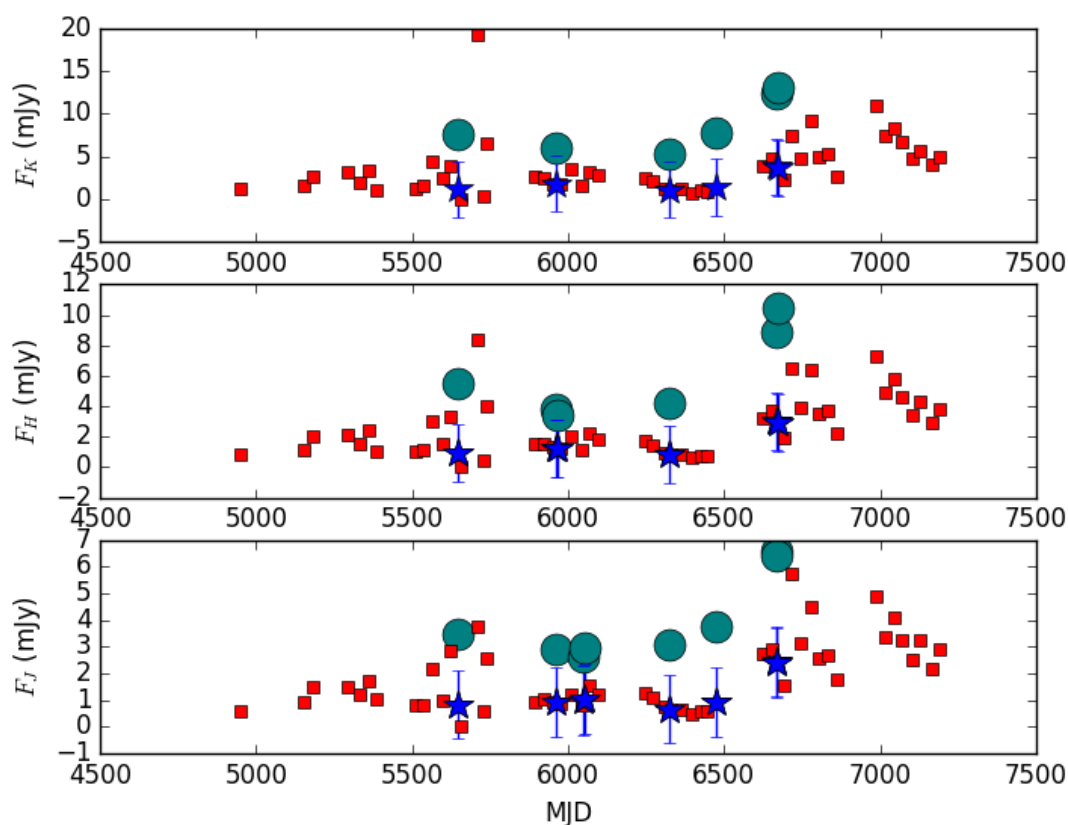


Fig. 5.1 The projected synchrotron flux values from the Steward Observatory spectra of 1222+216 (red squares) in the  $K_s$  (top),  $H$  (middle), and  $J$  (bottom), near-IR bands along with the measured values (green circles). The interpolated values of the flux used to determine the IR excess are also shown (blue stars). The  $1-\sigma$  uncertainty bars of the interpolated flux values were taken to be the standard deviation of the projected synchrotron flux values.

Utilizing the Steward Observatory spectra reported on in the previous chapter, it is still possible to search the IR emission for tentative evidence of emission from the dusty torus. To do so, I use the spectral indices and normalization values for the synchrotron component in the optical spectra, derived from the spectropolarimetric observations, in order to determine the synchrotron emission in the near-IR. I then perform synthetic photometry on the projected synchrotron spectrum, by convolving the projected spectrum,  $F_{\lambda,proj}$ , with the Mimir instrument response curves,  $R_{\lambda}$ , following the prescription:

$$F_{J,H,K_s} = \frac{\int F_{\lambda,proj} R_{\lambda} \lambda d\lambda}{\int R_{\lambda} \lambda d\lambda}. \quad (5.1)$$

I then compare these projected fluxes with ones that I measured. It should be noted that the epochs of the Steward Observatory observations do not always coincide with the epochs of the Lowell Observatory and IRTF observations, therefore some interpolation of flux values was required in order to determine the IR excess.

Because 1222+216 was one of the two blazars for which the thermal emission from hot dust was observed, it is perhaps instructive to first look at how its IR flux has changed since the 2007–2008 *Spitzer* observations. Figure 5.1 displays the measured IR flux in  $J$ ,  $H$ , and  $K_s$  bands from both Mimir and the IRTF along with the projected flux values of the fit synchrotron component to the Steward Observatory spectra. The projected and interpolated flux values were then subtracted from the observed flux in order to determine the IR-excess. From Figure 5.2 an IR-excess in the  $K_s$  band is apparent in 1222+216, with an average value of  $6 \pm 1$  mJy. There is a smaller observed IR-excess in the  $H$  and  $J$ -band flux as well. Flux in excess of the synchrotron emission in 1222+216 was expected, as the sublimation temperature

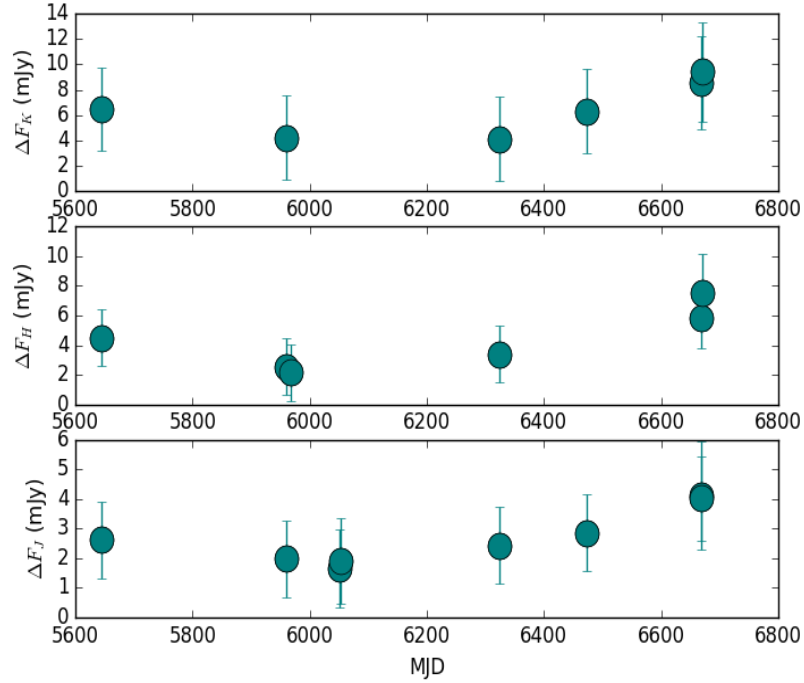


Fig. 5.2 The IR excess flux of 1222+216 obtained by subtracting the projected and interpolated flux values from Figure 5.1 from the measured values.

of silicate-based dust is approximately 1300 K, while it is 1800 K for graphite-based dust.

The wavelength of maximum emission for a blackbody with temperature  $T$  in Kelvin is  $\lambda_{max} = \frac{2.8 \times 10^{-3}}{T}$  m. For blackbodies at these two temperatures, the wavelength of maximum emission is  $2.2 \mu\text{m}$ , and  $1.6 \mu\text{m}$  respectively. The effective rest-wavelength of the  $K_s$  band after accounting for redshift is  $1.5 \mu\text{m}$ . For sources with redshifts similar to 1222+216, the hottest dust will be visible in the  $K_s$  band, while due to the exponential decline in thermal emission at  $H$ , and  $J$ , thermal emission from hot dust will be declining at those wavelengths. The apparent  $\nu F_\nu \times 4\pi d_L^2$  luminosity of the  $K_s$  band excess in 1222+216 is  $1.0 \pm 0.2 \times 10^{46} \text{ erg s}^{-1}$ , which is similar to the dust luminosity obtained in Malmrose et al. (2011). Figure 5.3 shows

the SED of the average near-IR flux values obtained for 1222+216, along with the SED of a 1200 K and 1800 K blackbody.

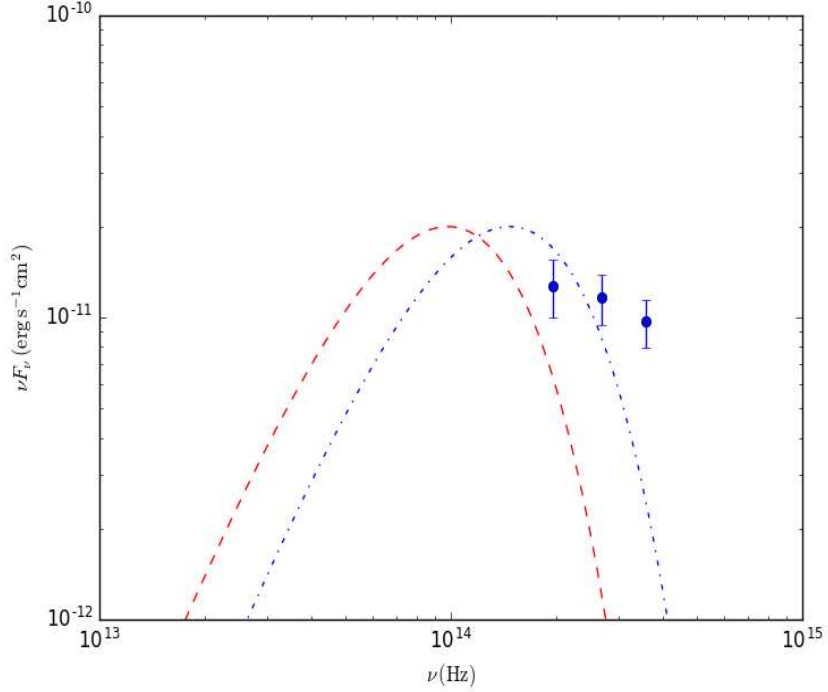


Fig. 5.3 The average IR excess obtained by subtracting the projected and interpolated flux values from Figure 5.1 from the measured values. Also shown are arbitrarily scaled SEDs of a  $T = 1200$  K blackbody (red dashed line) and a  $T = 1800$  K blackbody (blue dot-dashed line).

I define a near-IR variable flux parameter,

$$\Delta F = \frac{\sigma_{F_{excess}}}{F}, \quad (5.2)$$

where  $\sigma_{F_{excess}}$  is the standard deviation of the IR excess, in order to compare the observed variability of the excess in all three bands to the uncertainty of the measurements. For 1222+216, the value of  $\Delta F$  is 0.2, 0.2, and 0.1 for the  $J$ ,  $H$ , and  $K_s$  bands respectively. Unfortunately, it is therefore uncertain whether the dust

luminosity has changed since the *Spitzer* observations of the blazar were made in 2007–2008.

### 5.1.2 Near Infrared Variability of Other Blazars

Table 5.1 contains a list of sources for which the above analysis was performed, while a brief description of the results for each source follows.

#### 1219+285

1219+285 was another one of the objects included in the *Spitzer* study. No concrete evidence of an infrared excess was found for this source, and I derived a maximum dust luminosity of  $6 \times 10^{43}$  erg s<sup>-1</sup>. Because the optical polarization in this object has some wavelength dependence, I estimate the synchrotron flux in the near-IR by projecting the power-law fit to the total optical spectrum into the near-IR rather than the power-law fit to the polarized flux. Doing so leads to results similar to that of the *Spitzer* study. The measured and projected flux values display little evidence for an excess (Figure 5.4), while the IR SED, after removal of the synchrotron flux, looks quite similar to the SEDs of the source from 2007–2008 (Figure 5.5). Taking the upper-limit *K*-flux value from the SED results in an upper limit flux of  $1 \times 10^{44}$  erg s<sup>-1</sup>, while taking the average value results in a  $5 \times 10^{43}$  erg s<sup>-1</sup> excess. The second value is in agreement with the value quoted in the *Spitzer* study for the maximum dust luminosity of 1219+285.

#### 3C66A

3C66A presents an interesting case. The optical polarization slightly decreases in value toward higher frequencies, which could indicate a big blue bump (BBB) component. However, the spectra are well-fit by a synchrotron-only model. In order to determine if there is an excess in flux in the near-IR, I project the single component

Table 5.1. Near-IR Excess Flux in Selected Blazars

Source Name	$\bar{J}$ (mJy)	$\Delta J$	$\frac{\sigma J}{J}$	$\bar{H}$ (mJy)	$\Delta H$	$\frac{\sigma H}{H}$	$\bar{K}$ (mJy)	$\Delta K$	$\frac{\sigma K}{K}$	$\nu L_{\nu, K}$ ( $10^{45} \text{erg s}^{-1}$ )
3C66A	6.7	0.31	0.55	11.1	0.52	0.38	10.2	0.24	0.57	$10 \pm 5$
CTA26	-	-	-	-	-	-	-	-	-	-
0420-014	-	-	-	-	-	-	-	-	-	-
OJ248	3.19	1.26	0.26	2.11	0.79	0.17	3.10	0.8	0.43	$21 \pm 9$
1219+285	1.8	0.42	0.98	1.5	1.3	1.5	1.8	1.8	1.7	$< 0.1$
1222+216	3.3	0.25	0.42	5.0	0.35	0.37	7.3	0.26	0.37	$10 \pm 3$
3C273	31	0.31	0.11	44	0.20	0.11	86	0.37	0.09	$9.3 \pm 0.8$
3C279	4.9	0.1	0.3	7.4	0.1	0.3	12.2	0.2	0.3	$4 \pm 1 \times 10^1$
1510-089	1.7	0.19	0.32	2.5	0.51	0.38	4.4	0.22	0.32	$3 \pm 1$
BL Lac	10.7	1.4	1.2		15.0	1.2	1.3	17.0	1.6	$2.0 < 0.5$
CTA102	1.2	0.48	0.57	1.7	0.32	0.71	0.65	2.1	4.5	$< 30$
3C454.3	3.1	0.65	0.75	5.9	0.33	0.78	8.1	0.02	1.3	$< 90$



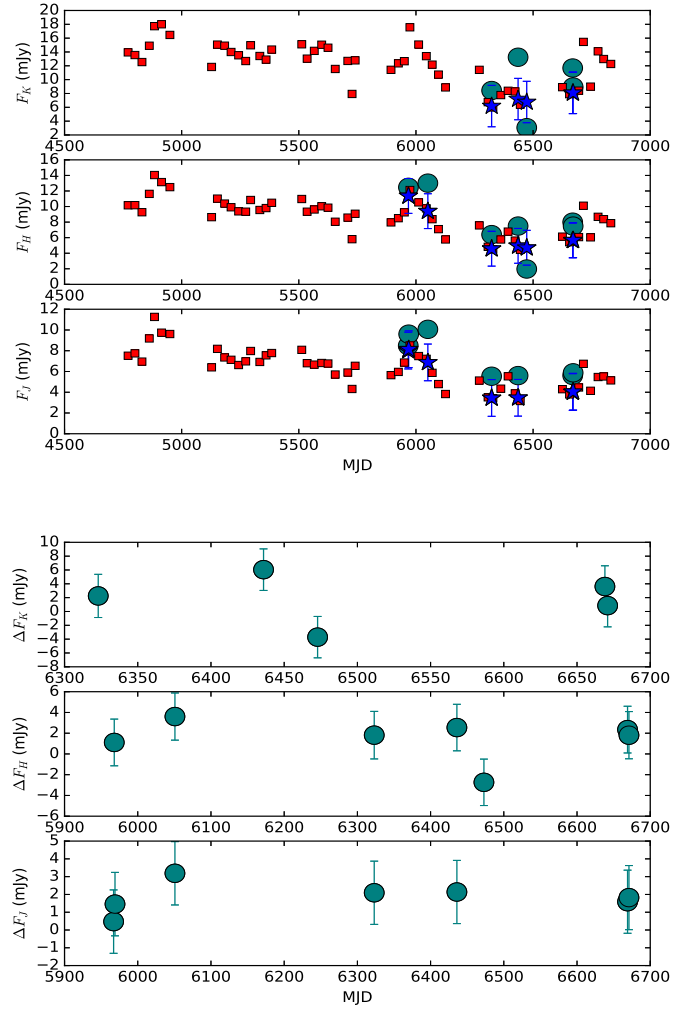


Fig. 5.4 *Top panel*: The projected synchrotron flux values from the Steward Observatory spectra of 1219+285. Symbols and colors are as in Figure 5.1. *Bottom*: Same as in Figure 5.2 for 1219+285.

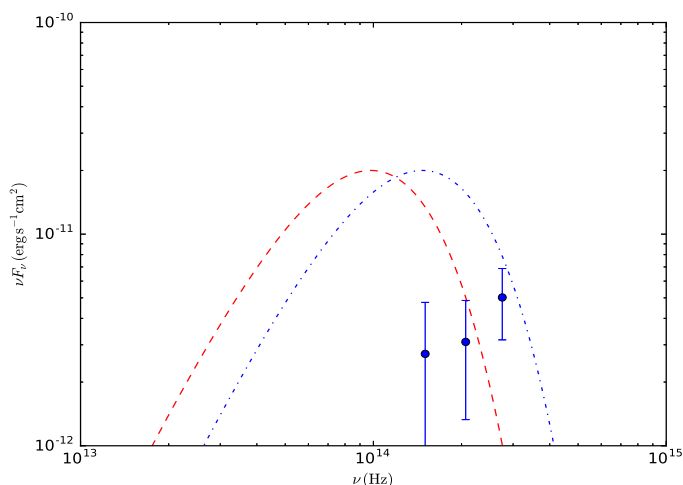


Fig. 5.5 As in Figure 5.3 for 1219+285. The  $K$ -band upper limit indicates a maximum dust luminosity for this BL Lac similar to that calculated in the *Spitzer* study.

power-law fit to the optical spectral into the NIR. Interestingly, the optical flux of 3C66A decreased to a low-state during the approximately 3 year period I observed it in the IR. While 3C66A was in this low-state, the measured IR flux shows an excess over the projected flux values (Figure 5.6). The average excess SED (Figure 5.7), meanwhile suggests that the average  $J$ ,  $H$ , and  $K_s$  excess can be fit with a blackbody at  $T = 3200$  K. This temperature is well beyond the sublimation temperature of dust, so it is unlikely that the IR excess in 3C66A is directly from a dusty torus. This excess to the projected synchrotron emission could result from a second synchrotron component in the IR, perhaps due to a moving knot of plasma, in which the highest energy electrons have cooled, thus, resulting in decreasing synchrotron flux toward the optical. Any variability of the excess cannot be confirmed, as variability in  $H$ -band is the strongest, and only a factor of 1.4 above  $\sigma_H$ .

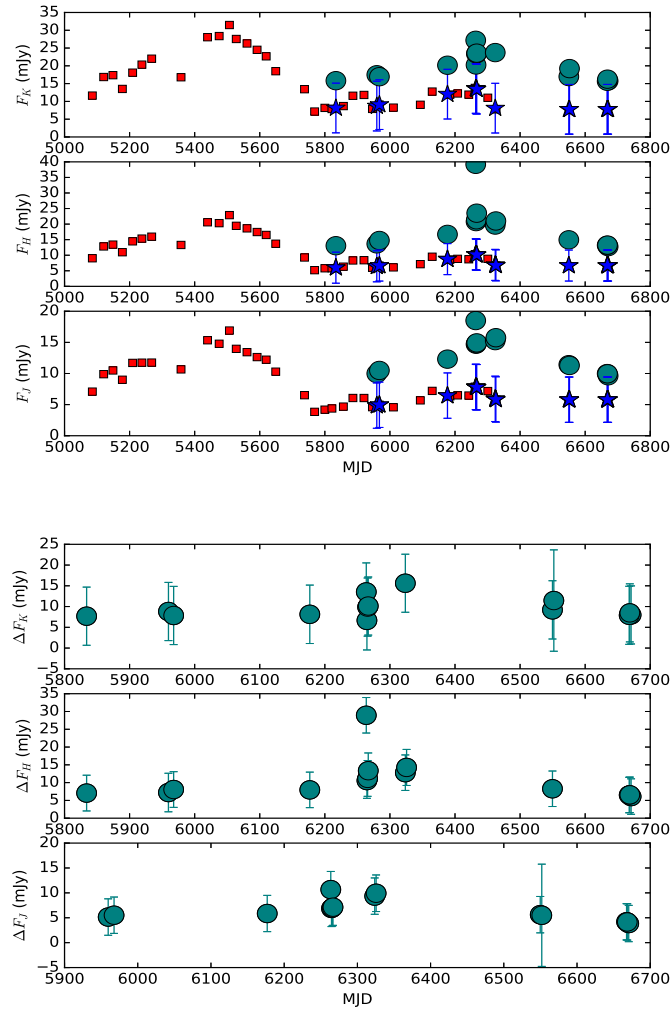


Fig. 5.6 *Top panel:* The projected synchrotron flux values from the Steward Observatory spectra of 3C66A. Symbols and colors are as in Figure 5.1. *Bottom:* Same as in Figure 5.2 for 3C66A.

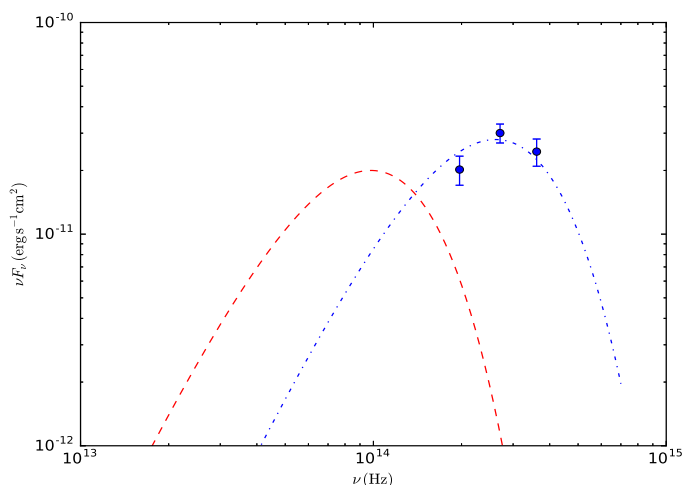


Fig. 5.7 As in Figure 5.3 but with the blue dot-dash line representing a  $T = 3200\text{K}$  blackbody fit to the IR excess of 3C66A.

### BL Lac

As in the previous chapter, I remove the host galaxy flux from the IR measurements of BL Lac using the values contained in Williamson et al. (2014). The eponymous BL Lac type object does not show much in way of a near-IR excess, in fact it shows a deficiency at  $K$ -band for some of the observations (Figure 5.8), however there is a slight excess in later observations. This indicates that a dust torus is not a significant component to the near-IR emission and that the excess likely arises from a second synchrotron component. From the average excess SED (Figure 5.9), a  $T = 1800\text{K}$  blackbody could be fit to the  $K$ -band excess flux. The dust luminosity can be constrained to  $L_{dust} < 5 \times 10^{44} \text{ erg s}^{-1}$ .

### 3C273

3C273 is a blazar for which the silicate feature of the dusty torus has been previously measured (see, e.g., Hao et al., 2005). Variability in the BBB has also been observed in Paltani et al. (1998), as well as in this work. The infrared measurements

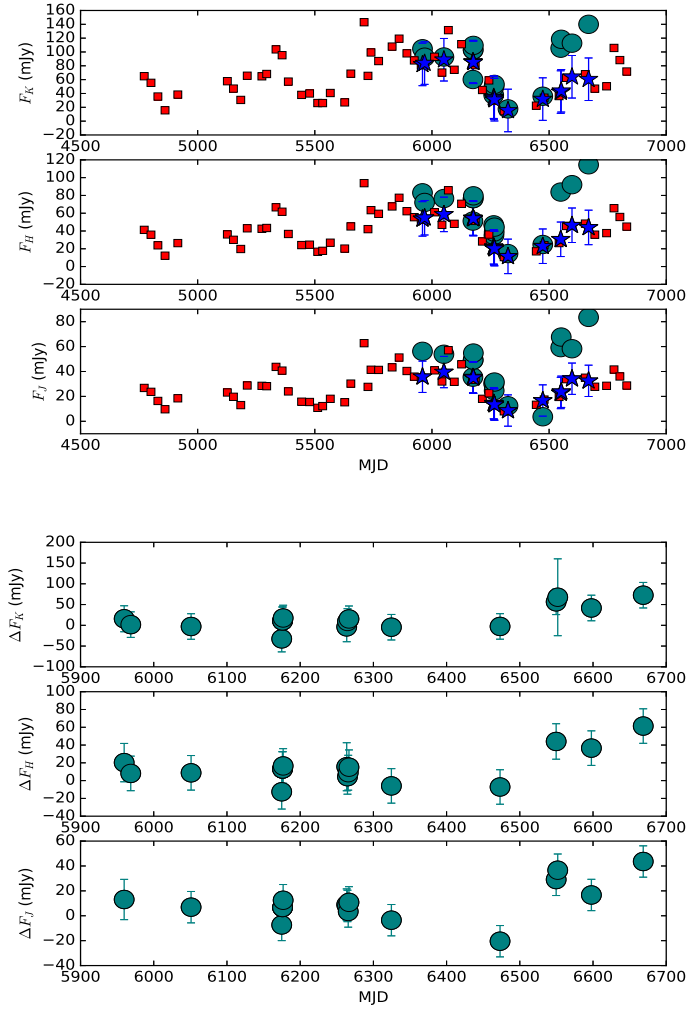


Fig. 5.8 *Top panel:* The projected synchrotron flux values from the Steward Observatory spectra of BL Lac. Symbols and colors are the same as in Figure 5.1. *Bottom:* NIR excess of BL Lac depicted as in Figure 5.2.

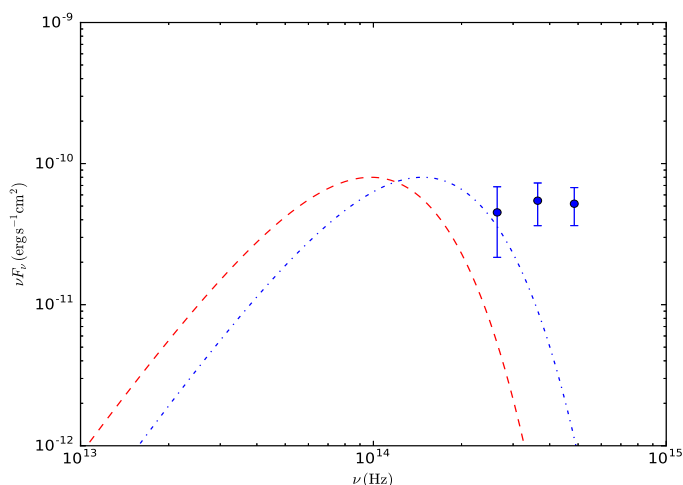


Fig. 5.9 IR excess SED of BL Lac. Same as in Figure 5.3.

(Figure 5.10) of 3C273 reveal a significant, sustained excess to the flux extrapolated from the synchrotron component in the optical. The  $\nu \times F_\nu$  luminosity at  $K_s$ -band results in an average IR excess luminosity of  $L = 9.3 \pm 0.8 \times 10^{45} \text{ erg s}^{-1}$ . The average  $H$  and  $K_s$ -band infrared excess can be fit by a  $T = 1800 \text{ K}$  blackbody (Figure 5.11). 3C273 is also one of the few sources analyzed in this work where variability in the IR excess is measured with high statistical significance; with the IR excess varying at the level of  $4\sigma$  in the  $K_s$  band over the duration of this study.

### 1510-089

Revisiting another source analyzed in the *Spitzer* study, the upper limit of dust emission in the 2007–2008 observations was found to be  $L_{dust} < 2.3 \times 10^{45} \text{ erg s}^{-1}$ . In this work, that value is adjusted upwards slightly to  $3 \pm 1 \times 10^{45} \text{ erg s}^{-1}$ . As with most of the other blazars in the sample, variability of the IR excess cannot be confirmed. The measurements of the near-IR excess and the average excess SED are displayed in Figure 5.12.

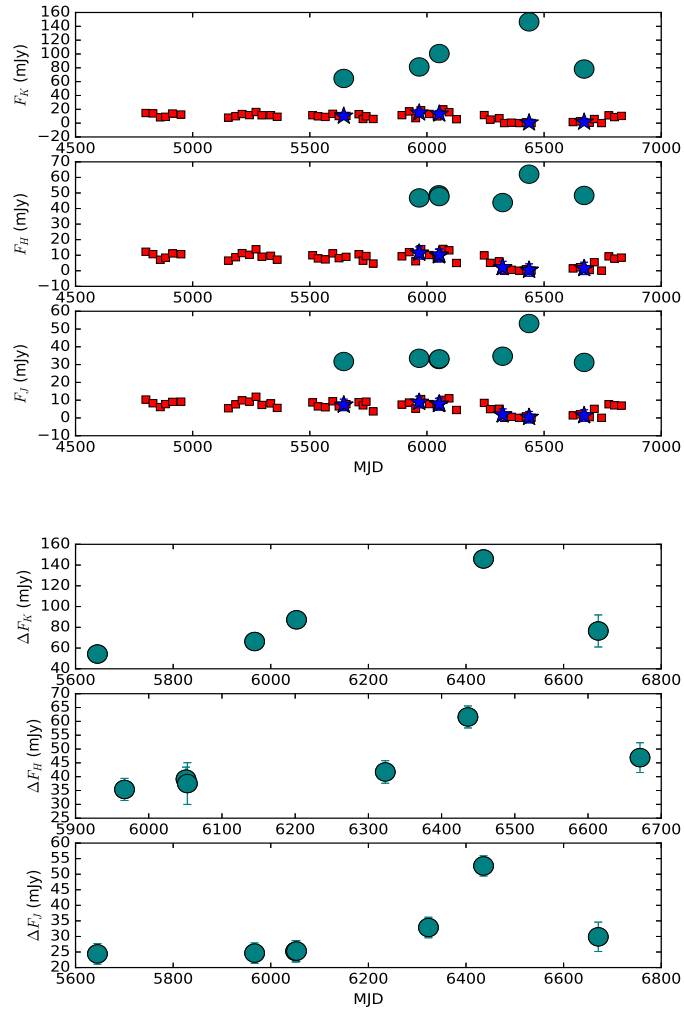


Fig. 5.10 *Top panel*: The projected synchrotron flux values from the Steward Observatory spectra of 3C273. Symbols and colors are as in Figure 5.1. *Bottom*: Same as in Figure 5.2 for 3C273.

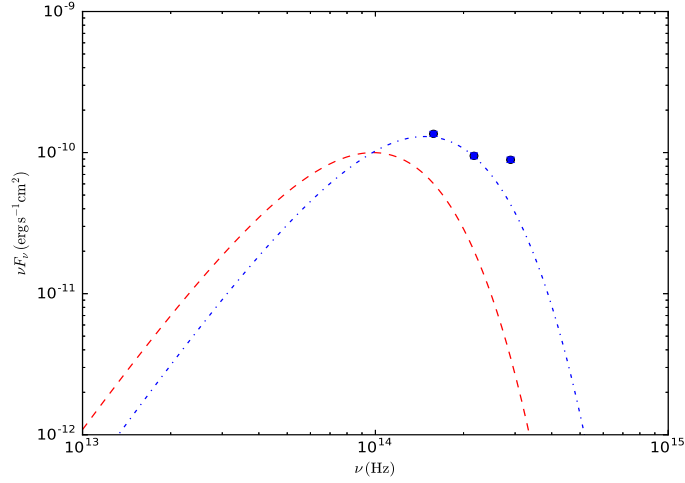


Fig. 5.11 As in Figure 5.3 for 3C273. An 1800 K blackbody can be fit to the average  $H$  and  $K_s$  IR excess.

### CTA102

For the final source that was also observed with *Spitzer* I reported a dust luminosity of  $7 \pm 2 \times 10^{45} \text{erg s}^{-1}$ . At a redshift of  $z = 1.037$  a strong signal from the dust emission in the near-IR flux was not expected. I find an upper-limit to the near-IR excess of  $L < 3 \times 10^{46} \text{ergs}^{-1}$  from CTA102, which is similar to the flux from the dusty torus in the *Spitzer* survey. As with many of the other blazars in the sample, variability of the non-synchrotron IR component cannot be confirmed or ruled out. A high temperature blackbody could be fit to the IR excess, as with 3C66A, however, such emission would be from a structure too hot to be the dust torus. A second synchrotron component is a more likely explanation for the excess emission.

### 3C454.3

The Mimir observations of 3C454.3 indicate a weak IR excess in the  $K_s$ -band, while the excess is more prominent in the  $H$  and  $J$  bands. The exponentially declining tail of the emission from an 1800 K blackbody may fit the  $K$  and  $H$ -band excess.



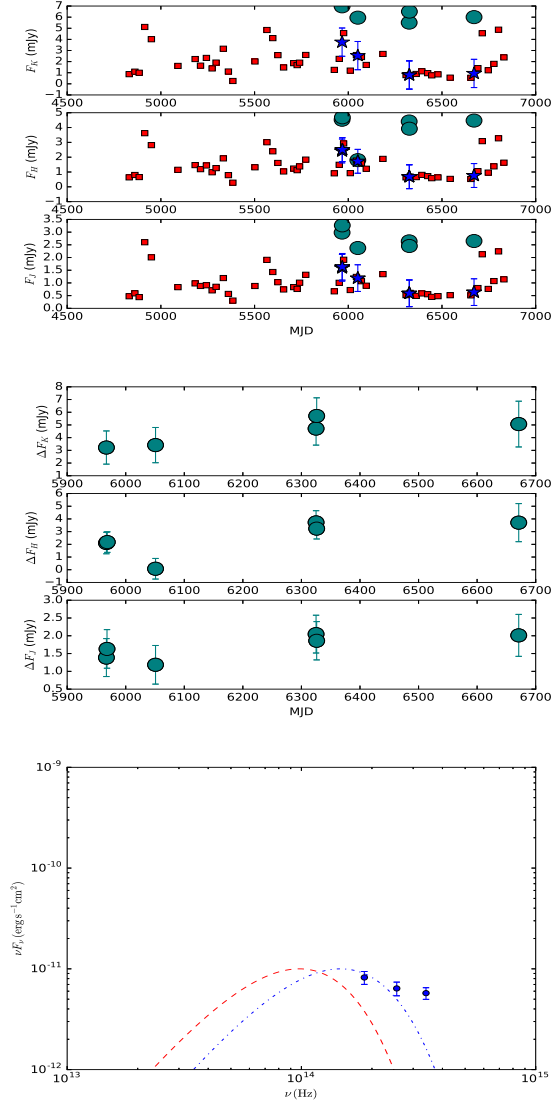


Fig. 5.12 *Top* : The projected synchrotron flux values from the Steward Observatory spectra of 1510-089. Symbols and colors are as in Figure 5.1. *Middle*: Same as in Figure 5.2 for 1510-089. *Bottom*: SED of the IR excess of 1510-089 as in Figure 5.3. An 1800 K blackbody can be fit to the average  $H$  and  $K_s$  IR excess. The maximum dust luminosity is adjusted slightly from the 2007–2008 observations, however it is unclear whether there was variability on the time scales over which the Mimir observations were performed.

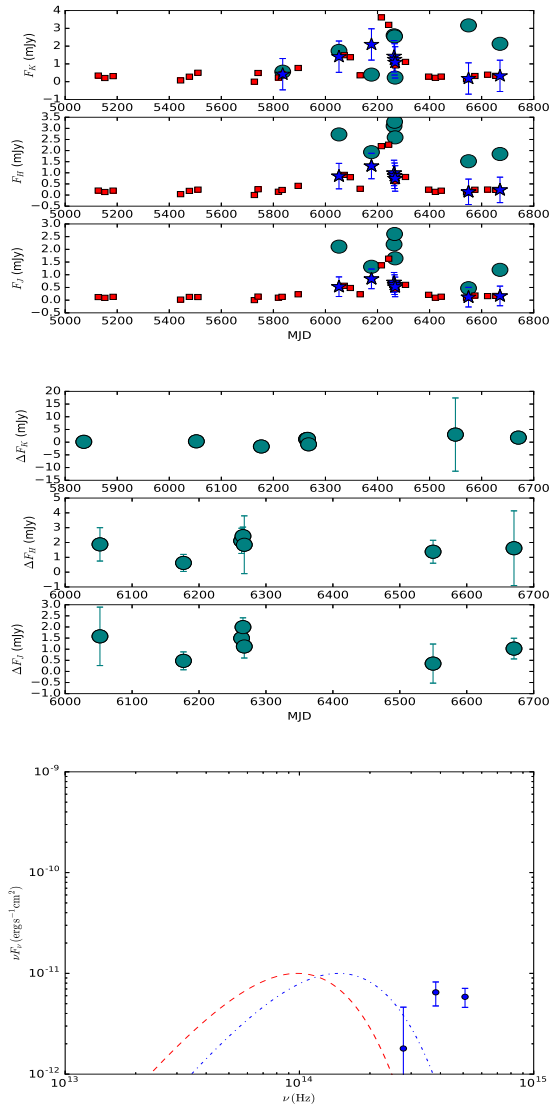


Fig. 5.13 As in Figure 5.12 for CTA102.

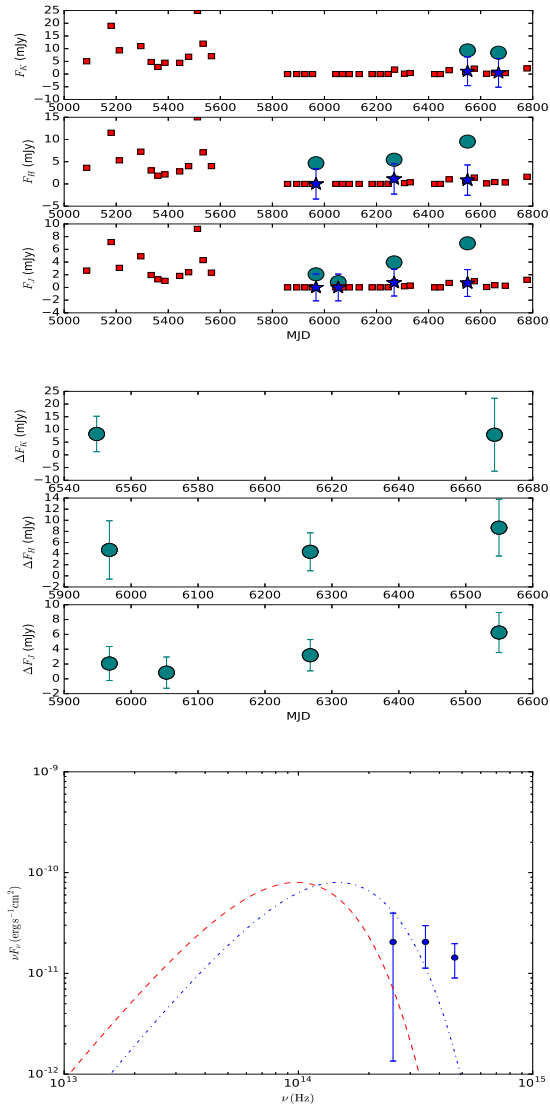


Fig. 5.14 As in Figure 5.12 for 3C454.3.

If the IR emission is thermal emission from sublimating dust, the  $\nu L_K$  luminosity is constrained to  $< 9 \times 10^{46} \text{erg s}^{-1}$ , nearly an order of magnitude higher than the dust luminosity observed in the other sources. If it exists, it is unclear how variable this component is in 3C454.3.

## CTA26

Because CTA26 is sampled infrequently in the Steward Observatory program, there is no overlap between when I observed the blazar in the IR, and when spectropolarimetric observations were performed. Nothing can be said about a measured IR excess in CTA26. However, at a redshift of  $z = 0.852$ , any measured excess is unlikely to be due to emission from a dusty torus.

## 0420-014

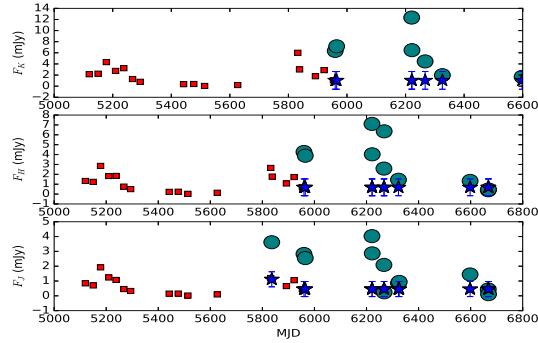


Fig. 5.15 Projected near-IR flux values for 0420-014 (red squares) along with measured values (green circles). Because the epochs I observed with Mimir do not have much overlap with the observations of the Steward Observatory, it is difficult to compare the near-IR flux of this source to the properties of its optical spectra.

Unfortunately, the dates of my observations of 0420-014 (Figure 5.15) do not coincide much with the Steward Observatory measurements, which were performed between 2009-10-09–2012-01-27. There is an epoch of overlap in September, 2011 in which an excess in all three IR bands is recorded, with a  $\nu \times F_K$  luminosity of

$5 \times 10^{46} \text{erg s}^{-1}$ . Even if this excess could have been confirmed with the additional observations, it is unlikely to be thermal in origin.

## OJ248

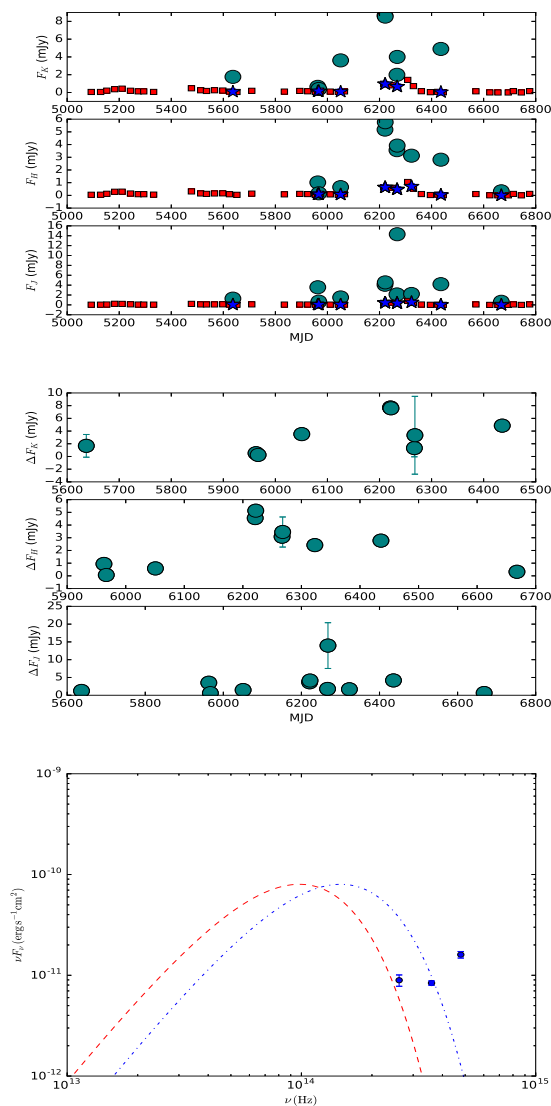


Fig. 5.16 As in Figure 5.12 for OJ248.

The IR lightcurve (Figure 5.16) of OJ248 shows an excess in all three bands between September, 2012–April, 2013. The IR data show no evidence of an excess

prior to 2012, however, and the excess vanished when the source was observed later in January, 2014. Interestingly, the epochs during which a significant IR excess was measured coincide with a major  $\gamma$ -ray outburst of OJ248.

## Chapter 6

# Gamma-Ray Variability of a Sample of Blazars Compared to Variability of the Accretion Disk

### 6.1 The Discrete Correlation Function

The subject of  $\gamma$ -ray variability, and its correlation with emission at other wavelengths, is one of great interest in blazar studies. A strong correlation between a  $\gamma$ -ray outburst and its timing relative to outbursts in other wavebands could help explain the origin of the  $\gamma$ -ray emission, which still remains a mystery. If a  $\gamma$ -ray outburst were to be observed preceding or following an outburst in another wavelength regime, a causal connection may be implied between the two, and the time delay could be used to infer the physical distance between the two emission components. If such a connection were to be found between the variable accretion disk and the  $\gamma$ -ray emission, its implications on the physics of  $\gamma$ -ray creation in blazars would be an interesting area for future exploration.

As shown in the previous chapter, the Steward Observatory spectra imply a variable accretion disk in two blazars, 1222+216 and OJ248. A variable accretion disk in 3C273 and CTA102 was also possibly detected, but not as robustly. In order to compare the variations in  $\gamma$ -ray emission in these blazars with the variations in the accretion disk emission, I compute the Discrete Correlation Function (DCF) pro-

posed by Edelson & Krolik (1988). The classical correlation function between two evenly sampled time-series of measurements is essentially the inner product of the two weighted by their standard deviations. Shifting one of the series in time by a factor of  $\Delta T$ , and recalculating the correlation function reveals the time delay between variations by determining the time delay that will maximize the correlation function.

Because of technical and physical limitations, time-domain astronomy cannot provide evenly sampled series of observations across multiple wavelengths; however, correlations between discretely sampled data can still be teased out. The DCF, proposed by Edelson & Krolik (1988), attempts to do just that. The first step is to compute an Unbinned Discrete Correlation Function (UDCF) for each pair of measurements. In two discretely sampled data series,  $X_i$ , and  $Y_j$ , UDCF is defined as:

$$UDCF_{i,j} = \frac{(X_i - \bar{X})(Y_j - \bar{Y})}{\sqrt{(\sigma_X^2 - err_X^2)(\sigma_Y^2 - err_Y^2)}}, \quad (6.1)$$

in which  $\sigma_{X,Y}$  are the standard deviations of the measurements, and  $err_{X,Y}$  are the individual measurement uncertainties. The time difference between each pair of measurements is also calculated in order to later calculate the DCF. Once calculated, the UDCF can be converted into the DCF by averaging the UDCF over a chosen time bin. The uncertainty of the DCF in any bin is then the standard deviation of the UDCF values in that bin divided by  $M - 1$ , where  $M$  is the number of data points contained in the bin.



## 6.2 Computing the DCF for a Small Sample of Blazars

### 6.2.1 1222+216

The  $\gamma$ -ray lightcurve of 1222+216, spanning energies from 100 MeV to 300 GeV, and binned to 7-day time resolution, is displayed in Figure 6.1, along with the light curve of the accretion disk hot-spot derived from the Steward Observatory spectra. The light curves show an extreme  $\gamma$ -ray outburst in 2010, in which the  $\gamma$ -ray photon flux increases by an order of magnitude from its quiescent level, followed by periods of relative quiescence and more minor outbursts in 2013 and 2014. Visually inspecting the light curve of the derived variable component of the accretion disk, shows a period of growing flux two years after the major  $\gamma$ -ray flare and another period of increasing flux coincident with the 2014 up-tick in  $\gamma$ -ray flux.

To compute the DCF, I chose a binning resolution of 30 days. A plot of the UDCF and the DCF at this resolution is shown in Figure 6.2. The most striking feature of the DCF is a spike centered at approximately  $\Delta T = -1200$  days, which is almost certainly an artifact introduced by the 2010  $\gamma$ -ray flare correlating with the long period of increasing BBB amplitude from 2012–2013. There is also a feature near a time lag of zero days, that is not quite centered on zero. A zoomed-in picture of the DCF of 1222+216 from  $\Delta T = -500 - 500$  days is displayed in Figure 6.3. From the zoomed-in look at the DCF, the signal becomes strongest near time delays of approximately 30–60 days, implying that the accretion disk flux begins to vary approximately 1–2 months after the  $\gamma$ -ray flux begins to vary. It is of note though, that the peak in the DCF is quite broad, and this leads to a high uncertainty in the time delay between  $\gamma$ -ray and accretion disk variability. The DCF displays a strong signal between  $\Delta T = -200$ –200 days, however with most of the signal indicating a positive time delay between variations in the  $\gamma$ -ray flux and BBB variations.

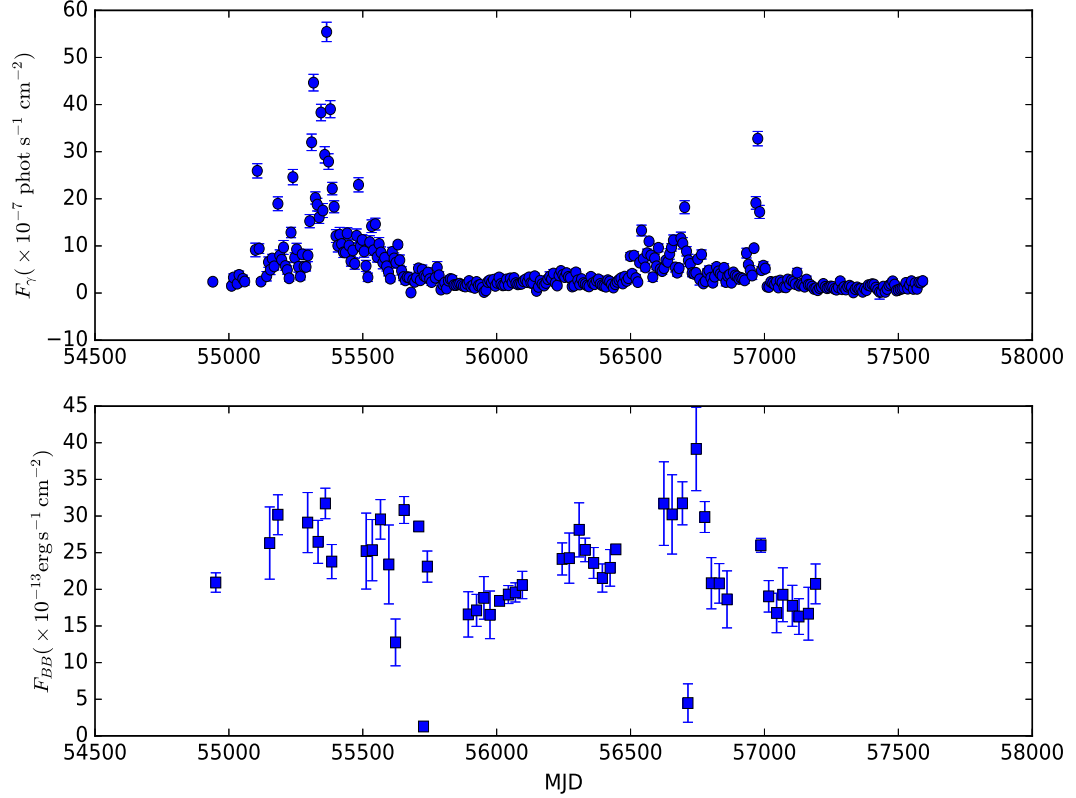


Fig. 6.1 *Top*: The  $\gamma$ -ray light curve of 1222+216 from 100 MeV to 300 GeV binned to a time resolution of one week. *Bottom*: Light curve of the variable part of the accretion disk during the same time frame.

This strongly suggests that either the  $\gamma$ -ray variations always lead variations in the accretion disk, or that  $\gamma$ -ray variability leads accretion disk variability most of the time in 1222+216 with a limited number of exceptions in which the hot-spot variation lead the  $\gamma$ -rays.

This result would seem to imply that the source of variability in the accretion disk and in the lower amplitude variability in  $\gamma$ -ray flux, are related. Using observed motion of superluminal knots in very long baseline interferometry (VLBI) images, Jorstad et al. (2016, in prep.), determined the apparent velocity and angle

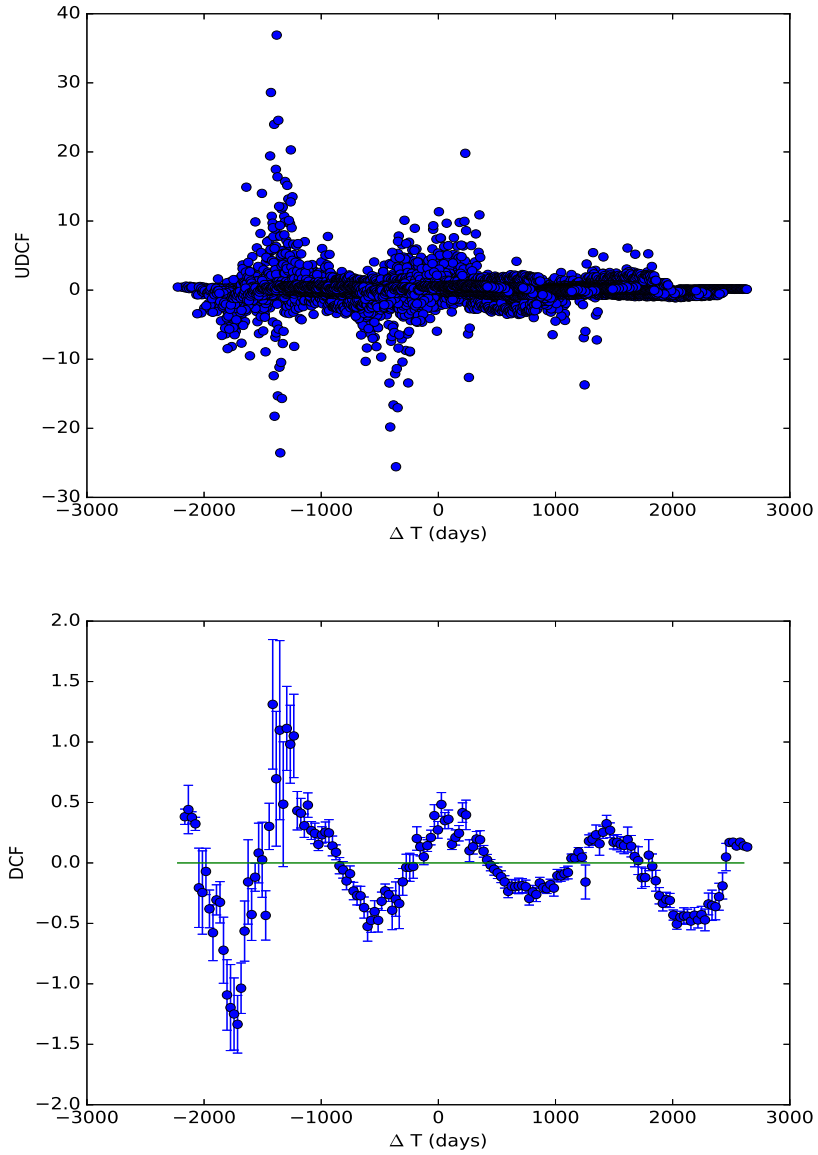


Fig. 6.2 *Top*: UDCF of 1222+216 between gamma-ray flux and accretion disk flux. *Bottom*: DCF generated from binning the UDCF to 30 day intervals.

Table 6.1. Parameters of Superluminal Motion in Two Blazars

Source Name	$\frac{v_{app}}{c}$	$\theta$ ( $^{\circ}$ )
1222+216	$12.5 \pm 0.5$	$3.5 \pm 1.0$
OJ248	$14 \pm 4$	$2.0 \pm 0.5$

between the direction of the jet outflow and the observed line of site for a number of blazars including 1222+216 and OJ248. The apparent superluminal velocity and angle to the line of site are reproduced in Table 6.1.

The product of  $v_{app}$  and  $\Delta T$  will yield the distance that a disturbance propagating down the jet will move in the transverse direction to the observer's line of sight. Dividing that quantity by  $\sin \theta$  will result in the distance traveled by the disturbance radially toward the observer. In the case of 1222+216, a disturbance originating near the black hole, and propagating down the jet at nearly the speed of light, can travel  $11 \pm 3$  parsecs (pcs) based on the observed properties of superluminal motion during a time period of 60 days.

The same disturbance, propagating through the accretion disk, may be slowed down due to the density of the disk. Taking a fiducial radius of the accretion disk to be approximately 100 gravitational radii,  $r_g$ , where  $r_g$  is defined as half the Schwarzschild radius of the black hole,

$$r_g = \frac{GM_{BH}}{c^2}. \quad (6.2)$$

Using a black-hole mass for 1222+216 of  $M_{BH} = 6 \times 10^8 M_{\odot}$  (Farina et al., 2012), a disturbance responsible for variations in the accretion disk flux and propagating downstream at nearly the speed of light, could potentially inject a population of

high energy electrons into the environment many tens of parsecs downstream which could then scatter photons up to  $\gamma$ -ray energies resulting in changes in the observed  $\gamma$ -ray flux. I find the velocity that the disturbance would need to travel through the accretion disk at,  $v_{disk} = \frac{100r_g}{\Delta T}$ , to be only  $0.06c$  in order for the cause of the changes in  $\gamma$ -ray flux and accretion disk flux to be possibly connected.

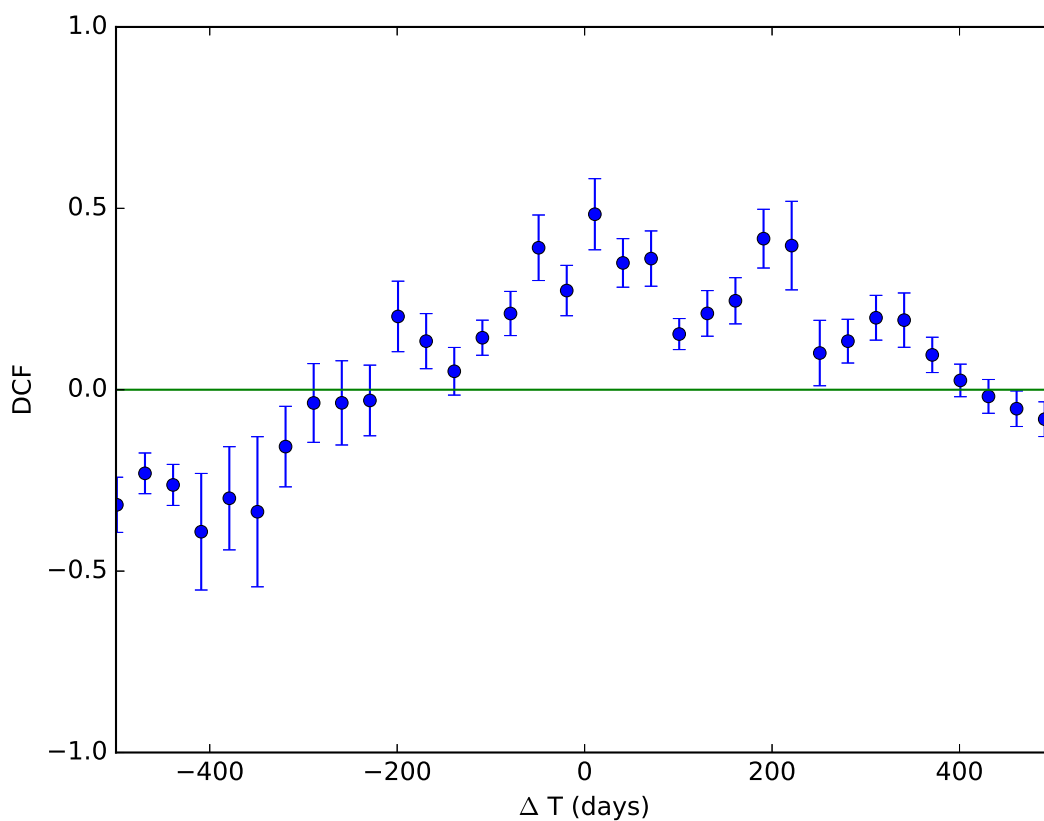


Fig. 6.3 As in Figure 6.2 but limited to a time interval of  $\pm 500$  days.

### 6.2.2 OJ248

The light curves of OJ248, displayed in Figure 6.4, show some interesting behavior. The  $\gamma$ -ray flux underwent a major outburst during late 2012 and early 2013. In the time leading up to the  $\gamma$ -ray outburst, the hot-spot component of the accretion

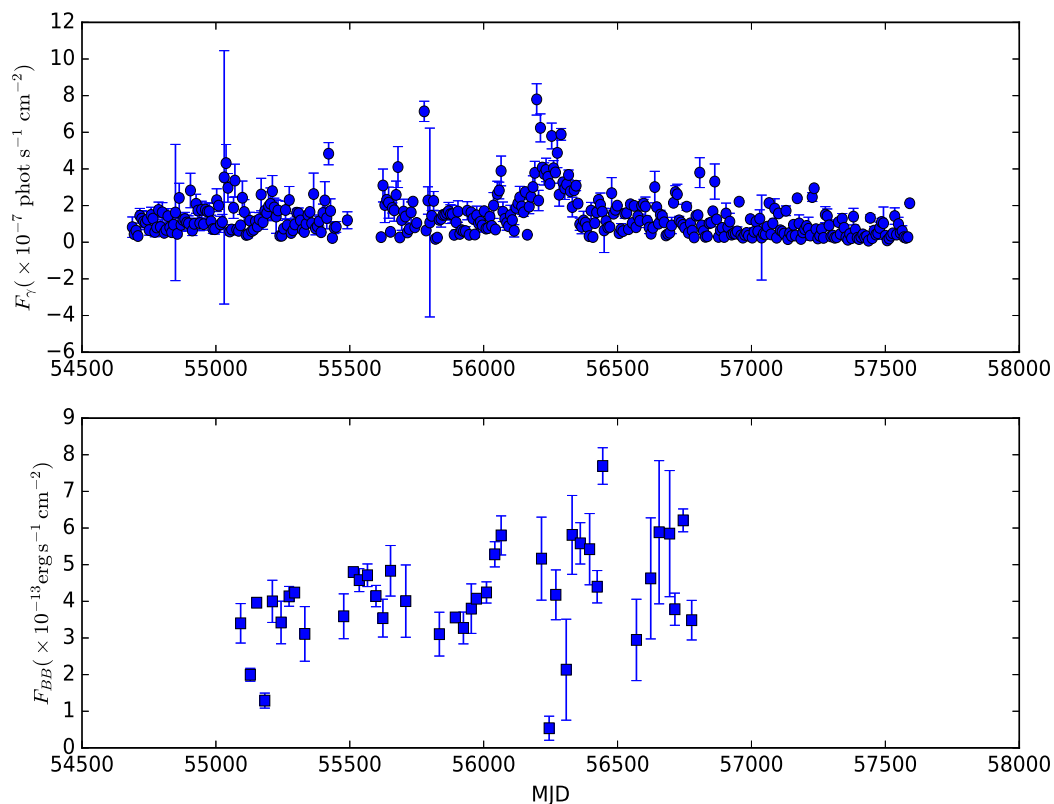


Fig. 6.4 As in Figure 6.1 for OJ248.

disk underwent a minor decrease in emission in late 2011 to early 2012, followed by a steady increase throughout 2012. The hot-spot flux increases by a factor of two leading up to the  $\gamma$ -ray outburst. The DCF, displayed in Figure 6.5, records a signal near  $\Delta T = -100$  days, implying, as the lightcurve does, that the accretion disk flux of OJ248 leads the  $\gamma$ -ray emission by approximately 100 days. The DCF also shows a strong negative correlation near  $\Delta T = 1000$  days, which is probably due to extreme noise in the  $\gamma$ -ray data at the beginning of the *Fermi* era correlating with the slight decrease in thermal flux before the factor of two increase in the hot-spot flux. Using the values in Table 6.1 and  $\Delta T = 100$  days for OJ248, I calculate the propagation distance down the jet of a disturbance originating near the blackhole

as nearly  $34 \pm 5$  pc. The central super-massive black hole (SMBH) of OJ248 has been estimated as  $M_{BH} \sim 10^9 M_{\odot}$  (Liang & Liu, 2003). Using this value suggests a propagation velocity of  $v_{disk} = 0.06c$ , the same as in 1222+216.

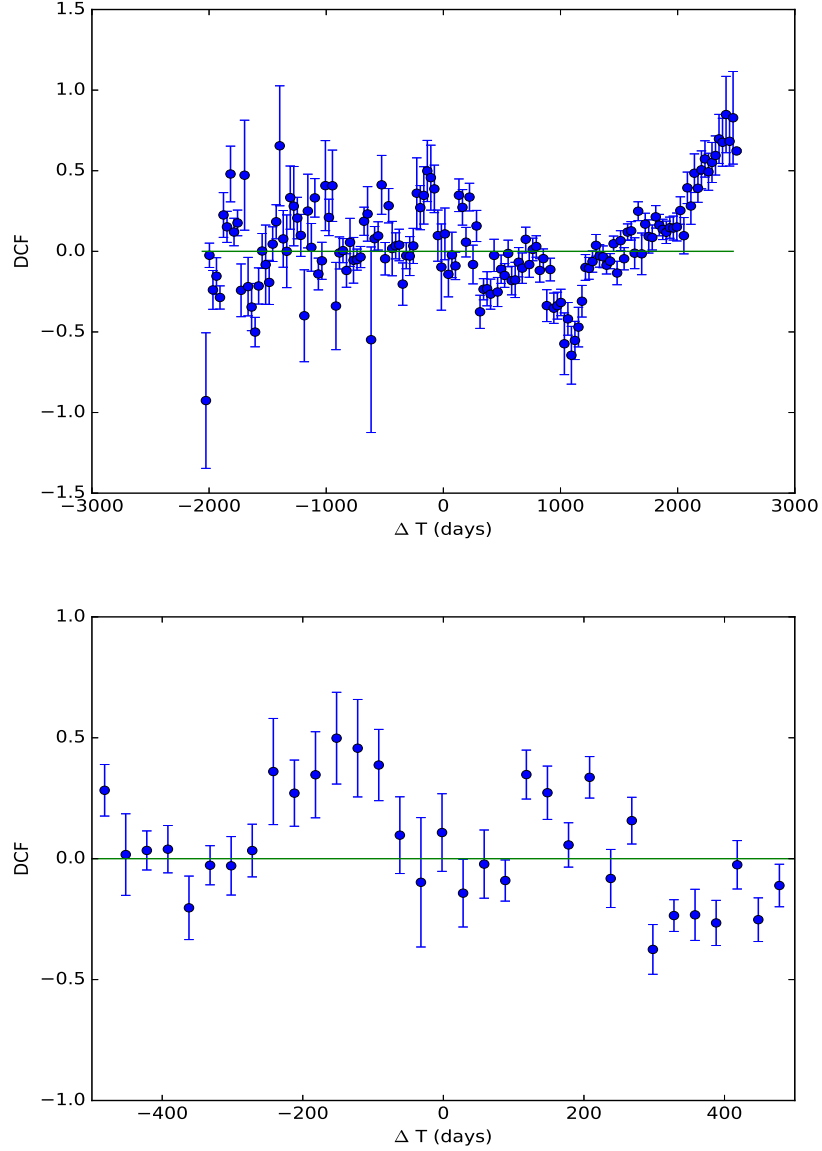


Fig. 6.5 *Top*: DCF of OJ248 between gamma-ray flux and accretion disk flux. *Bottom*: Same as top but zoomed in on  $\pm 500$  days.

## 6.2.3 3C273

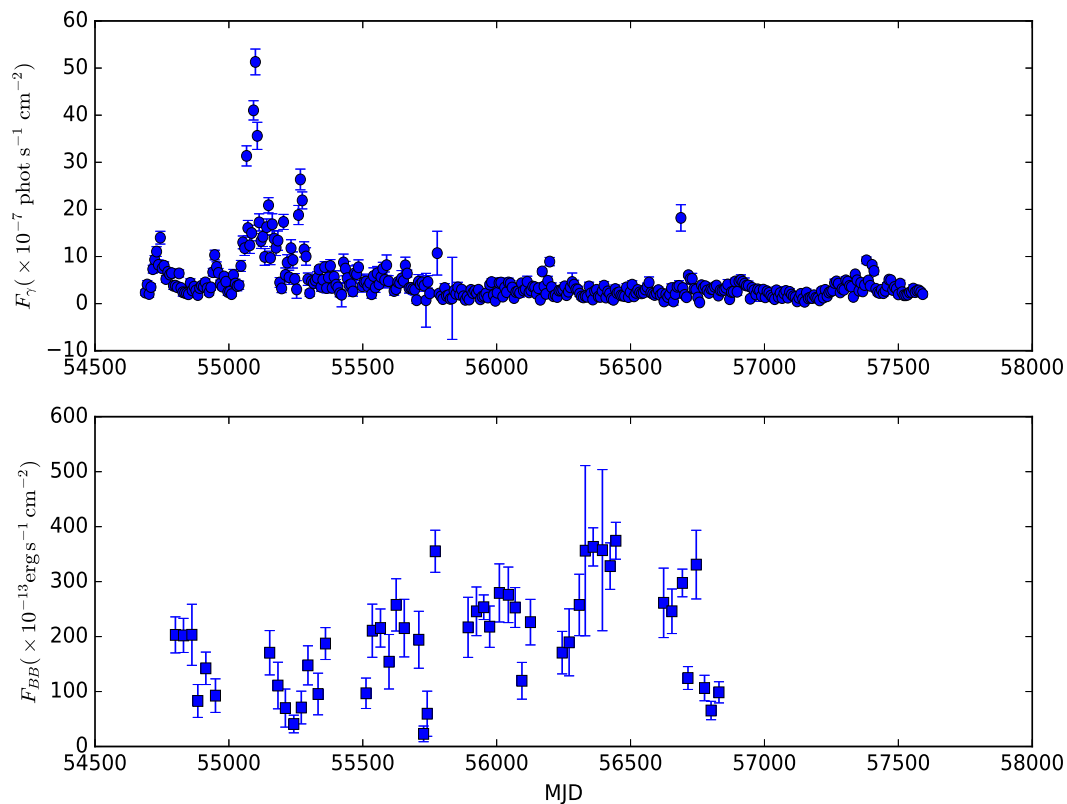


Fig. 6.6 As in Figure 6.4 for 3C273.

The lightcurves of 3C273 (Figure 6.6) show the accretion disk flux steadily increasing throughout the several years in which it was observed; however, the data set is quite noisy. Except for major outbursts in 2009 and in 2010, 3C273 has been relatively quiescent in  $\gamma$ -ray flux. This makes deriving a meaningful correlation between the  $\gamma$ -ray emission and accretion disk emission difficult. Prior to beginning a steady increase in flux, the light curve of 3C273 shows a short period of decreasing accretion disk flux in 2009. This period is followed by the 2010  $\gamma$ -ray outburst and then a steady increase in the accretion disk flux. This is reflected in the DCF for



3C273, in which an anti-correlation between the  $\gamma$ -ray and accretion disk flux levels is apparent at a time lag of  $\Delta T = -150$  days. However, because of the  $\gamma$ -ray quiescence of 3C273 following 2010, and the difficulty in measuring the accretion disk flux, the case for a connection between the accretion disk of 3C273 and the  $\gamma$ -ray emission cannot be established (Figure 6.7).

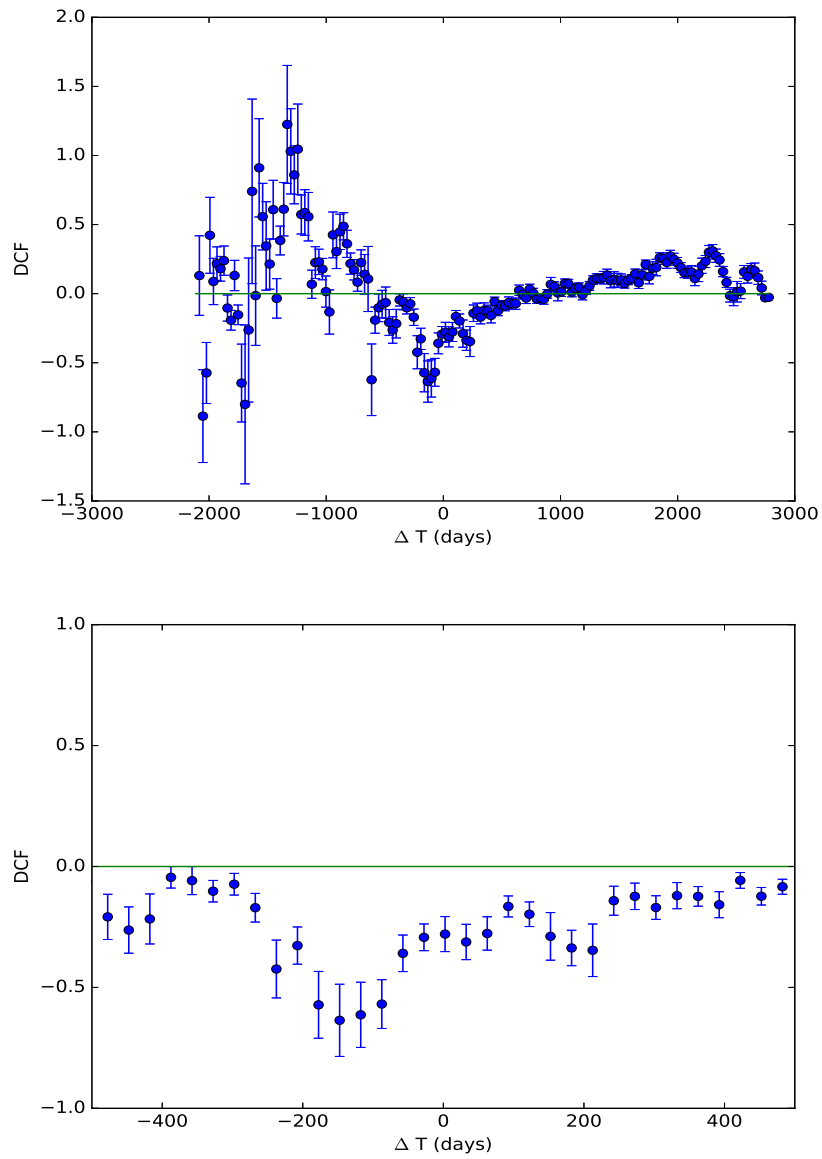


Fig. 6.7 As in Figure 6.5 for 3C273

## 6.2.4 CTA102

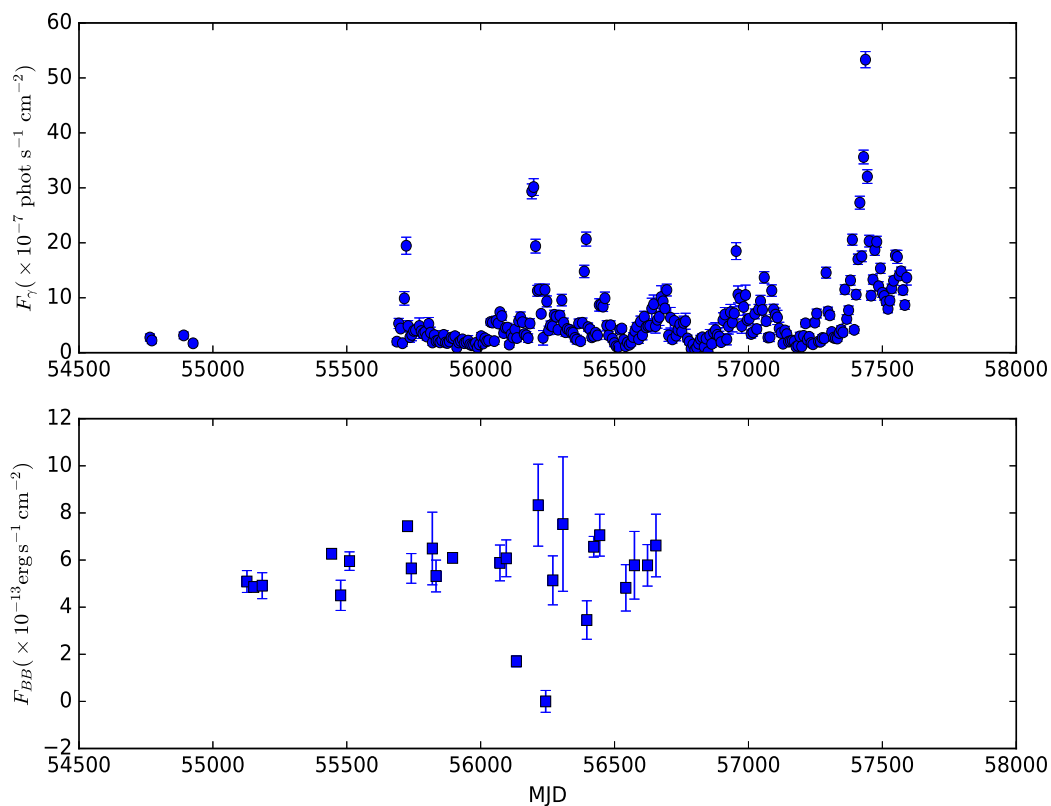


Fig. 6.8 As in Figure 6.4 for CTA102.

As in 3C273, variability in the accretion disk was not as robustly established through use of the Steward Observatory data as it was in OJ248 and 1222+216. This is evident in the light curve of the accretion disk component, which appears mostly constant, albeit with a large standard deviation (Figure 6.8). The DCF (Figure 6.9) shows a correlation at  $\Delta T = 1800$  days, yet the light curve derived from the Steward Observatory spectra does not span that many days, suggesting that this correlation is spurious. Another large correlation between the  $\gamma$ -ray flux and the accretion disk is

present near  $\Delta T = -200$  days, implying that the limited variability of the accretion disk could lead changes in the  $\gamma$ -ray flux by nearly 7 months.

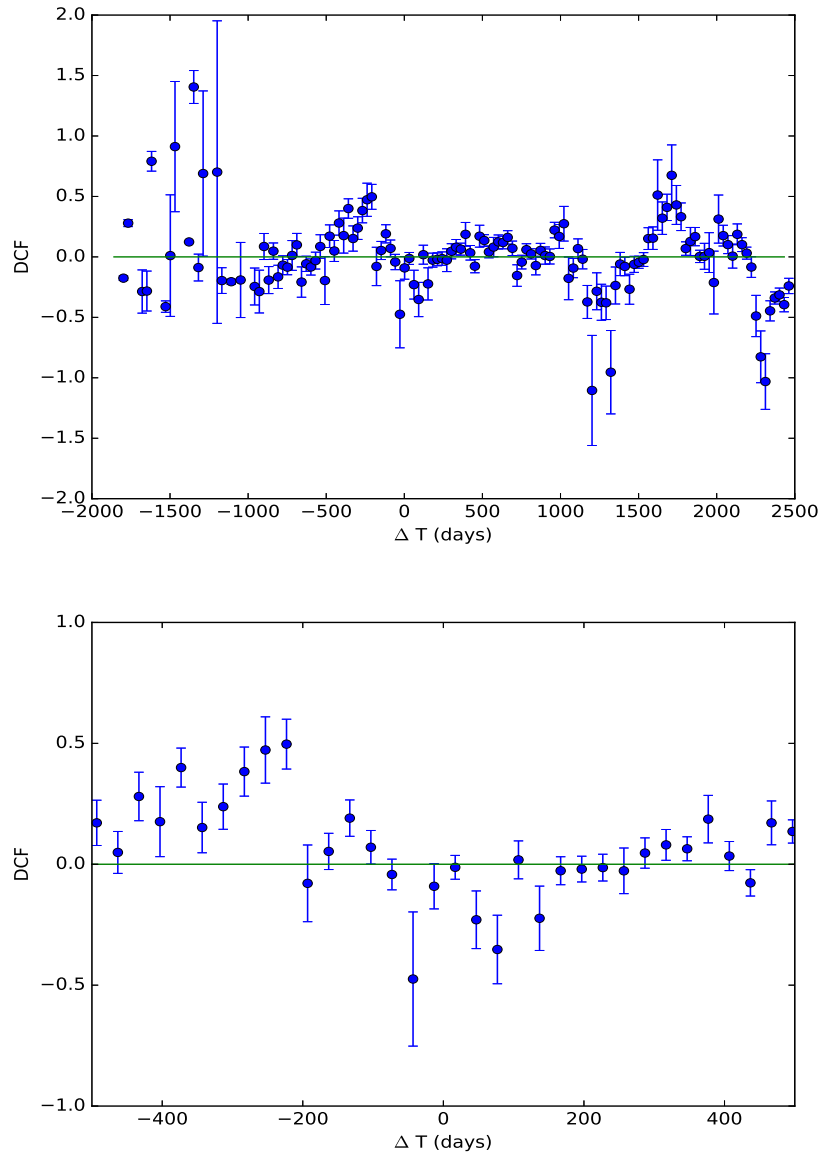


Fig. 6.9 As in Figure 6.9 for CTA102

## Chapter 7

# Conclusions

In this dissertation, I have studied the variability of emission components of a sample of  $\gamma$ -ray bright blazars across multiple wavelength regimes. I used data from the *Spitzer* space telescope to measure the hot dust emission from two flat-spectrum radio quasars (FSRQs), 1222+216 and CTA102, by subtraction of a synchrotron component derived from the R-band and far-infrared (IR) emission of those blazars. I showed that the hot dust luminosity in both blazars is nearly  $10^{46}$  erg s<sup>-1</sup> and that a large fraction of the bolometric luminosity of the blazar is processed and re-emitted by the dust torus in those two blazars. I found little evidence for hot dust emission in the IR spectral energy distribution (SED) of the lone BL Lac included in the study (1219+285).

I have made extensive use of a dataset of optical spectropolarimetry in order to determine that the flux of the accretion disk of the FSRQ 1222+216 varies with a standard deviation on the order of 20% over the course of several years, while the accretion disk flux of OJ248 shows significant variability as well. The thermal emission in the optical-UV regime takes the form of a relatively constant, thin, multi-temperature accretion disk, with a characteristic spectrum of  $F_{disk} \propto \nu^{1/3}$ , along with a varying hot-spot emitting as a blackbody. The blackbody component of the accretion disk of 1222+216 has a temperature  $T \sim 4 \times 10^4$  K, while the blackbody component of the accretion disk to the FSRQ OJ248 is cooler, ( $T \sim 1.5 \times 10^3$  K). I

have found that, through the use of spectropolarimetry, most BL Lacs do not show much evidence for any accretion disk component in their optical spectra, meaning that any accretion disk luminosity is dwarfed by the synchrotron radiation emanating from the jet. Curiously, I find an exception to this in BL Lac itself, which can be modeled with a constant thermal component in addition to a synchrotron component.

I found evidence that the total linear polarization of synchrotron radiation is slightly dependent on emission wavelength in a number of BL Lacs, in which the total linear polarization increases slightly toward higher frequencies. This is a result that agrees with some simulations of the emission from a blazar jet in which the emitting plasma is modeled with a turbulent magnetic field. I found the opposite effect (decreasing linear polarization toward higher frequency) in the majority of the FSRQs I studied, a result that is expected if the optical spectrum of this type of blazar contains emission from a non-polarized thermal component in which much of the emission originates in a large, multi-temperature disk orbiting and coalescing onto the central black hole of the blazar.

I undertook a campaign to monitor the near-IR variability of a number of blazars in both flux and polarized flux in order to search for evidence of a hidden dusty torus that is merely being out-shined by the jet of the blazar. In principle, the thermal emission in the near-IR ought to be recoverable with these measurements, as the flux from the thermal component should be non-polarized. In practice, because of the large redshift of many of the most interesting blazars, and due to poor weather during many of the observing campaigns leading to polarization measurements of poor quality, the IR excess to the flux was difficult to measure. I attempted to estimate the synchrotron luminosity in the near-IR through projection of the spectrum of the synchrotron component obtained from the analysis of the Steward Observatory spec-

tra into the near-infrared portion of the electromagnetic spectrum. Through this analysis, I found an infrared excess consistent with the previously estimated dust luminosity in 1222+216, 3C273, and CTA102. I found an infrared excess in many other sources as well, but as a result of the high temperature required to fit a black-body to the measured excess and the lack of accurate polarization measurements, it is difficult to attribute the apparent IR excesses to emission from the dusty torus.

Using data from the *Fermi* Gamma-ray Telescope, I have correlated the variable part of the accretion disk for two blazars with the variability in the 100 MeV to 300 GeV  $\gamma$ -ray flux. In 1222+216, I find that variability in  $\gamma$ -ray emission leads that of the accretion disk by 30–60 days, while in OJ248, I find that the variability in the accretion disk flux leads the variability in the  $\gamma$ -ray flux by  $\sim 100$  days. Taking into account the measured superluminal motion measured in components of the relativistic jets of these two blazars, this implies that a disturbance originating near the supermassive black hole and propagating down the jet while propagating through the accretion disk at a much slower speed could be observed to cause changes in the accretion disk luminosity and the  $\gamma$ -ray luminosity within  $\sim 100$  days of each other, even if the  $\gamma$ -rays originate on the order of ten parsecs downstream.

In the future, progress in our understanding of the variability of the various structures inside a blazar can be made through increasing the wavelength regime over which they are intensely monitored. The Steward Observatory Blazar Monitoring project, in concert with the continuous observations of the *Fermi*  $\gamma$ -ray Telescope, has provided insight by allowing the unveiling of the variability of the accretion disk component of the optical-UV spectrum, and allowing for its comparison to very-high energy emission. The Steward Observatory project, however, provides high quality spectra and polarization from a limited wavelength regime,  $\lambda = 4000 - 7500 \text{ \AA}$ .

Expanding this wavelength coverage through the use of ground-based polarimetry across all available optical, and IR bands, would provide a larger baseline of wavelengths for determining the spectral index of the optical synchrotron component, and allow for its easier extension into the near-IR. Such an expansion of polarization monitoring would much more accurately define the wavelength dependence of the linear polarization of the synchrotron emission from blazar jets. This would allow further progress in determining the physical conditions behind the multi-wavelength emission, and its evolution in time.

Monitoring the near-IR flux of a sample of blazars with Mimir did not result in much new information about the nature of the hot dust emission in blazars. However, I was able to detect excess near-IR fluxes consistent with previously reported values. With the upcoming launch of the James Webb Space Telescope (JWST), slated for October 2018, the mid-IR window left inaccessible since *Spitzer* Space Telescope (SST) ran out of coolant will be opened to determine the fraction of emission in blazars caused by warm-to-hot dust. In addition to quality imaging and spectroscopy that will be provided by JWST, the Stratospheric Observatory for Infrared Astronomy (SOFIA) will soon add IR polarimetry capabilities. These new capabilities, if proven to be sensitive enough that observations of high redshift blazars are appropriate, could potentially be useful in separating the dust and synchrotron emission components in the mid-IR providing a clear advantage over JWST. The Atacama Large Millimeter/submillimeter Array (ALMA), in operation since 2011, provides access to the mm/submm regime under which the cold dust radiates. An advantage that ALMA carries is that the array can measure the mm/submm polarization in addition to the blazar's flux, potentially allowing for the direct measurement of the synchrotron component of the emission. Molecular emission lines, from the coldest portion of the dust torus, are also potentially visible with ALMA observations.

Most of our insight about blazars comes from the variable nature of these objects. Therefore, it is imperative that future observing campaigns make use of intense, frequent monitoring of both flux and polarization, coordinated across many wavelengths. Investigations in the mid-IR with JWST and mm/submm with ALMA are likely to provide only snapshots, rather than high time-resolution monitoring, therefore it would be greatly advantageous if future observing campaigns would make use of coordination with observations at other wavebands in order to obtain a more complete SED at those times.



## List of Journal Abbreviations

A&A	Astronomy and Astrophysics
AJ	Astronomical Journal
ApJ	Astrophysical Journal
ApJL	Astrophysical Journal Letters
ApJS	Astrophysical Journal Supplement
ARA&A	Annual Review of Astronomy and Astrophysics
MNRAS	Monthly Notices of the Royal Astronomical Society
PASP	Publications of the Astronomical Society of the Pacific
Space Sci. Rev.	Space Science Reviews
Rev. Mod. Phys.	Review of Modern Physics

## References

- Abdo, A. A., & et al. 2010, *ApJ*, 715, 429
- Abdo, A. A., Ackermann, M., Agudo, I., et al. 2010, *ApJ*, 716, 30
- Antonucci, R. 1993a, *ARA&A*, 31, 473
- . 1993b, *ARA&A*, 31, 473
- Arbeiter, C., Pohl, M., & Schlickeiser, R. 2001, *International Cosmic Ray Conference*, 7, 2721
- Atwood, W. B., Abdo, A. A., Ackermann, M., et al. 2009, *ApJ*, 697, 1071
- Barvainis, R. 1987, *ApJ*, 320, 537
- . 1990, *ApJ*, 353, 419
- . 1992, *ApJ*, 400, 502
- Begelman, M. C., & Sikora, M. 1987, *ApJ*, 322, 650
- Bessell, M. S. 2005, *ARA&A*, 43, 293
- Błażejowski, M., Sikora, M., Moderski, R., & Madejski, G. M. 2000, *ApJ*, 545, 107
- Blumenthal, G. R., & Gould, R. J. 1970, *Rev. Mod. Phys.*, 42, 237
- Calzetti, D., Armus, L., Bohlin, R. C., et al. 2000, *ApJ*, 533, 682
- Casey, C. M., Narayanan, D., & Cooray, A. 2014, *Physics Reports*, 541, 45 ,  
dusty star-forming galaxies at high-redshift
- Clavel, J., Wamsteker, W., & Glass, I. S. 1989, *ApJ*, 337, 236
- Cleary, K., Lawrence, C. R., Marshall, J. A., Hao, L., & Meier, D. 2007, *ApJ*, 660, 117
- Clemens, D. P., Sarcia, D., Grabau, A., et al. 2007, *PASP*, 119, 1385
- Cohen, M., Wheaton, W. A., & Megeath, S. T. 2003, *AJ*, 126, 1090

- D'Elia, V., & Cavaliere, A. 2001, in *Astronomical Society of the Pacific Conference Series*, Vol. 227, *Blazar Demographics and Physics*, ed. P. Padovani & C. M. Urry, 252
- Dermer, C. D., & Schlickeiser, R. 1993, *ApJ*, 416, 458
- Dexter, J., & Agol, E. 2011, *ApJ*, 727, L24
- Donato, D. 2010, *The Astronomer's Telegram*, 2584, 1
- Edelson, R. A., & Krolik, J. H. 1988, *ApJ*, 333, 646
- Edelson, R. A., Alexander, T., Crenshaw, D. M., et al. 1996, *ApJ*, 470, 364
- Fanaroff, B. L., & Riley, J. M. 1974, *MNRAS*, 167, 31P
- Farina, E. P., Decarli, R., Falomo, R., Treves, A., & Raiteri, C. M. 2012, *MNRAS*, 424, 393
- Fazio, G. G., Hora, J. L., Allen, L. E., et al. 2004, *ApJS*, 154, 10
- Fortson, L., & VERITAS Collaboration. 2016, in *American Astronomical Society Meeting Abstracts*
- Gear, W. K., Robson, E. I., Gee, G., & Nolt, I. G. 1985, *MNRAS*, 217, 281
- Ghisellini, G., Celotti, A., Fossati, G., Maraschi, L., & Comastri, A. 1998, *MNRAS*, 301, 451
- Gomez, H. L., Krause, O., Barlow, M. J., et al. 2012, *ApJ*, 760, 96
- Hao, L., Strauss, M. A., Fan, X., et al. 2005, *AJ*, 129, 1795
- Hao, L., Spoon, H. W. W., Sloan, G. C., et al. 2005, *ApJ*, 625, L75
- Hao, L., Spoon, H. W. W., Sloan, G. C., et al. 2005, *ApJ*, 625, L75
- Harris, D. E., & Krawczynski, H. 2002, *ApJ*, 565, 244
- Hartman, R. C., Bertsch, D. L., Bloom, S. D., et al. 1999, *ApJS*, 123, 79
- Hönig, S. F., & Kishimoto, M. 2010, *A&A*, 523, A27
- Houck, J. R., Roellig, T. L., van Cleve, J., et al. 2004, *ApJS*, 154, 18
- Impey, C. D., & Neugebauer, G. 1988, *AJ*, 95, 307
- Isler, J. C., Urry, C. M., Bailyn, C., et al. 2015, *ApJ*, 804, 7

- Jackson, J. D. 1991, *Classical Electrodynamics*, 3rd edn. (New Jersey, USA: John Wiley & Sons, Inc.)
- Jaffe, W., Meisenheimer, K., Röttgering, H. J. A., et al. 2004, *Nature*, 429, 47
- Jones, T. W. 1988, *ApJ*, 332, 678
- Jorstad, S. G., & Marscher, A. P. 2006, *Astronomische Nachrichten*, 327, 227
- Jorstad, S. G., Marscher, A. P., Mattox, J. R., et al. 2001, *ApJ*, 556, 738
- Jorstad, S. G., Marscher, A. P., Stevens, J. A., et al. 2007, *AJ*, 134, 799
- Joshi, M., Marscher, A. P., & Böttcher, M. 2014, *ApJ*, 785, 132
- Kawaguchi, T., & Mori, M. 2010, *ApJ*, 724, L183
- Kellermann, K. I., Lister, M. L., Homan, D. C., et al. 2004, *ApJ*, 609, 539
- Kelly, B. C., Sobolewska, M., & Siemiginowska, A. 2011, *ApJ*, 730, 52
- Klein, O., & Nishina, Y. 1929, *Zeitschrift für Physik*, 52, 853
- Knacke, R. F., & Thomson, R. K. 1973, *PASP*, 85, 341
- Kovačević, J., Popović, L. Č., & Dimitrijević, M. S. 2010, *ApJS*, 189, 15
- Krolik, J. H. 1999, *Active galactic nuclei : from the central black hole to the galactic environment*, 1st edn. (Princeton, New Jersey, USA: Princeton University Press)
- Lähteenmäki, A., & Valtaoja, E. 2003, *ApJ*, 590, 95
- Landt, H., Buchanan, C. L., & Barmby, P. 2010, *MNRAS*, 408, 1982
- Lau, R. M., Herter, T. L., Morris, M., Li, Z., & Adams, J. D. 2015, in *American Astronomical Society Meeting Abstracts*
- Leinert, C. 1975, *Space Sci. Rev.*, 18, 281
- Leinert, C., Richter, I., Pitz, E., & Planck, B. 1981, *A&A*, 103, 177
- Leipski, C., Antonucci, R., Ogle, P., & Whysong, D. 2009, *ApJ*, 701, 891
- Liang, E. W., & Liu, H. T. 2003, *MNRAS*, 340, 632
- Liffman, K., & Clayton, D. D. 1989, *ApJ*, 340, 853

- Lister, M. L., & Marscher, A. P. 1997, *ApJ*, 476, 572
- MacDonald, N. R., Marscher, A. P., Jorstad, S. G., & Joshi, M. 2015, *ApJ*, 804, 111
- Malkan, M. A., & Sargent, W. L. W. 1982, *ApJ*, 254, 22
- Malmrose, M. P., Marscher, A. P., Jorstad, S. G., Nikutta, R., & Elitzur, M. 2011, *ApJ*, 732, 116
- Mannucci, F., Basile, F., Poggianti, B. M., et al. 2001, *MNRAS*, 326, 745
- Mariotti, M. 2010, *The Astronomer's Telegram*, 2684, 1
- Marscher, A. P. 1987, in *Superluminal Radio Sources*, ed. J. A. Zensus & T. J. Pearson, 280–300
- Marscher, A. P. 2010, in *The Jet Paradigm*, ed. T. Belloni, *Lecture Notes in Physics*, 794, 173
- Marscher, A. P. 2013, in *American Astronomical Society Meeting Abstracts* 221
- . 2014a, *ArXiv e-prints*, 1410.7819
- . 2014b, *ApJ*, 780, 87
- Marscher, A. P., Jorstad, S. G., D’Arcangelo, F. D., et al. 2008, *Nature*, 452, 966
- Marscher, A. P., Jorstad, S. G., Larionov, V. M., et al. 2010, *ApJ*, 710, L126
- Marziani, P., Sulentic, J. W., Dultzin-Hacyan, D., Calvani, M., & Moles, M. 1996, *ApJS*, 104, 37
- Matsuura, M., Dwek, E., Barlow, M. J., et al. 2015, *ApJ*, 800, 50
- May, B. 2008, *A Survey of Radial Velocities in the Zodiacal Dust Cloud* (Berlin, Germany: Springer)
- Meegan, C., Lichti, G., Bhat, P. N., et al. 2009, *ApJ*, 702, 791
- Minezaki, T., Yoshii, Y., Kobayashi, Y., et al. 2004, *ApJ*, 600, L35
- Mor, R., Netzer, H., & Elitzur, M. 2009, *ApJ*, 705, 298
- Morgan, C. W., Kochanek, C. S., Morgan, N. D., & Falco, E. E. 2010, *ApJ*, 712, 1129

- Nenkova, M., Sirocky, M. M., Ivezić, Ž., & Elitzur, M. 2008a, *ApJ*, 685, 147
- Nenkova, M., Sirocky, M. M., Nikutta, R., Ivezić, Ž., & Elitzur, M. 2008b, *ApJ*, 685, 160
- Nilsson, K., Pasanen, M., Takalo, L. O., et al. 2007, *A&A*, 475, 199
- Nolan, P. L., Abdo, A. A., Ackermann, M., et al. 2012, *ApJS*, 199, 31
- Ogle, P., Whysong, D., & Antonucci, R. 2006, *ApJ*, 647, 161
- Paltani, S., Courvoisier, T. J.-L., & Walter, R. 1998, *A&A*, 340, 47
- Pier, E. A., & Krolik, J. H. 1992, *ApJ*, 401, 99
- . 1993, *ApJ*, 418, 673
- Poole, T. S., Breeveld, A. A., Page, M. J., et al. 2008, *MNRAS*, 383, 627
- Raban, D., Jaffe, W., Röttgering, H., Meisenheimer, K., & Tristram, K. R. W. 2009, *MNRAS*, 394, 1325
- Raiteri, C. M., Villata, M., Larionov, V. M., et al. 2007, *A&A*, 473, 819
- Rayner, J. T., Toomey, D. W., Onaka, P. M., et al. 2003, *PASP*, 115, 362
- Rieke, G. H., Young, E. T., Engelbracht, C. W., et al. 2004, *ApJS*, 154, 25
- Roming, P. W. A., Kennedy, T. E., Mason, K. O., et al. 2005, *Space Sci. Rev.*, 120, 95
- Rowan-Robinson, M., & May, B. 2013, *MNRAS*, 429, 2894
- Ruan, J. J., Anderson, S. F., Dexter, J., & Agol, E. 2014, *ApJ*, 783, 105
- Rybicki, G. B., & Lightman, A. P. 1986, *Radiative Processes in Astrophysics* (Weinheim, Germany: Wiley-VCH Verlag GmbH & Co.)
- Salpeter, E. E. 1977, *ARA&A*, 15, 267
- Savolainen, T., Homan, D. C., Hovatta, T., et al. 2010, *A&A*, 512, A24+
- Schlafly, E. F., & Finkbeiner, D. P. 2011, *ApJ*, 737, 103
- Schlegel, D. J., Finkbeiner, D. P., & Davis, M. 1998, *ApJ*, 500, 525
- Schmidt, G. D., Stockman, H. S., & Smith, P. S. 1992, *ApJ*, 398, L57
- Schneider, D. P., Richards, G. T., Hall, P. B., et al. 2010, *AJ*, 139, 2360

- Schweitzer, M., Groves, B., Netzer, H., et al. 2008, *ApJ*, 679, 101
- Shakura, N. I., & Sunyaev, R. A. 1976, *MNRAS*, 175, 613
- Shang, Z., Brotherton, M. S., Green, R. F., et al. 2005, *ApJ*, 619, 41
- Shields, G. A. 1978, *Nature*, 272, 706
- Siebenmorgen, R., Haas, M., Krügel, E., & Schulz, B. 2005, *A&A*, 436, L5
- Sikora, M., Begelman, M. C., & Rees, M. J. 1994, *ApJ*, 421, 153
- Sikora, M., Stawarz, L., Moderski, R., Nalewajko, K., & Madejski, G. M. 2009, *ApJ*, 704, 38
- Skrutskie, M. F., Cutri, R. M., Stiening, R., et al. 2006, *AJ*, 131, 1163
- Smith, P. S., Montiel, E., Rightley, S., et al. 2009, *ArXiv e-prints*, 0912.3621
- Smith, P. S., Schmidt, G. D., Hines, D. C., & Foltz, C. B. 2003, *ApJ*, 593, 676
- Sokolov, A., & Marscher, A. P. 2005, *ApJ*, 629, 52
- Soldi, S., Türler, M., Paltani, S., et al. 2008, *A&A*, 486, 411
- Spoon, H. W. W., Marshall, J. A., Houck, J. R., et al. 2007, *ApJ*, 654, L49
- Sturm, E., Schweitzer, M., Lutz, D., et al. 2005, *ApJ*, 629, L21
- Suganuma, M., Yoshii, Y., Kobayashi, Y., et al. 2006, *ApJ*, 639, 46
- Tanaka, Y. T., Stawarz, L., Thompson, D. J., et al. 2011, *ArXiv e-prints*, 1101.5339
- Tokunaga, A. T., Simons, D. A., & Vacca, W. D. 2002, *PASP*, 114, 180
- Urry, C. M., & Padovani, P. 1995, *PASP*, 107, 803
- van Breugel, W., Miley, G., & Heckman, T. 1984, *AJ*, 89, 5
- von Montigny, C., Bertsch, D. L., Chiang, J., et al. 1995, *ApJ*, 440, 525
- Wardle, J. F. C., & Kronberg, P. P. 1974, *ApJ*, 194, 249
- Werner, M. W., Roellig, T. L., Low, F. J., et al. 2004, *ApJS*, 154, 1
- Whittet, D. C. B. 1992, *Dust in the galactic environment*, 2nd edn. (Bristol, UK & Philadelphia, USA: Institute of Physics Publishing)

- Williamson, K. E., Jorstad, S. G., Marscher, A. P., et al. 2014, ApJ, 789, 135
- Wills, B. J. 1989, in Lecture Notes in Physics, Berlin Springer Verlag, Vol. 334, BL Lac Objects, ed. L. Maraschi, T. Maccacaro, & M.-H. Ulrich, 109
- Yee, H. K. C. 1980, ApJ, 241, 894



# Curriculum Vitae

Michael Paul Malmrose

**Office Address**

Boston University  
 Department of Astronomy  
 725 Commonwealth Avenue  
 Room 605A  
 Boston, MA 02215  
**Phone:** (801) 710-1294

**E-mail:** michaelmalmrose@gmail.com

**Education**

**Boston University** Sep. 2008–Aug. 2016  
 Boston, MA USA  
 Ph.D. in Astrophysics, Aug. 2016  
 M.A. in Astrophysics, May 2010  
 Ph.D. Dissertation: “Thermal Emission Signatures in Non-thermal  
 Blazars”  
*Thesis Advisor: Alan P. Marscher*

**Weber State University** Aug. 2002–May 2007  
 Ogden UT, USA  
 B.S. in Physics, Minor in Mathematics

**Honors**

**GK-12 Fellow**  
 Boston University, 2013–2014  
**Outstanding Physics Graduate**  
 Weber State University, 2007  
**Student Support Services Outstanding Tutor**  
 Weber State University, 2007

**Research  
 Experience**

**Graduate Research Assistant** May 2009–Present  
 BOSTON UNIVERSITY  
 Boston, MA  
*Supervisor: Alan Marscher*

Research Assistant for Boston University blazar group. Performed optical and IR imaging, and polarization measurements. Analyzed optical and infrared spectra including optical spectropolarimetry. Developed a model to separate the optical spectra of blazars into components arising from different emission mechanisms through the use of polarization measurements. Used data from the *Spitzer* space telescope in order to search the infrared emission of blazars for evidence of a thermal component emitted by hot dust.

**Student Research Assistant** Jan. 2004–Aug. 2007

WEBER STATE UNIVERSITY

*Supervisor: Stacy Palen*

Student research assistant on a project using public-domain data from the MaCHO database searching for tertiary companions to eclipsing binary stars. Developed a method to predict the flux from sparsely sampled lightcurves in order to search for offsets in the timing of eclipses from predictions.

**Student Research Assistant** May 2005–Aug. 2005

WEBER STATE UNIVERSITY

Ogden, UT

*Supervisor: John Armstrong*

Student research assistant working on testing the output of JPL's Virtual Planetary Laboratory (VPL). Compiled output from simulations of climate models of exoplanets based on physical parameters in order to determine habitability. Sampled a wide range of the available parameter space in order to determine where the output of the VPL became unphysical.

**Teaching  
and  
Outreach**

**Teaching Fellow** 2014–Present

BOSTON UNIVERSITY

2008–2009

Boston, MA

Served as a teaching assistant for introductory astronomy courses including courses on cosmology, exoplanets, the solar system, and introductory astrophysics. Graded coursework, was available for office hours, led discussions about past and upcoming lecture topics, and supervised laboratory activities.

**GK–12 Fellow** June 2013–June 2014

BOSTON UNIVERSITY

Boston, MA

*Supervisor: Sucharita Gopal*

*Teacher Partner: Yana Davis*

Visited 7th and 8th grade classrooms three days a week at the

Michael Driscoll School in Brookline, MA. Developed and implemented curriculum to teach school children Massachusetts science standards in a hands-on way by allowing them to gather data and draw evidence-based conclusions.

**Instructor** Aug. 2007–May 2008

ASTROCAMP  
Idyllwild, CA

Taught introductory science classes to students in grades 4–6 in fulfillment of California state science requirements. Topics included light, astronomy, sound, energy, Newton’s laws, and optics.

**Tutor** Aug. 2005–May 2007

WEBER STATE UNIVERSITY  
Ogden, UT

Tutored students in courses including introductory physics, calculus-based physics remedial mathematics, calculus, and astronomy. Strong emphasis on working with non-traditional college students; selected as Student Support Services Outstanding Tutor of the Year for 2007.

## Publications

*Thermal Emission Signatures in Non-thermal Blazars*

**M. P. Malmrose**, A. P. Marscher, S. G. Jorstad, & P. Smith, *in prep.*

*Comprehensive Monitoring of Gamma-Ray Bright Blazars. I. Statistical Study of Optical, X-Ray, and Gamma-Ray Spectral Slopes*

K. E. Williamson, A. P. Marscher, S. G. Jorstad, ..., **M. P. Malmrose**, ..., B. W. Taylor, & I. S. Troitsky, 2014, ApJ, 789, 135.

*Emission from Hot Dust in the Infrared Spectra of Gamma-ray Bright Blazars*

**M. P. Malmrose**, A. P. Marscher, S. G. Jorstad, R. Nikutta, & M. Elitzur, 2011, ApJ, 732, 116.

## Conferences

*Components of the Optical Spectra of Gamma-Ray Bright Blazars: The Search for Variability in the Big Blue Bump.*

**M. P. Malmrose**, A. P. Marscher, S. G. Jorstad, 2016, poster presented at Blazars Through Sharp Multi-Wavelength Eyes, Málaga Spain.

*The NIR to UV SEDs of Gamma-Ray Bright Blazars.*

**M. P. Malmrose**, 2015, dissertation talk presented at the 225th meeting of the American Astronomical Society, Seattle WA.

*The Spectral Energy Distributions of Gamma-Ray Bright Blazars.*

**M. P. Malmrose** et al., 2014, poster presented at the 224th meeting of the American Astronomical Society, Boston MA.

*Investigating the Role of Infrared Emission From a Dusty Torus as a Source of Seed Photons for Gamma-ray Emission.*

**M. P. Malmrose**, 2012, poster presented at the Fourth International Fermi Symposium, Monterey CA.

*The Detection of Hot Dust in the Infrared Spectra of Gamma-Ray Blazars*

**M. P. Malmrose**, 2011, talk presented at the 21st Annual New England Regional Quasar/AGN Meeting, New Haven CT.

*Emission from Hot Dust in the Infrared Spectra of a Gamma-Ray Bright Blazar.*

**M. P. Malmrose**, et al., 2011, poster presented at the 217th meeting of the American Astronomical Society, Seattle WA.

*Searching for Tertiary Companions to Eclipsing Binary Systems in the LMC.*

**M. P. Malmrose**, S. E. Palen, 2006, poster presented at the American Physical Society Four Corners Regional Meeting, Logan UT.

*Tertiary Companions to MaCHO Eclipsing Binaries*

B. Bailey, K. Smith, B. Edinger, D. Whelan, **M. P. Malmrose**, A. Johnson, & S. E. Palen, 2004, poster presented at the 204th meeting of the American Astronomical Society, Denver CO.

*Properties of Eclipsing Binary Stars in the MaCHO Database*

B. Bailey, K. Smith, B. Edinger, D. Whelan, **M. P. Malmrose**, A. Johnson, & S. E., Palen 2004 poster presented at the 204th meeting of the American Astronomical Society, Denver CO.

## Professional Memberships

American Astronomical Society (AAS), Jr. Member, 2010–present